Title

Right Ventricular Remodeling in Pulmonary Arterial Hypertension

Permalink

Author

Kwan, Ethan D

Publication Date

2024

UNIVERSITY OF CALIFORNIA SAN DIEGO

Right Ventricular Remodeling in Pulmonary Arterial Hypertension

A Dissertation submitted in partial satisfaction of the requirements
for the degree Doctor of Philosophy

in

Bioengineering

by

Ethan Dillon Kwan

Committee in charge:

Professor Daniela Valdez-Jasso, Chair
Professor Andrew McCulloch
Professor Robert Ross
Professor Francisco Villarreal

2024

The Dissertation of Ethan Dillon Kwan is approved, and it is acceptable in quality and form for publication on microfilm and electronically.

University of California San Diego

2024

DEDICATION

This dissertation is dedicated to my family. To Nathan: forever my role model and inspiration in academics and (more importantly) beyond. To Mom: none of this would have been possible without your support and sacrifice. I love you both dearly.

TABLE OF CONTENTS

DISSERTATION APPROVAL PAGE iii

DEDICATION iv

TABLE OF CONTENTS v

LIST OF FIGURES x

LIST OF TABLES xv

LIST OF ABBREVIATIONS xvi

ACKNOWLEDGEMENTS xviii

VITA xx

ABSTRACT OF THE DISSERTATION xxi

Chapter 1 INTRODUCTION 1

1.1 Background 1

1.2 Clinical Indications, treatment, and prognosis of PAH 7

1.3 Right-Ventricular Hemodynamics 12

1.4 Animal models of PAH 19

1.5 Characterizing RV biomechanics 23

1.6 Sex Differences 27

1.7 Current Knowledge Gaps 31

1.8 Our Approach 33

1.9 References 37

Chapter 2 LONGITUDINAL RIGHT VENTRICULAR HEMODYNAMIC AND MORPHOLOGIC CHANGES IN PULMONARY ARTERIAL HYPERTENSION 45

2.1 Introduction 45

2.2 Approach 46

- 2.2.1 Animal Model of PAH 46
- 2.2.2 Assessing *in-vivo* Hemodynamics 48

2.2.3 Pressure-Volume Catheter Measurements 49
2.2.4 Raw Data Processing 51
2.2.5 Computing Right-Ventricular Hemodynamics from Raw Data 53
2.2.6 Non-Invasive Right-Ventricular Measurements 55
2.2.7 Histological Measurements of Right-Ventricular Hypertrophy and Fibrosis 55
2.2.7 Statistical analysis 57
2.3 Results: Distinct Time courses of Hypertrophy and Stiffening 57
2.3.1 Ventricular Hemodynamics and Morphology 58
2.3.2 Insights from extending SuHx treatment up to 26 weeks 65
2.4 Discussion: Time Course of Hypertrophy and Diastolic Stiffening 69
2.4.1 Systolic Function 70
2.4.2 Diastolic Function 71
2.4.3. Longitudinal Progression 72
2.5 Conclusion 73
2.6 Acknowledgements 73
2.7 References 74
Chapter 3 SEX-DEPENDENT RIGHT VENTRICULAR HEMODYNAMIC AND MORPHOLOGIC CHANGES IN PULMONARY ARTERIAL HYPERTENSION 78
3.1 Introduction 78
3.2 Approach 79
3.2.1 Experimental Design 79
3.2.2 Hemodynamic Measures 80
3.2.3 Histological measurements of Right-Ventricular Hypertrophy and Fibrosis 82
3.2.4 Cardiac Magnetic Resonance Imaging 83
3.2.6 Statistical Analysis 84
3.3 Results: Sex-based rat study 85

  3.3.1 Effects due to SuHx 85
  3.3.2 Effects due to sex 87
  3.3.3 Histology: RV tissue shows myocyte hypertrophy and fibrosis in all SuHx groups. 89
  3.3.4 Female RVs become rounder due to SuHx 93
3.4 Discussion 100
  3.4.1 Systolic Function in Patients 102
  3.4.2 Diastolic Function in Patients 103
  3.4.3 Sex Dependent Remodeling of Right-Ventricular Geometry 104
3.5 Conclusion 106
3.6 Acknowledgements 106
3.7 References 106
Chapter 4 COMPUTATIONAL MODELS OF RV BIOMECHANICS 112
4.1 Introduction 112
4.2 Approach 113
  4.2.1 Implementing a Laplace Model of Right-Ventricular Biomechanics 113
4.3 Results 128
  4.3.1 10-week SuHx male longitudinal study 128
  4.3.3 Sex differences 134
4.4 Discussion 139
  4.4.1 Model Analysis Insights into Longitudinal Right-Ventricular Changes 139
  4.4.2 Sex Differences in Patients with PAH 143
4.5 Conclusion 144
4.6 Acknowledgements 145
4.7 References 146
Chapter 5 REMODELING OF RIGHT VENTRICULAR MYOCYTE MECHANICS IN PULMONARY ARTERIAL HYPERTENSION 150

5.1 Introduction 150

Excitation-Contraction Coupling in Pulmonary Hypertension........ 150

5.2 Approach 153

5.2.1 Right-Ventricular Cardiomyocyte Isolation 154

5.2.2 Right-Ventricular Myocyte Drug Testing 156

5.2.3 Statistical Analysis.. 157

5.3 Results 158

5.3.1 Myocyte Shortening and Calcium 158

5.3.2 SR Calcium Load.. 161

5.4 Discussion.. 164

5.5 Conclusion.. 168

5.6 Acknowledgements 168

5.7 References 169

Chapter 6 CORRELATIONAL AND CLUSTER ANALYSES OF HEMODYNAMIC DATA USING MACHINE LEARNING.. 174

6.1 Introduction 174

6.2 Approach 175

6.2.1 Data.. 176

6.2.2 Numerical Methods 177

6.3 Results 178

Clustering Results.. 181

6.4 Discussion.. 184

6.5 Conclusion.. 186

6.6 Acknowledgements 187

6.7 References 187

Chapter 7 CONCLUSIONS 189

7.1 Clinical applications 192
7.2 Limitations 195
    7.2.1 Animal Model 195
    7.2.2 Experimental Measurements 196
    7.2.3 Computational Modeling 198
7.3 Future directions 199
7.4 References 200

LIST OF FIGURES

Figure 1.1. Pressure-volume loops depict the stages of the cardiac cycle, from which key hemodynamic parameters can be determined. The end-systolic and end-diastolic points are marked by blue dots, separating systolic and diastolic stages of contraction and relaxation... 16

Figure 2.1. Sprague-Dawley rats were treated with sugen-hypoxia. The vascular endothelial growth factor receptor antagonist Sugen5416 was subcutaneously injected, after which rats were exposed to chronic hypoxia. After three weeks of hypoxia exposure, rats were returned to normoxia, during which the disease was augmented by time 47

Figure 2.2. In a different cohort of 28 male rats, SuHx treatment duration was extended to augment the severity of the disease. Although the hypoxia duration was kept at 3 weeks, time in normoxia was extended up to 23 weeks for a total of 26 weeks of SuHx treatment. 48

Figure 2.3. The RV chamber was catheterized with a pressure-volume admittance catheter (**A**) which recorded continuous pressure-volume timeseries (**B**), from which pressure-volume loop analysis was performed during steady state, and during preload variation (**C**). 52

Figure 2.4. *In-vivo* hemodynamic measurements in SuHx rats through the 10-week time course of the study showed significant increases by week 3 in end-systolic (ES) right ventricular pressure (**A**) and mean pulmonary arterial pressure (**C**), significant increases in total pulmonary vascular resistance by week 4 (**F**) 59

Figure 2.5. While SuHx treatment increased ES volume (**A**), ED volume (**B**) was preserved throughout the study apart from a small but significant increase at week 3. The unloaded RV volume (**C**), approximated from caval occlusions, did not significantly change. Stroke volume (**D**) and cardiac output (**E**)... 60

Figure 2.6. Masses of right ventricle (**A**) left ventricle plus septum (**B**), and their mass ratio (**C**), right ventricular wall thickness (**D**) and estimated V_o (**E**). Data shown as mean ± standard error, $*p < 0.05$ and $\# p < 0.01$ compared with the control group.. 61

Figure 2.7. Pressure-volume (P-V) during caval occlusion to determine end-systolic (ES) and end-diastolic (ED) P-V relations for a control (**A**) and a 6-week SuHx (**B**) animal. ES elastance E_{es} (**C**), ED elastance E_{ed} (**D**), arterial elastance E_a (**E**) and ventricular-vascular coupling E_{es}/E_a (**F**). 61

Figure 2.8. The average tricuspid annular plane systolic excursion (TAPSE) was measured from echocardiography in a small subset of animals. These measures show an overall reduction in the RV longitudinal shortening in rats treated with 4 weeks of SuHx. 63

Figure 2.9. Histologic collagen to myocyte area fraction (**A**) from Masson's trichrome-stained RV sections in control (**D**) rats and SuHx rats at weeks 3 (**E**), 4 (**F**), 6 (**G**), 8 (**H**), and 10 (**I**) was only significantly different from control at week 6 ($p<0.05$). RV myocardial total collagen content (**B**) and collagen type I to III ratio (**C**)... 64

Figure 2.10. Immunosorbent assays were used to measure the concentration of advance glycation end products, a measure of non-enzymatic collagen crosslinking. AGE concentration only showed a significant change at 4 weeks of SuHx treatment and returned to control levels through ten weeks. Data shown as mean ± standard error................................ 65

Figure 2.11. Immunosorbent assays were used to measure the concentration of pyridinoline cross-linked collagen peptides. No accumulation of PYD was observed and PYD was not significantly changed through 18 weeks of SuHx. Data shown as mean ± standard error. 66

Figure 2.12. Longitudinal hemodynamic and morphologic measurements at timepoints extending to 26 weeks of SuHx treatment were acquired in male rats. Shown are ES pressure (**A**), ED pressure (**B**), PVR (**C**), ES volume (**D**), ED volume (**E**), stroke volume (**F**), ejection fraction (**G**), RV mass (**H**), and the Fulton Index (**I**). 67

Figure 2.13. Longitudinal measurements of RV ES elastance (**A**), ED elastance (**B**), arterial elastance (**C**), and ventricular-vascular coupling (**D**). ES, ES, and arterial elastance gradually increased, peaking at W8-10, before reversing in the later weeks. Ventricular-vascular coupling decreased to a minimum at W12 before reversing and stabilizing 68

Figure 2.14. Longitudinal measurements of the liver mass show no progressive increases in liver mass in male rats treated with SuHx for up to 26 weeks. 69

Figure 3.1. Invasive hemodynamic measurements of RV function in normotensive (control, solid) and hypertensive (SuHx, patterned) rats from male (grey), ovary-intact female (female, blue) and ovariectomized female (OVX, green) rats. 86

Figure 3.2. Mean end-systolic (top) and end-diastolic (bottom) pressure-volume measurements for control (black) and sugen-hypoxia (SuHx, teal) male (**A**), ovary-intact (**B**), and ovariectomized (OVX) female (**C**) rats during preload variation. 88

Figure 3.3. Longitudinal cross-sections of the RV myocardium demonstrate thickening of the myofiber in SuHx (right) compared to control (left). 89

Figure 3.4. Histological cross-sections of RV myocardium excised from male (top), female (middle), and ovariectomized female (bottom) rats treated with SuHx (right) were compared to control (left). In all groups, acute myocyte hypertrophy was observed, characterized by enlargement of myofiber diameter. 90

Figure 3.5. Transverse cross-sections of the RV myocardium were automatically segmented and revealed increases in average myocyte cross-sectional area (left) and myocyte diameter (right) due to SuHx treatment. Increases were most pronounced in female SuHx. 91

Figure 3.6. Hydroxyproline total collagen assay revealed significant increases in all SuHx-treated groups in the RV myocardium excluding the thickened tissue near the RV inlet. Data shown as means ± standard error of the mean. 91

Figure 3.7. Hydroxyproline assays show total collagen content in RV myocardium samples from male (top), female (middle), and OVX (bottom) female rats across multiple weeks of SuHx. No significant or progressive accumulation of collagen was found in any groups at week 8 92

Figure 3.8. SuHx treatment resulted in no significant changes in the hydroxyproline/tissue density in the RV myocardium from the infundibulum, when all weeks of data were combined. Data shown as mean ± standard error. 93

Figure 3.9. Cardiac MRI in control (top) and SuHx-treated (bottom) hearts of male (left), female (middle), and ovariectomized female (right) rats. CMR images reveal a more pronounced rounding of the RV chamber geometry after 8 weeks of SuHx in female and OVX

than in male rats. Images were acquired for control (2 male, 2 female, 2 OVX) and SuHx (3 male, 4 female, 3 OVX) rats. 94

Figure 3.10. CMR images of male rats treated with SuHx, paired between three time points for Male rat 1 (top), and paired between two time points for male rats 2-4. The crescent RV shape was largely maintained in male rats seen clearly in rats 1, 2, and 4. 95

Figure 3.11. CMR images of female rats treated with SuHx, paired between three timepoints for female rat 1-2 (top) and two timepoints for female rats 3-4 (bottom). SuHx W4 and W8 corresponded to more changes to RV shape. 96

Figure 3.12. Both the intact (blue) and ovariectomized (green) female rats increased RV-septal mid-wall diameter (**A**) in SuHx (patterned) compared to control (solid). RV cross-sectional area to perimeter ratio (**B**) increased in female and OVX SuHx but not male rats (grey) with the largest increases in the OVX rat groups. 96

Figure 3.13. Paired rat-specific measurements of the RV-septum midwall diameter (**A**), the ratio of RV short-to-long diameter (**B**), and the RV area to perimeter ratio (**C**) derived from CMR images in male (black), female (blue), and ovariectomized female (gold) rats. 97

Figure 3.14. Minimum RV pressure was computed from caval occlusions and increased in response to SuHx treatment in all three groups. Data shown as mean ± standard error. #p<0.05 97

Figure 3.15. Longitudinal measurements at timepoints extending to 26 weeks of SuHx treatment were performed in males (black), as well as compared with female (blue) and ovariectomized females (green). 99

Figure 3.16. Measurements of left ventricular hemodynamics in male (grey), female (blue), and ovariectomized female (gold) rats treated with 0 (solid), 4, 8, or 12 weeks of SuHx (dashed). 100

Figure 4.1. Model representation of the RV chamber geometry (**A**), comprised of a sphere of radius R, wall thickness of *h* and mid-wall radius *r*. The RV was composed of RV chamber (V_{RV}), RV free wall (V_W), and Septal wall (V_{SW}) volumes, as indicated from cardiac magnetic resonance images at end of systole (**B**) and end of diastole (**C**). 114

Figure 4.2. RV to RV + LV volume ratios obtained from invasive morphological measurements from excised hearts. The ratio had a mean of 0.54 in controls and 0.61 in SuHx, justifying the model assumption of 0.55. 115

Figure 4.3. Model predictions of the end-systolic pressure volume relationship in a representative control (**A**) and SuHx Week 8 (**B**) male rat, based on changing the isometric length-tension shape parameter *B*. 120

Figure 4.4. Root mean squared errors for the male rat models over a range of timepoints fitted to end-diastolic (**A**) and end-systolic (**B**) pressure-volume data shown as a percent of the measured end-diastolic volume and end-systolic pressure. For each animal group, the median RMSE is shown. 123

Figure 4.5. Illustration of the rat-specific modeling pipeline which inputs hemodynamic and morphologic data, fits biomechanics models, and identifies the material parameters of those rat-specific models. 124

Figure 4.6. Comparison of the accuracy of the models of the male group average PV data (**A**) compared to models fitted to rat-specific average data (**B**). This analysis indicates that both models reproduce the measured PV data. 125

Figure 4.7. Measurements of control (white bars) and SuHx (gray bars) RV pressure for end systole (**A**) and end diastole (**B**) compared with model predictions of pressure 129

Figure 4.8. Model-predicted mean active end-systolic (*top*) and passive end-diastolic (*bottom*) fiber stress-sarcomere length relations for control (green) and SuHx (blue) male rats at weeks 3 (**A**), 4 (**B**), 5 (**C**), 6 (**D**), 8 (**E**), and 10 (**F**). 131

Figure 4.9. Model material parameters used to fit the measured pressure-volume relation for each male rat included in the study. Passive material parameters k_1 (**A**), k_2 (**B**), their product k_1k_2 (**C**), and myofilament activation material parameter k_3 (**D**). *$p < 0.05$ compared with control group. 133

Figure 4.10. The relative contributions of changes in RV geometry (black, patterned) and myocardial material properties (teal, patterned) to changes in ES pressure (**A**) and ED pressure (**B**) were distinguished using the model. 136

Figure 4.11. Model predicted sarcomere length-tension relations in control (black) and SuHx (teal) animals. 137

Figure 4.12. Active and passive wall stresses were computed at the average end-systolic and end-diastolic point for each group. While active wall stresses significantly increased in all groups, increases to passive wall stress were significant only in male SuHx. 138

Figure 5.1. Diagram illustrating the myocyte experimental pipeline. Animals (**A**) were studied with invasive hemodynamic measurements (**B**), after which myocytes were isolated via Langendorff enzymatic digestion (**C**), then seeded onto a microscopy platform (**D**), viewed through a fluorescent 40x immersion objective lens (**E**). 155

Figure 5.2. Repeated rat-specific and cell-specific measurements were represented as group measurements as indicated by the schematic. From each animal, multiple cells (typically 8-15) were measured (top left), with the mean calcium transient shown in bold. 156

Figure 5.3. RV myocyte cell survival was determined following isolation. Across all groups, SuHx treatment resulted in decreased cell survival. Data shown as mean ± standard error. . 158

Figure 5.4. Calcium transients (**A-C**) in isolated RV myocytes derived from male (grey), ovary-intact female (blue), and ovariectomized female (green) normotensive (solid) compared with SuHx (patterned) rats. 160

Figure 5.5. Peak-aligned and amplitude normalized calcium transients were compared for male, female, and OVX groups (left), and illustrated for baseline and SuHx groups (right). While there were no significant differences in the calcium transient shape across treatment or groups, the OVX group showed the most prolonged relaxation 161

Figure 5.6. Acute administration of the drug caffeine resulted in acute complete release of the calcium reserves within the sarcoplasmic reticulum. The subsequent calcium transient profile was captured, along with the sarcomere length during contraction. 162

Figure 5.7. Diastolic intracellular calcium showed a significant increase in myocytes derived from SuHx treated male and ovariectomized female rats, but not in ovary-intact female rats.

The increase was the greatest in male SuHx. #$p < 0.05$ compared with control group. Data shown as mean ± standard error. 163

Figure 5.8. Administration of the drug caffeine resulted in acute release of SR calcium stores. 164

Figure 6.1. An illustration of the analysis approach. Pressure-volume hemodynamic measurements obtained at various stages of disease are the primary data to input into machine learning analyses. 175

Figure 6.2. Pair plots illustrate correlations between predictors. 178

Figure 6.3. Pair plots were used to investigate correlations between parameters of interest, such as the relation between RV hypertrophy (y-axis), and RV systolic function (dP/dt_{max}, E_{es}), and pulmonary vascular resistance (PVR). 179

Figure 6.4. The cumulative eigensum, representing the proportion of variance in the dataset explained by each additional principal component was calculated for the first ten principal components. The majority of the variance in the dataset was explained by the first three principal components (PC1-3). 179

Figure 6.5. The loadings for Principal components 1-4 are shown (left to right, top to bottom) and reveal which predictors were most important for explaining each principal component. For PC 1, ES pressure was the most important predictor. For PC2-4, cardiac output, ES volume, and heart rate were the most important predictors respectively. 181

Figure 6.6. Elbow analysis was used to select the number of clusters n to include in the analysis. Elbow analysis revealed multiple inflection points, including at $n = 2$, 3, and 6. ... 182

Figure 6.7. Average predictor values for each cluster are shown for the top contributors to the first two principal components, which comprised half (~47%) of the total variance in the dataset. 184

LIST OF TABLES

Table 2.1. RV chamber volumes, ejection fractions and stroke volumes measured by invasive catheterization for control and SuHx week 4 groups (mean ± standard deviation) compared with those in individual animals measured using cardiac magnetic resonance imaging (cMRI). 62

Table 4.1. RV to RV+LV volume ratios obtained from cardiac MRI. This ratio increased with SuHx treatment, primarily due to RV wall hypertrophy. 115

Table 4.2. Model-derived radius and radius-to-wall-thickness ratios for a range of control and PAH treated animals demonstrate the radius to wall-thickness ratio remaining above 5:1 in all groups, justifying the Laplace thin-walled assumption. 121

Table 4.3. Model material parameters of stiffness (k_1, k_2) and calcium dependent contractility (k_3) for male, female, and ovariectomized female control groups. 125

Table 4.4. In a subset of female control animals, ED PV relations were fitted based on general linear and exponential formulations. The linear EDPVR showed a small improvement (n.s.) in the R^2 value. Data shown as mean ± standard error. 126

Table 4.5. In a subset of female SuHx animals, ED PV relations were fitted based on general linear and exponential formulations. While the non-linear EDPVR showed a larger mean R^2 compared to the linear EDPVR (n.s.), the differences were negligible. Both models showed improved fits compared to the model fits in female control animals. 127

Table 4.6. The model was used to decouple the relative effects of volume, geometry, and material properties on systolic and diastolic function. 128

Table 4.7. Average myocardial fiber stress in the four model conditions is shown across 10 weeks of SuHx in males. Active stress and strain were calculated based on end-systolic pressure and volume while passive stress and strain were based on end-diastolic pressure and volume. 134

Table 4.8. Wall stresses calculated for control and SuHx rats show that ED fiber stress significantly increased in the male SuHx group but not the female and OVX female groups. Conversely, ES fiber stress showed similar increases in all three SuHx groups. 138

Table 6.1. In total, 27 experimental measurements were categorized as structural or hemodynamic predictors and input into the analysis. 176

Table 6.2. Hierarchical clustering results. Cluster 1 discriminated the role of sex and Cluster 2 discriminated the role of weeks, while Cluster 3 was primarily composed of later-week male animals. Group-treatment combinations that were primarily sorted (>66%) into a single cluster were bolded for emphasis. 183

LIST OF ABBREVIATIONS

PAH	Pulmonary Arterial Hypertension
RV	Right Ventricle
LV	Left Ventricle
CT	Computed Tomography
MRI	Magnetic Resonance Imaging
cMR	Cardiac Magnetic Resonance
ES	End-Systole/End-Systolic
ED	End-Diastole/End-Diastolic
P-V	Pressure-Volume
EDP	End-Diastolic Pressure
ESP	End-Systolic Pressure
EDV	End-Diastolic Volume
EDP	End-Diastolic Pressure
EF	Ejection Fraction
SV	Stroke Volume
CO	Cardiac Output
E_{es}	End-Systolic Elastance
E_{ed}	End-Diastolic Elastance
PVR	Pulmonary Vascular Resistance
mPAP	Mean Pulmonary Arterial Pressure
6MWD	6-Minute Walk Distance
TAPSE	Tricuspid Annular Plane Systolic Excursion

SuHx	Sugen-Hypoxia
MCT	Monocrotaline
BMPR2	Bone Morphogenic Protein Receptor Type 2
PDE5	Phosphodiesterase-5
ELISA	Enzyme Linked Immunosorbent Assays
SR	Sarcoplasmic Reticulum
SERCA	Sarco-Endoplasmic-Reticulum Ca-ATPase

ACKNOWLEDGEMENTS

I would like to acknowledge Professor Valdez-Jasso for their support as the chair of my committee. Their mentorship has resulted in much personal and professional growth over the past years.

Chapter 2, in full, is a reprint of the material as it appears in Distinct Time Courses of Right Ventricular Hypertrophy and Diastolic Stiffening in a Male Rat Model of Pulmonary Arterial Hypertension. Kwan, Ethan D.; Velez-Rendon, Daniela; Zhang, Xiaoyan; Mu, Hao; Patel, Megh; Pursell, Erica; Stowe, Jennifer; Valdez-Jasso, Daniela. American Journal of Physiology Heart and Circulatory Physiology. 2021. The dissertation author was the primary investigator and author of this paper.

Chapter 3, in full, is a reprint of the material as it appears in Sex-Dependent Remodeling of Right Ventricular Function in a Rat Model of Pulmonary Arterial Hypertension. Kwan, Ethan D.; Hardie, Becky A.; Garcia, Kristen M.; Mu Hao; Wang, Tsui-Min; Valdez-Jasso, Daniela. American Journal of Physiology Heart and Circulatory Physiology. 2024. The dissertation author was the primary investigator and author of this paper.

Chapter 4, in part, is a reprint of the material as it appears in Distinct Time Courses of Right Ventricular Hypertrophy and Diastolic Stiffening in a Male Rat Model of Pulmonary Arterial Hypertension. Kwan, Ethan D.; Velez-Rendon, Daniela; Zhang, Xiaoyan; Mu, Hao; Patel, Megh; Pursell, Erica; Stowe, Jennifer; Valdez-Jasso, Daniela. American Journal of Physiology Heart and Circulatory Physiology. 2021. The dissertation author was the primary investigator and author of this paper.

Chapter 4, in part, is a reprint of the material as it appears in Sex-dependent Remodeling of Right-Ventricular Function in a Rat Model of Pulmonary Arterial Hypertension. Kwan,

Ethan D.; Hardie, Becky A.; Garcia, Kristen M.; Mu, Hao; Wang, Tsui-Min; Valdez-Jasso, Daniela. American Journal of Physiology Heart and Circulatory Physiology. 2024. The dissertation author was the primary investigator and author of this paper.

Chapter 4, in part, is a reprint of the material as it appears in A Computational Study of Right Ventricular Mechanics in a Rat Model of Pulmonary Arterial Hypertension. Odeigah, Oscar O.; Kwan, Ethan D.; Garcia, Kristen M.; Valdez-Jasso, Daniela; Sundnes, Joakim. Frontiers in Physiology. 2024. The dissertation author was the second author of this paper.

Chapter 5, in part, is a reprint of the material as it appears in Sex-dependent Remodeling of Right-Ventricular Function in a Rat Model of Pulmonary Arterial Hypertension. Kwan, Ethan D.; Hardie, Becky A.; Garcia, Kristen M.; Mu, Hao; Wang, Tsui-Min; Valdez-Jasso, Daniela. American Journal of Physiology Heart and Circulatory Physiology. 2024. The dissertation author was the primary investigator and author of this paper.

Chapter 5 contains unpublished material coauthored with Kwan, Ethan D; Wang, Tsui-Min; and Valdez-Jasso, Daniela. The dissertation author was the primary author of this chapter.

Chapter 6 contains unpublished material coauthored with Kwan, Ethan D; Hui, Jingwen; Moylan, Leah; and Valdez-Jasso, Daniela. The dissertation author was the primary investigator and author of this chapter.

VITA

2018 Bachelor of Science in Biomedical Engineering, The University of Texas at Austin

2021 Master of Science in Bioengineering, University of California San Diego

2024 Doctor of Philosophy in Bioengineering, University of California San Diego

PUBLICATIONS

Kwan, Ethan D.; Velez-Rendon, Daniela; Zhang, Xiaoyan; Mu, Hao; Patel, Megh; Pursell, Erica; Stowe, Jennifer; and Valdez-Jasso, Daniela. *Distinct Time Courses of Right Ventricular Hypertrophy and Diastolic Stiffening in a Male Rat Model of Pulmonary Arterial Hypertension.* American Journal of Physiology Heart and Circulatory Physiology. 2021 Oct 1; 321(4): H702-H715.

Odeigah, Oscar O.; Kwan, Ethan D.; Garcia, Kristen M.; Finsberg, Henrik; Valdez-Jasso, Daniela; Sundnes, Joakim. *A Computational Study of Right Ventricular Mechanics in a Rat Model of Pulmonary Arterial Hypertension.* Frontiers in Physiology. 2024 Mar 10.

Kwan, Ethan D.; Hardie, Becky A.; Garcia, Kristen M.; Mu, Hao; Wang, Tsui-Min; and Valdez-Jasso, Daniela. *Sex-dependent Remodeling of Right Ventricular Function in a Rat Model of Pulmonary Arterial Hypertension.* American Journal of Physiology Heart and Circulatory Physiology. 2024 Jul 15; 327(2): H351-H363.

FIELD OF STUDY

Major Field: Bioengineering
    Studies in Cardiac Biomechanics
    Studies in Computational Mechanics
    Studies in Data Analysis

ABSTRACT OF THE DISSERTATION

Right Ventricular Remodeling in Pulmonary Arterial Hypertension

by

Ethan D. Kwan

Doctor of Philosophy in Bioengineering

University of California San Diego, 2024

Professor Daniela Valdez-Jasso, Chair

Pulmonary Arterial Hypertension is a severe disease defined by sustained elevated pulmonary arterial pressures. This progressive vasculopathy is characterized by structural and mechanical remodeling of the pulmonary arteries that chronically impose a pressure overload on the right ventricle, stimulating myocardial hypertrophy and remodeling of the RV chamber. Although PAH is confirmed in the pulmonary arteries, the health and function of the right

ventricle is the most important clinical predictor of patient outcomes. The RV progressively adapts to pressure overload and can transiently maintain its output, but PAH commonly leads to RV dysfunction and premature death. Why and how the RV transitions from adaptive to maladaptive function remains unknown. This knowledge gap helps to explain why, despite its significant role in determining morbidity and mortality, no current therapies specifically target the RV.

Importantly, clinical management of PAH is confounded by the estrogen paradox, whereby PAH primarily and disproportionally affects women, but with women also exhibiting improved RV function and outcomes in the face of PAH compared to men. Clinical studies have highlighted the association between sex and RV hemodynamic function, with previous research indicating correlations between improved RV function and both endogenous and exogenous estrogens. However, most animal studies have focused on males, resulting in limited sex-specific RV data. Consequently, the role of sex and ovarian hormones in PAH remains unclear.

In this dissertation, we explore the pathological remodeling of the right ventricle in pulmonary arterial hypertension and the evolution of hemodynamic, structural, and mechanical properties of the RV during the progression of PAH. By leveraging experimental measurements of cardiac hemodynamics, morphology, and myocardial mechanics, and by analyzing computational biomechanics models, we investigate organ, tissue, and cell changes to enhance our understanding of right ventricular remodeling in the context of PAH.

We characterized the longitudinal evolution of RV hemodynamics during the progression of PAH using an established animal model. Implementing a computational model of RV biomechanics, we decoupled the relative contributions of geometric and material remodeling of the RV myocardium to changes in RV function. We identified distinct stages of RV adaptation whereby myocardial hypertrophy initially stabilized systolic function after which substantial diastolic myocardial stiffening occurred and prevented RV dilation. We then investigated the effects of sex- and ovarian-hormone presence on systolic and diastolic function. We identified distinct phenotypes of RV adaptation that were sex- and ovarian hormone dependent. We found that male rats responded to PAH with the most severe diastolic stiffening of any group. Female rats that were ovariectomized demonstrated increases in systolic elastance that were explained by myocyte contractility upregulation via calcium transient enhancement. By contrast, ovary-intact female rats adapted to PAH with the fewest changes to RV mechanical properties compared to the other groups. These results provide evidence of sex-dependent changes that could be specifically targeted for therapies. By combining in-vivo measurements with our computational modeling, we reached important conclusions about the decoupled effects of myocardial changes to RV function at varying stages of disease. These findings provide new insights into the mechanisms underlying stages of adaptation to PAH.

Chapter 1 INTRODUCTION

1.1 Background

The foundation of our modern-understanding of cardiac physiology was laid in 1628 when British physician William Harvey published his now-renowned book "Exercitatio Anatomica de Motu Cordis et Sanguinis in Animalibus" (on the movement of the heart and blood in animals)[1]. In this seminal work 4 centuries ago, Harvey described the 4-chambered anatomy, the motion of the heart in contraction and relaxation, observed the role of muscle mass to metabolic demands, identified the heart's role in generating the mechanical work to sustain blood flow, and was the first to describe the importance of the role of the right heart: "the right ventricle may be said to be made for the sake of transmitting blood through the lungs"[1].

However, for many years to follow, cardiology focused on left ventricular physiology. Experimental canine studies from the early 20th century suggested the RV had a relatively insignificant role on cardiac output and systemic venous and pulmonary arterial pressure regulation compared to the left ventricle (LV)[2,3]. In 1971, Fontan and others demonstrated the success of a surgical procedure bypassing the right ventricle and directing vena caval blood directly to the pulmonary arteries to treat tricuspid atresia[4], which further perpetuated the notion that the function of the right ventricle was not necessary for maintenance of normal circulation. This historical context helps to illustrate why many knowledge gaps remain with respect to mechanisms of healthy right heart function, right heart failure, and recovery. More recently, alongside advancements in technologies facilitating the study of the RV, the importance of the size, health, and function of the right heart on cardiac outcomes in a variety of conditions including left heart failure, myocardial infarction, congenital heart disease, and tricuspid valve disease has become increasingly recognized[5].

The physiology, hemodynamic function, and developmental etiological origin of the right ventricle differs greatly compared to the left ventricle and extrapolating existing knowledge of left ventricular remodeling and disease (that is more commonly studied) to the right ventricle is limited[5]. Therefore, not only is understanding the RV's function important due to a historical attention gap, but understanding the RV's function is vitally important in PAH, in which the health and function of the RV is the most important determinant of outcomes.

Anatomy and Right- Left- Ventricular Relation

The heart plays a vital role in distributing blood to support the normal functioning of all organs. Through coordinated contraction of the myocardium, pressure is generated that propels blood flow through arteries to the entire body. This consistent rhythmic pumping maintains circulation to all bodily tissues, ensuring proper nourishment and function. Blood primarily carries oxygen, glucose, and nutrients essential for survival through the circulatory system. The heart, the mechanical driver of this system, is divided into four chambers: left and right atria and left and right ventricles. The circulatory system is commonly considered in two parts: the pulmonary circulation describes the passage of blood through the vessels of the lungs and is mechanically powered by the right half of the heart, and the systemic circulation describes the movement of blood through the remainder of the body and is mechanically driven by the left half of the heart[6]. The RV and LV walls are encircled by many shared muscle fibers, share a myocardial septum wall, and are enclosed within the boundaries of the pericardium, meaning the function of both ventricles are affected by the other and it is important to remember the fundamental coupling between the function and remodeling of both ventricles.

The mechanical forces that primarily drive the movement of blood come from the ventricles: the two muscularized chambers of the heart that contract via electro-chemical response to electrical stimuli to deliver the mechanical energy to the blood that sustains its movement through the circulation[7]. While the left ventricle is generally described as cylindrical/circular, the right ventricle has a crescent-shaped geometry that wraps around the left ventricle. Some anatomical studies divide the RV chamber into three components: the inlet region that comprises the tricuspid valve and attached chordae tendineae and papillary muscles; the outflow region that comprises the infundibulum, a smooth tubular myocardium; and the apex which comprises muscularized and trabeculated myocardium that form the bottom of the heart[7]. Other studies separate the right ventricular myocardial wall based on the relative internal blood pressures felt at the inflow, apex, and outflow tract. Anatomically, the right ventricle can be divided into a free wall and a septal wall which divides the right and left ventricles.[8] RV contraction consists of three parts: the circumferential compression of the free wall towards the central cardiac axis; contraction of the longitudinal fibers; and free wall traction. Functionally, the RV can be divided into the sinus, primarily comprises the free wall and the apex, and the infundibulum, which comprises of the outflow region that extends to the pulmonary valve. The volume of the RV chamber is larger than the volume of the LV, despite RV myocardial mass being 15-30% of that of the LV myocardial mass[8]. These geometric differences correspond to significant differences in wall thickness and wall stresses that develop in the two chambers. Because of the higher surface to volume ratio of the thin-walled RV, it may be more capable of adapting to increased preload without increasing end-diastolic pressure, however, may also be more sensitive to afterload. These biomechanical changes to the RV play a critical role in determining health and function, as we discuss later in this work.

Pathophysiology of Pulmonary Arterial Hypertension

Pulmonary Hypertension (PH) describes a range of clinical conditions whereby mean pulmonary arterial blood pressure is chronically elevated above healthy physiological ranges. The latest world health organization guidelines define this threshold at 20mmHg, or two standard deviations above healthy values[9]. Pulmonary hypertension is rarely an isolated disorder, nor is it even often a primary disorder, but commonly presents as a complex phenotype affecting the cardiopulmonary circuit with associated comorbidities. While the RV can transiently adapt to pulmonary hypertension in the short term, it commonly results in right ventricular dysfunction, failure, and death. Some of the RV changes commonly seen in patients with PAH include myocardial hypertrophy (muscle wall growth), RV dilation (expansion of the RV chamber), and contractility (capability of the muscle cells to generate force) changes. It is believed that RV failure develops once the RV's compensatory mechanisms are exhausted to insufficiency against progressive pressure increases. RV failure remains inadequately defined and is frequently benchmarked to the RV ejection fraction (ejection volume/filled volume)[10,11]. A more robust definition (suggested by the American Thoracic Society in 2018) defines RV failure as a syndrome of insufficient blood delivery by the RV and elevated systemic venous pressure at rest or exercise, occurring as a consequence of alterations in preload, changes in RV mechanics, lusitropy or contractility, and/or increases in afterload[11].

Pulmonary Hypertension Categories

Currently, pulmonary hypertension is divided by the World Health Organization into five separate classifications based on distinct diagnostic criteria, to better standardize patient care[9]. Group 1 pulmonary hypertension refers to pulmonary arterial hypertension (PAH), characterized by progressive remodeling and vascular obliterative lesions that result in pulmonary arterial vasoconstriction, vascular cell proliferation and increases to pulmonary vascular resistance. Group 1 PAH is associated with progressive remodeling of the right ventricle, as the increases to vascular resistance impose an increase in afterload on the right ventricle. While the RV can initially compensate for these changes, PAH commonly leads to increased RV failure. Group 1 PAH is often referred to as idiopathic, as the mechanisms and mediators of this subgroup remain unclear. PAH may be associated with cardiac comorbidities such as scleroderma, infection (such as HIV), or drug-induced, and there are very likely strong genetic components (BMPR2 mutation) associated with PAH susceptibility.

Group 2 pulmonary hypertension is associated with and often secondary to left-heart disease. Cardiac insufficiency in the left ventricle results in a buildup of blood and pressure in the pulmonary vasculature. Group 3 pulmonary hypertension is associated with chronic pulmonary disease or alveolar hypoxia. These chronic pulmonary conditions initiate a downstream cascade that results in vasoconstriction and pulmonary hypertension. Clinically, group 2 and group 3 PH are the most diagnosed forms of PH. Group 4 pulmonary hypertension is associated with thromboembolisms which partially or completely occlude pulmonary vascular branches. Group 5 is a catch-all subgroup characterized by multifactorial pulmonary hypertension or pulmonary hypertension with unclear mechanisms.

Within the scope of this dissertation, we will consider group 1 pulmonary hypertension – Pulmonary Arterial Hypertension, as our primary disease to narrow the heterogeneous disease landscape to a single – albeit still complex and varied – pathological challenge resulting in subsequent remodeling to the right ventricle. PAH is a disease of high morbidity and mortality. Advances in palliative treatment, PAH awareness, and patient management have improved survival, with 1 year survival improving from 65% to 90% since the 1990s and 3 year survival around 75%, but long-term survival remains challenging between 21-75% at 5 years[12]. Median survival time is now 6 years following diagnosis, over twice the 2.8 year estimate from the 1980s[12].

Pulmonary Arterial Remodeling

Whether the cause of pulmonary vascular pressure elevation is known (such as in pulmonary hypertension secondary to LV failure) or unknown (such as in idiopathic PAH described in this dissertation), many features of the downstream remodeling cascade are shared. Elevated pulmonary arterial pressure increases pulmonary vascular wall stress and strain, as well as endothelial cell fluid shear stress. These mechanical changes activate biochemical signaling cascades that promote vascular constriction and fibrosis that further alter the mechanical environment of the pulmonary arteries. These mechanical and structural changes to the pulmonary arteries correspond to changes in biological processes, including the stimulation of cell proliferation, migration, and apoptosis, as well as extracellular matrix protein expression and deposition, and endothelial cell dysfunction. As an acute response to chronic intra-arterial pressure elevation, the pulmonary artery wall undergoes transmural thickening due to increased hypertrophy, activation, and proliferation of pulmonary arterial smooth muscle cells. Endothelial cells and adventitial fibroblasts similarly increase proliferation and deposition in the pulmonary arterial wall with some endothelial cells transforming into activated myofibroblasts, resulting in deposition of extracellular matrix proteins (collagens, glycosaminoglycans, fibronectin, elastin). Altogether, these changes result in the formation of obliterative vascular occlusions known as plexiform lesions. Importantly, induced vascular cell remodeling in turn increases mechanical stresses upon the wall which further induces vascular remodeling in a feedback loop. The pulmonary arterial remodeling and restricted pulmonary arterial blood flow increases pulmonary vascular resistance that consequently leads alterations to RV function and exercise capacity. These changes culminate in hypertensive pressure overload on the right ventricle.

Right-Ventricular Remodeling

RV-specific experimental studies in animal models of pressure overload have demonstrated remodeling responses including myocyte hypertrophy, contractile regulation[13,14], myocardial stiffening[15], and fibrosis[16,17], and have shown that remodeling is highly dependent on the animal model, treatment, and design of these studies. Previous studies have reported distinct observations in RV remodeling, such as both upregulation[18–20] and downregulation[21] of myocardial contractility while other studies have reported both presence[22,23] and absence[24,25] of RV dilation in similarly treated RV pressure overloaded animals[22–24,26]. The extent to which these differences are due to the choices in animal models or treatment remains unclear. In particular, the contributions of specific RV remodeling processes to stages of systolic and diastolic ventricular function and dysfunction remains unclear. Therefore, there is a critical need to better connect biological remodeling to changes in organ function at multiple stages of ventricular function and dysfunction.

1.2 Clinical Indications, treatment, and prognosis of PAH

Pulmonary Vascular Changes, Hemodynamic Changes, and the Clinical Picture

Patients with Pulmonary Arterial Hypertension (PAH) commonly present with dyspnea, reduced exercise capacity, and chronic fatigue. PAH diagnosis may also be delayed or misattributed to PAH-related comorbidities such as age, fitness, left heart failure or lung disease. This is significant because early recognition and treatment of PAH may meaningfully prolong lifespan and quality of life[27]. PAH is diagnosed with pulmonary artery catheterization, by which a pressure sensing catheter (usually with a balloon-tip) is inserted into a central vein and advanced into a branch of the pulmonary artery. Patients with PAH are diagnosed by mean pulmonary arterial pressures (mPAP) measured above 20 mmHg. During catheterization, occlusion of the pulmonary artery branch (wedged) by balloon inflation also provides a pulmonary capillary wedge pressure reading approximating the left atrial pressure without requiring direct LA catheterization. Patients with PAH will have pulmonary capillary wedge pressures < 15 mmHg, with normal pulmonary capillary wedge pressures between 4-12 mmHg[28], whereas elevated capillary wedge pressure is suggestive of pulmonary hypertension secondary to left heart failure[29]. While cardiac catheterization can provide valuable insights into right ventricular function and biomechanics, there are no clear guidelines on the timing and recommendation of right heart catheterization, which varies by provider practice, comorbidities, and geography[30].

Standard of Treatment

No current therapy exists that specifically targets the pulmonary vasculature and right ventricle and reverses the pathological remodeling seen in PAH. The current standard of treatment for patients with PAH can be divided into three categories: general health measures, background therapies for PAH, and PAH-specific therapies. General health measures are usually prescribed quite readily due to their relatively low risk and reasonable potential for benefit. Reduction of dietary sodium intake is often recommended to reduce systemic blood volume and pressure, which may alleviate the burden of right ventricular volume overload in a challenged cardiac system with reduced right ventricular reserve. Aerobic exercise training has been shown to improve six-minute walk distance, oxygen uptake, and quality of life metrics in patients with PAH[31]. Supplemental oxygen therapy is also commonly used in cases where systemic oxygen saturation declines due to impaired right ventricular function and may help improved exercise capacity and quality of life[32].

Background therapies include therapies commonly prescribed for comorbidities associated with PAH. Patients with PAH experiencing RV dysfunction and failure may benefit from diuretics, which are used to alleviate venous congestion by reducing the systemic blood volume.

Antithrombotics have long been prescribed for patients with PAH due to thrombosis in small vessels of the pulmonary vasculature (potentially with increased resistance and reduced diameter) posing a significant risk. Some previous studies of have reported improved survival in patients with PAH with long term treatment of the anticoagulant warfarin[33,34]. These benefits may be acute to idiopathic PAH, as shown in the COMPERA registry[35], or negligible, as indicated in the REVEAL registry[36].

PAH-specific therapies primarily and specifically target one of four currently identified PAH-relevant molecular pathways: L-type calcium channels, nitric oxide, cyclic guanosine monophosphate, (cGMP) endothelin, or prostacyclin. Given that pulmonary pressure elevation is seen as the driver of the pathological changes that lead to RV remodeling, it is unsurprising that the most common current PAH therapies focus on palliative reduction of vascular pressure via vasodilation. While vasodilative drugs do not directly target the vascular changes that obstruct and stiffen the pulmonary arteries and microvasculature, they may indirectly regress adverse remodeling if they result in pulmonary arterial pressure reduction. The current standard of care for patients at most stages of PAH is combination therapy with prostacyclins, phosphodiesterase 5 inhibitors, and endothelin-1 antagonists[37]. Endothelin is a potent vasoconstrictor overexpressed in the lungs of patients with PAH. Endothelin-1 receptor antagonists (bosentan) prevent binding of vasoconstrictive endothelin-1 peptides on smooth muscle cells, resulting in vasodilative effects. Patients with PAH have increased expression of phosphodiesterase 5 (PDE5), which converts cGMP to 5’-GMP, a protein associated with adverse pulmonary vascular remodeling in PAH. Phosphodiesterase-5 inhibitors (sildenafil, tadalafil) upregulate nitric-oxide pathways, reducing cytosolic calcium and resulting in relaxation of pulmonary arterial alpha-smooth muscle cells. Sildenafil has been found improves 6-minute walk distance and mean pulmonary arterial pressure[38,39] and tadalafil improves 6-minute walk distance, time to clinical worsening, and quality of life[40]. Prostacyclins are cardioprotective hormones released by the vascular endothelium that have antithrombotic, antiproliferative, and anti-inflammatory properties, the expression of which is reduced in the lungs of patients with PAH[41,42]. Administration of prostacyclin analogues (Iloprost, Treprostinil, epoprostenol) increases the production of cyclic adenosine monophosphate to reduce intracellular calcium through adenylate cyclase activation, an effect that results in vasodilation. For patients with PAH, prostacyclin therapy has been shown to improve 6-minute walk distance, hemodynamics, and quality of life[43,44].

For patients who respond favorably to vasodilator therapy with improvements in both mPAP and pulmonary vascular resistance over 20%, calcium-channel blockers may be beneficial[45]. Pharmacologic aromatase inhibition is a relatively new strategy for PAH treatment that reduces endogenous estradiol production and can improve RV function. Metformin is one such aromatase inhibitor originally prescribed for diabetes care that improves insulin sensitivity and enhances exercise capacity and is often prescribed to women with earlier stage PAH[46].

Combination administration of these therapies have been shown to improve resting and exercised cardiovascular performance and ameliorate symptoms of PAH in many patients. However, many patients do not respond to combination vasodilator therapies. Moreover, vasodilation therapies do not address the underlying structural and mechanical changes in the pulmonary vasculature or myocardium.

The fact that RV failure can be reversed by lung transplantation and pulmonary endarterectomy (blood clot and fatty atheroma removal) implies that RV failure can also be preventable if we can better understand the pathophysiological progression of RV failure and the mechanisms that govern the transition. Two key problems with the current standard of care remain:

1) Vasodilative treatments do not address the underlying structural and mechanical changes in the vasculature or the myocardium. 2) The mechanisms of the transition from adapted function to RV failure remain unknown, as well as the importance of biomechanical changes to the pulmonary vasculature and myocardium, a knowledge gap that limits the ability to discover new therapeutics.

It is clinically important to recognize that RV remodeling is a dynamic and progressive process. Remodeling of the RV in PAH is a continuum of complex remodeling cascades affected by metabolic changes, neurohormonal activation, stage and progression of disease, and epigenetic factors. To begin to unpack these complex processes, RV remodeling in experimental or clinical studies is commonly triaged into adaptive or maladaptive remodeling based on holistic descriptions of RV function that include the presence or absence of concentric RV hypertrophy, RV chamber dilation, and preserved systolic and/or diastolic function. Generally, adaptive remodeling is characterized by the preservation of systolic and diastolic RV function and the maintenance of the RV myocardium wall to chamber volume ratio. By contrast, maladaptive ventricular remodeling is characterized by more severe impairment of systolic and diastolic function and a decreased RV wall to chamber volume ratio (RV dilation). Maladaptive ventricular remodeling may lead to tricuspid annular prolapse and tricuspid regurgitation, and impairment of synchronous RV conduction[47].

These descriptions provide important guidance for the diagnosis and management of PAH patients, but the mechanisms and mediators of the transition from adapted to maladapted RV remodeling remains poorly understood. Furthermore, the mechanism by which PAH induces, regulates, and is regulated by changes to the pulmonary vasculature remains unclear. As such, there is a tremendous need for research into the pathophysiology of PAH progression, the mechanisms governing remodeling of the RV, and the associated effects on RV health and function.

1.3 Right-Ventricular Hemodynamics

The most important clinical indicator for patients with PAH is not pulmonary arterial pressure, but the health and function of the right ventricle. The current clinical standard for a complete evaluation of RV function combines noninvasive imaging-based assessment (echocardiography and magnetic resonance imaging) with invasive right heart catheterization. Right heart catheterization allows for a detailed evaluation of the blood pressure, hemodynamics and mechanical behavior of the RV, while cardiac imaging provides the best measurements of cardiac chamber size and shape.

The first option for measuring heart function clinically is to describe the shape and size of the heart. In the LV, this is usually done via echocardiography, an inexpensive and quick ultrasound of the chest, from which measures of ventricle chamber volumes and myocardial wall thicknesses can be made, however echocardiography is not optimal for assessing RV size and function. Computed tomography scans are commonly used to measure cardiac function and provide greater resolution than echocardiography at the cost of added time and ionizing radiation. Although echocardiography and CT scans are common, the gold standard for assessing cardiac dimensions, geometry, and global hemodynamic performance is cardiac magnetic resonance imaging. Cardiac MR imaging offers extremely detailed geometrical information by combining magnetic field and radiofrequency waves to create detailed images of the heart.

While these volumetric measurements are suitable for describing global ventricular function, they do not provide a complete biomechanical description. Methods have therefore been developed to assess region-specific and local contractile function and strain. Early studies implanted physical radiopaque fiduciary markers on the surfaces of the ventricular wall to allow them to be tracked by radiographic methods[48]. Advances in MRI now allow for transient or virtual tags to be placed on the heart and to be tracked throughout the cardiac cycle to examine local tissue deformation. One such method relies on localizing tags to specific tissue regions by applying a spatially distinct magnetic field gradient and measuring the deformation of these tags through the cardiac cycle, providing insights into region-specific strain fields. Similarly, use of ultrasonic contrast agents such as microspheres and the development of speckle-tracking and Doppler tissue imaging can allow echocardiography to provide measurements of local regional strain.

Volumetric measurements and region-specifical strain still do not provide a complete biomechanical description. The clinical standard for assessing intra-ventricular chamber pressures requires the insertion of a pressure sensor (commonly along with a volume sensor) via cardiac catheterization into the heart. Catheter-derived measurements allow for the determination of pressure-volume loops as well as the identification of abnormal pressure gradients which could provide insights into regions of dysfunction. In experimental studies, one of the important mechanical tests facilitated by cardiac catheterization is the occlusion test, during which the vena cava is temporarily occluded (using a suture line). This dramatically reduces the filling of the ventricle, which subsequently reduces the contractile force (via the Frank-Starling relation). By recording pressure-volume loops at distinct filling volumes, the end-diastolic and end-systolic pressure-volume relations can be determined. These pressure-volume relations provide quantifiable insights into systolic (contraction) and diastolic (relaxation) function of the heart. Understandably, caval occlusion is unfeasible in patients, which may limit the ability to obtain detailed clinical pressure-volume data[49].

The Cardiac Pressure-Volume Relationship

To characterize RV function, one can decompose it into two functions: systolic function (the ability to contract and eject blood) and diastolic function (the ability to relax and fill with blood). Systolic function is primarily determined by two “external” factors: the preload and afterload imposed on the ventricle; one “internal” factor: the contractility; and one mixed factor: the heart rate. Systolic function was traditionally considered to be the most vital predictor of patient outcomes, but studies have increasingly shown the importance of diastolic dysfunction as an indicator of RV function (similar to left heart failure with preserved ejection fraction)[50].

Right ventricular preload refers to the forces exerted on the RV walls prior to contraction, which is directly related to the total amount of blood in the ventricle (end-diastolic volume). Mechanical factors that affect the preload include the venous return, diastolic wall stiffness, RV filling time and right atrial stiffness. Changes to these mechanical properties can alter the end-diastolic volume and the RV preload. The relationship between preload and systolic function is described by the Frank-Starling relationship, by which the heart can intrinsically respond to an increase in end-diastolic volume with an increase in ventricular contraction. Under normal circumstances, this mechanism allows the heart to respond to an increased delivery of blood to the ventricle by increasing the cardiac output. The exact mechanism that allows for this adaptation remains incomplete, but evidence suggests it is largely related to the force-length relationship of cardiomyocytes, whereby an increase in sarcomere length results in an increase in the active tension generated during contraction[51].

Right ventricular afterload refers to the resistance imposed on the ventricle by the vasculature against which the heart is pumping blood. An increase in afterload, such as in pulmonary hypertension, means that the ventricle is required to develop a greater pressure to overcome the increased resistance of the vasculature. Mechanical factors that affect the afterload include pulmonary arterial pressure, arterial resistance, and function of the pulmonary valve (such as coaptation efficiency). An increase in afterload generally corresponds to a decrease in stroke volume and an increase in cardiac work.

Right ventricular contractility describes the intrinsic ability for the myocardial apparatus to generate force, shorten, and contract the ventricular chamber to eject blood. This can be affected at the cell level, such as via changes in sarcomere length, calcium cycling, actin-myosin cross bridge formation, energetics, calcium sensitivity, or any of a wide range of changes to the regulation, synthesis, and function of calcium-myofiber machinery, at the tissue level, such as via fibrotic deposition and crosslinking, or at the organ level, such as electrophysiological contractile dyssynchrony, etc.

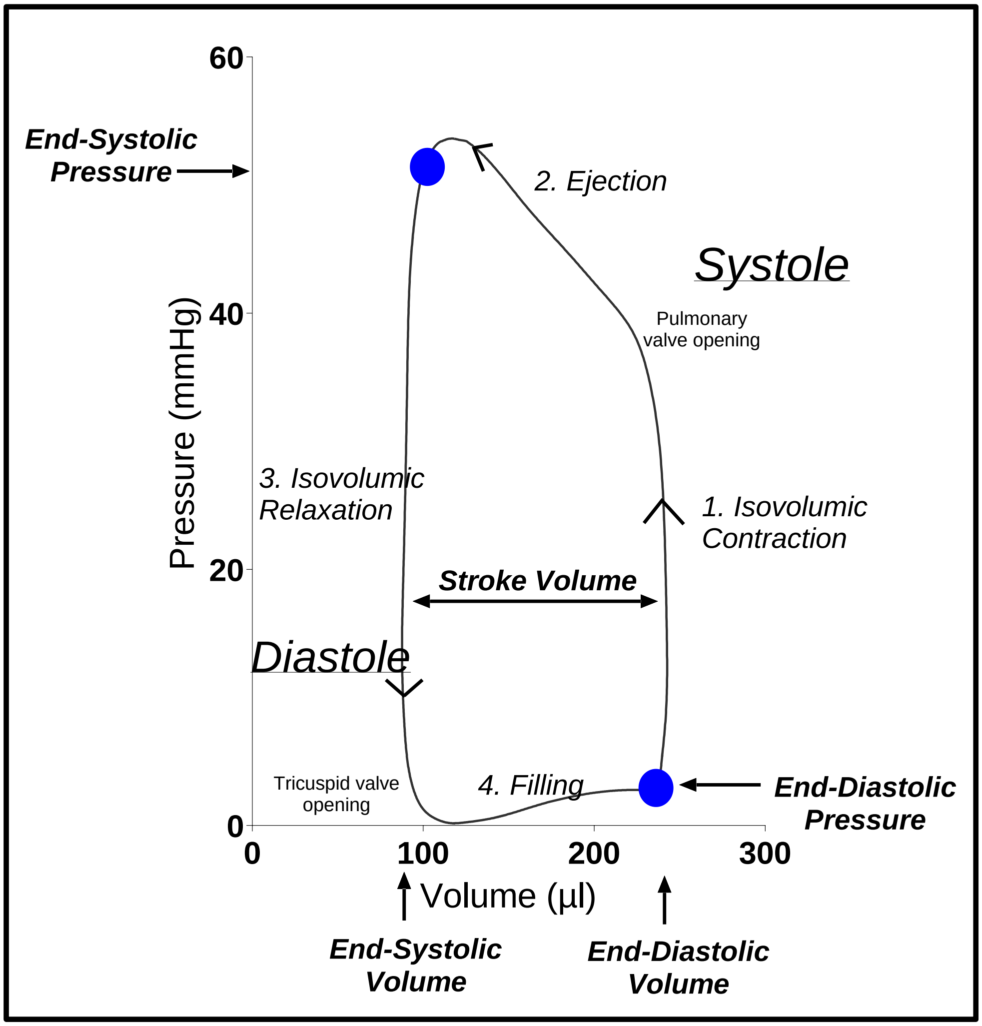

Figure 1.1. Pressure-volume loops depict the stages of the cardiac cycle, from which key hemodynamic parameters can be determined. The end-systolic and end-diastolic points are marked by blue dots, separating systolic and diastolic stages of contraction and relaxation.

The cardiac cycle (Fig. 1.1) can be divided into four phases:

(1). Isovolumic contraction: The phase beginning with the closing of the tricuspid valve (RV inlet) during which the pulmonary valve (RV outlet) remains closed, corresponding to increases in ventricular blood pressure as the myocardium contracts.

(2). Ejection: The phase beginning with the opening of the pulmonary valve due to ventricular pressure surpassing pulmonary pressure. During this phase, blood is ejected from the ventricle into the pulmonary artery.

(3). Isovolumic relaxation: The phase beginning with the closing of the pulmonary valve. As the myocardial relaxes, ventricular blood pressures decline.

(4). Filling: The phase beginning with the opening of the tricuspid valve, allowing blood to flow from the atria into the ventricle.

The phases of isovolumic contraction and ejection are characterized as systole, during which the myocardium is contracting, while isovolumic relaxation and filling are characterized as diastolic, during which the myocardium is relaxing.

The most comprehensive description of RV function and mechanics is by combining RV chamber blood pressure and volume measurements into pressure volume loops. The PV loop illustrates the corresponding changes in ventricular blood pressure and chamber volume that occur during the cardiac cycle. At the basic level, PV loops contain the following information about

RV chamber pressure:

- End-systolic blood pressure: The amount of blood pressure in the RV at the end of contraction.
- End-diastolic blood pressure: the amount of blood pressure in the RV at the end of relaxation.
- Peak blood pressure: The maximal blood pressure that develops in the RV during systole

RV chamber volume:

- End-systolic volume: The amount of residual blood in the RV when the pulmonary valve closes
- End-diastolic volume: the amount of blood filling the RV once the tricuspid valve closes

  - Stroke volume: The difference between end-systolic and end-diastolic volumes, or the amount of blood being ejected by the RV each heartbeat,
  - Ejection fraction: The stroke volume normalized by the end-diastolic volume, a measure of the efficiency of blood pumping.

In addition, the following information can be derived from analyzing the PV loop:

I. Assessments of the four phases of the cardiac cycle:
    a. Ejection: Period during systole when the pulmonary valve is open and the tricuspid valve is closed, allowing for the ejection of blood from the ventricle into the pulmonary vasculature
    b. Filling: Period during diastole when pulmonary valve is closed and the tricuspid valve is open, allowing for the filling of blood into the ventricle from the atrium.
    c. Isovolumic contraction: Period during systole when the pulmonary valve is closed and the tricuspid valve is closed, causing blood pressure to build as the myocardium contracts
    d. Isovolumic relaxation: Period during diastole when the pulmonary valve is closed and the tricuspid valve is closed, causing blood pressure to fall as the myocardium relaxes.

II. End-diastolic pressure-volume relationship: The relation between end-diastolic pressure and volume during changes in preload is known as end-diastolic elastance, or diastolic stiffness.

III. End-systolic pressure-volume relationship: the relation between end-systolic pressure and volume during changes in preload is known as end-systolic elastance, or contractility.

IV. Arterial elastance: An approximation for the afterload effectively imposed on the RV, calculated by connecting the ES PV point with the ED volume point.

V. Potential/stored mechanical energy: The integral of the end-systolic pressure-volume relationship, a measure of the potential energy stored in the RV free wall.

VI. Work: The total area of the PV loop, a measure of the total mechanical energy of the RV through one cardiac cycle.

Pressure-volume loop analyses is an important standard method for assessing load-independent contractility. This allows for descriptions of RV preload (RV ED volume), afterload (PA pressure or vascular resistance), and RV output (stroke volume, ejection fraction, etc) to be produced. Established quantitative descriptors of RV funharction such as systolic and diastolic elastance and cardiac work can subsequently be derived from these loops.

1.4 Animal models of PAH

Because of the severity, complexity, and heterogeneity of pulmonary arterial hypertension, several knowledge gaps remain in the understanding of the underlying molecular mechanisms of pulmonary arterial hypertension. In addition to the rapid and severe disease progression, as well as the capability of the right ventricle to transiently compensate RV function, PAH is challenging to study for the lack of human tissue samples and the lack of data across varied stages of the disease progression.

The development and study of animal models of pulmonary hypertension and of RV remodeling are vital to bridge the knowledge gap that remains in elucidating the mechanisms of the transition from adapted to maladapted RV remodeling. Animal models are essential in helping to decipher the molecular mechanisms underlying the disease, identifying robust drug targets, and for clinical translation. That pulmonary arterial hypertension is a multifaceted umbrella of diseases of varying pathologies remains a challenge and no single animal model recapitulates the range of clinical features in pulmonary arterial hypertension, or any specific pulmonary hypertension subgroup. Nevertheless, animal models have been developed that mimic key features of human PAH. Below, we discuss some commonly used animal models of PAH.

Sugen Hypoxia

Chronic hypoxia exposure has long been recognized to produce pulmonary hypertension in rodents, but does not necessarily match the severity of the disease seen in human PAH, necessitating the need for a more robust animal model[52]. Noting that the vascular endothelial growth factor receptor antagonist sugen 5416 resulted in pulmonary endothelial cell apoptosis and vascular pruning, sugen 5416 was combined with chronic hypoxia and demonstrated to result in more severe pulmonary hypertension and plexiform lesion formation[53]. A general protocol for sugen-hypoxia in small rodent (most commonly in rat) models combines a single bolus subcutaneous injection of the chemical Sugen5416 (20mg/kg), usually suspended in a solvent such as carboxymethylcellulose, benzyl alcohol or dimethyl sulfoxide to facilitate complete sugen dissolution. Sugen administration is typically followed by 3-4 weeks of continuous hypoxic exposure (at 10% oxygen), after which animals are returned to normoxia to prolong the vascular and ventricular remodeling[23,53,54]. In support of one of the prevailing theories regarding PAH development, sugen-hypoxia in rats results in initial apoptosis of PA endothelial cells followed by extensive subsequent proliferation of PA smooth-muscle cells and PA endothelial cells resistant to apoptosis. Additionally, due to the severe and irreversible remodeling of the PA with angio-obliterative lesions along with subsequent RV remodeling, the sugen-hypoxia rat model has become one of the most commonly used preclinical models of PAH[55]. Evidence of RV dysfunction has been shown after varying weeks of hypoxia over 3-10 weeks, but the longitudinal progression of cardiac function remains unclear[22,54,56].

Importantly, the response to sugen-hypoxia is strain-dependent, with Fisher rats developing RV dysfunction and death at higher rates than the more commonly used Sprague-Dawley lab rat, despite similarities in RV afterload and pulmonary vascular remodeling[57]. Sugen-hypoxia has been more recently adapted to mice to leverage existing tools to genetically modify mice and gain mechanistic insights into PAH. Some studies have found that repeated administration of sugen can help augment or maintain vascular and ventricular remodeling, such as in mouse models which are prone to recovering from sugen-hypoxia[20,25,53,58]. However, sugen-hypoxia in mice tend to gradually recover from sugen-hypoxia, with RV pressure, hypertrophy, and vascular remodeling all decreasing over time[23,59], a critical difference from human PAH. The sugen-hypoxia rat model remains one of the most useful for studying RV changes and evaluating the potential for novel anti-remodeling therapeutics, demonstrating progressive intimal proliferation, vascular obliteration, and right ventricular systolic pressure increases that correlate to changes in the pulmonary vasculature[60].

Monocrotaline

Injection of the inflammatory pneumotoxin monocrotaline (MCT) has been studied as an in vivo model of PAH for over 50 years, dating back to initial animal studies in rodents to large animal studies in porcine and canine models[61–63]. Monocrotaline is a naturally occurring plant alkaloid which is metabolized into the cytotoxin dehydromonocrotaline in mammalian liver cells[64]. Monocrotaline-induced PAH is usually studied in rat models and is largely ineffective in mice, due to the inability of mice to convert MCT to the active metabolite MCT-pyrrole. MCT administration results in robust pulmonary vascular remodeling leading to significant PA pressure elevation and RV dysfunction within 4-6 weeks. While the exact mechanism of action remains unclear, it is known that MCT induces PA endothelial cell dysfunction and proliferation, interstitial edema, pulmonary vasoconstriction, adventitial fibrosis, and medial hypertrophy[63,64]. MCT response has been shown to be dose sensitive with resulting effects ranging from PA muscularization and increased pulmonary vascular resistance at 4 weeks that can recover by 8-12 weeks[65] to vascular remodeling, RV disfunction, and death within 4-6 weeks[63,66]. While MCT is commonly studied as a late-stage model of severe PA and RV remodeling, the formation of obliterative plexiform lesions in the vasculature, which are a key feature of severe human PAH, do not occur in MCT treated animals. To mimic these features, MCT has been combined with other acute challenges, such as chronic hypoxia exposure, left pneumonectomy, or abdominal aortocaval shunting to produce models that more closely approximate the advanced stages of human disease[67]. The MCT rat model remains a valuable model that is low cost, technically simple, capable of reversal, and has a wealth of literature associated with it, despite its limitations in capturing human features of PAH such as plexiform lesions and it’s confounding damage to other organs[67].

BMPR2 Transgenic Models

Linkage studies of PAH have provided evidence of genetic contributions to PAH, in which heterozygous germline mutations of BMPR2 were detected. Although only 20-30% of BMPR2 mutation carriers develop the disease, BMPR2 loss-of-function mutations are the underlying cause in as high as 75% of patients with hereditary PAH and are present in 10-40% of patients with idiopathic PAH[68]. This low penetrance (proportion of individuals with the genotype expressing the associated phenotype) implies the importance of additional environmental challenges or additional genetic factors that result in the development of PAH. To investigate the genetic contributions, multiple engineered mouse lines have been developed to investigate the impact of BMPR2 mutations on the development of PAH. As it turns out, complete BMPR2 knockout is embryonically lethal, so inducible mutations or inducible post-translational modifications are required[69]. Most studies of BMPR2 mice demonstrate that BMPR$^{+/-}$ mice are more susceptible to developing PH in the presence of additional environmental stimuli, such as prolonged hypoxia, interleukin-1 and serotonin infusion, and chronic lipid-mediated inflammation[70]. Rodents expressing a postnatal cytoplasmic mutation R899X of the BMPR2 gene developed pulmonary hypertension, with elevated RV systolic pressure and significant pulmonary vascular structural changes[70]. Advances in rat genome editing (such as the CRISPR/Cas9 system) have allowed for similar studies in rats that develops more robust PAH[71]. Collectively, studies of BMPR2 suggest an incomplete penetrance of BMPR2 mutations and support a model by which multiple insults are required (such as BMPR2 deficiency combined with vascular remodeling due to hypoxia) for robust development of PAH.

1.5 Characterizing RV biomechanics

Biological processes and mechanical forces are fundamentally linked. In the cardiovascular system, mechanical stimuli in the form of fluid forces regulate smooth muscle and cardiac muscle function and extracellular matrix structure via endothelial signaling. These responses themselves impact the mechanical environment in a feedback loop that ultimately controls heart function. The most important function of the heart is to maintain circulation and ensure delivery of oxygenated blood to the tissues and organs of the body. As such, cardiac disorders are often described by their impacts to pump function, manifesting as alterations in hemodynamic function, cardiac output, and mechanical work. In cardiac diseases such as cardiomyopathies or in myocardial infarction, mechanical stresses play critical roles in regulating tissue fibrosis and scar formation[5]. Mechanical stresses also play a role in driving myocardial hypertrophy, so pharmacological or surgical alteration of mechanical stress patterns can provide effective approaches for treatment of disease. Analysis of the cardiac mechanics that regulate heart function, therefore, is critically important under both normal and pathological conditions.

In this section, to properly discuss considerations for a mechanical analysis of the heart, we briefly review some general mechanical engineering terms and their relation to our work. "Mechanics" generally refers to the relationship between the physical forces applied to an object (that can be either solid or fluid), and the resulting physical changes by which the object responds (such as rotation, translation, or deformation). First, we would like to clarify that the use of the term "mechanics" within the scope of this dissertation is more accurately described as "biomechanics", whereby we additionally consider the dynamic nature of our objects and the multitude of biological pathways and processes (such as cell signaling, gene expression regulation, etc) that respond to these forces in addition to physical changes that inert objects may respond with. Below is a list of relevant terms and their definition:

- Stress: the force applied normalized by the area to which the force is applied – this term describes the intensity of the mechanical force
- Strain: the relative deformation that an applied force results in – this term describes the intensity of the deformation (non-dimensional)
- Stretch: the ratio of deformed to undeformed length.
- Cauchy stress: the force per unit area in the deformed configuration – this is a tensor with 9 components in 3 dimensions (3x3)
- Mechanical properties: an object's intrinsic relationship between stress and strain

- Strain energy density: a description of how mechanical energy in an object changes/is converted to deformation of an object –a mathematical description of the mechanical properties of the tissue.

The study of cardiovascular tissue mechanics traditionally employs the framework of solid continuum mechanics, by which objects are assumed to have continuous distributions of mass without spaces or gaps in the material. This assumption is typically applied at the tissue scale, ignoring the fact that objects are comprised of constituent components which themselves are comprised of atoms and molecules with defined sizes and. The mathematical frameworks used to describe the “mechanical properties” described above are termed constitutive equations. In biomechanics and in cardiac biomechanics, these mechanical properties determined by the properties of intracellular and extracellular proteins, the myocytes, local mechanical stresses, and the higher-dimension organization of the ventricular wall. The myocardium tissue itself is organized into ventricular wall of a complex structure, with myofibers wrapped in layered sheets with a rotating orientation. In the mid-ventricle, the myofibers are predominantly organized circumferentially, whereas they are organized more longitudinally near the infundibulum and the cardiac apex[72]. There is also transmural changes in myofiber orientation, where myocytes on the outer-facing epicardial surface tend to be aligned at negative angle relative to the circumferential axis while myocytes on the endocardial surface tend to align at a positive angle to the circumferential axis, with this alignment varying depending on the location within the heart[73,74]. This heterogeneity in myocyte orientation is important to consider because of effects on the mechanical properties of the myocardial tissue.

Mechanical Testing

Ex vivo mechanical tests of cardiac tissue have been performed for over 150 years and experimental methods have been developed to describe organ, tissue and cell-level mechanical properties. The earliest mechanical tests of the left ventricle were *ex vivo* inflation tests in which the entire LV would be excised and inflated to various volumes and pressures, producing the equivalent of the end-diastolic pressure-volume relation. In the 19th century, Ludwig and Langendorff developed a perfusion method for maintaining cardiac contraction in the ex-vivo setting which allowed for the determination of active properties (end-systolic pressure volume relation) and full pressure-volume loop analysis, a method which is still commonly used today as a cost-effective method for studying pharmaceutical effects on cardiac cytotoxicity[75]. These measurements of organ-level mechanics provide similar insights into the pressure and volume hemodynamic function as the in-vivo assessments of organ function described above, albeit in an *ex vivo* experimental setting.

Traditional mechanical tests of stress of strain employed in more traditional non-cardiac and non-biological tissues are also commonly applied, primarily to characterize mechanical properties at the tissue level, whereby the myocardium is considered the material. Mechanical testing of small, excised pieces of cardiac tissue often occurs in the form of biaxial mechanical testing, which was first employed in myocardial tissue half a century ago, however have been primarily limited to LV myocardial samples[76]. In these tests, a flat section of myocardium from the ventricular wall was excised and stretched in two orthogonal directions, allowing for accurate quantification of stresses and strains used to determine the anisotropic and non-linear mechanical properties of the myocardial tissue. These tests also provide region-specific local insights into the mechanical properties of the myocardium. As shown by Lin et al., myocardial tissue treated with tetanus can also allow biaxial tests to measure mechanical properties of contracted myocardium[77].

Ex-vivo biaxial mechanical testing remains a staple of cardiac mechanics testing and has been adapted for a variety of tissues from experimental models ranging in size from rodents to larger porcine and ovine models of various cardiac disorders[78,79].

Recognition of the importance of the cardiac myocyte as an important constituent of the myocardial tissue has also motivated development of mechanical tests to describe their properties. Cardiac myocytes are the primary unit responsible for developing contractile force, although they also provide important passive mechanical stiffness to the myocardium material. Mechanical testing of isolated cardiac myocytes ex vivo have been developed whereby myocytes can then be subjected to forces and the passive and active mechanical properties could be determined[80]. Isolated myocytes offer an excellent platform for studying the effects of pharmaceutical agents on cytotoxicity, as well as the corresponding changes to myocyte mechanics. Similar mechanical tests have also been performed on isolated sarcomeres: the organizational unit of the myofiber[81]. From these experimental data, constitutive models provide a framework with which to quantify mechanical changes to the myocardium and systematically characterize remodeling of the RV myocardium in health and disease.

1.6 Sex Differences

Several forms of cardiovascular disease, including pulmonary hypertension demonstrate sex-differences in incidence, presentation, progression, and in patient outcomes. These sex-differences are specifically commonly described in pulmonary arterial hypertension, where the clinical effects are remarkably pronounced. Multiple large-scale patient registry studies show that women are as much as 2-4x likely to develop PAH, yet women with PAH also paradoxically tend to display improved RV function and improved survival compared to men with PAH. This discrepancy is commonly referred to in the literature as the “estrogen paradox.” Recent studies have demonstrated that multiple sex hormones, including estrogen, play a role in determining PAH progression and the remodeling of the RV, yet the time course, mechanisms, and mediators of these differences remain unclear. It is possible that the underlying physiological mechanisms explaining sex-differences may provide crucial insights into the mechanisms of RV remodeling, as well as provide potential therapeutic targets for PAH. It is also very likely that the underlying mechanisms are complex, multi-faceted, and heterogeneous amongst patient populations.

Epidemiological Data

The first multicenter patient registry from the National Institutes of Health (NIH, 1991) reported a ratio of women:men with PAH of 1.7:1. Differences in epidemiology across many registries since then have described sex differences between men and women that are similar or more pronounced. The largest US-based registry, the Registry to Evaluate Early And Long-term PAH disease management (REVEAL) began enrolling patients in 2006 and reported among patients with idiopathic PAH an average age of 53 ±15 years, 80% of whom were women[82,83]. In China, where targeted PAH therapies have only recently become available, the earliest registries showed patients with a 2.4:1 ratio of women:men, while recent cohorts showed a 3.1:1 ratio of women: men[84]. Importantly, it is unclear whether these epidemiological data are the results of changes in disease biology, a response to survival bias among women due to improvements in therapies, or differences in study population remains unclear. While it is well established that female sex is a significant risk factor for PAH, the US REVEAL and French registries both showed in 2010 that male sex doubled the risk of death due to PAH[85]. 5-year survival estimates for newly diagnosed men were 53%±4% for men with PAH compared to 63%±2% for women with PAH[86,87].

It is important to note that sex biases in PAH epidemiology are very likely dependent on age. Sex differences in PAH prevalence diminish with age. This was shown in a large study of patient data from 11 clinical trials of PAH, in which women with idiopathic PAH had more favorable hemodynamics (lower PVR, higher cardiac index) than men[88]. In the same study, men under the age of 45 had higher mean pulmonary arterial pressures than women under the age of 45, but the differences were negated in men and women over 45 years old. This was similarly shown in the COMPERA registry, which showed a strong bias in PAH prevalence towards women that dissipated after the age of 65[86]. Taken together, these PAH registry studies indicate pronounced differences between men and women with PAH in both incidence and outcome, particularly in younger men and women that dissipate with age. Whether this sex-age interaction can be explained by sex-hormones or confounded by age-related co-morbidities remains unclear. It is also very likely that race and ethnicity affect the relationship between sex and PAH. The NIH registry indicates that the sex ratio of PAH prevalence was even more pronounced among black Americans (4.3:1), a finding matched by the REVEAL registry which showed a ratio of 5.4:1 among black Americans[82,89]. In the United Kingdom and Ireland, a 5.6:1 ratio of women to men were found in non-white patients with PAH, compared to a 2.3:1 ratio in white patients with PAH[90].

As introduced above, the health and function of the right ventricle is the most important indicator of patient outcomes in PAH. Therefore, sex differences in patient outcomes are directly linked to sex bias in RV function in PAH. The Multi-Ethnic Study of Atherosclerosis (MESA)-RV is the largest population-based study with RV indices measured via cardiac MRI and showed that female gender was associated with higher RV ejection fraction, decreased RV mass, and smaller RV volumes, even after adjusting for body size and comorbid factors[91,92]. These differences in RVEF and volume were also shown in the Framingham Heart Study Offspring cohort[93]. In more recent patient studies of the RV in PAH, it has also been shown that male sex is associated with lower RV ejection fraction[91]. In a Dutch cohort of idiopathic PAH, RV ejection fraction declined in men and improved in women over time with PAH therapies[94]. In fact, a significant proportion of the transplant-free survival differences between men and women are explained by differences in response to PAH therapy. In a patient-level analysis from 6 randomized clinical trials, Gabler *et al.* found that women exhibited a better response in their exercise capacity, determined by 6-minute walk distance (6MWD) than men when treated with estrogen-receptor antagonists[95]. Similarly, women were more likely to respond to treatment with prostacyclins. By contrast, a post-hoc analysis of patients with PAH enrolled in the PDE5 inhibitor tadalafil found men improved their 6MWD and quality of life more than women in response to tadalafil[40]. In summary, sex differences in epidemiology and patient outcomes are well established and sex differences in RV systolic function and in response to therapies are reasonably established.

While the estrogen paradox in PAH originally referred to the noted discrepancy between incidence and outcome between men and women with PAH, it has since been noted that a second estrogen-related paradox has been identified in experimental and cellular studies, in which estrogens are cardioprotective in some animal models of disease, but detrimental in others[96,97]. Some PAH studies also refer to an estrogen-paradox in which estrogens appear to be uniformly cardioprotective in the RV but may exert disease-promoting effects in the pulmonary vasculature[98]. These findings suggest many potential biological explanations may exist for the observed sex differences in PAH that have not yet been identified[99].

1.7 Current Knowledge Gaps

Tthe mechanisms and mediators of PAH, as well as the mechanisms and mediators of RV remodeling, adaptation, and dysfunction, remain unclear. No standard definition of RV failure exists, in part because of the lack of a standardized metric that can capture the vast heterogeneity of structural and mechanical changes seen in PAH. The latest definitions of RV failure, such as presented by the American Thoracic Society describe RV failure as “a complex clinical syndrome characterized by insufficient delivery of blood from the RV and elevated systemic venous pressure at rest or exercise”. Establishing baseline healthy and diseased values for such universal RV metrics would allow patients to be identified and treated before the onset of severe RV failure. However, descriptions of RV geometry and chamber shape are challenging due to the heterogenous crescent-shape thin-walled normal RV. While hemodynamic measures (such as mean pulmonary arterial pressure, pulmonary vascular resistance, and corresponding RV blood pressures) are robust, reproducible, and serve as good correlates of patient outcomes, they are not good surrogate endpoints of RV function and only explain a small proportion of the impact of PAH therapies[100]. The most widely used and reliable RV clinical endpoint is the ejection fraction (EF)[11]. RVEF is a strong predictor of outcomes and changes to the EF explain improvements in survival in response to PAH-specific therapies[47,101] and is readily acquirable via echocardiography or cardiac MRI. While **the RVEF is frequently used as a benchmark to characterize RV function, it is an incomplete description**. Changes to the RV ejection fraction do not discriminate systolic and diastolic changes, though both have been individually identified as prognostic indicators of RV function[50]. This has contributed to the disconnect between the most used clinical descriptors of RV function (RVEF) and experimental studies of the underlying physical and biomechanical changes. While it is known that changes to RV geometry and size are predictors of patient outcomes**, the relationship between RV hypertrophy and systolic and diastolic function is unclear**. This knowledge gap limits the identification of robust descriptions of RV changes over time and across stages of disease.

The best reference points for longitudinal changes to RV function are large-cohort population studies with comprehensive RV imaging and functional data (MESA-RV) and long-term patient registries (COMPERA)[86,91]. From these studies, important epidemiological and survival data have been identified[89,90]. However, patient data is often insufficient for robust studies of RV changes and for determining the transitions between stages of RV adaptation, in part because patients are diagnosed at different stages. Furthermore, population studies do not address a mechanistic understanding of the mediators determining these transitions. The evolution of cardiac biomechanical properties is rarely tracked or analyzed in detail beyond summary metrics such as cardiac output and ejection fraction. What is currently known about the time-course of changes during the progression of PAH are based on a limited number of longitudinal studies, and the **need to describe RV biomechanics** during the **progression** of PAH using multi-scale longitudinal studies remains[20,23,26,66,102].

Clinical[93,94,103] and preclinical studies[56] have highlighted the association between sex and RV hemodynamic function, with correlations found between improved RV function and endogenous or exogenous estrogens.[104,105] However, most animal studies have focused on male subjects, limiting sex-specific data on RV remodeling. As a result, the role of **sex in PAH remains unclear**. Estrogen may influence RV myocardial remodeling, explaining the sex-specific differences in disease progression.[56,104] Therefore, there is a critical need to understand the influence of sex on the pathological remodeling of the RV that occurs in PAH. Because of the severity, complexity, and heterogeneity of pulmonary arterial hypertension, several knowledge gaps remain in the understanding of the underlying molecular mechanisms of pulmonary arterial hypertension. The rapid and severe disease progression seen in patients with PAH, as well as the capability of the right ventricle to transiently compensate RV function make PAH challenging to study for the lack of human tissue samples and the lack of data across varied stages of the disease progression.

1.8 Our Approach

1.8.1 Multiscale Measures Approach

While cardiac MRI and echocardiography data are the clinical standards for describing RV function, obtaining robust hemodynamic data is often unfeasible. Additionally, biopsy and explant tissue are limited for study and do not allow for robust comparisons of distinct periods of adaptation and remodeling. To address these knowledge gaps, we designed experiments and made measurements at different scales of RV function from the organ to the tissue and cell using an animal model of PAH. Our approach combines measures of hemodynamic, morphological, biochemical, and mechanical data to identify evolving properties of the RV during the progression of PAH up to 26 weeks post-induction. We combined these experimental data with a computational model of RV biomechanics and developed a framework to characterize and distinguish the individual effects of RV geometric and material changes.

This framework characterizes a) the health and function of the RV at the organ level b) describes the underlying changes to the myocardial material properties c) identifies the contributions of hypertrophy and material changes to changes in systolic and diastolic RV function and can d) be used as a predictive model to investigate active and passive myocardium mechanics. These model predictions were validated with biaxial testing of myocardium passive mechanics, measurements of myocyte contractile mechanics, and biochemical assays. These models and their subsequent experimental validation are then applied to distinguish and characterize stages of RV remodeling and sex-differences in RV remodeling.

1.8.2 Animal Model Study Design

Experimental data was primarily obtained from a well-established animal model of PAH to bridge the knowledge gap that remains in elucidating the mechanisms of the transition from adapted to maladapted RV remodeling. In particular, the chosen sugen-hypoxia rat model has been shown to mimic plexiform vascular lesion development seen in explant tissue of patients with PAH and result in RV remodeling[54]. Using an animal model facilitated invasive cardiac catheterization that, in addition to the cardiac output, provided functional hemodynamic measurements including RV pressures and ventricular-arterial coupling using P-V loops to characterize RV function. The animal model also allowed for the complete excision of and isolation of cardiac tissue and cells following terminal surgeries, from which further experimental measurements were made. Furthermore, the severity of RV remodeling has been shown to be augmented by the duration of sugen-hypoxia treatment, a feature we leverage to study RV changes over a wide range of time points of known duration up to 26 weeks.[23,54] This is a unique advantage of the sugen-hypoxia animal model which cannot be emulated in patients, where the stage and progression of disease is unknown and uncontrollable. Therefore, the animal model facilitated experimental study design across a range of time points, beyond previous long-term SuHx studies[23], to address the knowledge gap regarding the staging and progression of RV remodeling in PAH.

1.8.3 Using Biomechanics Models to Relate Hemodynamics to Tissue Properties

In our biomechanics model, the RV geometry is approximated as a fraction of a sphere with a defined radius and thickness, comprised of RV chamber volume and RV myocardial free wall and septum wall volumes. RV blood pressure measurements are related to myocardial wall stresses by Laplace’s Law. The modeling approach is explained in greater detail in chapter 3 (RV biomechanics model). We fit our computational model to experimental measurements, producing rat-specific biomechanics models of systolic and diastolic function. Results from model fitting of control and PAH hemodynamic measurements show that the biomechanics model can closely predict end-systolic and end-diastolic pressure-volume relationships by accounting for measured morphology and by optimizing three myocardial material parameters. The model also allows for the relative contributions of volume, geometry, and material property changes to chamber blood pressure to be discerned. This makes our modeling approach a powerful and appropriate framework for characterizing changes to the underlying RV properties that could explain changes to RV function in health and at various stages of disease.

1.8.4 Insights Gained from Incorporating Sex as an Experimental Variable

By utilizing an animal model of PAH, our approach also facilitates the study of biological sex and ovarian hormones on changes to RV function. As previously noted, sex differences in PAH epidemiology and patient outcomes are well established and believed to be attributed to sex differences in RV systolic function, therefore it is reasonable to assume that RV function is differentially compensated in male PAH vs female PAH. Specifically, we hypothesize that sex differences in RV changes may explain clinical sex differences in RV function and patient outcomes. Based on previous findings that diastolic stiffening is a prognostic indicator in patients with PAH and women have improved RV function and outcomes[50], we hypothesized that RV diastolic stiffening is an important differential indicator that is severely increased in male PAH but moderated in female PAH. By contrast, we proposed that female PAH rats would instead show increased contractility with mild diastolic stiffening, diverging with the severe stiffening in male

PAH rats. By designing a comparative study of male and female (intact and ovariectomized) rats, we applied our framework to distinguish sex-differences in RV function, PAH progression, myocardial material property changes, and the contributions of hypertrophy and material changes to systolic and diastolic RV function.

1.8.5 Specific Aims

Given the clinical significance of the differences between PAH in women and men, we propose to investigate differences in adaptation to pressure overload at multiple stages of disease. *Our central hypothesis is that cardiac output is primarily maintained by hypertrophy in male PAH and by altered myocyte contractility in female PAH.* To test our hypothesis, we propose the following aims.

Specific Aim 1. To investigate the relative contributions of myocardial material properties vs geometrical remodeling to changes in systolic and diastolic chamber mechanics in an animal model of PAH. We hypothesized that end-diastolic volume is preserved in male PAH rats by increased chamber stiffening by contrast to female PAH rats, which will have fewer alterations to diastolic pressure and stiffness. We fitted our computational model to experimental measurements to determine the contributions of altered RV geometry (hypertrophic wall thickening) compared to changes in material properties (passive stiffness and contractility) to maintaining cardiac output in male and female PAH rats. We investigated the mechanisms underlying the changes in myocardial end-systolic and end-diastolic material properties during compensated PAH and identify novel descriptions of changes to RV biomechanics over a wide range of timepoints.

Specific Aim 2. To investigate the mechanisms of changes in myocardial systolic and diastolic material properties during compensated PAH. We hypothesize that in compensated PAH, myocyte calcium transient remodeling and force development are upregulated in females but not males, whereas passive myocardial stiffening (attributed to the collagen matrix) adapts male PAH but not female PAH. Completion of these aims will improve our understanding of right ventricular pathophysiology in PAH and the relationship between remodeling myocardial properties and evolving RV chamber function. This may help identify mechanisms and clinically relevant biomarkers of the transition from adapted to maladapted RV function.

1.9 References

1. Harvey W. *Exercitatio anatomica de motu cordis et sanguinis in animalibus*.; 1737.

2. Starr I, Jeffers WA, Meade RH. The absence of conspicuous increments of venous pressure after severe damage to the right ventricle of the dog, with a discussion of the relation between clinical congestive failure and heart disease. *Am Heart J*. 1943;26(3):291-301.

3. BAKOS ACP. The Question of the Function of the Right Ventricular Myocardium: An Experimental Study. *Circulation*. 1950;1(4):724-732.

4. Fontan F, Baudet E. Surgical repair of tricuspid atresia. *Thorax*. 1971;26(3):240-248.

5. Voorhees AP, Han HC. Biomechanics of Cardiac Function. *Compr Physiol*. 2015;5(4):1623-1644.

6. Sanz J, Sánchez-Quintana D, Bossone E, Bogaard HJ, Naeije R. Anatomy, Function, and Dysfunction of the Right Ventricle: JACC State-of-the-Art Review. *J Am Coll Cardiol*. 2019;73(12):1463-1482.

7. Anatomy, Function, and Dysfunction of the Right Ventricle: JACC State-of-the-Art Review - PubMed.

8. Shahim B, Hahn RT. Right Ventricular-Pulmonary Arterial Coupling and Outcomes in Heart Failure and Valvular Heart Disease. *Struct Heart*. 2021;5(2):128-139.

9. Simonneau G, Montani D, Celermajer DS, et al. Haemodynamic definitions and updated clinical classification of pulmonary hypertension. *Eur Respir J*. 2019;53(1):1801913.

10. Purmah Y, Lei LY, Dykstra S, et al. Right Ventricular Ejection Fraction for the Prediction of Major Adverse Cardiovascular and Heart Failure-Related Events. *Circ Cardiovasc Imaging*. 2021;14(3):e011337.

11. Lahm T, Douglas IS, Archer SL, et al. Assessment of Right Ventricular Function in the Research Setting: Knowledge Gaps and Pathways Forward. An Official American Thoracic Society Research Statement. *Am J Respir Crit Care Med*. 2018;198(4):e15-e43.

12. Thenappan T, Ormiston ML, Ryan JJ, Archer SL. Pulmonary arterial hypertension: pathogenesis and clinical management. *The BMJ*. 2018;360:j5492.

13. Neto-Neves EM, Frump AL, Vayl A, Kline JA, Lahm T. Isolated heart model demonstrates evidence of contractile and diastolic dysfunction in right ventricles from rats with sugen/hypoxia-induced pulmonary hypertension. *Physiol Rep*. 2017;5(19):e13438.

14. Sabourin J, Boet A, Rucker-Martin C, et al. Ca2+ handling remodeling and STIM1L/Orai1/TRPC1/TRPC4 upregulation in monocrotaline-induced right ventricular hypertrophy. *J Mol Cell Cardiol*. 2018;118:208-224.

15. Rain S, Andersen S, Najafi A, et al. Right Ventricular Myocardial Stiffness in Experimental Pulmonary Arterial Hypertension. *Circ Heart Fail*. 2016;9(7):e002636.

16. Baicu CF, Li J, Zhang Y, et al. Time course of right ventricular pressure-overload induced myocardial fibrosis: Relationship to changes in fibroblast postsynthetic procollagen processing. *Am J Physiol - Heart Circ Physiol*. 2012;303(9):H1128-34.

17. Legchenko E, Chouvarine P, Borchert P, et al. PPARγ agonist pioglitazone reverses pulmonary hypertension and prevents right heart failure via fatty acid oxidation. *Sci Transl Med*. 2018;10(438):eaao0303.

18. Karunanithi MK, Michniewicz J, Copeland SE, Feneley MP. Right ventricular preload recruitable stroke work, end-systolic pressure- volume, and dP/dt(max)-end-diastolic volume relations compared as indexes of right ventricular contractile performance in conscious dogs. *Circ Res*. 1992;70(6):1169-1179.

19. De Man FS, Handoko ML, Van Ballegoij JJM, et al. Bisoprolol delays progression towards right heart failure in experimental pulmonary hypertension. *Circ Heart Fail*. 2012;5(1):97-105.

20. Wang Z, Patel JR, Schreier DA, Hacker TA, Moss RL, Chesler NC. Organ-level right ventricular dysfunction with preserved Frank-Starling mechanism in a mouse model of pulmonary arterial hypertension. *J Appl Physiol*. 2018;124(5):1244-1253.

21. Nagendran J, Archer SL, Soliman D, et al. Phosphodiesterase type 5 is highly expressed in the hypertrophied human right ventricle, and acute inhibition of phosphodiesterase type 5 improves contractility. *Circulation*. Published online 2007.

22. Jayasekera G, Wilson KS, Buist H, et al. Understanding longitudinal biventricular structural and functional changes in a pulmonary hypertension Sugen–hypoxia rat model by cardiac magnetic resonance imaging. *Pulm Circ*. 2020;10(1):1-11.

23. Vitali SH, Hansmann G, Rose C, et al. The Sugen 5416/hypoxia mouse model of pulmonary hypertension revisited: Long-term follow-up. *Pulm Circ*. 2014;4(4):619-629.

24. da Silva Gonçalves Bos D, Happé C, Schalij I, et al. Renal Denervation Reduces Pulmonary Vascular Remodeling and Right Ventricular Diastolic Stiffness in Experimental Pulmonary Hypertension. *JACC Basic Transl Sci*. 2017;2(1):22-35.

25. Wang Z, Schreier DA, Hacker TA, Chesler NC. Progressive right ventricular functional and structural changes in a mouse model of pulmonary arterial hypertension. *Physiol Rep*. 2013;1(7):e00184.

26. Kwan ED, Velez-Rendon D, Zhang X, et al. Distinct time courses and mechanics of right ventricular hypertrophy and diastolic stiffening in a male rat model of pulmonary arterial hypertension. *Am J Physiol - Heart Circ Physiol*. Published online 2021.

27. Brown LM, Chen H, Halpern S, et al. Delay in recognition of pulmonary arterial hypertension: factors identified from the REVEAL Registry. *Chest*. 2011;140(1):19-26.

28. Nair R, Lamaa N. Pulmonary Capillary Wedge Pressure. In: *StatPearls*. StatPearls Publishing; 2024.

29. Naeije R, Tonelli AR. Pulmonary Artery Wedge Pressure in the Diagnosis of Pulmonary Arterial Hypertension. *Am J Respir Crit Care Med*. 2024;209(3):242-244.

30. Hansmann G, Rich S, Maron BA. Cardiac catheterization in pulmonary hypertension: doing it right, with a catheter on the left. *Cardiovasc Diagn Ther*. 2020;10(5):1718-1724.

31. Pandey A, Garg S, Khunger M, et al. Efficacy and Safety of Exercise Training in Chronic Pulmonary Hypertension: Systematic Review and Meta-Analysis. *Circ Heart Fail*. 2015;8(6):1032-1043.

32. Ulrich S, Hasler ED, Saxer S, et al. Effect of breathing oxygen-enriched air on exercise performance in patients with precapillary pulmonary hypertension: randomized, sham-controlled cross-over trial. *Eur Heart J*. 2017;38(15):1159-1168.

33. Fuster V, Steele PM, Edwards WD, Gersh BJ, McGoon MD, Frye RL. Primary pulmonary hypertension: natural history and the importance of thrombosis. *Circulation*. 1984;70(4):580-587.

34. Frank H, Mlczoch J, Huber K, Schuster E, Gurtner HP, Kneussl M. The effect of anticoagulant therapy in primary and anorectic drug-induced pulmonary hypertension. *Chest*. 1997;112(3):714-721.

35. Olsson KM, Delcroix M, Ghofrani HA, et al. Anticoagulation and survival in pulmonary arterial hypertension: results from the Comparative, Prospective Registry of Newly Initiated Therapies for Pulmonary Hypertension (COMPERA). *Circulation*. 2014;129(1):57-65.

36. Preston IR, Roberts KE, Miller DP, et al. Effect of Warfarin Treatment on Survival of Patients With Pulmonary Arterial Hypertension (PAH) in the Registry to Evaluate Early and Long-Term PAH Disease Management (REVEAL). *Circulation*. 2015;132(25):2403-2411.

37. Sommer N, Ghofrani HA, Pak O, et al. Current and future treatments of pulmonary arterial hypertension. *Br J Pharmacol*. Published online 2021.

38. Galiè N, Ghofrani HA, Torbicki A, et al. Sildenafil citrate therapy for pulmonary arterial hypertension. *N Engl J Med*. 2005;353(20):2148-2157.

39. Gan CTJ, Holverda S, Marcus JT, et al. Right ventricular diastolic dysfunction and the acute effects of sildenafil in pulmonary hypertension patients. *Chest*. 2007;132(1):11-17.

40. Mathai SC, Hassoun PM, Puhan MA, Zhou Y, Wise RA. Sex Differences in Response to Tadalafil in Pulmonary Arterial Hypertension. *Chest*. 2015;147(1):188-197.

41. Mitchell JA, Ahmetaj-Shala B, Kirkby NS, et al. Role of prostacyclin in pulmonary hypertension. *Glob Cardiol Sci Pract*. 2014;2014(4):382-393.

42. Moncada S. Prostacyclin, from discovery to clinical application. *J Pharmacol*. 1985;16 Suppl 1:71-88.

43. Simonneau G, Barst RJ, Galie N, et al. Continuous Subcutaneous Infusion of Treprostinil, a Prostacyclin Analogue, in Patients with Pulmonary Arterial Hypertension. *Am J Respir Crit Care Med*. 2002;165(6):800-804.

44. Vanderpool RR, Gorelova A, Ma Y, et al. Reversal of Right Ventricular Hypertrophy and Dysfunction by Prostacyclin in a Rat Model of Severe Pulmonary Arterial Hypertension. *Int J Mol Sci*. 2022;23(10):5426.

45. Sitbon O, Humbert M, Jaïs X, et al. Long-term response to calcium channel blockers in idiopathic pulmonary arterial hypertension. *Circulation*. 2005;111(23):3105-3111.

46. Spiekerkoetter E, Kawut SM, de Jesus Perez VA. New and Emerging Therapies for Pulmonary Arterial Hypertension. *Annu Rev Med*. 2019;70:45-59.

47. Van De Veerdonk MC, Kind T, Marcus JT, et al. Progressive right ventricular dysfunction in patients with pulmonary arterial hypertension responding to therapy. *J Am Coll Cardiol*. 2011;58(24):2511-2519.

48. Brewis MJ, Bellofiore A, Vanderpool RR, et al. Imaging right ventricular function to predict outcome in pulmonary arterial hypertension. *Int J Cardiol*. 2016;218:206-211.

49. Naeije R, Manes A. The right ventricle in pulmonary arterial hypertension. *Eur Respir Rev*. 2014;23(145):476-487.

50. Rain S, Handoko ML, Trip P, et al. Right ventricular diastolic impairment in patients with pulmonary arterial hypertension. *Circulation*. 2013;128(18):2016-2025.

51. LaCombe P, Jose A, Basit H, Lappin SL. Physiology, Starling Relationships. In: *StatPearls*. StatPearls Publishing; 2024.

52. Kasahara Y, Tuder RM, Taraseviciene-Stewart L, et al. Inhibition of VEGF receptors causes lung cell apoptosis and emphysema. *J Clin Invest*. 2000;106(11):1311-1319.

53. TARASEVICIENE-STEWART L, KASAHARA Y, ALGER L, et al. Inhibition of the VEGF receptor 2 combined with chronic hypoxia causes cell death-dependent pulmonary endothelial cell proliferation and severe pulmonary hypertension. *FASEB J*. Published online 2001.

54. Abe K, Toba M, Alzoubi A, et al. Formation of plexiform lesions in experimental severe pulmonary arterial hypertension. *Circulation*. 2010;121(25):2747-2754.

55. Sztuka K, Jasińska-Stroschein M. Animal models of pulmonary arterial hypertension: A systematic review and meta-analysis of data from 6126 animals. *Pharmacol Res*. 2017;125:201-214.

56. Frump AL, Albrecht M, Yakubov B, et al. 17β-estradiol and estrogen receptor α protect right ventricular function in pulmonary hypertension via BMPR2 and apelin. *J Clin Invest*. Published online 2021.

57. Suen CM, Chaudhary KR, Deng Y, Jiang B, Stewart DJ. Fischer rats exhibit maladaptive structural and molecular right ventricular remodelling in severe pulmonary hypertension: a genetically prone model for right heart failure. *Cardiovasc Res*. 2019;115(4):788-799.

58. Bueno-Beti C, Hadri L, Hajjar RJ, Sassi Y. The Sugen 5416/Hypoxia Mouse Model of Pulmonary Arterial Hypertension. In: Ishikawa K, ed. *Experimental Models of Cardiovascular Diseases: Methods and Protocols*. Springer; 2018:243-252.

59. Boucherat O, Agrawal V, Lawrie A, Bonnet S. The Latest in Animal Models of Pulmonary Hypertension and Right Ventricular Failure. *Circ Res*. 2022;130(9):1466-1486.

60. Vitali SH. CrossTalk opposing view: The mouse SuHx model is not a good model of pulmonary arterial hypertension. *J Physiol*. 2019;597(4):979-981.

61. Smith P, Kay JM, Heath D. Hypertensive pulmonary vascular disease in rats after prolonged feeding with Crotalaria spectabilis seeds. *J Pathol*. 1970;102(2):97-106.

62. Heath D, Kay JM. Medial Thickness of Pulmonary Trunk in Rats with Cor Pulmonale induced by Ingestion of Crotalaria spectabilis Seeds. *Cardiovasc Res*. 1967;1(1):74-79.

63. Zeng G qiao, Liu R, Liao H xing, et al. Single Intraperitoneal Injection of Monocrotaline as a Novel Large Animal Model of Chronic Pulmonary Hypertension in Tibet Minipigs. *PLOS ONE*. 2013;8(11):e78965.

64. Roth RA, Dotzlaf LA, Baranyi B, Kuo CH, Hook JB. Effect of monocrotaline ingestion on liver, kidney, and lung of rats. *Toxicol Appl Pharmacol*. 1981;60(2):193-203.

65. Ruiter G, Man FS de, Schalij I, et al. Reversibility of the monocrotaline pulmonary hypertension rat model. *Eur Respir J*. 2013;42(2):553-556.

66. Vélez-Rendón D, Zhang X, Gerringer J, Valdez-Jasso D. Compensated right ventricular function of the onset of pulmonary hypertension in a rat model depends on chamber remodeling and contractile augmentation. *Pulm Circ*. 2018;8(4):1-13.

67. Hill NS, Gillespie MN, McMurtry IF. Fifty Years of Monocrotaline-Induced Pulmonary Hypertension: What Has It Meant to the Field? *CHEST*. 2017;152(6):1106-1108.

68. Evans JDW, Girerd B, Montani D, et al. BMPR2 mutations and survival in pulmonary arterial hypertension: an individual participant data meta-analysis. *Lancet Respir Med*. 2016;4(2):129-137.

69. Beppu H, Kawabata M, Hamamoto T, et al. BMP Type II Receptor Is Required for Gastrulation and Early Development of Mouse Embryos. *Dev Biol*. 2000;221(1):249-258.

70. West J, Harral J, Lane K, et al. Mice expressing BMPR2R899X transgene in smooth muscle develop pulmonary vascular lesions. *Am J Physiol-Lung Cell Mol Physiol*. 2008;295(5):L744-L755.

71. Hautefort A, Mendes-Ferreira P, Sabourin J, et al. Bmpr2 Mutant Rats Develop Pulmonary and Cardiac Characteristics of Pulmonary Arterial Hypertension. *Circulation*. 2019;139(7):932-948.

72. Campanale CM, Scherrer B, Afacan O, Majeed A, Warfield SK, Sanders SP. Myofiber organization in the failing systemic right ventricle. *J Cardiovasc Magn Reson*. 2020;22:49.

73. Zhang X, Haynes P, Campbell KS, Wenk JF. Numerical Evaluation of Myofiber Orientation and Transmural Contractile Strength on Left Ventricular Function. *J Biomech Eng*. 2015;137(4):044502.

74. Avazmohammadi R, Mendiola EA, Li DS, Vanderslice P, Dixon RAF, Sacks MS. Interactions Between Structural Remodeling and Hypertrophy in the Right Ventricle in Response to Pulmonary Arterial Hypertension. *J Biomech Eng*. 2019;141(9):910161-910613.

75. Zimmer HG. The Isolated Perfused Heart and Its Pioneers. *Physiology*. 1998;13(4):203-210.

76. Demer LL, Yin FC. Passive biaxial mechanical properties of isolated canine myocardium. *J Physiol*. 1983;339:615-630.

77. Lin J, Lopez EF, Jin Y, et al. Age-Related Cardiac Muscle Sarcopenia: Combining experimental and mathematical modeling to identify mechanisms. *Exp Gerontol*. 2008;43(4):296-306.

78. Passive biaxial mechanical properties of isolated canine myocardium. - PMC.

79. Vélez-Rendón D, Pursell ER, Shieh J, Valdez-Jasso D. Relative Contributions of Matrix and Myocytes to Biaxial Mechanics of the Right Ventricle in Pulmonary Arterial Hypertension. *J Biomech Eng*. 2019;141(9):091011.

80. Zile MR, Richardson K, Cowles MK, et al. Constitutive properties of adult mammalian cardiac muscle cells. *Circulation*. 1998;98(6):567-579.

81. Rassier DE, Pavlov I. Contractile characteristics of sarcomeres arranged in series or mechanically isolated from myofibrils. *Adv Exp Med Biol*. 2010;682:123-140.

82. Badesch DB, Raskob GE, Elliott CG, et al. Pulmonary arterial hypertension: baseline characteristics from the REVEAL Registry. *Chest*. 2010;137(2):376-387.

83. Farber HW, Miller DP, Poms AD, et al. Five-Year outcomes of patients enrolled in the REVEAL Registry. *Chest*. 2015;148(4):1043-1054.

84. Jing ZC, Xu XQ, Han ZY, et al. Registry and survival study in chinese patients with idiopathic and familial pulmonary arterial hypertension. *Chest*. 2007;132(2):373-379.

85. Humbert M, Sitbon O, Yaïci A, et al. Survival in incident and prevalent cohorts of patients with pulmonary arterial hypertension. *Eur Respir J*. 2010;36(3):549-555.

86. Hoeper MM, Huscher D, Ghofrani HA, et al. Elderly patients diagnosed with idiopathic pulmonary arterial hypertension: results from the COMPERA registry. *Int J Cardiol*. 2013;168(2):871-880.

87. McGoon MD, Krichman A, Farber HW, et al. Design of the REVEAL registry for US patients with pulmonary arterial hypertension. *Mayo Clin Proc*. 2008;83(8):923-931.

88. Ventetuolo CE, Praestgaard A, Palevsky HI, Klinger JR, Halpern SD, Kawut SM. Sex and haemodynamics in pulmonary arterial hypertension. *Eur Respir J*. 2014;43(2):523-530.

89. D'Alonzo GE, Barst RJ, Ayres SM, et al. Survival in patients with primary pulmonary hypertension. Results from a national prospective registry. *Ann Intern Med*. 1991;115(5):343-349.

90. Ling Y, Johnson MK, Kiely DG, et al. Changing demographics, epidemiology, and survival of incident pulmonary arterial hypertension: results from the pulmonary hypertension registry of the United Kingdom and Ireland. *Am J Respir Crit Care Med*. 2012;186(8):790-796.

91. Kawut SM, Lima JAC, Barr RG, et al. Sex and Race Differences in Right Ventricular Structure and Function: The MESA-Right Ventricle Study. *Circulation*. 2011;123(22):2542-2551.

92. Ventetuolo CE, Ouyang P, Bluemke DA, et al. Sex hormones are associated with right ventricular structure and function: The MESA-right ventricle study. *Am J Respir Crit Care Med*. 2011;183(5):659-667.

93. Foppa M, Arora G, Gona P, et al. Right Ventricular Volumes and Systolic Function by Cardiac Magnetic Resonance and the Impact of Sex, Age, and Obesity in a Longitudinally Followed Cohort Free of Pulmonary and Cardiovascular Disease. *Circ Cardiovasc Imaging*. 2016;9(3):e003810.

94. Jacobs W, Van De Veerdonk MC, Trip P, et al. The Right Ventricle Explains Sex Differences in Survival in Idiopathic Pulmonary Arterial Hypertension. *Chest*. Published online 2014.

95. Gabler NB, French B, Strom BL, et al. Race and Sex Differences in Response to Endothelin Receptor Antagonists for Pulmonary Arterial Hypertension. *Chest*. 2012;141(1):20-26.

96. Rodriguez-Arias JJ, García-Álvarez A. Sex Differences in Pulmonary Hypertension. *Front Aging*. 2021;2:727558.

97. Cheron C, McBride SA, Antigny F, et al. Sex and gender in pulmonary arterial hypertension. *Eur Respir Rev*. 2021;30(162):200330.

98. Umar S, Rabinovitch M, Eghbali M. Estrogen Paradox in Pulmonary Hypertension. *Am J Respir Crit Care Med*. 2012;186(2):125-131.

99. Hester J, Ventetuolo C, Lahm T. Sex, Gender, and Sex Hormones in Pulmonary Hypertension and Right Ventricular Failure. *Compr Physiol*. 2019;10(1):125-170.

100. Ventetuolo CE, Gabler NB, Fritz JS, et al. Are Hemodynamics Surrogate Endpoints in Pulmonary Arterial Hypertension? *Circulation*. 2014;130(9):768-775.

101. van Wolferen SA, Marcus JT, Boonstra A, et al. Prognostic value of right ventricular mass, volume, and function in idiopathic pulmonary arterial hypertension. *Eur Heart J*. 2007;28(10):1250-1257.

102. Sharifi Kia D, Kim K, Simon MA. Current Understanding of the Right Ventricle Structure and Function in Pulmonary Arterial Hypertension. *Front Physiol*. 2021;12:641310.

103. Shigeta A, Tanabe N, Shimizu H, et al. Gender Differences in Chronic Thromboembolic Pulmonary Hypertension in Japan. *Circ J*. 2008;72(12):2069-2074.

104. Lahm T, Frump AL, Albrecht ME, et al. 17β-Estradiol mediates superior adaptation of right ventricular function to acute strenuous exercise in female rats with severe pulmonary hypertension. *Am J Physiol-Lung Cell Mol Physiol*. 2016;311(2):L375-L388.

105. Liu A, Schreier D, Tian L, et al. Direct and indirect protection of right ventricular function by estrogen in an experimental model of pulmonary arterial hypertension. *Am J Physiol - Heart Circ Physiol*. Published online 2014.

Chapter 2 LONGITUDINAL RIGHT VENTRICULAR HEMODYNAMIC AND MORPHOLOGIC CHANGES IN PULMONARY ARTERIAL HYPERTENSION

2.1 Introduction

Right-ventricular (RV) function is an important predictor of long-term outcomes in PAH, but the chronic progression of RV remodeling leading to RV dysfunction and failure remains unclear. While the RV can initially adapt to maintain cardiac output, how and why these adaptive responses become insufficient or exhausted remains unclear. Preclinical studies of RV pressure overload have revealed common components of the remodeling response are hypertrophy of the RV free wall, myocardial fibrosis, changes to RV contractility, and increased myocardial stiffness. How these changes result in functional changes to systolic and diastolic RV function is also unknown. For example, RV hypertrophy can initially serve to reduce myocardial wall stress, alleviating the burden due to increased chamber fluid pressure, but these changes also have long-term implications such as contractile and metabolic alterations. While increases to contractility may be beneficial by facilitating increased wall contraction, they may result in long-term dysfunction. Therefore, identifying the triggers and mediators of the functional switch from compensated RV function to maladaptive RV function is of tremendous clinical importance. However, longitudinal long-term studies of RV function are limited and long-term studies that analyze comprehensive RV biomechanics and hemodynamics are warranted.

To characterize multiple stages of disease progression, we induced pulmonary arterial hypertension using a well-established animal model. In particular, the sugen-hypoxia rat model was chosen for study because it develops similar features to human PAH, including vascular lesions resembling those found in explant tissues of PAH patients and RV remodeling. By studying the response of the right ventricular to pressure overload over 10 weeks, we will establish a longitudinal description of changes to RV hemodynamics, particularly in the early stage of remodeling. We characterized the changes to the RV that result from PAH treatment, with a particular focus on describing the hemodynamics and changes to RV systolic and diastolic chamber function. The results of this 10-week study were published in 2021[1].

2.2 Approach

2.2.1 Animal Model of PAH

The sugen-hypoxia (SuHx) animal model of PAH was chosen for this study as it develops vascular lesions resembling those found at autopsy in patients with PAH, followed by RV remodeling[2,3]. The vascular endothelial growth factor receptor antagonist Sugen 5416 inhibits vascular adaptation that might otherwise occur in response to chronic hypoxia via micro-vascular angiogenesis[4]. Consequently, sugen-hypoxia treatment results in vascular damage and obliterative lesions similar to those found in patients with PAH at autopsy and subsequently imposes a pressure overload on the right ventricle, leading to progressive RV changes[2]. These factors make the SuHx rat model one of the specific, established and most widely used preclinical models of PAH[5]. Animal care, housing, and feed were approved by the Institutional Animal Care and Use Committees at the University of Illinois at Chicago and the University of California San Diego. Seven-week-old male Sprague-Dawley rats weighing 216 ± 9.6g (Charles River Labs, Wilmington, MA, USA) were randomized into control (n = 22) and SuHx (n = 52) groups. Pulmonary arterial hypertension was induced in rats by a single subcutaneous injection (20mg/Kg) of the vascular endothelial growth factor receptor antagonist sugen (SU5416, S8442 MilliporeSigma, CAS Number 204005-46-9, PubChem Substance ID 24278606 Sigma-Aldrich, MO, USA). Sugen solution was prepared by mixing 25mg sugen powder in 1.25mL solvent dimethylsulfoxide (anhydrous DMSO, Thermofisher Scientific, Catalog #D12345, MA, USA) using an 18G needle. The subsequent mixture was mixed with a stand vortex mixer to ensure dissolution and the resulting solution was filtered through a 0.2um syringe filter. Sugen injections were followed by exposure to chronic hypoxia (10% O2) for 3 weeks. The animals were then returned to normoxia. The severity of the disease was augmented by the time (in weeks) elapsed after returning to normoxia (up to 10 weeks post-injection). Timepoints included in the study were three (W3), four (W4), five (W5), six (W6), eight (W8) and ten (W10) weeks post injections. The disease phenotype was confirmed by invasive catheter measurements of mean pulmonary arterial pressure (>20 mmHg). Age-matched normotensive control animals kept in normoxia throughout the study comprised the control group.

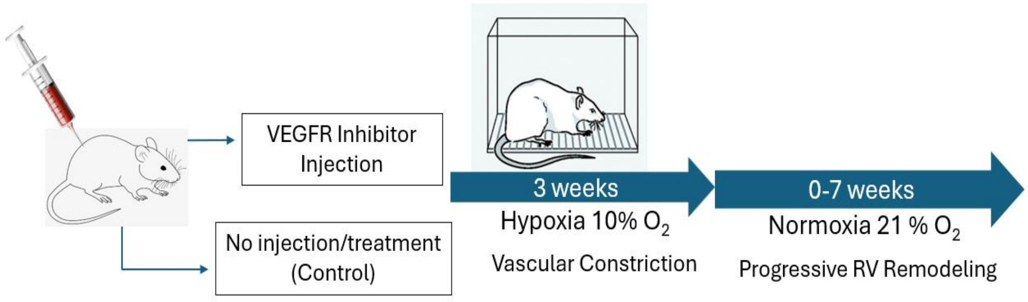

Figure 2.1. Sprague-Dawley rats were treated with sugen-hypoxia. The vascular endothelial growth factor receptor antagonist Sugen5416 was subcutaneously injected, after which rats were exposed to chronic hypoxia. After three weeks of hypoxia exposure, rats were returned to normoxia, during which the disease was augmented by time, varying from three to ten total weeks of sugen-hypoxia treatment before being studied.

Following the ten-week study, a separate cohort of 28 animals was studied in which the duration of normoxia was extended to timepoints up to 23 weeks while the duration of hypoxia was kept at 3 weeks, resulting in totals of up to 26 weeks of SuHx treatment. The timepoints added were twelve (W12), fifteen (W15), eighteen (W18), twenty (W20), twenty-one (W21), and twenty-six (W26) weeks post injections. In these animals, identical experimental procedures were performed, by which we acquired hemodynamic and morphologic measurements, as well as measurements of tissue collagen content.

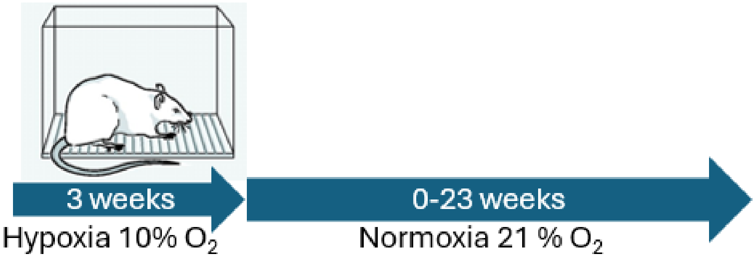

Figure 2.2. In a different cohort of 28 male rats, SuHx treatment duration was extended to augment the severity of the disease. Although the hypoxia duration was kept at 3 weeks, time in normoxia was extended up to 23 weeks for a total of 26 weeks of SuHx treatment.

2.2.2 Assessing *in-vivo* Hemodynamics

Measurements of RV hemodynamics (pressure-volume relationships) were the main data used to quantify the longitudinal progression of RV function. RV hemodynamics were obtained *via* invasive catheterization of the RV chamber, as described in Kwan *et al*[1]. During terminal surgical procedures, animals were continuously administered 2.5% isoflurane (MWI Veterinary Supply, USA) mixed with oxygen *via* a nose cone. Animals were intubated following a tracheotomy and ventilated at 40-50 breaths per minute, with a tidal volume ranging from 1.7-4.2 mL, based on the bodyweight. Body temperature and heart rate were continuously monitored throughout the procedure using a rectal probe (MicroTherma 2, ThermoWorks, UT, USA) and a 4-lead electrocardiogram. The isoflurane dose was occasionally adjusted from 2.5% to maintain a heartrate range between 280-360 beats per minute within the range 1.0-2.5%. To record pressure-volume timeseries, a 1.9F admittance PV catheter was inserted into the RV chamber through the apical myocardium wall. To measure pulmonary arterial pressures, a 1.6F dual-pressure sensor catheter (model FTH-1615B, Transonic Science, ON, Canada) was advanced into the pulmonary arteries through the pulmonary valve, with a mPAP measurement above 20mmHg confirming

PAH. Mean PA pressure was approximated during surgeries as the sum of the end-systolic PA pressure and twice the end-diastolic PA pressure divided by three (Eq. 2.1) and confirmed afterwards by the integral of the PA pressure waveform[6].

$$mean\ PA\ pressure = \frac{2 \cdot EDP + ESP}{3} \qquad \text{Eq. 2.1}$$

When possible, the pressure-volume catheter was also inserted into the LV chamber to record LV pressure-volume through the cardiac cycle during steady state and during occlusive preload variation.

2.2.3 Pressure-Volume Catheter Measurements

The outputs of the PV catheter were three direct measurements (admittance signal phase and magnitude and RV pressure) and two indirect measurements (RV chamber volume and heart rate). RV blood pressure can be readily measured via simple technologies such as a strain gage, which converts a mechanical force to an electrical force that can be calibrated to a corresponding blood pressure. Ventricular volumes, however, are more difficult to measure accurately and reproducibly. This is especially true in the right ventricular, which normally presents an asymmetric crescent shape and whose systolic and diastolic kinematic motion can be difficult to track. Pressure-volume catheters today typically rely on measurements of the conductivity and permittivity properties of blood and myocardium to produce measurements of the ventricular chamber volume. The relationship between ventricular volume and the electrical catheter signal is derived from Ohm's Law, whereby voltage is the ratio of current to conductance. Therefore, the strength of the electrical signal (voltage) directly corresponds to the conductance, according to the equation:

$$V = \frac{I}{G} \qquad \text{Eq. 2.2}$$

where V is voltage, I is current, and G is conductance (the inverse of resistance) of an electrical circuit. Conductance catheters apply an alternating current of constant magnitude to generate an electrical field inside the heart. The voltage change as the electric field interacts with the surrounding ventricle (blood and myocardium) is recorded and corresponds to a change in conductance. The measured conductance value is affected by the conductance values of blood and myocardium. Time-varying measurements of total conductance have been used to describe time-varying changes to ventricular volume according to Baan's Equation:

$$Volume = \frac{1}{\alpha}\rho L^2(G_{blood} - G_{myocardium}) \qquad \text{Eq. 2.3}$$

where L is the distance between the recording electrodes, ρ is the resistivity of blood, and α is a correction factor dependent on the geometry of the ventricular chamber. The correction factor α was originally estimated to be 1 for a stacked cylindrical model of the left ventricle, and 0.69 for a spherical ventricle but has more recently been defined according to a range of values between 0.07 in mice to 1.01 in large mammals, based on cuvette calibration[7,8]. Importantly, the correction factor α is assumed to be constant, but electrical field strength decreases non-linearly with distance. Blood conductance is a relatively larger contributor to total conductance at diastole while myocardial conductance is a larger contributor at systole, making the measurement of both systolic and diastolic blood volumes in the dynamic ventricular chambers challenging.

To address this, the admittance technique was developed to account for a non-linear relationship between conductance and volume. Under the admittance technique, the resistive and capacitive properties of blood are separated, allowing it to be distinguished from blood, which is purely resistive. Therefore, the time delay caused by the myocardial capacitance property corresponds to the motion of the myocardial wall, with the largest phase values at systole and the smallest at diastole. Using this approach, blood volumes in real time are calculated by measuring myocardial parallel conductance is measured as a dynamic variable, allowing more accurate measures throughout the cardiac cycle. This relationship is described by Wei's Equation[9]:

$$Volume = \frac{1}{1-\frac{G_{blood}}{\gamma}}\rho L^2 G_{blood} \qquad \text{Eq. 2.4}$$

Here L is the distance between the recording electrodes, ρ is the resistivity of blood, and a new electric field correction factor γ is the solution to the quadratic formula relating blood conductance and stroke volume, calibrated to known measurements of stroke volume and blood conductance at end-systole and end-diastole according to the formula:

$$\gamma = -b \pm \frac{\sqrt{b^2-4ac}}{2a} \qquad \text{Eq. 2.5}$$

where

$$a = SV - \rho L^2\left(G_{blood,ED} - G_{blood,ES}\right) \qquad \text{Eq. 2.6}$$

$$b = -SV\left(G_{blood,ED} + G_{blood,ES}\right) \qquad \text{Eq. 2.7}$$

$$c = SV * G_{blood,ED} * G_{blood,ES} \qquad \text{Eq. 2.8}$$

This approach allows blood volume to be measured in real-time, accounts for a non-linear relationship between volume and electric field distance, and has been validated via non-invasive measurements of blood volume by cardiac MRI and echocardiography in the RVs of normotensive and hypertensive rodents[10–12]. This method also precludes the need for hypertonic saline injection to calculate parallel conductance (such as traditional conductance catheters used).

2.2.4 Raw Data Processing

The outputs of the P-V catheter consisted of continuous pressure-volume timeseries and were post-processed *via* a semi-automated custom written Matlab script. Pressure-volume timeseries averaging 80-200 steady state heartbeats were separated into individual pressure-volume loops. Heartbeats were separated at the timepoint of peak RV chamber pressure, corresponding to mid-systole, according to a local maximum searching algorithm (*findpeaks* command, MatLab v2023A, MathWorks, MA, USA).

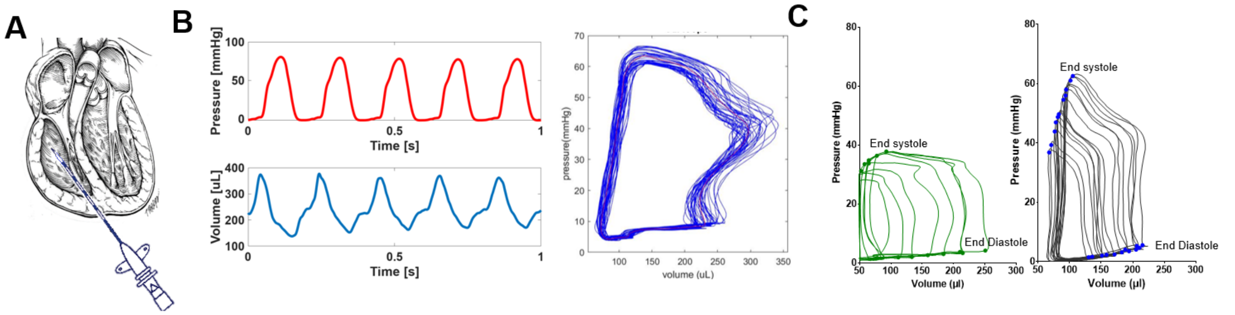

Figure 2.3. The RV chamber was catheterized with a pressure-volume admittance catheter (**A**) which recorded continuous pressure-volume timeseries (**B**), from which pressure-volume loop analysis was performed during steady state, and during preload variation (**C**).

P-V loops were analyzed to describe RV function. While we qualitatively observed a large degree of heterogeneity in the PV loop shape, particularly in PAH treated rats, our P-V analysis was primarily based on the end-systolic and end-diastolic points, the behavior of which were used to characterize systolic and diastolic function. The end-systolic point was determined as the point with the maximum ratio of pressure to volume. This selection was almost always distinct from the systolic timepoint corresponding to peak RV pressure. The end-diastolic point was determined as the point of minimal RV pressure, during which pressure rate change was increasing. RV function was described during two parts: First a comprehensive description of the hemodynamic status was produced from P-V loop analysis performed during steady state (period of stable and reproducible cardiac rhythm), representing 80-200 heartbeats on average. This description included measurements of the RV hemodynamics (pressures and volumes) at end-systole and end-diastole, measurements of RV function and output (ejection fraction, stroke volume, cardiac output), measurements of contractility and relaxation (dP/dt max and min), and measurements of RV preload and afterload (ED volume, total pulmonary vascular resistance). Second, a description of RV chamber biomechanics was produced from P-V loop analysis performed during preload variation. The right ventricular preload was varied by temporarily occluding the inferior vena cava by suture line during pressure-volume measurements. Vena caval occlusion reduces the filling of the RV and allows for the determination of the end-systolic and end-diastolic pressure volume relationships. Occlusions were screened primarily for consistency (determined by reproducible occlusion pressure-volume behavior) and secondarily by preferentially selecting those measured earlier in the surgery (to minimize isoflurane exposure, manual ventilation, and potential blood loss).

2.2.5 Computing Right-Ventricular Hemodynamics from Raw Data

Steady-state P-V measurements immediately preceding caval occlusion, ranging from 80-200 heartbeats, were separated into single heartbeats, aligned within the cardiac cycle, and averaged to generate a representative P-V loop. The end-systolic (ES) P-V point was identified as the timepoint in the loop with the maximum pressure-to-volume ratio. The end-diastolic (ED) P-V point was identified as the pressure and volume at the first time following isovolumic relaxation when the volume was at a maximum (i.e., dV/dt ~0). With the heart rate, ES and ED volumes were used to compute stroke volume (SV), ejection fraction (EF) and cardiac output (CO). Total pulmonary vascular resistance (tPVR) was determined by dividing RV ES pressure by CO. These hemodynamic parameters are described in the equations below (Eq. 2.9-2.12).

$$SV = EDV - ESV \qquad \text{Eq. 2.9}$$

$$EF = \frac{SV}{EDV} \qquad \text{Eq. 2.10}$$

$$EF = SV \cdot HR \qquad \text{Eq. 2.11}$$

$$tPVR = \frac{ESP}{CO} \qquad \text{Eq. 2.12}$$

ES and ED chamber elastance were identified by computing chamber stiffness, defined as the rate change of the pressure-volume relation (*dP/dV*) at the ES and ED points. A linear function (Eq. 2.13) through the ES P-V points during caval occlusion, end-systolic elastance (E_{es}) was determined (Eq. 2.14). End-diastolic elastance (E_{ed}) on the other hand was computed by fitting a nonlinear exponential function, shown below in Eq. 2.15 through the ED P-V points during caval occlusion. ED chamber elastance was identified by computing chamber stiffness (Eq. 2.16) at the steady-state ED volume (as illustrated in Fig. 3A-B).

$$ESPVR = P(V) = \alpha \cdot V + C \qquad \text{Eq. 2.13}$$

$$E_{ES} = \frac{dP}{dV}(ESPVR(ESP, ESV)) = \alpha \qquad \text{Eq. 2.14}$$

$$EDPVR = P(V) = \alpha e^{\beta V} \qquad \text{Eq. 2.15}$$

$$E_{ED} = \frac{dP}{dV}(EDPVR(EDP, EDV)) = \alpha\beta e^{\beta V} \qquad \text{Eq. 2.16}$$

Effective arterial elastance (E_a) was calculated as the ratio of ES pressure to SV and ventricular-vascular coupling was calculated as the ratio of E_{es} to E_a per animal. Maximum and minimum pressure rate changes were found by identifying the largest local maxima and smallest local minima of the time derivative of pressure measurements, respectively. To avoid extrapolating volumes to pressures below zero, the unloaded volume Vo was set to the RV volume measured during caval occlusions with the lowest end-diastolic pressure. For animals with repeated steady-state measurements, ED and ES pressures and volumes, SV, EF, CO, tPVR, dP/dt_{max}, and dP/dt_{min} of each steady-state measurement were averaged per animal. For animals in which multiple caval occlusions were performed, occlusions were averaged. By normalizing RV volumes by V_o, the pressure-volume curves were averaged across occlusions. P-V loops for a single animal were then averaged and interpolated over the measured volume ranges. Volumes were then un-normalized by multiplying by the mean minimum volume. Mean pulmonary arterial pressure was computed by integrating the mean pulmonary arterial pressure waveform over three cardiac cycles.

2.2.6 Non-Invasive Right-Ventricular Measurements

In a small subset of rats, transthoracic two-dimensional M-mode echocardiography (Vevo 770 Micro-Ultrasound imaging system, Visual Sonics, Toronto, Canada) was performed on rats under 2% isoflurane anesthesia to describe RV function non-invasively. RV systolic function was characterized by the tricuspid annular plane systolic excursion (TAPSE). The TAPSE measures the one-dimensional distance the tricuspid valve moves in the cardiac cycle as a surrogate measure of (longitudinal) contractile function[13].

2.2.7 Histological Measurements of Right-Ventricular Hypertrophy and Fibrosis

Immediately following *in vivo* hemodynamic measurements, animals were exsanguinated, and the heart was flushed with ice-cold phosphate-buffered saline (pH 7.4), consisting of 0.137M NaCl, 0.0027M KCl, 0.01M Na_2HPO_4, 0.0018M KH_2HPO_4, and 5000U/mL heparin solution (USP, MWI veterinary Supply, Cat. No. 054255). The heart was excised, and the RV free wall was isolated and weighed. RV thickness was measured at three locations near the mid region of the free wall using a precision gaugce (1010Z, Starrett, Athol, MA, with a range of 0-0.375" and accuracy of 0.001") and averaged per animal. Left ventricular and septum walls were massed and used to compute septum volume and Fulton Index (the ratio of RV to LV and septum masses). Tissue samples from the mid region of the RV free wall were taken for histological analysis. Samples were fixed in 10% formalin (Thermo Fisher Scientific, MA, Cat. No. SF100-4) for 48 hours, stored in 70% ethanol, then paraffin embedded and sectioned parallel to myofiber direction. The samples were stained with Masson's Trichrome to identify collagen (blue) myocytes (red), and nuclei (black). Samples were imaged at 40x magnification with a fluorescent microscope (Evos FL Auto Fluorescent Microscope, Thermo Fisher Scientific, MA, USA) and the collagen to myocyte area fractions were determined by converting bright-field images to the hue-saturation value (HSV) scale to screen for different tissue constituents.

A hydroxyproline Assay (Quickzyme Total Collagen Assay, QuickZyme BioSciences, Lei, NL) was used to measure totalo RV collagen content. Free wall tissue samples weighing 5-15 mg were prepared and assayed according to the manufacturer's recommended protocol. Hydroxyproline residues were quantified using a microplate reader (Tecan M200, Tecan LifeSciences, CH). Absorbances were calibrated with a linear collagen standard curve, adjusted for sample dilution and expressed as total collagen content.

Collagen types I and III contents were quantified using enzyme-linked immunosorbent assay kits (Rat Collagen type I ELISA Kit, NBP2-75823, Collagen type III ELISA Kit, NBP2-81205, Novus Biologicals, CO). Tissue samples were isolated in cold 1× PBS at a 1:9 wt/vol ratio and diluted 1:100. Collagen I and III concentrations were measured at 450-nm wavelength (Tecan F200 Microplate Reader, Tecan LifeSciences, CH). Absorbances were calibrated with collagen I and collagen III standard curves ranging from 0 to 100 ng/mL and expressed as the ratio of collagen I to collagen III.

Collagen crosslinking was determined using competitive enzyme linked immunoassays (ELISA) for the collagen crosslink pyridinoline (PYD ELISA, MyBioScience, cat. No: MBS015115) and quantified with both linear and best-fit quadratic standard curves. Non-enzymatic collagen cross-linking was assessed using competitive ELISA for advanced glycation end products (AGE Assay Kit, Abcam, cat. No: ab238539). RV myocardial tissue samples weighing 15-200mg were rinsed in 1x PBS, blotted dry, diluted 1:10 in 1x PBS and homogenized in BeadBug tubes with 1.55mm Zirconium beads (Benchmark Sci, cat. No: D1032-5), then sonicated in ice cold water for 10 minutes. After centrifugation at 5000xg for 5 minutes, the supernatant was saved for assays. Assays were performed according to manufacturer specified protocols.

2.2.7 Statistical analysis

Group comparisons of hemodynamics were analyzed with descriptive statistics using the JMP Pro Statistical software package (version 16, SAS Institute Inc., NC, USA). For longitudinal measurements, the Shapiro-Wilkes test was used to determine normality of data. Non-normally distributed data was analyzed using the Wilcoxon-Kruskal-Wallis statistic, followed by the Dunn test for comparisons across weeks of treatment. For normally distributed data, one-factor ANOVA was used to test differences in treatment groups followed by the Dunnett's post-hoc test. Otherwise, the non-parametric Wilcoxon-Kruskal-Wallis statistic was used followed by the Dunnett's post-hoc test. For all statistical tests, a p-value < 0.05 was considered statistically significant. All figures were generated using Prism software (version 8.4.3, GraphPad, CA, USA).

2.3 Results: Distinct Time courses of Hypertrophy and Stiffening

In a longitudinal study, we made measurements of RV hemodynamics and chamber mechanics at six time points over ten weeks in the sugen-hypoxia male rat model of PAH. Hemodynamic and morphological measurements were obtained from 22 control and 52 SuHx rats. While age-matched control animals corresponding to each SuHx time point were studied, no changes in hemodynamics were found, so these animals were aggregated into a single group for the purposes of presentation and statistical analysis. The group sizes for hemodynamic measures at each disease stage were $n_{CNT} = 22$, $n_{W3} = 9$, $n_{W4} = 9$, $n_{W5} = 7$, $n_{W6} = 9$, $n_{W8} = 7$, and $n_{W10} = 6$. A total of 5 SuHx-treated animals died during surgeries before hemodynamic measurements were completed. No rats died prior to the terminal procedure.

2.3.1 Ventricular Hemodynamics and Morphology

In SuHx-treated rats, RV ES pressure (Fig. 2.3A), RV ED pressure (Fig. 2.3B), tPVR (Fig. 2.3F), and RV Fulton Index (Fig. 2.5C) had all increased significantly ($p<0.05$) and more than doubled compared with control by 5 weeks post-induction and these increases were all sustained through week 10. Immediately after hypoxia (week 3), ES volume ($p<0.01$, Fig 2.4A) and wall thickness ($p<0.01$, Fig. 2.5D) were both significantly higher than control. By week 4, EF (Fig. 2.4F was significantly lower than control (from 66±10% to 40±6%, $p<0.01$, Fig. 2.4F), but thereafter ejection fraction stabilized, coinciding with significant increases in peak positive and negative dP/dt by week 5 compared with controls ($p<0.05$, Fig. 2.4D-E). Despite the significant increase in RV ED pressure by week 5, ED volume (Fig. 2.5B) remained unchanged.

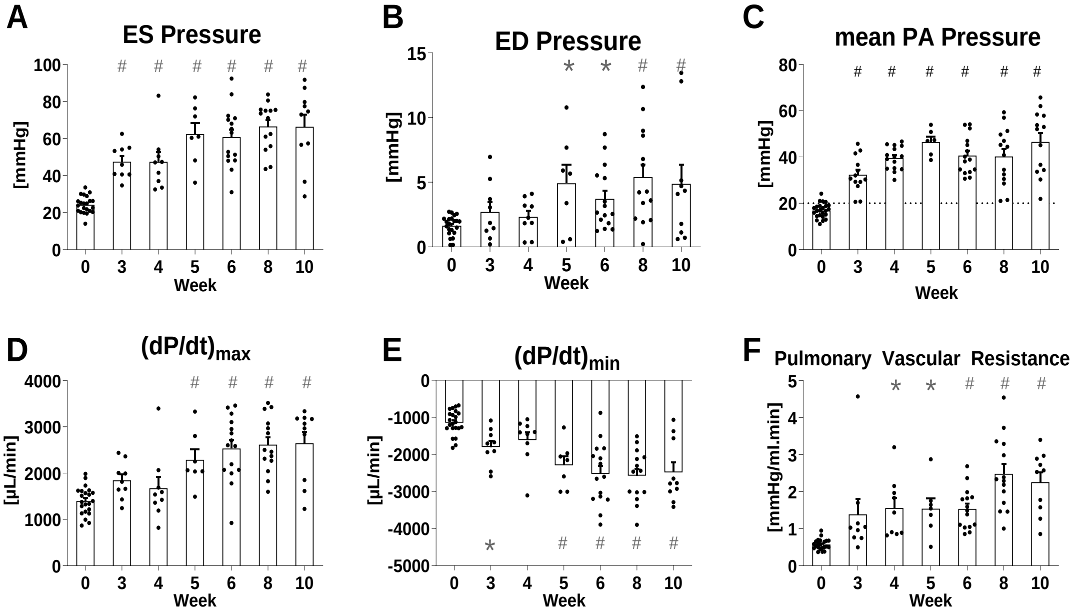

Figure 2.4. *In-vivo* hemodynamic measurements in SuHx rats through the 10-week time course of the study showed significant increases by week 3 in end-systolic (ES) right ventricular pressure (**A**) and mean pulmonary arterial pressure (**C**), significant increases in total pulmonary vascular resistance by week 4 (**F**) , and significant increases by week 5 in end-diastolic (ED) pressure (**B**) and peak positive time derivative of right ventricular pressure (**D**). The magnitude of peak negative time derivative of pressure increased significantly at week 3 and after week 4 (**E**). Data shown as mean ± standard error, *p < 0.05 and # p < 0.01 compared with the control group.

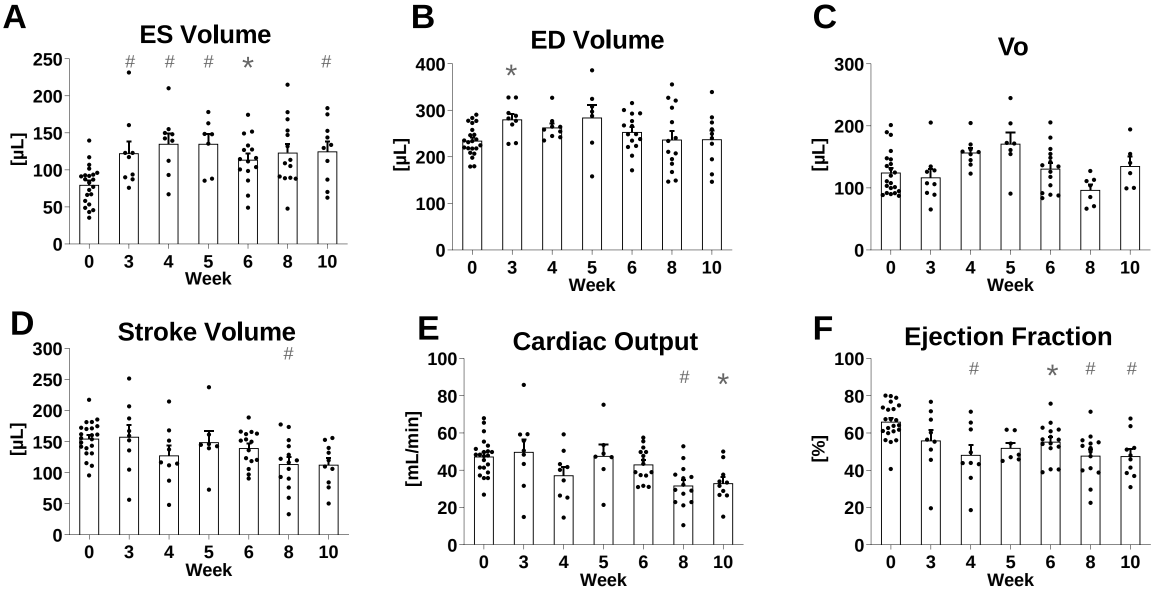

Figure 2.5. While SuHx treatment increased ES volume (**A**), ED volume (**B**) was preserved throughout the study apart from a small but significant increase at week 3. The unloaded RV volume (**C**), approximated from caval occlusions, did not significantly change. Stroke volume (**D**) and cardiac output (**E**) were only significantly lower than control after week 6. Mean ejection fraction (**F)** decreased significantly by week 4 but did not change after week 4 (p>0.05, comparison not shown). Data shown as mean ± standard error, *$p < 0.05$ and #$p < 0.01$ compared with the control group.

No changes in LV end-systolic pressure (from 91±9 mmHg, n = 8 to 87±7 mmHg, n = 12, p = 0.77) or in LV ejection fraction (from 76±3%, n = 8 to 70±5%, n = 12, p = 0.38) were found in the SuHx animals compared with control animals. The sum of LV and septum masses increased in SuHx week 5 and week 8 (Fig 2.5B) compared with control animals but remained unchanged at all other time points (p>0.05).

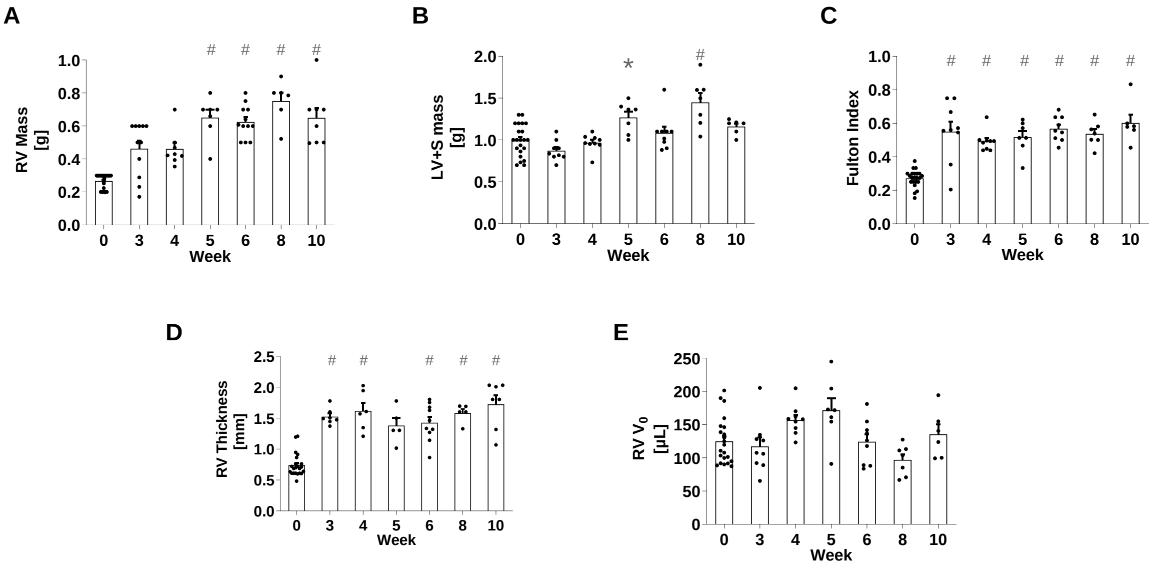

Figure 2.6. Masses of right ventricle (**A**) left ventricle plus septum (**B**), and their mass ratio (**C**), right ventricular wall thickness (**D**) and estimated *V*$_o$ (**E**). Data shown as mean ± standard error, *p < 0.05 and # p < 0.01 compared with the control group. Figure 2.6. is a reproduction in part of data published in the American Journal of Physiology. doi: 10.1152/ajpheart.00046.2021. Epub 2021 Aug 27. PMID: 34448637; PMCID: PMC8794227.

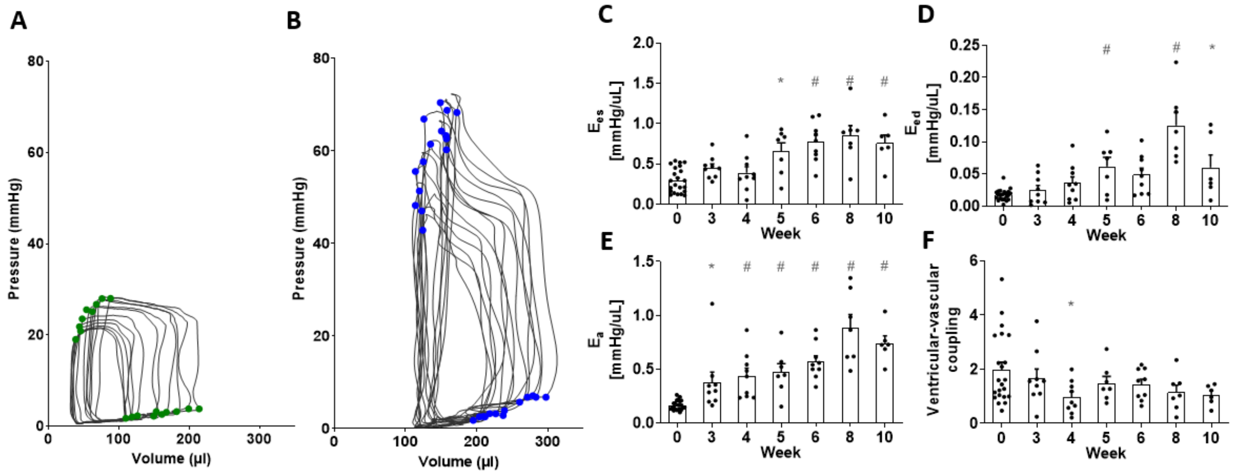

Figure 2.7. Pressure-volume (P-V) during caval occlusion to determine end-systolic (ES) and end-diastolic (ED) P-V relations for a control (**A**) and a 6-week SuHx (**B**) animal. ES elastance E_{es} (**C**), ED elastance E_{ed} (**D**), arterial elastance E_a (**E**) and ventricular-vascular coupling E_{es}/E_a (**F**). Data shown as mean ± standard error, *p < 0.05 and # p < 0.01 compared with the control group. Figure 2.7. is a reproduction in part of data published in the American Journal of Physiology. doi: 10.1152/ajpheart.00046.2021. Epub 2021 Aug 27. PMID: 34448637; PMCID: PMC8794227.

RV volumes of individual rats obtained noninvasively *via* cMRI were compared with the respective group's distribution. While end-diastolic and end-systolic volumes were smaller in the cMRI measures, volumes were within two standard deviations of the invasive group means (Table 1) and the differences between control and SuHx RV volumes were consistent. CMRI derived ejection fractions were 54% and 44% for the SuHx animals compared with the group mean of 48±16%, and 72% in the control animal compared with the group mean of 66±10%. Similarly, cMRI derived stroke volumes were 127µL and 118µL in the SuHx rats compared with group mean of 128 ± 48 µL, and 129 µL in the control animal compared with the group mean of 155±28 µL (**Table 2.1**).

Table 2.1. RV chamber volumes, ejection fractions and stroke volumes measured by invasive catheterization for control and SuHx week 4 groups (mean ± standard deviation) compared with those in individual animals measured using cardiac magnetic resonance imaging (cMRI). Table 2.1 is a reproduction in part of data published in the American Journal of Physiology. doi: 10.1152/ajpheart.00046.2021. Epub 2021 Aug 27. PMID: 34448637; PMCID: PMC8794227.

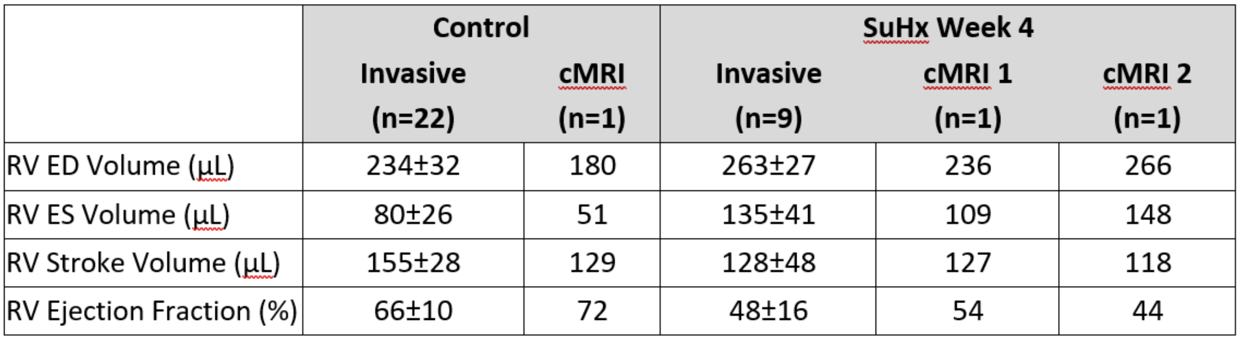

	Control		**SuHx Week 4**		
	Invasive (n=22)	**cMRI (n=1)**	**Invasive (n=9)**	**cMRI 1 (n=1)**	**cMRI 2 (n=1)**
RV ED Volume (µL)	234±32	180	263±27	236	266
RV ES Volume (µL)	80±26	51	135±41	109	148
RV Stroke Volume (µL)	155±28	129	128±48	127	118
RV Ejection Fraction (%)	66±10	72	48±16	54	44

Non-invasive echocardiographic measures show a decrease in the tricuspid annular plane systolic excursion, a measurement of the RV's longitudinal systolic shortening and a surrogate for contractile function, in rats treated with 4 weeks of SuHx compared to control rats.

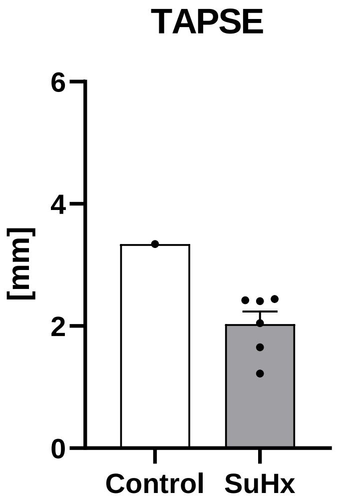

Figure 2.8. The average tricuspid annular plane systolic excursion (TAPSE) was measured from echocardiography in a small subset of animals. These measures show an overall reduction in the RV longitudinal shortening in rats treated with 4 weeks of SuHx.

Collagen to myocyte histological-area ratios remained unchanged in SuHx RV samples, except for a transient increase at week 6 (*p* = 0.04, Fig. 2.9A, D-I). Hydroxyproline assays showed no significant changes in RV free wall collagen content (*p* = 0.16, Fig. 2.9B) when compared with the control group at all timepoints. There were also no significant differences in RV collagen type I to III ratios between SuHx and control rats at any timepoint studied (Fig. 2.9C).

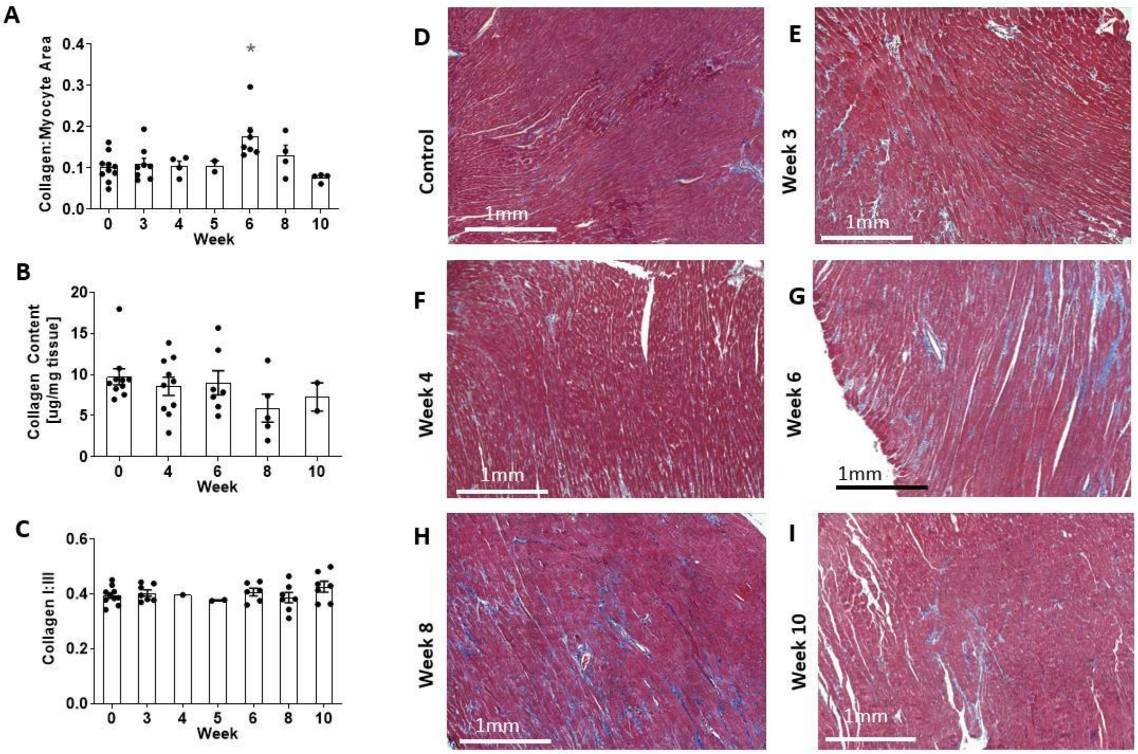

Figure 2.9. Histologic collagen to myocyte area fraction (**A**) from Masson's trichrome-stained RV sections in control (**D**) rats and SuHx rats at weeks 3 (**E**), 4 (**F**), 6 (**G**), 8 (**H**), and 10 (**I**) was only significantly different from control at week 6 ($p<0.05$). RV myocardial total collagen content (**B**) and collagen type I to III ratio (**C**) showed no significant changes throughout the study ($p>0.05$). Data shown as mean ± standard error. Figure 2.9 is a reproduction in part of data published in the American Journal of Physiology. doi: 10.1152/ajpheart.00046.2021. Epub 2021 Aug 27. PMID: 34448637; PMCID: PMC8794227.

Collagen crosslinking was investigated as a contributor to diastolic stiffening. Immunosorbent assay measurements of advanced glycation end-products, a measure of non-enzymatic collagen crosslinking revealed only a significant increase at 4 weeks of SuHx ($p < 0.05$, Fig. 2.10), a difference which was not maintained afterwards.

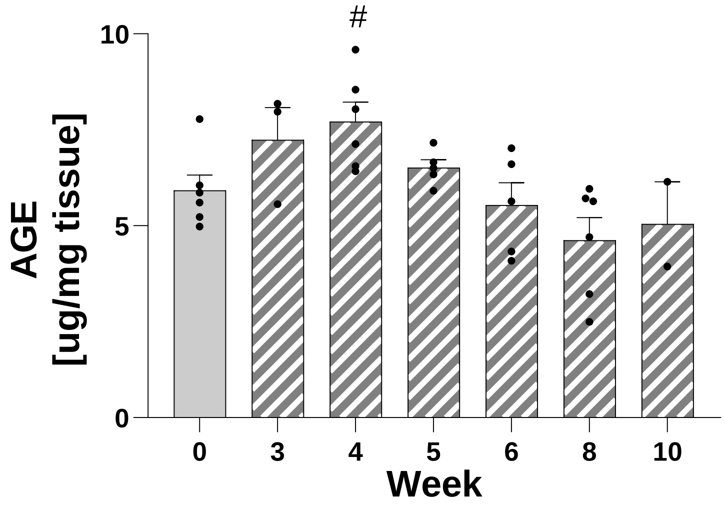

Figure 2.10. Immunosorbent assays were used to measure the concentration of advance glycation end products, a measure of non-enzymatic collagen crosslinking. AGE concentration only showed a significant change at 4 weeks of SuHx treatment and returned to control levels through ten weeks. Data shown as mean ± standard error.

2.3.2 Insights from extending SuHx treatment up to 26 weeks

Pyridinoline cross-linking was measured using immunosorbent assays as a measurement of both enzyme-linked collagen cross-linking and total collagen degradation. These results revealed no significant changes ($p > 0.05$) through 18 weeks of SuHx in male rats (Fig. 2.11).

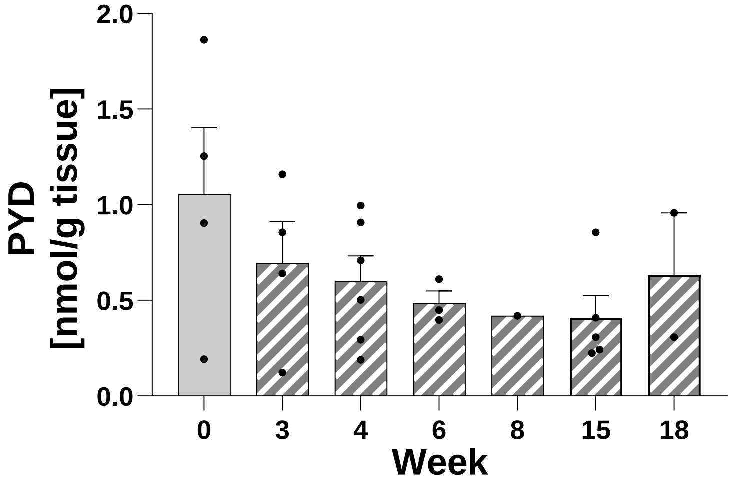

Figure 2.11. Immunosorbent assays were used to measure the concentration of pyridinoline cross-linked collagen peptides. No accumulation of PYD was observed and PYD was not significantly changed through 18 weeks of SuHx. Data shown as mean ± standard error.

Longitudinal hemodynamic and morphological data collected from the SuHx rat model with the treatment duration extended to time points up to 26 weeks is presented in Fig. 2.12. These data revealed that the longitudinal progression of RV hemodynamics and morphologic measurements showed monotonic changes through the first ten weeks in PVR, RV mass, and Fulton Index; through the first twelve weeks in ES pressure, ES volume, stroke volume and ejection fraction; and through the first fifteen weeks in ED pressure. After these periods of steady increases some measurements stabilized, including ES volume, RV mass, and Fulton Index. Other metrics began to reverse, including ES pressure, ED pressure, PVR, stroke volume, and ejection fraction. While the ED volume was maintained at control levels during week 6-10, periods of severe diastolic stiffening, ED volume in the later weeks increased, corresponding to animals with relatively lower diastolic pressure and diastolic chamber elastances. ES, ED, arterial elastance, and vascular-ventricular coupling all showed monotonic increases through our ten week study. When we extended the treatment duration through 26 weeks, however, these trends reversed (Fig 2.13).

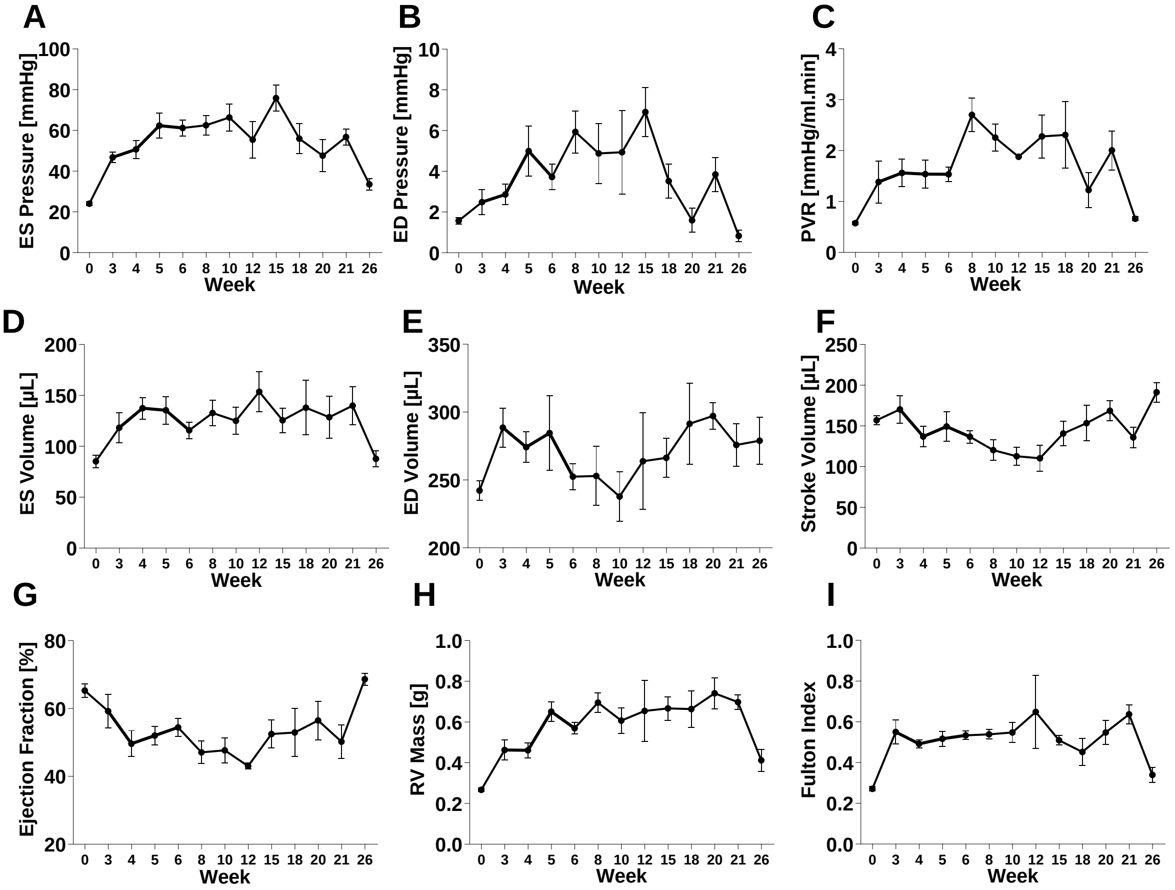

Figure 2.12. Longitudinal hemodynamic and morphologic measurements at timepoints extending to 26 weeks of SuHx treatment were acquired in male rats. Shown are ES pressure (**A**), ED pressure (**B**), PVR (**C**), ES volume (**D**), ED volume (**E**), stroke volume (**F**), ejection fraction (**G**), RV mass (**H**), and the Fulton Index (**I**). While the changes due to SuHx were largely monotonic through 10-12 weeks, the changes began to plateau or reverse beginning around week 12-15. Measurements in individual weeks were not paired. Data shown as mean ± standard error.

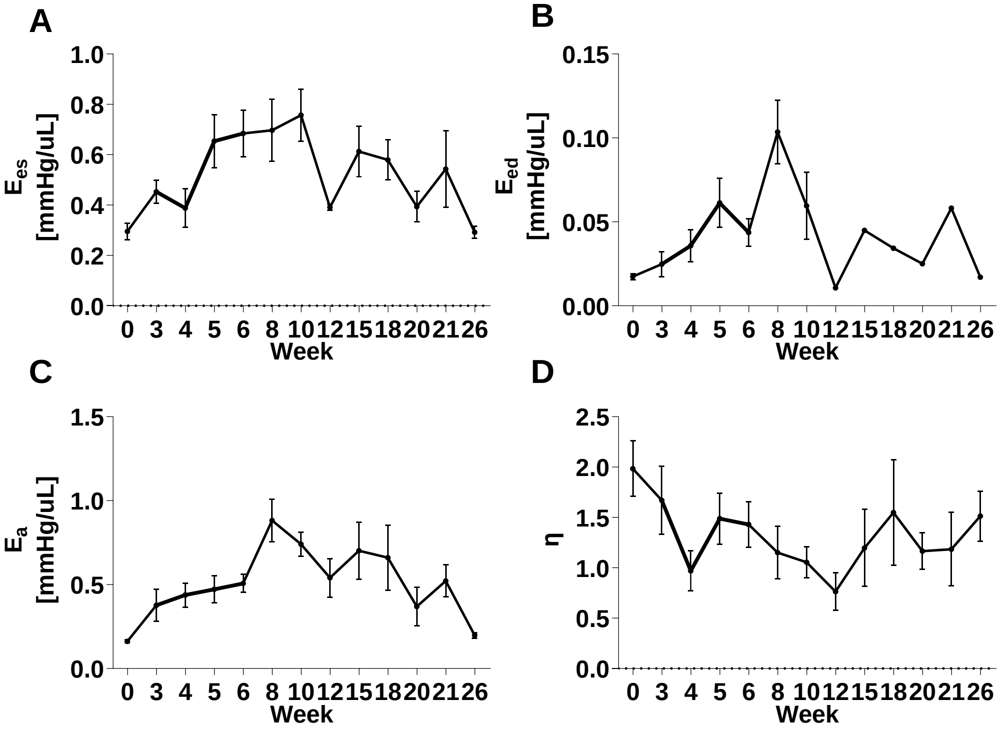

Figure 2.13. Longitudinal measurements of RV ES elastance (**A**), ED elastance (**B**), arterial elastance (**C**), and ventricular-vascular coupling (**D**). ES, ES, and arterial elastance gradually increased, peaking at W8-10, before reversing in the later weeks. Ventricular-vascular coupling decreased to a minimum at W12 before reversing and stabilizing in the later weeks. Data shown as mean ± standard error.

Right-heart failure leading to hepatic congestion and resulting in liver cirrhosis, fibrosis, and mass increases have been reported as potential biomarkers of congestive right heart failure[14], so the liver was excised, generally examined, and massed. However, no differences in the mass of the liver were observed in male SuHx rats over 26 weeks. The largest liver mass was observed after 18 and 26 weeks of SuHx treatment, while the smallest liver masses were observed after 3-4 weeks of SuHx. Fig 2.14. shows a gradual increase over the duration of treatment, but there were no significant increases compared to baseline, and these increases were small when normalized by bodyweight.

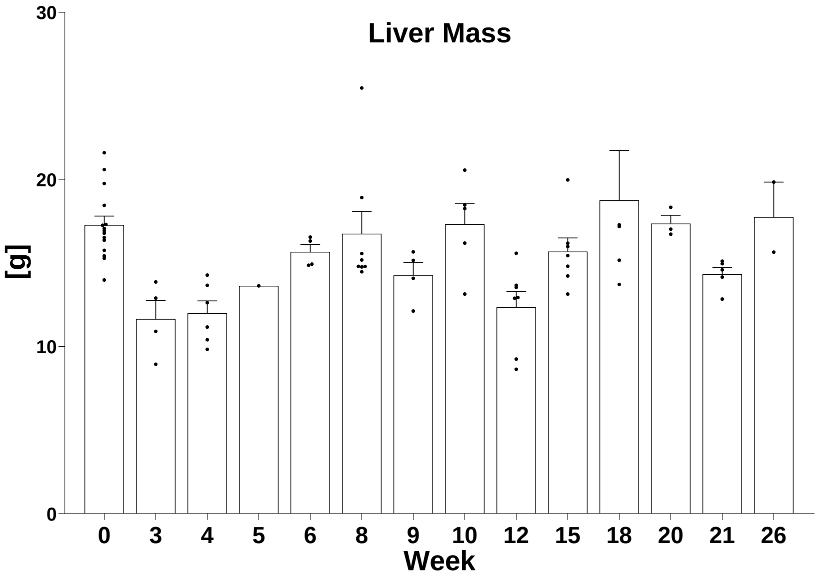

Figure 2.14. Longitudinal measurements of the liver mass show no progressive increases in liver mass in male rats treated with SuHx for up to 26 weeks.

2.4 Discussion: Time Course of Hypertrophy and Diastolic Stiffening

In this chapter, we analyzed RV hemodynamic and morphological ventricular remodeling in the male SuHx rat model of PAH up to 10-wk post disease induction. Initially, RV ejection fraction decreased in response to increased pulmonary arterial pressure but then stabilized after week 4. In contrast RV end-diastolic pressure increased after week 4 with no change in RV end-diastolic volume. Our analysis therefore identified distinct phases of RV remodeling by which systolic function was initially stabilized in conjunction with rapid RV hypertrophy, followed by subsequent remodeling where end-diastolic pressures and chamber elastance rose. We followed up this analysis using computational models of RV biomechanics fitted to measured pressure-volume relations to discriminate the contributions of changes in measured RV geometry from those due to changes in resting and active RV myocardial material properties to altered systolic and diastolic RV chamber function (discussed in Chapter 4). We also observed that longitudinal time course of RV adaptation differed across male and female animals. This finding motivated a more thorough comparative study of RV mechanics based on sex- and ovarian hormone presence (discussed in Chapter 3).

2.4.1 Systolic Function

In the SuHx-treated rats, total pulmonary vascular resistance and right ventricular end-systolic pressures were significantly larger than in control rats. At week 4, there was an initial decrease in ejection fraction with no significant changes in the ES P-V relation. Pressure-volume analysis explained this decrease by the increased end-systolic volume due to the observed increase in RV end-systolic pressure. Ejection fraction and end-systolic volumes stabilized after week 4 despite further substantial increases in RV ES pressures (from 48 ± 5 mmHg at week 4 to 74 ± 8 mmHg at week 10). Our results suggest that this preservation of systolic function was associated with increasing Ees and Rv hypertrophy. This effect was due to the increase in RV wall thickness to radius ratio, corresponding to the experimentally observed increase in RV mass to volume ratio from 3.4 mg/μL at week 4 to 4.3 mg/μL by week 10, and corroborated by our model analysis (Chapter 3).

Compensatory RV hypertrophy or increased contractility in response to increased afterload has been described in patients[15–17] and animal models[18,19]. Over the time course in this model, essentially all the RV hypertrophy was explained by RV wall thickening. We saw the same pattern in the monocrotaline-treated rat model, which displayed comparable increases in wall thickness and mass after 4 wk as seen over the same time course in this study[20]. Jayasekera et al. observed RV dilatation in SuHx rats at 8 wk and also observed no significant decreases in ejection fraction (from 68 ± 5% to 62 ± 6%) and concluded that RV systolic function remained compensated[21]. SuHx rats in the present study did exhibit a significant reduction in mean EF, but this stabilized by week 4 and never fell below the threshold of 35% that has been reported to correlate with significantly reduced survival in patients with PAH[22,23].

2.4.2 Diastolic Function

Right ventricular end-diastolic pressures also rose and were significantly higher than control by week 5. However, this increase was not accompanied by any increase in end-diastolic volume due to corresponding increases in RV end-diastolic chamber stiffness. Some researchers have reported RV chamber dilation in eight-week SuHx rats[21] and increased RV inner diameter in SuHx mice after three weeks[24]. In contrast, other groups using SuHx rats have reported no changes to RV end-diastolic volume in SuHx rats at eight weeks[25] or in SuHx mice at four weeks[26]. Thus, there is no consistent evidence that RV dilation in the first ten weeks is a phenotype of the male rodent sugen-hypoxia model of PAH. While ED stiffening was sufficient to prevent RV dilation in this study, it may subsequently reverse, become maladaptive, and contribute to diastolic dysfunction or become insufficient permitting subsequent RV enlargement and decompensation. Diastolic RV chamber stiffening has been observed in patients[27–29] and animal models[25,30–32] of PAH and has been shown to be a prognostic indicator of diastolic dysfunction and PAH disease severity.[27,28] In skinned RV myocytes isolated from PAH patients who had significantly increased RV diastolic stiffness with significant fibrosis and titin dephosphorylation but no changes in titin isoform composition, Rain *et al.*[27] reported increased passive sarcomere stiffness. The same group[32] measured increased passive trabecular stiffness in pulmonary artery banded rats that was reversed by incubating tissues in protein kinase A. Interestingly, they also found changes in collagen type I:III ratio, but only in rats with severe RV systolic dysfunction. In another study in pulmonary artery banded rats, Baicu *et al.*[31] reported increased myocardial insoluble collagen, indicative of increased cross-linking. Extracellular matrix (ECM) remodeling in response to right[26,33] and left[34] ventricular pressure overload, and myocardial stiffness is modulated by many properties of the collagen matrix including fiber diameter[35], tortuosity[36,37] and cross-linking[34,38,39]. While our findings are consistent with previous human and animal studies showing highly significant diastolic chamber and myocardial stiffening before the onset of severe systolic dysfunction in PAH, the extent to which stiffness is due to collagen matrix structural remodeling, titin isoform switching or phosphorylation or all three remains unclear.

2.4.3. Longitudinal Progression

Data from the ten-week study revealed largely monotonic changes in RV mechanics, hemodynamics, and morphology. Analysis of these patterns revealed distinct patterns of remodeling. Initially, RV ejection fraction decreased in response to increased pulmonary arterial pressure but then stabilized after week 4. In contrast RV end-diastolic pressure increased after week 4 with no change in RV end-diastolic volume. The ED volume was maintained at control volumes between week 6-10, corresponding with periods of severe diastolic stiffening. Our analysis therefore identified distinct phases of RV remodeling by which systolic function was initially stabilized in conjunction with rapid RV hypertrophy, followed by subsequent remodeling where end-diastolic pressures and chamber elastance rose.

However, when the duration of SuHx was extended to timepoints between W12 and W26, the group mean behavior either plateaued or reversed. After the periods of steady increases some measurements stabilized, including ES volume, RV mass, and Fulton Index. Other metrics began to reverse, including ES pressure, ED pressure, PVR, stroke volume, and ejection fraction. ED volume in the later weeks increased, corresponding to group average diastolic pressure and diastolic chamber elastance that were reduced compared to the elevated levels seen in weeks 6-10 that peaked after 8 weeks of SuHx. The extent to which this behavior represents a pathophysiological reversal of RV remodeling in the extended weeks or a limitation of the animal model in recapitulating progressive RV dysfunction remains unclear. Hemodynamic measurements were not paired between animals and weeks, therefore extrapolating on changes between the early and late weeks may be inappropriate. In a small number of animals, sudden death occurred in normoxia, which may have resulted in a sampling bias, whereby animals that tended to develop less severe PAH survived to later weeks while animals with more severe PAH died prior to measurements. Future work aimed at characterizing intermediate stages between adaptive RV function (captured in this study), and stages of RV failure would benefit the identification of the transition from adaptation to maladaptation.

2.5 Conclusion

In this chapter, we designed an experimental study to compare the longitudinal progression of right ventricular remodeling in response to pulmonary arterial hypertension. We utilized a combination of structural and hemodynamic measurements to characterize the progression of systolic and diastolic RV chamber function. In a study of PAH-induced male Sprague-Dawley rats treated with up to ten weeks of sugen-hypoxia, we identified a novel sequence of rapid hypertrophic wall thickening which stabilized RV function, which was proceeded by a sequence of end-diastolic passive chamber stiffening. This previously unrecognized increase in myocardial stiffness, only after RV hypertrophy stabilized systolic function may transiently compensate RV function, but progressive RV stiffening could be a contributor to long-term RV dysfunction.

2.6 Acknowledgements

Chapter 2, in full, is a reprint of the material as it appears in Distinct Time Courses of Right Ventricular Hypertrophy and Diastolic Stiffening in a Male Rat Model of Pulmonary Arterial

Hypertension. Kwan, Ethan D.; Velez-Rendon, Daniela; Zhang, Xiaoyan; Mu, Hao; Patel, Megh; Pursell, Erica; Stowe, Jennifer; Valdez-Jasso, Daniela. American Journal of Physiology Heart and Circulatory Physiology. 2021. The dissertation author was the primary investigator and author of this paper.

2.7 References

1. Kwan ED, Velez-Rendon D, Zhang X, et al. Distinct time courses and mechanics of right ventricular hypertrophy and diastolic stiffening in a male rat model of pulmonary arterial hypertension. *Am J Physiol - Heart Circ Physiol*. Published online 2021.

2. Abe K, Toba M, Alzoubi A, et al. Formation of plexiform lesions in experimental severe pulmonary arterial hypertension. *Circulation*. 2010;121(25):2747-2754.

3. TARASEVICIENE-STEWART L, KASAHARA Y, ALGER L, et al. Inhibition of the VEGF receptor 2 combined with chronic hypoxia causes cell death-dependent pulmonary endothelial cell proliferation and severe pulmonary hypertension. *FASEB J*. Published online 2001.

4. Kasahara Y, Tuder RM, Taraseviciene-Stewart L, et al. Inhibition of VEGF receptors causes lung cell apoptosis and emphysema. *J Clin Invest*. 2000;106(11):1311-1319.

5. Boucherat O, Agrawal V, Lawrie A, Bonnet S. The Latest in Animal Models of Pulmonary Hypertension and Right Ventricular Failure. *Circ Res*. 2022;130(9):1466-1486.

6. Chemla D, Hervé P. Estimation of Mean Pulmonary Artery Pressure: Simpler Than Expected. *CHEST*. 2008;133(3):592-593.

7. BAAN J, JONG TTA, KERKHOF PLM, et al. Continuous stroke volume and cardiac output from intra-ventricular dimensions obtained with impedance catheter. *Cardiovasc Res*. 1981;15(6):328-334.

8. Porterfield JE, Kottam ATG, Raghavan K, et al. Dynamic correction for parallel conductance, GP, and gain factor, α, in invasive murine left ventricular volume measurements. *J Appl Physiol*. 2009;107(6):1693-1703.

9. Wei CL, Valvano JW, Feldman MD, Pearce JA. Nonlinear conductance-volume relationship for murine conductance catheter measurement system. *IEEE Trans Biomed Eng*. 2005;52(10):1654-1661.

10. Hansmann G, Rich S, Maron BA. Cardiac catheterization in pulmonary hypertension: doing it right, with a catheter on the left. *Cardiovasc Diagn Ther*. 2020;10(5):1718-1724.

11. Tabima DM, Hacker TA, Chesler NC. Measuring right ventricular function in the normal and hypertensive mouse hearts using admittance-derived pressure-volume loops. *Am J Physiol - Heart Circ Physiol*. 2010;299(6):H2069-H2075.

12. Clark JE, Kottam A, Motterlini R, Marber MS. Measuring left ventricular function in the normal, infarcted and CORM-3-preconditioned mouse heart using complex admittance-derived pressure volume loops. *J Pharmacol Toxicol Methods*. 2009;59(2):94-99.

13. Middleton R, Fournier M, Xu X, Marbán E, Lewis M. Therapeutic benefits of intravenous cardiosphere-derived cell therapy in rats with pulmonary hypertension. *PLOS ONE*. 2017;12:e0183557.

14. Aspromonte N, Fumarulo I, Petrucci L, et al. The Liver in Heart Failure: From Biomarkers to Clinical Risk. *Int J Mol Sci*. 2023;24(21):15665.

15. Naeije R, Manes A. The right ventricle in pulmonary arterial hypertension. *Eur Respir Rev*. 2014;23(145):476-487.

16. Vonk Noordegraaf A, Chin KM, Haddad F, et al. Pathophysiology of the right ventricle and of the pulmonary circulation in pulmonary hypertension: an update. *Eur Respir J*. 2019;53(1):1801900.

17. Van De Veerdonk MC, Bogaard HJ, Voelkel NF. The right ventricle and pulmonary hypertension. *Heart Fail Rev*. 2016;21(3):259-271.

18. Karunanithi MK, Michniewicz J, Copeland SE, Feneley MP. Right ventricular preload recruitable stroke work, end-systolic pressure- volume, and dP/dt(max)-end-diastolic volume relations compared as indexes of right ventricular contractile performance in conscious dogs. *Circ Res*. 1992;70(6):1169-1179.

19. De Man FS, Handoko ML, Van Ballegoij JJM, et al. Bisoprolol delays progression towards right heart failure in experimental pulmonary hypertension. *Circ Heart Fail*. 2012;5(1):97-105.

20. Vélez-Rendón D, Zhang X, Gerringer J, Valdez-Jasso D. Compensated right ventricular function of the onset of pulmonary hypertension in a rat model depends on chamber remodeling and contractile augmentation. *Pulm Circ*. 2018;8(4):1-13.

21. Jayasekera G, Wilson KS, Buist H, et al. Understanding longitudinal biventricular structural and functional changes in a pulmonary hypertension Sugen–hypoxia rat model by cardiac magnetic resonance imaging. *Pulm Circ*. 2020;10(1):1-11.

22. Van De Veerdonk MC, Kind T, Marcus JT, et al. Progressive right ventricular dysfunction in patients with pulmonary arterial hypertension responding to therapy. *J Am Coll Cardiol*. 2011;58(24):2511-2519.

23. Brewis MJ, Bellofiore A, Vanderpool RR, et al. Imaging right ventricular function to predict outcome in pulmonary arterial hypertension. *Int J Cardiol*. 2016;218:206-211.

24. Vitali SH, Hansmann G, Rose C, et al. The Sugen 5416/hypoxia mouse model of pulmonary hypertension revisited: Long-term follow-up. *Pulm Circ*. 2014;4(4):619-629.

25. da Silva Gonçalves Bos D, Happé C, Schalij I, et al. Renal Denervation Reduces Pulmonary Vascular Remodeling and Right Ventricular Diastolic Stiffness in Experimental Pulmonary Hypertension. *JACC Basic Transl Sci*. 2017;2(1):22-35.

26. Wang Z, Schreier DA, Hacker TA, Chesler NC. Progressive right ventricular functional and structural changes in a mouse model of pulmonary arterial hypertension. *Physiol Rep*. 2013;1(7):e00184.

27. Rain S, Handoko ML, Trip P, et al. Right ventricular diastolic impairment in patients with pulmonary arterial hypertension. *Circulation*. 2013;128(18):2016-2025.

28. Vanderpool RR, Pinsky MR, Naeije R, et al. RV-pulmonary arterial coupling predicts outcome in patients referred for pulmonary hypertension. *Heart*. 2015;101(1):37-43.

29. Gan CTJ, Holverda S, Marcus JT, et al. Right ventricular diastolic dysfunction and the acute effects of sildenafil in pulmonary hypertension patients. *Chest*. 2007;132(1):11-17.

30. Andersen S, Schultz JG, Andersen A, et al. Effects of bisoprolol and losartan treatment in the hypertrophic and failing right heart. *J Card Fail*. 2014;20(11):864-873.

31. Baicu CF, Li J, Zhang Y, et al. Time course of right ventricular pressure-overload induced myocardial fibrosis: Relationship to changes in fibroblast postsynthetic procollagen processing. *Am J Physiol - Heart Circ Physiol*. 2012;303(9):H1128-34.

32. Rain S, Andersen S, Najafi A, et al. Right Ventricular Myocardial Stiffness in Experimental Pulmonary Arterial Hypertension. *Circ Heart Fail*. 2016;9(7):e002636.

33. Dias-Neto M, Luísa-Neves A, Pinho S, et al. Pathophysiology of Infantile Pulmonary Arterial Hypertension Induced by Monocrotaline. *Pediatr Cardiol*. 2015;36(5):1000-1013.

34. Norton GR, Tsotetsi J, Trifunovic B, Hartford C, Candy GP, Woodiwiss AJ. Myocardial stiffness is attributed to alterations in cross-linked collagen rather than total collagen or phenotypes in spontaneously hypertensive rats. *Circulation*. 1997;96(6):1991-1998.

35. MacKenna DA, Vaplon SM, McCulloch AD. Microstructural model of perimysial collagen fibers for resting myocardial mechanics during ventricular filling. *Am J Physiol - Heart Circ Physiol*. 1997;273(3 pt 2):H1576-86.

36. MacKenna DA, Omens JH, Covell JW. Left ventricular perimysial collagen fibers uncoil rather than stretch during diastolic filling. *Basic Res Cardiol*. 1996;91(2):111-122.

37. Robinson TF, Geraci MA, Sonnenblick EH, Factor SM. Coiled perimysial fibers of papillary muscle in rat heart: Morphology, distribution, and changes in configuration. *Circ Res*. 1988;63(3):577-592.

38. Herrmann KL, McCulloch AD, Omens JH. Glycated collagen cross-linking alters cardiac mechanics in volume-overload hypertrophy. *Am J Physiol-Heart Circ Physiol*. 2003;284(4):H1277-H1284.

39. Herum KM, Lunde IG, Skrbic B, et al. Syndecan-4 is a key determinant of collagen cross-linking and passive myocardial stiffness in the pressure-overloaded heart. *Cardiovasc Res*. 2015;106(2):217-226.

Chapter 3 SEX-DEPENDENT RIGHT VENTRICULAR HEMODYNAMIC AND MORPHOLOGIC CHANGES IN PULMONARY ARTERIAL HYPERTENSION

3.1 Introduction

PAH disproportionally affects women, with pre-menopausal women exhibiting less severe RV remodeling and better cardiac outcomes than post-menopausal women or men.[1,2] Clinical[3–5] and preclinical studies[6] have highlighted the association between sex and RV hemodynamic function, with correlations found between improved RV function and endogenous or exogenous estrogens.[7,8] However, most animal studies have focused on male subjects, limiting sex-specific data on RV remodeling. As a result, the role of sex in PAH remains unclear. Estrogen may influence RV myocardial remodeling, explaining the sex-specific differences in disease progression.[6,7] Therefore, there is a critical need to understand the influence of sex on the pathological remodeling of the RV that occurs in PAH. Clinically, changes in RV diastolic stiffness and contractility have been closely associated with disease severity in patients with PAH.[9,10] As discussed in Chapter 2, a 10-week study on the progression of PAH in male sugen-hypoxia (SuHx) rats showed significant increases in RV end-diastolic pressures and chamber stiffness, peaking at 8 weeks following disease induction. These changes were primarily attributed to increased passive myocardial stiffness, rather than alterations in RV geometry.[11] Hypertrophy and wall thickening appeared to stabilize systolic function in the early stages of the disease, despite subsequent mechanical changes.[11,12] However, it remains unclear whether these findings in male animals would be affected by sex- and by ovarian-hormones, as believed clinically.

To address the knowledge gap in sex-specific RV remodeling, we conducted a study using hemodynamic and morphologic measurements, and a biomechanics model of the RV. We aimed to determine the effects of chamber geometry and myocardial material properties on end-systolic and end-diastolic pressure-volume (P-V) relations. Our study used the sugen-hypoxia (SuHx) model of PAH male, ovary-intact female, and ovariectomized (OVX) female rats. We hypothesized that sex differences in RV organ-level performance would correspond with differences in myocardial material remodeling. Specifically, female SuHx-treated rats would show increased contractility with mild diastolic stiffening, contrasting with severe chamber stiffening in male SuHx-treated rats. Ovariectomized SuHx rats, lacking ovarian hormones, would display a more severe RV remodeling phenotype compared to ovary-intact females but less severe than males. Using RV P-V measurements, we predicted myocardial mechanics and validated these predictions with myocyte mechanics data.

3.2 Approach

3.2.1 Experimental Design

To investigate the effects of sex- and ovarian hormones on remodeling of RV function, we designed a study of the well-established sugen-hypoxia rat model of PAH, as described in Chapter 1. The study comprised 56 male and 86 female Sprague-Dawley rats, with a subset of 38 female rats undergoing ovariectomy procedures performed at 6 weeks of age by an external surgeon at the vendor (OVX, Charles River Laboratories, Hollister, CA, USA). Differences in bodyweight between male and female rats were controlled for by treating animals at approximately 200g, which corresponded to male rats at 7 weeks of age, and female and ovariectomized female rats at 8 weeks of age. These animals, weighing approximately 200 g were randomly assigned to control and SuHx groups. The SuHx groups were administered a vascular endothelial growth factor receptor antagonist sugen (SU5416, S8442 MilliporeSigma, CAS Number 204005-46-9, PubChem Substance ID 24278606 Sigma-Aldrich, MO, USA) at a dose of 20 mg/kg and exposed to chronic hypoxia (10% O_2) for 3 weeks, as described in Chapter 2.2. Following this, the animals were then returned to normoxia for 5 weeks. Age-matched normotensive animals were kept in normoxia throughout the study as control groups.

Following this study (SuHx W8), cohorts of animals were studied in which the duration of normoxia was extended to timepoints up to 23 weeks while the duration of hypoxia was kept at 3 weeks, resulting in totals of up to 26 weeks of SuHx treatment, for comparison with males. The timepoints added were twelve (W12), fifteen (W15), eighteen (W18), twenty (W20), twenty-one (W21), and twenty-six (W26) weeks post injections. In these animals, identical experimental procedures were performed, by which we acquired hemodynamic and morphologic measurements, as well as measurements of tissue collagen content.

3.2.2 Hemodynamic Measures

Right ventricular blood pressure and volume were measured simultaneously during an open-chest procedure, following previously described methods (Chapter 1).[11–13] In this terminal procedure, animals were continuously administered 2.5% isoflurane (MWI Veterinary Supply, USA, cat #502017) mixed with oxygen (100% O_2) *via* a nose cone. Following a tracheotomy, the animals were intubated and ventilated at a respiratory rate of 40-50 breaths per minute with tidal volume ranging from 1.7-4.2 mL, determined by the animal's weight. Body temperature and heart rate were continuously monitored throughout the procedure using a rectal probe (MicroTherma 2, ThermoWorks, UT, USA) and a 4-lead electrocardiogram. The isoflurane concentration was occasionally adjusted up to 1.5% to maintain a heartrate range between 280-360 beats per minute. P-V timeseries were recorded with a 1.9F admittance catheter (Transonic Scisense, Ontario, Canada)[14–17] which was inserted apically into the RV chamber. P-V data obtained during caval occlusion were used to determine end-systolic (ES) and end-diastolic (ED) chamber elastances. Data were collected using LabChart software (version 8 Pro, ADInstruments Inc., Colorado

Springs, CO, USA) and analyzed offline using custom-written MATLAB code (version R2021a, MathWorks, Natick, MA, USA).

A growing body of literature has investigated the differential responses of sex on isoflurane sensitivity under anesthesia[18,19], which is important to consider given the documented effects of isoflurane anesthesia on cardiac function[20]. It is well documented that isoflurane and other volatile inhaled anesthetics cause effects on cardiovascular function, such as altered vascular resistance, sympathetic output, or myocardial contractility[21]. However, in our studies with over 300 rats, the effect of isoflurane has been found to be very small when compared to the effects of sugen-hypoxia[11,12,22], monocrotaline-induced pulmonary hypertension[12,23], and pulmonary arterial banding[24]. Therefore, we conclude that, while isoflurane and other anesthetics can alter cardiovascular function, isoflurane was carefully regulated at 2% (in 100% O2), below reported doses that drastically alter heart rate and hemodynamics[25]. The effects on hemodynamics due to isoflurane were likely small compared with the differences due to the PAH treatment, as seen previously. However careful attention was paid in this study to ensuring the differential effects of isoflurane on sex were minimized, such as by dynamically adjusting isoflurane dose to minimize fluctuations in the heart rate.

The right ventricle and left ventricle are fundamentally coupled: 1) myofibers are shared 2) pulmonary hypertension often occurs secondary to left ventricular failure or leads to left ventricular failure. As such, we measured left ventricular hemodynamics to validate the specificity of SuHx-induced RV pressure overload, assess the impact of SuHx treatment and to validate changes to the RV in the setting of acute RV pressure overload. Following RV and PA measurement, the same 1.9F PV catheter was inserted into the LV chamber and continuous pressure-volume timeseries were recorded during terminal surgeries, as described in Chapter 2.2.

3.2.3 Histological measurements of Right-Ventricular Hypertrophy and Fibrosis

After *in vivo* hemodynamic measurements, the animals were exsanguinated, and the heart flushed with ice-cooled phosphate-buffered saline (pH 7.4) consisting of 0.137 M NaCl, 0.0027 M KCl, 0.01 M Na_2HPO_4, 0.0018 M KH_2HPO_4 and heparin solution (USP 5000 units/mL, MWI Veterinary Supply, USA, cat #054255). The heart was excised, and the RV free wall, left ventricular free wall, and septum were isolated and weighed. The Fulton index (the ratio of RV mass to the sum of LV and septal masses) was calculated, while myocardial volumes were determined by converting excised masses at a density of 1.053 g/mL[26] and used as model inputs.

The excised RV myocardium near the infundibulum (outflow tract) was immediately fixed in 10% formalin (Thermo Fisher Scientific, MA, Cat. No. SF100-4) for 48 hours at room temperature and then stored in 70% ethanol (Decon Laboratories, PA, Cat. No. V1001) at room temperature. The fixed RV samples were paraffin-embedded and sectioned transmurally. Myocyte hypertrophy was quantified using the semi-automated histological analysis Fiji package HeartJ.[27] Analysis was performed on H&E stained images captured at 40x magnification with a resolution of 4.6pixels/µm. Myocytes, nuclei, and capillaries were segmented using the MorphoLibJ Fiji plug-in.[27] Myocyte hypertrophy was characterized with the minimum Feret diameter (the distance between two parallel lines enclosing the myocyte) to account for variations in myofiber alignment. An average of 351±54 cells per animal were measured.

A hydroxyproline assay (QuickZyme Total Collagen Assay, QuickZyme BioSciences, Lei, NL) was used to measure total RV collagen content. Tissue was collected from the entire free wall. In SuHx treated RVs, we noticed pronounced RV free wall thickening localized to the myocardium near the inlet region. We conducted hydroxyproline assays that both included and excluded this thickened inlet region. Free wall tissue samples weighing 5–15 mg were prepared and assayed according to the manufacturer's recommended protocol. Hydroxyproline residues were quantified using a microplate reader (Tecan M200, Tecan LifeSciences, CH). Absorbances were calibrated with a linear collagen standard curve, adjusted for sample dilution and expressed as total collagen content.

Collagen types I and III contents were quantified using enzyme-linked immunosorbent assay kits (Rat Collagen type I ELISA Kit, NBP2-75823, Collagen type III ELISA Kit, NBP2-81205, Novus Biologicals, CO). Tissue samples were isolated in cold 1× PBS at a 1:9 wt/vol ratio and diluted 1:100. Collagen I and III concentrations were measured at 450-nm wavelength (Tecan F200 Microplate Reader, Tecan LifeSciences, CH). Absorbances were calibrated with collagen I and collagen III standard curves ranging from 0 to 100 ng/mL and expressed as the ratio of collagen I to collagen III.

3.2.4 Cardiac Magnetic Resonance Imaging

RV chamber morphology was measured *via* cardiac magnetic resonance imaging (cMRI) in a 11.7T pre-clinical scanner (Bruker Biospec, Billerica, MA, USA) both prior to administering SuHx treatment and after 8 weeks of SuHx (n = 2 animals per control group, n = 3 males and OVX, and n = 4 females). Rats were anesthetized using 1-2% isoflurane in 100% O_2 while their body temperature was maintained at 37°C using an external warm air flow. Electrocardiogram (ECG) and respiration were continuously monitored throughout the procedure. For each heart, five to eight short-axis images spanning the biventricular length were acquired. Each image consisted of twenty ECG-gated short-axis frames. Endocardial contours were drawn manually on short axis slices using ImageJ (ImageJ version 1.5.3, NIH, Bethesda, MD). Two metrics were calculated and averaged to represent RV shape changes across the biventricular length: (i) the RV-septal mid-wall diameter, which was determined as the in-plane distance between the midpoint of the septum and the midpoint of the RV free-wall, and (ii) the RV cross-sectional area to perimeter ratio. Cardiac MR images were acquired at a slice thickness of 1.50 mm, image resolution of 200x200 microns, imaging matrix of 250x250 pixels, field of view of 50x50 mm, and frame acquisition duration of 312 ms.[11]

3.2.6 Statistical Analysis

Group comparisons of hemodynamics, morphological measurements, myocyte mechanics, and model-derived results were analyzed with descriptive statistics in JMP Pro Statistical software (version 16, SAS Institute Inc., NC, USA). Two-factor ANOVA was used for normally distributed data to evaluate differences due to treatment (control vs. SuHx) and animal group (male, ovary-intact female, and ovariectomized female). Post-hoc comparisons were performed using the Dunnett's test for treatment comparisons and the Tukey test for animal group differences. Following two-factor ANOVA, simple main effects were analyzed with the F-statistic for group and treatment. Interaction effects between group and treatment were reported as ($F_{\text{df-a,df-b}}$ = $F_{\text{interaction}}$, p-value), where df-a and df-b refer to the degrees of freedom of each factor (treatment, group), and $F_{\text{interaction}}$ is the ratio of interaction mean squares to mean squared error. For non-parametric data, the Wilcoxon-Kruskal-Wallis statistic was used, followed by the Dunnett's test for treatment comparisons and the Dunn test for animal group comparisons. Rat-specific sarcomere mechanics predictions were analyzed using a general linear model with mixed factors to compare treatment (inter-group) and sarcomere length (inter-level) effects. For fixed factors, two-factor ANCOVA and analysis of means were applied to assess the means and slopes of sarcomere length for ED-derived data, and fiber stress for ES-derived data. Statistical significance was set at α = 0.05. All figures were generated using Prism software (version 8.4.3, GraphPad, CA, USA).

3.3 Results: Sex-based rat study

3.3.1 Effects due to SuHx

Pulmonary arterial hypertension was successfully induced in 96% of the rats (defined as SuHx-treated rats with mean pulmonary arterial pressures >20 mmHg), regardless of sex. SuHx rats exhibited significantly higher mean pulmonary arterial ($p < 0.001$) and RV end-systolic ($p < 0.001$) and end-diastolic ($p < 0.001$) pressures compared to their control groups (Fig. 3.1A-B). After normalizing the excised RV mass by the sum of LV and septum mass, the Fulton index showed similar increases in all SuHx animals. Specifically, the Fulton index increased from 0.26-0.28 in control groups to 0.53-0.55 in SuHx groups ($p < 0.001$, Fig. 3.1C). RV end-systolic volume (Fig. 3.1D) increased significantly in SuHx rats ($p < 0.001$). End-diastolic volumes (Fig. 3.1E) were largely unchanged by SuHx ($p = 0.068$), however there was a significant interaction between treatment and group effects ($F_{1,2} = 4.75$, $p = 0.012$). Post-hoc analysis revealed a significant increase in ED volume only between the OVX control and SuHx group ($p < 0.001$).

No significant effects of SuHx on stroke volume (Fig. 3.1F) were found ($p = 0.35$). End-systolic elastance (E_{es}) significantly increased in SuHx animals ($p < 0.001$, Fig. 3.1G). For end-diastolic elastance (E_{ed}, Fig. 3.1H), a significant interaction effect was observed between treatment and group ($F_{1,2} = 11.98$, $p < 0.001$) and the main effects analysis showed that ED elastance significantly increased in SuHx animals ($p < 0.001$).

Ejection fraction (Fig. 3.1I) significantly decreased in SuHx rats ($p = 0.0012$), falling from 63.7% to 50.9% in male SuHx, 58.4% to 52.7% in female SuHx, and 60.1% to 51.9% in OVX SuHx groups, with no decline exceeding 12.8% in any group. SuHx treatment resulted in significant increases in mean pulmonary arterial pressure (mPAP, $p < 0.001$, Fig. 3.1J) and arterial elastance (E_a, $p < 0.001$, Fig. 3.1K). However, the E_{es} to E_a ratio (ventricular-vascular coupling,

Fig. 3.1L) did not change due to SuHx ($p = 0.21$), indicating no changes in right-ventricular pulmonary-arterial coupling.

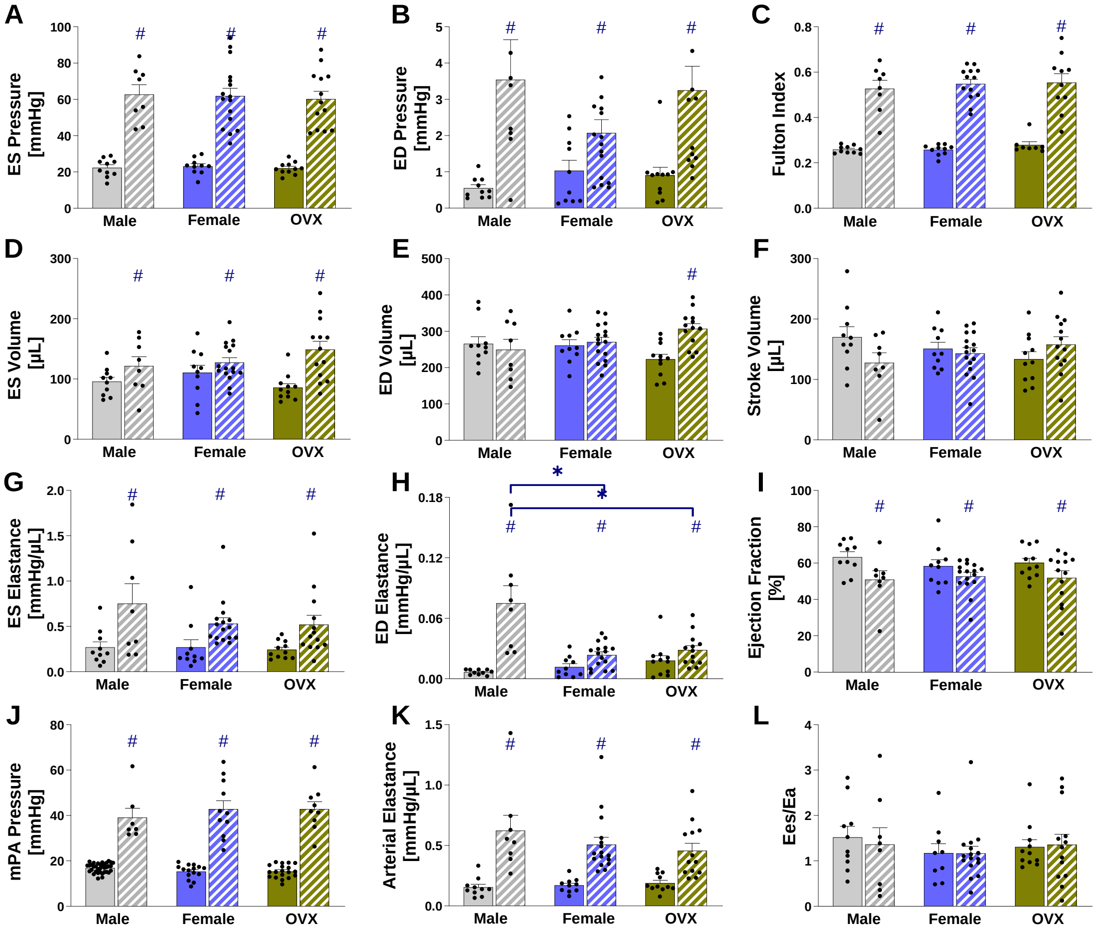

Figure 3.1. Invasive hemodynamic measurements of RV function in normotensive (control, solid) and hypertensive (SuHx, patterned) rats from male (grey), ovary-intact female (female, blue) and ovariectomized female (OVX, green) rats. There are significant increases in right-ventricular end-systolic pressure (**A**), end-diastolic pressure (**B**), and Fulton Index (**C**) across all SuHx-treated groups. End-systolic volume (**D**) notably increased in SuHx rats, while end-diastolic volume (**E**) only increased in the ovariectomized female rats. Stroke volume (**F**) remained comparable among groups. Both end-systolic (**G**) and end-diastolic (**H**) elastance increased with SuHx treatment, with the greatest rise observed in males. RV ejection fraction (**I**) decreased significantly due to SuHx. Mean pulmonary arterial pressure (**J**) and arterial elastance (**K**) also increased with SuHx treatment, irrespective of group. RV end-systolic elastance and arterial elastance remained coupled across all groups (**L**). #$p < 0.05$ effect of SuHx compared with controls, *$p < 0.05$ difference between animal groups. Figure 3.1. is a reproduction in part of data published in the American Journal of Physiology. doi: 10.1152/ajpheart.00098.2024. Epub 2024 Jul 15. PMID: 38847755.

3.3.2 Effects due to sex

There were no significant differences in RV ES pressures ($p = 0.91$, Fig. 3.1A) or Fulton Index ($p = 0.44$, Fig. 3.1C) between the three animal groups. While ED pressures (Fig. 3.1B) increased in all SuHx animals ($p < 0.001$), no significant interactions between group and treatment were found ($F_{1,2} = 1.63$, $p = 0.20$). However, we note male SuHx rats exhibited a six-fold increase, compared to a two-fold increase in female SuHx and a three-fold increase in OVX SuHx rats. Male control rats had mean pulmonary arterial pressures of 16.9±0.4 mmHg, compared to 15.3±0.8 mmHg in the female group and 15.4±0.7 mmHg in the OVX controls. SuHx treatment increased mPAP to 39.1±4.0 mmHg in males, 42.7±3.8 mmHg in females, and 42.8±3.3 mmHg in OVX females. Two-factor ANOVA revealed no significant effects of group ($p = 0.87$) nor significant interactions between group and treatment ($F_{1,2}= 0.76$, $p = 0.47$).

RV ES volume (Fig. 3.1D) increased significantly in all SuHx-treated animals ($p < 0.001$), but no significant group effects on ES volume were found ($p = 0.64$), nor were there significant interactions between group and treatment ($F_{1,2} = 2.57$, $p = 0.084$). It is noteworthy that the mean ES volume was greater in the OVX SuHx group than in the male or female SuHx groups. Two-factor ANOVA revealed significant interactions between treatment and group on ED volume ($F_{1,2} = 4.75$, $p = 0.012$, Fig. 3.1E). Post-hoc analysis showed a significant increase in ED volume in the OVX group (37% increase, $p < 0.001$ compared with OVX controls), but not in the female group (6% increase, $p = 0.85$) or the male group (3% decrease, $p = 0.99$). There were no significant effects of treatment ($p = 0.35$), group ($p = 0.98$), or interactions between treatment and group ($F_{1,2} = 2.86$, $p = 0.0647$) on RV stroke volume (Fig. 3.1F). No significant group effects on ejection fraction were observed ($p = 0.89$, Fig. 3.1I), nor were there significant interaction effects between treatment and group ($F_{1,2}= 0.51$, $p = 0.60$). However, the largest mean decrease in ejection fraction was observed in the male rats (from 63.7% to 50.9%), followed by OVX rats (from 60.1% to 51.9%) and female rats (from 58.4% to 52.7%).

Both ES and ED chamber elastance (Fig. 3.1G-H) significantly increased in SuHx animals, with the largest increases observed in male SuHx. Significant effects due to animal group were found for ED elastance ($p < 0.001$), with significant interaction effects between group and treatment ($F_{1,2} = 11.98$, $p < 0.001$). Post-hoc analysis revealed that ED elastance was higher in male SuHx rats compared to female SuHx ($p = 0.002$) or OVX SuHx rats ($p = 0.0194$).

Remodeling of the P-V relationships varied between SuHx groups (Fig. 3.2). RV ES pressures were elevated to similar levels in all SuHx groups, but RV ES volume increased the most in the OVX group. While increases in end-diastolic pressure were comparable in male and OVX SuHx groups, RV chamber volume was preserved in male SuHx rats. Increases in the ED chamber volume tempered the steepening of the ED P-V relationship in the OVX SuHx group. In ovary-intact female animals, SuHx led to the smallest diastolic pressure-volume changes.

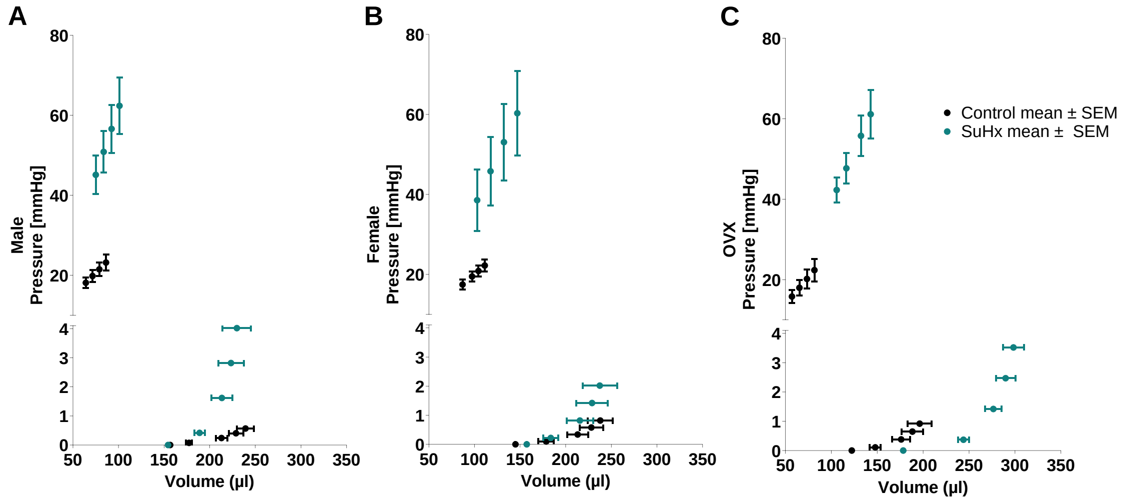

Figure 3.2. Mean end-systolic (top) and end-diastolic (bottom) pressure-volume measurements for control (black) and sugen-hypoxia (SuHx, teal) male (**A**), ovary-intact (**B**), and ovariectomized (OVX) female (**C**) rats during preload variation. Data shown as mean ± standard error of the mean. Figure 3.2. is a reproduction in part of data published in the American Journal of Physiology. doi: 10.1152/ajpheart.00098.2024. Epub 2024 Jul 15. PMID: 38847755.

3.3.3 Histology: RV tissue shows myocyte hypertrophy and fibrosis in all SuHx groups

Myocyte diameter (Fig. 3.5B) increased with SuHx in all groups. A two-factor ANOVA, followed by a main effects analysis showed a significant effect due to treatment ($p < 0.001$) and group ($p = 0.0179$), with significant interactions between treatment and group ($F_{1,2} = 27.73$, $p < 0.001$). Post-hoc analysis revealed a significant difference between the female and OVX groups ($p = 0.0173$).

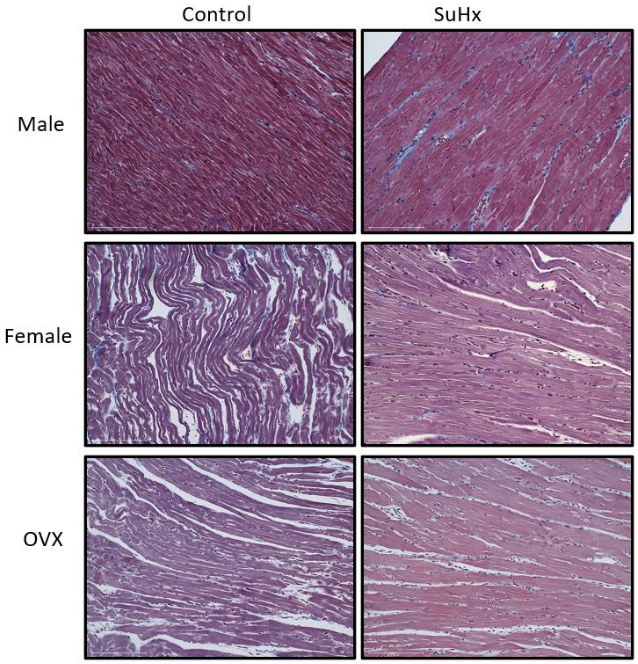

Figure 3.3. Longitudinal cross-sections of the RV myocardium demonstrate thickening of the myofiber in SuHx (right) compared to control (left).

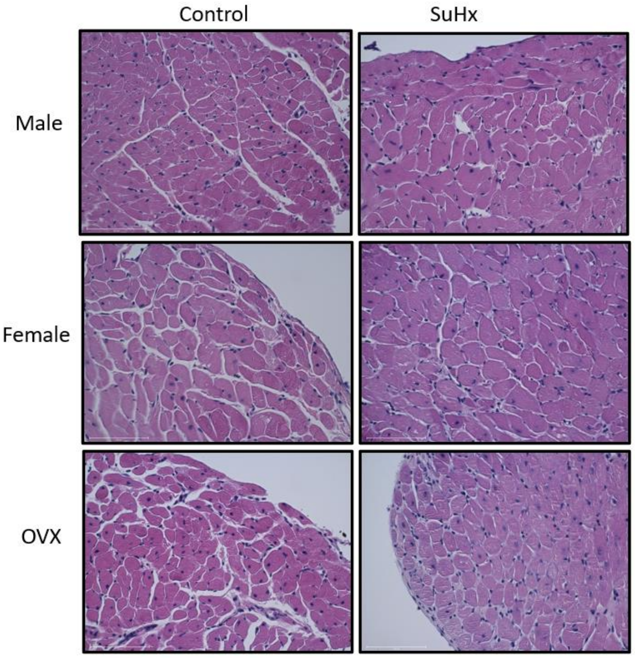

Figure 3.4. Histological cross-sections of RV myocardium excised from male (top), female (middle), and ovariectomized female (bottom) rats treated with SuHx (right) were compared to control (left). In all groups, acute myocyte hypertrophy was observed, characterized by enlargement of myofiber diameter.

Increases to RV myocyte cross-sectional area and diameter (Fig. 3.5) reflect the increases to RV myocardial mass due to PAH treatment and confirm that thickening of the RV myofibers themselves contributed to the significant increases in myocardial mass. We next looked at the collagen content of RV myocardium of these SuHx-treated rats. We observed significant and non-uniform RV free wall thickening in the portion of the RV near the apex and excluded this portion in this hydroxyproline assay (Fig. 3.6). A two-factor ANOVA revealed a significant increase with respect to treatment ($p < 0.001$) but not group ($p = 0.23$) in collagen content in myocardium tissue that excluded the severely thickened RV wall nearest the apex. No significant interaction effects between treatment and group were found ($F_{1,2} = 0.91$, $p = 0.41$).

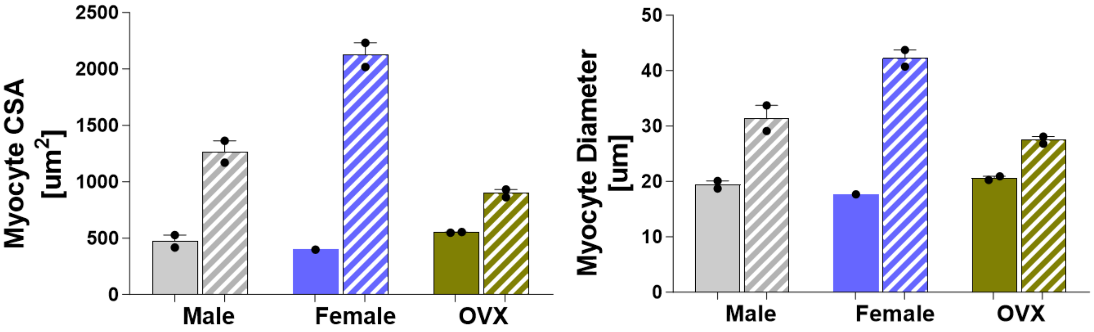

Figure 3.5. Transverse cross-sections of the RV myocardium were automatically segmented and revealed increases in average myocyte cross-sectional area (left) and myocyte diameter (right) due to SuHx treatment. Increases were most pronounced in female SuHx.

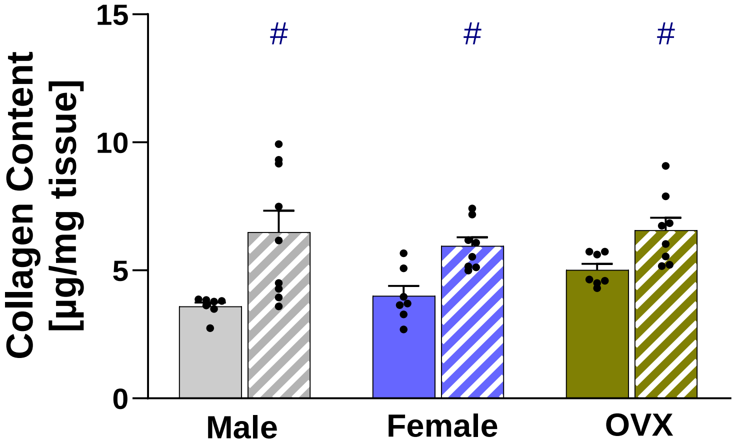

Figure 3.6. Hydroxyproline total collagen assay revealed significant increases in all SuHx-treated groups in the RV myocardium excluding the thickened tissue near the RV inlet. Data shown as means ± standard error of the mean.

We next investigated if dynamic changes to fibrosis corresponding to dynamic hemodynamic remodeling may result in the accumulation of total RV myocardial bulk collagen over time. We tested tissue excised from male, female, and ovariectomized rats treated with varying durations of SuHx up to 21 weeks in males, 18 weeks in females, and 12 weeks in ovariectomized females. For these assays, RV myocardium near the infundibulum was tested. No significant accumulation of collagen was found in any groups at week 8, the timepoint at which hemodynamic and morphologic measurements were compared for this study. While the mean normalized density for some individual weeks increased up to 46% in male SuHx (at Week 21) and 84% in female SuHx (at week 15), two-factor ANOVA revealed no significant changes dues to treatment. These results are shown across multiple timepoints in Fig. 3.7.

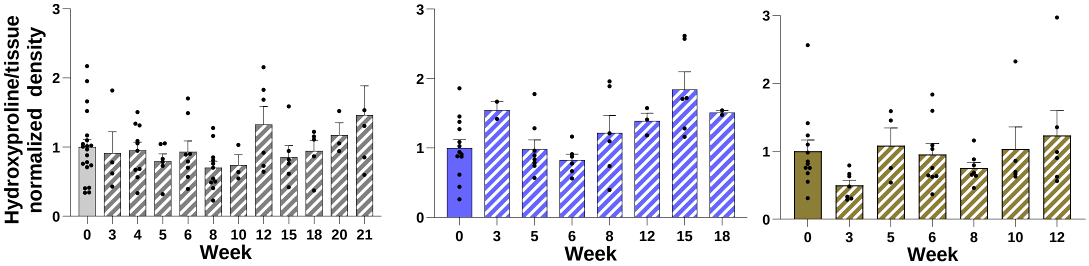

Figure 3.7. Hydroxyproline assays show total collagen content in RV myocardium samples from male (top), female (middle), and OVX (bottom) female rats across multiple weeks of SuHx. No significant or progressive accumulation of collagen was found in any groups at week 8 , the timepoint at which hemodynamic and morphologic measurements were compared. Female SuHx showed a slight trend towards gradual increases, peaking at 15 weeks of SuHx treatment.

We then combined the results of these collagen assays across all weeks to visualize the changes due to SuHx in each of the sex groups. We observed no significant increases to hydroxyproline total collagen content in any of the three groups (Fig. 3.6), although the group with the largest mean difference was the female SuHx group (21% increase, $p = 0.26$).

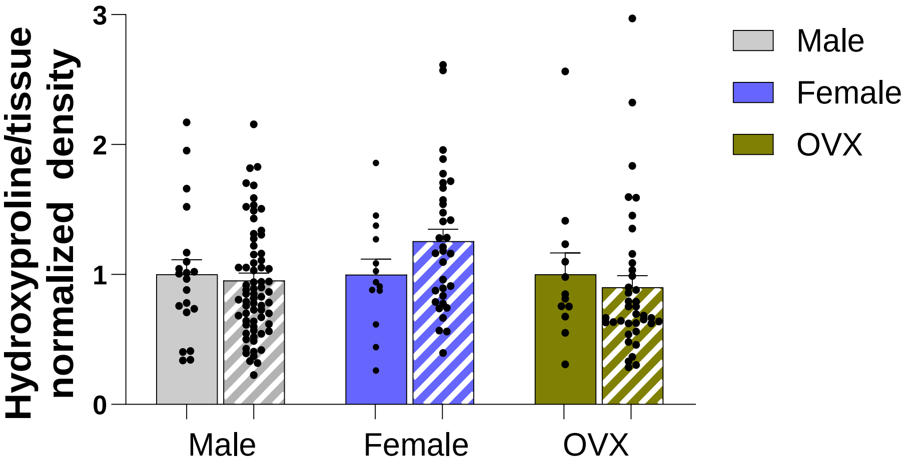

Figure 3.8. SuHx treatment resulted in no significant changes in the hydroxyproline/tissue density in the RV myocardium from the infundibulum, when all weeks of data were combined. Data shown as mean ± standard error.

3.3.4 Female RVs become rounder due to SuHx

The remodeling of the RV chamber geometry induced by SuHx treatment exhibited sex-specific characteristics, with intact female and OVX SuHx rats showing a rounding of the RV chamber that was not observed in male SuHx rats (Fig. 3.9). The cross-sectional area to perimeter ratio increased in both male and female SuHx animals, but the increases were more pronounced in females (Fig. 3.9B). Additionally, RV mid-wall to septal mid-wall diameter (two-factor ANOVA, *p*=0.013) increased due to SuHx in female rats, while no significant changes were observed in male rats (Fig. 3.12A). Furthermore, a higher RV short-to-long diameter ratio was observed in cardiac MR images of female SuHx rats, but not in male SuHx rats (Fig. 3.12B). These morphological changes align with the observed increases in end-diastolic volume in female SuHx rats that were not present in male SuHx rats (Fig. 3.1E).

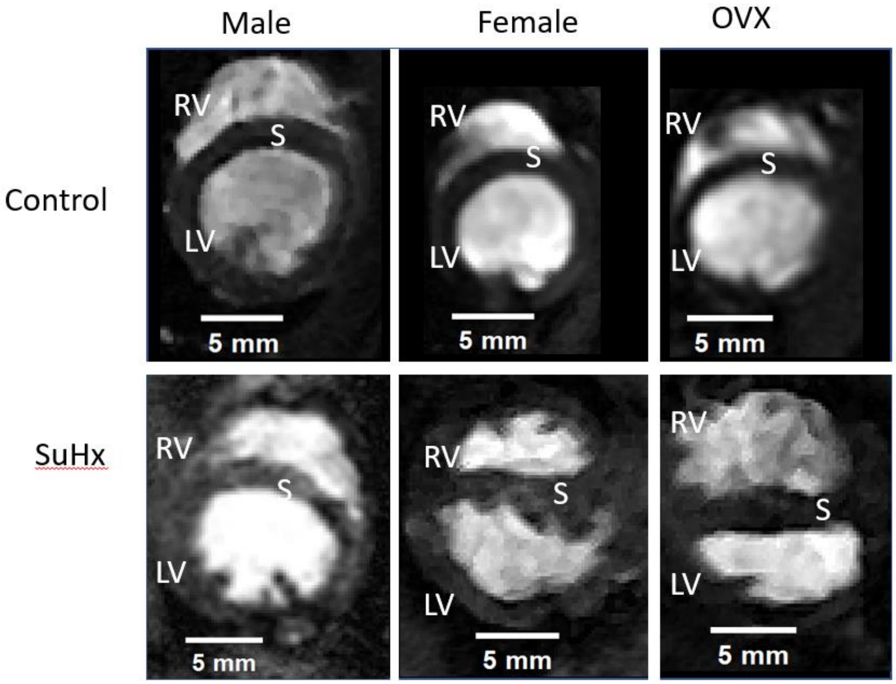

Figure 3.9. Cardiac MRI in control (top) and SuHx-treated (bottom) hearts of male (left), female (middle), and ovariectomized female (right) rats. CMR images reveal a more pronounced rounding of the RV chamber geometry after 8 weeks of SuHx in female and OVX than in male rats. Images were acquired for control (2 male, 2 female, 2 OVX) and SuHx (3 male, 4 female, 3 OVX) rats.

Paired CMR images for 4 male and 4 female rats are shown in Fig 3.10 and 3.11. These images were selected from the mid-section of the short-axis scans that spanned the biventricular apex-to-outflow tract dimension (approximately slice 4-5 out of 8). These scans reveal that RV shape was more frequently maintained in male SuHx than in female SuHx, which showed more changes to the RV chamber, RV wall and septum wall geometry.

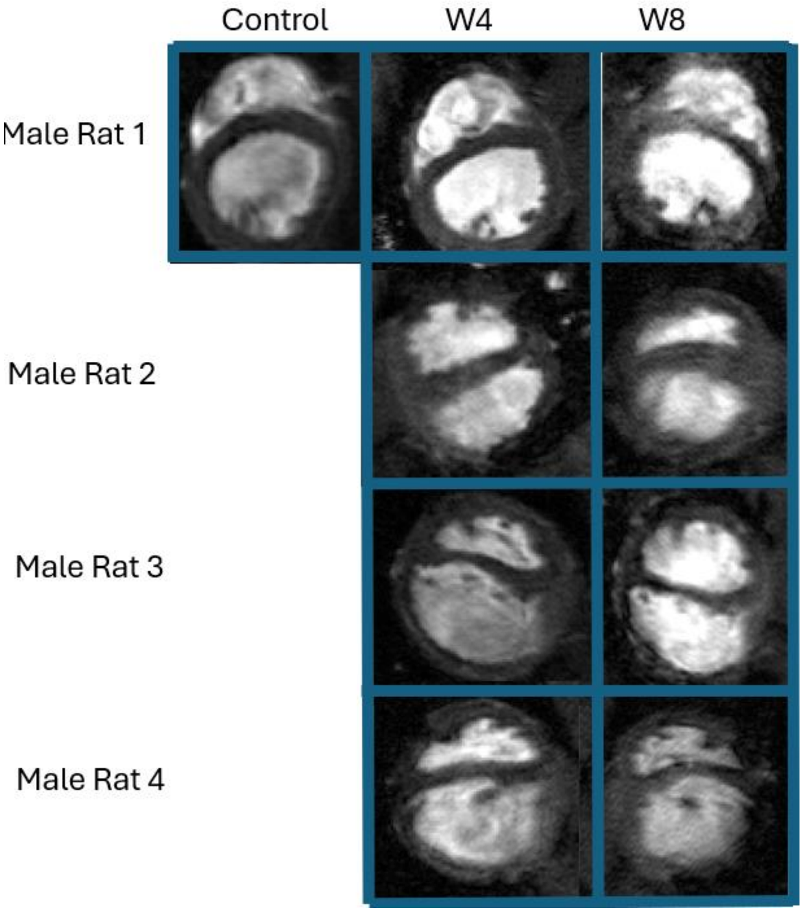

Figure 3.10. CMR images of male rats treated with SuHx, paired between three time points for Male rat 1 (top), and paired between two time points for male rats 2-4. The crescent RV shape was largely maintained in male rats seen clearly in rats 1, 2, and 4.

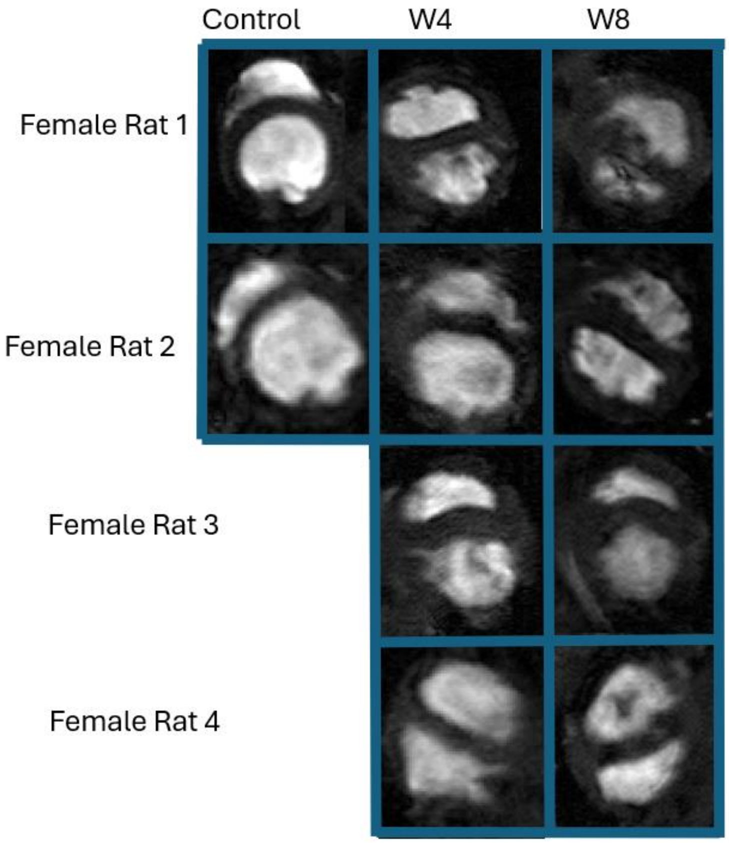

Figure 3.11. CMR images of female rats treated with SuHx, paired between three timepoints for female rat 1-2 (top) and two timepoints for female rats 3-4 (bottom). SuHx W4 and W8 corresponded to more changes to RV shape.

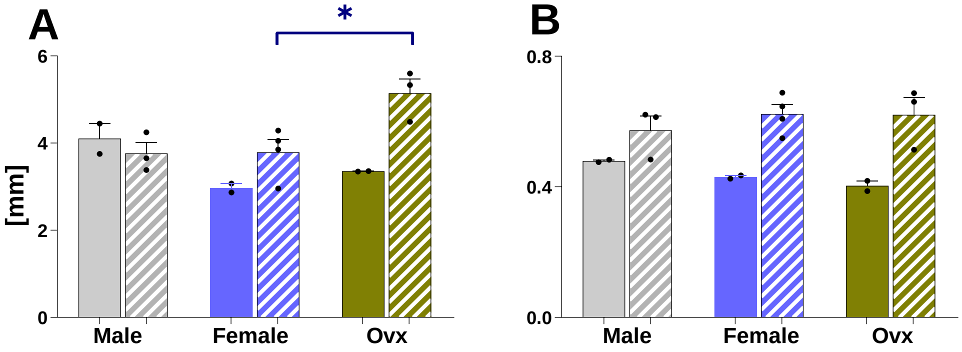

Figure 3.12. Both the intact (blue) and ovariectomized (green) female rats increased RV-septal mid-wall diameter (**A**) in SuHx (patterned) compared to control (solid). RV cross-sectional area to perimeter ratio (**B**) increased in female and OVX SuHx but not male rats (grey) with the largest increases in the OVX rat groups. *p<0.05 difference in means between animal groups.

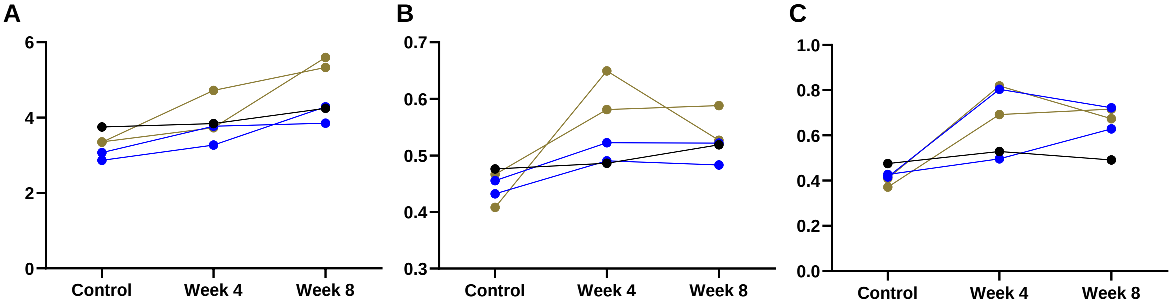

Figure 3.13. Paired rat-specific measurements of the RV-septum midwall diameter (**A**), the ratio of RV short-to-long diameter (**B**), and the RV area to perimeter ratio (**C**) derived from CMR images in male (black), female (blue), and ovariectomized female (gold) rats. While the male rat was largely unchanged in all three indices of RV shape, CMR images revealed the largest changes to RV shape in female (intact and ovariectomized) rats from control compared to 4 and 8 weeks of SuHx treatment.

SuHx treatment increased RV minimum pressure in all three groups ($p < 0.001$, Fig. 3.14), matching RV end-diastolic pressures (Fig. 3.1B). RV minimum pressure in ovary-intact female rats was less than half that of RV minimum pressure in ovariectomized rats, although these differences were not significant and no differences between groups were found ($p = 0.0824$).

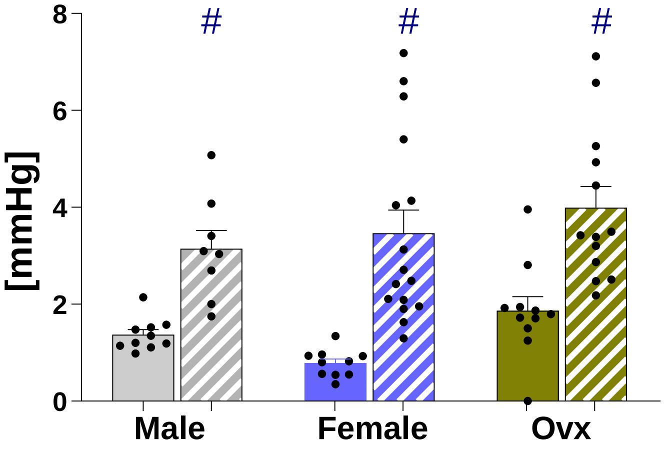

Figure 3.14. Minimum RV pressure was computed from caval occlusions and increased in response to SuHx treatment in all three groups. Data shown as mean ± standard error. #p<0.05

The time course of hemodynamics differed between male, female, and OVX rats treated with up to 26 weeks of SuHx. ES pressures, ES volumes, and Fulton index followed similar patterns, showing monotonic initial increases to SuHx followed by stabilization over 26 weeks. RV mass was the greatest in males, which showed increases that were 2x those of the smallest group, the ovary-intact females. ED pressures were similar in males and OVX females through the 26 weeks timecourse, but these increases due to SuHx were much less pronounced in the female group. ED volumes were maintained through W10 in males, but showed increases in the female and OVX female group. Stroke volume and ejection fraction were greater in the female group than in the male group at all weeks except for W3, W18, and W26.

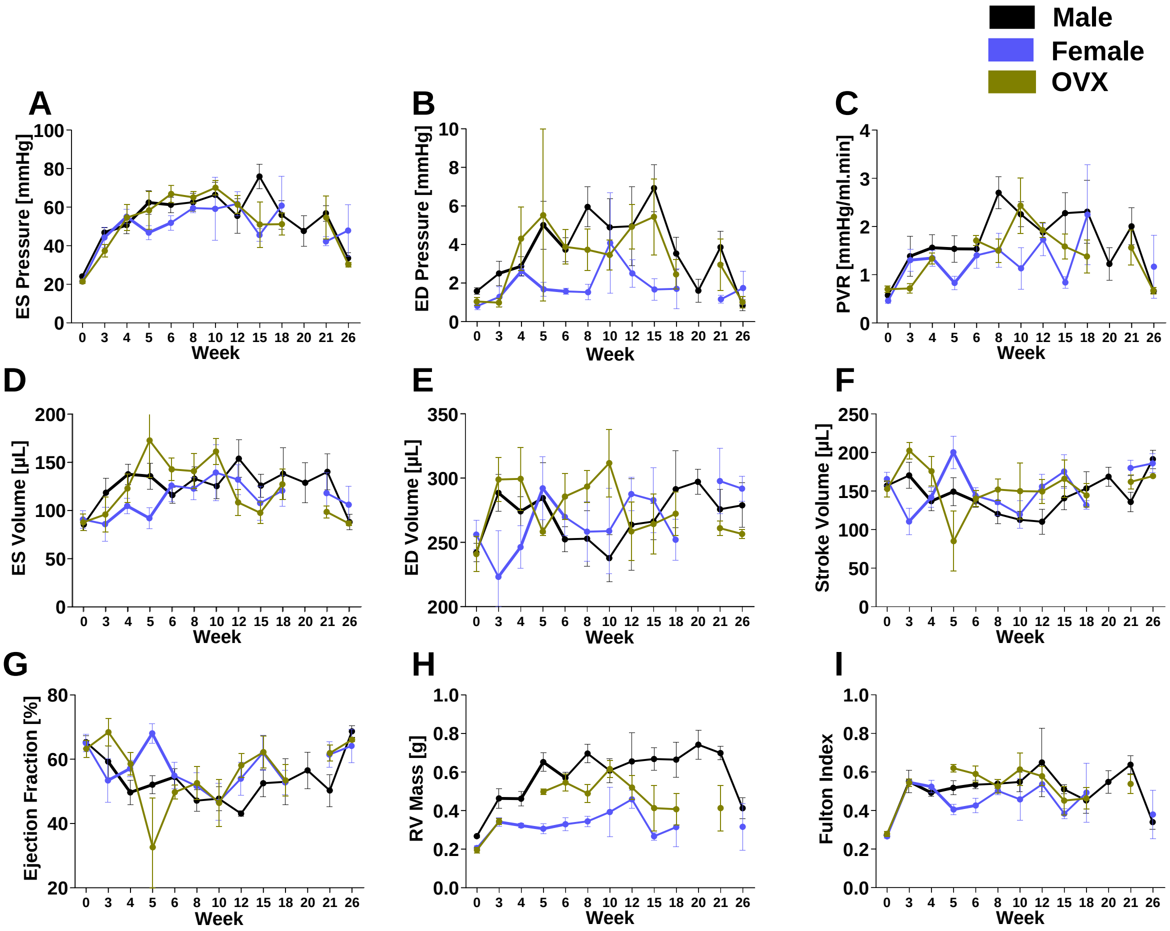

Figure 3.15. Longitudinal measurements at timepoints extending to 26 weeks of SuHx treatment were performed in males (black), as well as compared with female (blue) and ovariectomized females (green). We observed that the hemodynamic and morphological progression of ES pressure (**A**), ES volume (**D**), and Fulton Index (**I**) were similar, other measures, like ED pressure (**B**), PVR (**C**), ED volume (**E**), stroke volume (**F**), ejection fraction (**G**), and RV mass (**H**) differed, suggesting distinct RV adaptation between the three groups.

In Fig. 3.16, LV hemodynamics are shown for male, female, and OVX groups at 4, 8, and 12 weeks of SuHx treatment compared to respective controls. Left ventricular hemodynamics showed no significant changes ($p > 0.05$) in LV chamber end-systolic or end-diastolic pressures (Fig. 3.16A-B), volumes (Fig. 3.16C-D, or in total output (Fig. 3.16E-F).

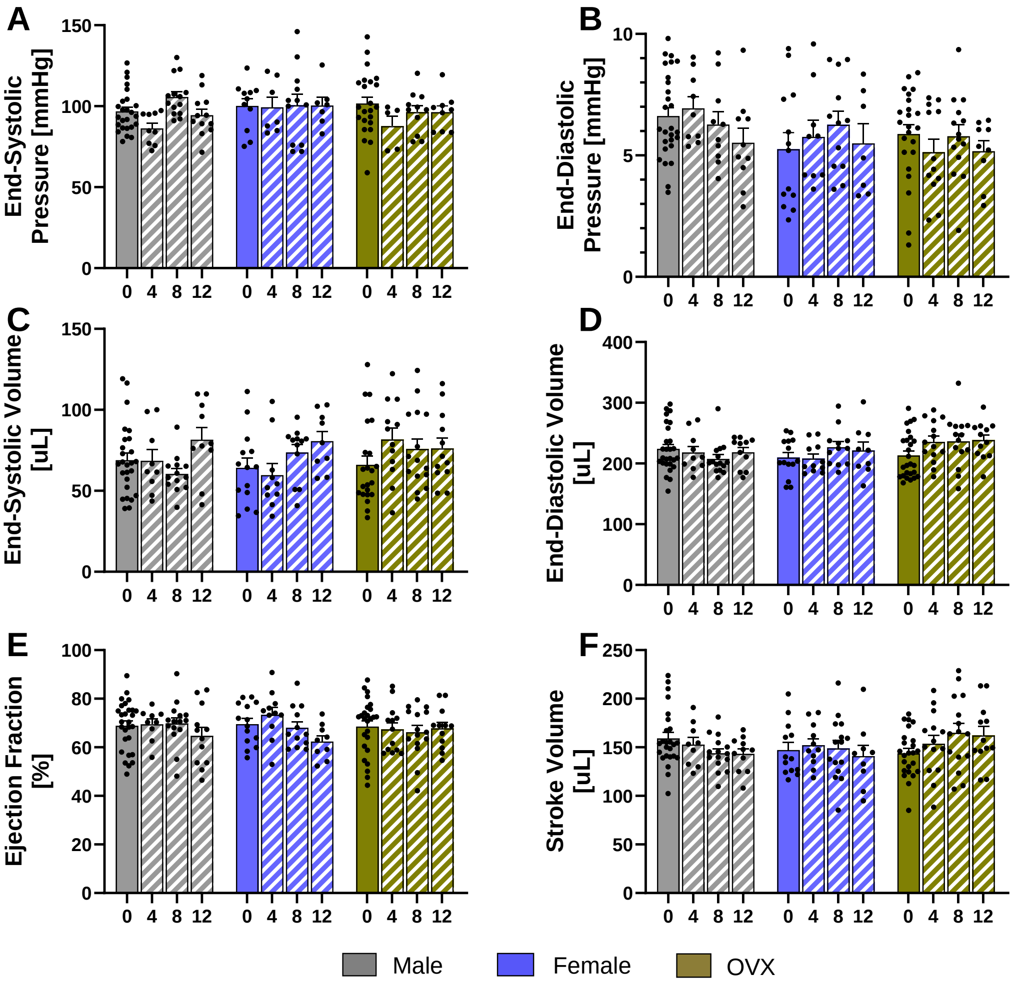

Figure 3.16. Measurements of left ventricular hemodynamics in male (grey), female (blue), and ovariectomized female (gold) rats treated with 0 (solid), 4, 8, or 12 weeks of SuHx (dashed). No significant changes in LV end-systolic (**A**) or end-diastolic pressure (**B**) were found. End-systolic volumes (**C**) showed the largest increases in males and females at week 12, while end-systolic and end-diastolic volumes (**D**) increased at W4 in ovariectomized female rats and remained slightly elevated through W12. Ejection fraction (**E**) and stroke volume (**F**) were maintained in all groups at all weeks, with a small increase in stroke volume in ovariectomized rats at week 8 to 12.

3.4 Discussion

In this chapter, we investigated the impact of sex and the depletion of ovarian hormones on RV remodeling in pulmonary hypertensive rats. After eight weeks of SuHx, all three groups exhibited similar increases in mean pulmonary arterial pressures, end-systolic RV chamber pressures, and RV hypertrophy. Consistent with previous observations,[11,28]RV hypertrophic wall thickening was identified as an adaptive remodeling response, contributing to the increased end-systolic chamber elastance in both male and ovary-intact female groups. In male rats, the RV maintained its end-diastolic volume but with a severe increase in passive myocardial stiffness. SuHx female rats exhibited the smallest reduction in ejection fraction. Although they showed RV hypertrophy with small increases in stiffness and diastolic volume. In the ovariectomized female rats, SuHx resulted in a significant increase in RV end-diastolic volume, despite the increase in diastolic chamber elastance.

Although the incidence of PAH is influenced by sex, several studies have reported similar pulmonary vascular hemodynamics between men and women following diagnosis. Multiple cohort studies of PAH[29–31] and chronic thromboembolic pulmonary hypertension (CTEPH)[5] have consistently shown no significant sex differences in mean pulmonary arterial pressure (mPAP) or pulmonary vascular resistance (PVR). Similarly, large-scale studies in US military veterans found no differences in mPAP between men and women with PAH, although women had a higher average pulmonary vascular resistance at diagnosis.[32] Our findings align with these reports, showing only minor differences in mPAP and PVR between male and female rats. However, some PAH studies in younger adults have observed sex differences in mPAP, with young men exhibiting higher mPAP and hemodynamic burden than young women.[29,33,34] These discrepancies may be due to differences in disease stage between preclinical models and studies focusing on patients near heart failure. Age-related changes in sex-hormone concentration may significantly affect PAH risk and severity. Previous studies have demonstrated that sex differences in mPAP diminish by age 45 to 65,[34,35] suggesting that the relationship between sex and hemodynamics is not only influenced by ovarian hormone presence (e.g. menopause), but also by age and age-related comorbidities.

In patients with PAH, RV mass hypertrophy varies by sex, with greater hypertrophy in men, and decreases with age in both men and women with PAH.[31,36] Our study confirms RV myocyte hypertrophy, but we did not observe significant differences in acute RV hypertrophy (Fulton Index) between groups or in myocyte diameter between males and females after eight weeks of SuHx treatment. Further research is needed to better understand the interplay between sex, age, and PAH.

Hemodynamics in the left ventricle were largely unchanged by SuHx, despite the large changes to the relative intraventricular pressure gradient, and the sex-dependent remodeling and intrusion of the intraventricular septum wall into the LV chamber in female rats. This demonstrates the acute right-hearted impact of RV pressure overload under these SuHx treatment parameters. It is possible that prolonged exposure or subsequent stages of remodeling may lead to left ventricular dysfunction which itself may have consequences on PA pressures and subsequently the RV, as seen clinically[37].

3.4.1 Systolic Function in Patients

Several studies have indicated that women with PAH often exhibit a less pronounced reduction in ejection fraction compared to men with PAH, even with similar RV afterload.[3,38] In our study, no significant differences in ejection fraction were found between groups, although male and OVX SuHx groups showed a decline in ejection fraction that was 1.5 times greater (over 2 times in the male group) greater than the decline observed in the female group. However, none of the SuHx groups had an ejection fraction below 50%. Changes to ejection fraction observed in this study are consistent with previous reports in similar male rat SuHx models.[13,39] Although female patients with PAH may tolerate RV pressure overload for a longer duration, they may experience more severe RV impairment at the end-stage of the disease,[31] as observed in a Dutch PAH cohort by van Wezenbeek *et al*.. Interestingly, post-menopausal women in this cohort demonstrated preserved RV function prior to adverse events, indicating that this prolonged period of tolerated RV pressure-overload may occur independently of menopausal status, although this finding may be confounded by other age-related comorbidities. Tello *et al.* recently investigated sex differences in ventricular-vascular coupling in patients with PAH and found that women with PAH had improved ventricular-vascular coupling than men with PAH, despite similar RV afterload parameters, pulmonary arterial pressure and resistance, and RV chamber volumes.[40] Similarly, sex differences in survival were linked to improved systolic function and RV-PA coupling in women with CTEPH.[41] In our study, no differences in ventricular-vascular coupling were observed between groups or due to SuHx, and the E_{es}/E_a ratio remained within the healthy coupling ratio of 1.1-1.5.[42] Nevertheless, our findings are consistent with clinical reports, highlighting sex-dependent RV adaptations that occur independently of RV afterload.

3.4.2 Diastolic Function in Patients

RV diastolic stiffening (E_{ed} increase) is known to be a strong prognostic indicator for patients with PAH.[9,43] However, the relationship between diastolic stiffening and systolic output is complex and influenced by various factors such as RV loading conditions, RV wall thickness, myocardial fibrosis, and myocyte properties. Studies by Trip *et al.* and Vanderpool *et al.* have emphasized the importance of E_{ed} as an early predictor of therapeutic response in advanced PAH and as a potential mediator of age-related differences in PAH prognosis.[43,44] E_{ed} alterations are suggested to improve stroke volume by restoring the Frank-Starling volume reserve independently of contractility recruitment.[44,45] Additionally, diastolic stiffening may serve as an adaptive mechanism that helps prevent or delay RV dilation and dysfunction.[11]

However, the relationship between sex and diastolic stiffening in the RVs of patients with PAH remains unclear. Previous studies investigating diastolic stiffening in patients with PAH either did not examine sex differences or found no significant differences.[9,31,43,44] In our study, we observed increased end-diastolic chamber elastance in male and female (both ovary-intact and OVX) SuHx rats that was the greatest in male SuHx rats. Thus, we provide novel evidence of sex differences in RV diastolic stiffening in the remodeled RV.

When the RV myocardium is tested *ex vivo* via planar biaxial loading, significant stiffening was found in SuHx-treated animals, with the most pronounced stiffening in males and the least in females.[46,47] Conversely, Cheng *et al*. reported diastolic stiffening without sex differences in a pressure overload murine model.[48] These discrepancies may be attributed to the specific animal model or stage of the disease. It is very likely that diastolic stiffening in PAH is a dynamic process that evolves over time, even during the early-stage of compensated RV remodeling.[11] Therefore, additional studies on diastolic function in PAH, particularly with respect to age and sex, are warranted.

3.4.3 Sex Dependent Remodeling of Right-Ventricular Geometry

Previous studies in male rats have shown that increased diastolic stiffness, resulting from passive myocardial stiffening, prevents RV dilation, with the greatest stiffness observed after 8 weeks of SuHx treatment.[11] By contrast, we observed increases in end-diastolic volume in both female and OVX SuHx groups. While passive myocardial stiffening was also present in female rats, the severity was reduced. Our findings suggest that passive myocardium stiffening prevented the RV chamber from dilating in male SuHx animals, unlike female SuHx animals, despite comparable pressure overload between the sexes.

Previous studies have reported increases in the RV short-to-long-diameter ratio (eccentricity) and chamber rounding as notable features of RV pathological remodeling and RV dilation.[49–51] We observed increased RV sphericity (ratio of RV long to short diameter) and eccentricity, consistent with previous noninvasive studies in PAH patients.[49,52–54] Furthermore, our findings identify a sex dependence in the basal bulge and RV sphericity, which differs from previous clinical reports.[52] The sex-dependent remodeling of RV shape identified in this study could contribute to the significant differences in organ-level RV hemodynamic function between sexes or at different stages of the disease. Notably, the acute RV pressure overload induced by SuHx increased RV eccentricity, which was accompanied by a corresponding decrease in LV eccentricity across all groups, consistent with previous reports.[54–56] Although our analysis focused on changes in RV hemodynamic function, it is crucial to note that RV failure often corresponds to changes in the function of the left ventricle.[57,58] These changes may be explained by remodeling of the RV-LV inter-ventricular pressure gradient and bulging of the septal wall into the LV chamber, affecting LV chamber hemodynamics.[55]

RV shape change was illustrated by selecting representative images from the middle of the RV, as well as quantified in multiple short axis images per animal that spanned the RV chamber. While these averaged measurements were sufficient to identify SuHx- and animal group –dependent changes, they do not capture regional heterogeneity in RV shape change, particularly in the apex-outflow tract dimension.

3.5 Conclusion

In this chapter, we designed an experimental study to compare the sex-dependent differential remodeling of the right ventricular in response to pulmonary arterial hypertension. In male, female, and ovariectomized female Sprague-Dawley rats induced with eight weeks of sugen-hypoxia treatment, we compared the changes to systolic and diastolic function, as well as the correspondence between organ function, RV chamber geometry, myocyte hypertrophy, and material remodeling. We identified sex-specific differences in end-systolic and end-diastolic chamber function, despite similarities in pressure overload between groups. Particularly, passive myocardial stiffening was the most severe in the male SuHx group, while female rats adapted to pressure overload primarily with hypertrophy. Unlike male or ovary-intact female rats, ovariectomized rats increased end-diastolic volume despite significant increases to end-diastolic chamber elastance.

3.6 Acknowledgements

Chapter 3, in full, is a reprint of the material as it appears in Sex-Dependent Remodeling of Right Ventricular Function in a Rat Model of Pulmonary Arterial Hypertension. Kwan, Ethan D.; Hardie, Becky A.; Garcia, Kristen M.; Mu Hao; Wang, Tsui-Min; Valdez-Jasso, Daniela. American Journal of Physiology Heart and Circulatory Physiology. 2024. The dissertation author was the primary investigator and author of this paper.

3.7 References

1. Ventetuolo CE, Ouyang P, Bluemke DA, et al. Sex hormones are associated with right ventricular structure and function: The MESA-right ventricle study. *Am J Respir Crit Care Med*. 2011;183(5):659-667.

2. Lahm T, Tuder RM, Petrache I. Progress in solving the sex hormone paradox in pulmonary hypertension. *Am J Physiol - Lung Cell Mol Physiol*. Published online 2014.

3. Jacobs W, Van De Veerdonk MC, Trip P, et al. The Right Ventricle Explains Sex Differences in Survival in Idiopathic Pulmonary Arterial Hypertension. *Chest*. Published online 2014.

4. Foppa M, Arora G, Gona P, et al. Right Ventricular Volumes and Systolic Function by Cardiac Magnetic Resonance and the Impact of Sex, Age, and Obesity in a Longitudinally Followed Cohort Free of Pulmonary and Cardiovascular Disease. *Circ Cardiovasc Imaging*. 2016;9(3):e003810.

5. Shigeta A, Tanabe N, Shimizu H, et al. Gender Differences in Chronic Thromboembolic Pulmonary Hypertension in Japan. *Circ J*. 2008;72(12):2069-2074.

6. Frump AL, Albrecht M, Yakubov B, et al. 17β-estradiol and estrogen receptor α protect right ventricular function in pulmonary hypertension via BMPR2 and apelin. *J Clin Invest*. Published online 2021.

7. Lahm T, Frump AL, Albrecht ME, et al. 17β-Estradiol mediates superior adaptation of right ventricular function to acute strenuous exercise in female rats with severe pulmonary hypertension. *Am J Physiol-Lung Cell Mol Physiol*. 2016;311(2):L375-L388.

8. Liu A, Schreier D, Tian L, et al. Direct and indirect protection of right ventricular function by estrogen in an experimental model of pulmonary arterial hypertension. *Am J Physiol - Heart Circ Physiol*. Published online 2014.

9. Rain S, Handoko ML, Trip P, et al. Right ventricular diastolic impairment in patients with pulmonary arterial hypertension. *Circulation*. 2013;128(18):2016-2025.

10. Hsu S, Kokkonen-Simon KM, Kirk JA, et al. Right ventricular myofilament functional differences in humans with systemic sclerosis-associated versus idiopathic pulmonary arterial hypertension. *Circulation*. 2018;137(22):2360-2370.

11. Kwan ED, Velez-Rendon D, Zhang X, et al. Distinct time courses and mechanics of right ventricular hypertrophy and diastolic stiffening in a male rat model of pulmonary arterial hypertension. *Am J Physiol - Heart Circ Physiol*. Published online 2021.

12. Vélez-Rendón D, Zhang X, Gerringer J, Valdez-Jasso D. Compensated right ventricular function of the onset of pulmonary hypertension in a rat model depends on chamber remodeling and contractile augmentation. *Pulm Circ*. 2018;8(4):1-13.

13. Jayasekera G, Wilson KS, Buist H, et al. Understanding longitudinal biventricular structural and functional changes in a pulmonary hypertension Sugen–hypoxia rat model by cardiac magnetic resonance imaging. *Pulm Circ*. 2020;10(1):1-11.

14. Wei CL, Valvano JW, Feldman MD, Pearce JA. Nonlinear conductance-volume relationship for murine conductance catheter measurement system. *IEEE Trans Biomed Eng*. 2005;52(10):1654-1661.

15. Raghavan K, Porterfield JE, Kottam ATG, et al. Electrical conductivity and permittivity of murine myocardium. *IEEE Trans Biomed Eng*. 2009;56(8):2044-2053.

16. Lai N, Lu W, Wang J. Ca2+ and ion channels in hypoxia-mediated pulmonary hypertension. *Int J Clin Exp Pathol*. 2015;8(2):1081-1092.

17. Hsu S, Houston BA, Tampakakis E, et al. Right ventricular functional reserve in pulmonary arterial hypertension. *Circulation*. 2016;133(24):2413-2422.

18. Wasilczuk AZ, Rinehart C, Aggarwal A, et al. Hormonal basis of sex differences in anesthetic sensitivity. *Proc Natl Acad Sci U S A*. 121(3):e2312913120.

19. Mansouri MT, Fidler JA, Meng QC, Eckenhoff RG, García PS. Sex effects on behavioral markers of emergence from propofol and isoflurane anesthesia in rats. *Behav Brain Res*. 2019;367:59-67.

20. Ewalenko P, Brimioulle S, Delcroix M, Wauthy P, Lejeune P, Naeije R. EFFECTS OF ISOFLURANE VERSUS PROPOFOL ON RIGHT VENTRICULOVASCULAR COUPLING IN CANINE EMBOLIC PULMONARY HYPERTENSION. *Anesthesiology*. Published online 1994.

21. Loushin MK. The Effects of Anesthetic Agents on Cardiac Function. In: Iaizzo PA, ed. *Handbook of Cardiac Anatomy, Physiology, and Devices*. Humana Press; 2005:171-180.

22. Kwan ED, Hardie BA, Garcia KM, Mu H, Wang TM, Valdez-Jasso D. Sex-dependent Remodeling of Right-Ventricular Function in a Rat Model of Pulmonary Arterial Hypertension. *Am J Physiol-Heart Circ Physiol*. Published online June 7, 2024.

23. Gerringer JW, Wagner JC, Vélez-Rendón D, Valdez-Jasso D. Lumped-parameter models of the pulmonary vasculature during the progression of pulmonary arterial hypertension. *Physiol Rep*. 2018;6(3):e13586.

24. Hill MR, Simon MA, Valdez-Jasso D, Zhang W, Champion HC, Sacks MS. Structural and Mechanical Adaptations of Right Ventricle Free Wall Myocardium to Pressure Overload. *Ann Biomed Eng*. 2014;42(12):2451-2465.

25. Yang B, Liang G, Khojasteh S, et al. Comparison of Neurodegeneration and Cognitive Impairment in Neonatal Mice Exposed to Propofol or Isoflurane. *PLoS ONE*. 2014;9(6):e99171.

26. Yipintsoi T, Scanlon PD, Bassingthwaighte JB. Density and Water Content of Dog Ventricular Myocardium. *Proc Soc Exp Biol Med*. 1972;141(3):1032-1035.

27. Droste P, Wong DWL, Hohl M, von Stillfried S, Klinkhammer BM, Boor P. Semiautomated pipeline for quantitative analysis of heart histopathology. *J Transl Med*. 2023;21(1):666.

28. Baicu CF, Li J, Zhang Y, et al. Time course of right ventricular pressure-overload induced myocardial fibrosis: Relationship to changes in fibroblast postsynthetic procollagen processing. *Am J Physiol - Heart Circ Physiol*. 2012;303(9):H1128-34.

29. Hoeper MM, Pausch C, Grünig E, et al. Idiopathic pulmonary arterial hypertension phenotypes determined by cluster analysis from the COMPERA registry. *J Heart Lung Transplant*. Published online 2020.

30. Kozu K, Sugimura K, Aoki T, et al. Sex differences in hemodynamic responses and long-term survival to optimal medical therapy in patients with pulmonary arterial hypertension. *Heart Vessels*. Published online 2018.

31. van Wezenbeek J, Groeneveldt JA, Llucià-Valldeperas A, et al. Interplay of sex hormones and long-term right ventricular adaptation in a Dutch PAH-cohort. *J Heart Lung Transplant*. 2022;41(4):445-457.

32. Ventetuolo CE, Hess E, Austin ED, et al. Sex-based differences in veterans with pulmonary hypertension: Results from the veterans affairs-clinical assessment reporting and tracking database. *PLoS ONE*. Published online 2017.

33. Shapiro S, Traiger GL, Turner M, McGoon MD, Wason P, Barst RJ. Sex Differences in the Diagnosis, Treatment, and Outcome of Patients With Pulmonary Arterial Hypertension Enrolled in the Registry to Evaluate Early and Long-term Pulmonary Arterial Hypertension Disease Management. *Chest*. 2012;141(2):363-373.

34. Ventetuolo CE, Praestgaard A, Palevsky HI, Klinger JR, Halpern SD, Kawut SM. Sex and haemodynamics in pulmonary arterial hypertension. *Eur Respir J*. Published online 2014.

35. Mair KM, Johansen AKZ, Wright AF, Wallace E, Maclean MR. Pulmonary arterial hypertension: Basis of sex differences in incidence and treatment response. *Br J Pharmacol*. Published online 2014.

36. Kawut SM, Lima JAC, Barr RG, et al. Sex and Race Differences in Right Ventricular Structure and Function: The MESA-Right Ventricle Study. *Circulation*. 2011;123(22):2542-2551.

37. Kalogeropoulos AP, Georgiopoulou VV, Borlaug BA, Gheorghiade M, Butler J. Left Ventricular Dysfunction with Pulmonary Hypertension. *Circ Heart Fail*. 2013;6(3):584-593.

38. Swift AJ, Capener D, Hammerton C, et al. Right Ventricular Sex Differences in Patients with Idiopathic Pulmonary Arterial Hypertension Characterised by Magnetic Resonance Imaging: Pair-Matched Case Controlled Study. *PLOS ONE*. 2015;10(5):e0127415.

39. Vanderpool RR, Gorelova A, Ma Y, et al. Reversal of Right Ventricular Hypertrophy and Dysfunction by Prostacyclin in a Rat Model of Severe Pulmonary Arterial Hypertension. *Int J Mol Sci*. 2022;23(10):5426.

40. Tello K, Richter MJ, Yogeswaran A, et al. Sex Differences in Right Ventricular–Pulmonary Arterial Coupling in Pulmonary Arterial Hypertension. *Am J Respir Crit Care Med*. 2020;202(7):1042-1046.

41. Barco S, Klok FA, Konstantinides SV, et al. Sex-specific differences in chronic thromboembolic pulmonary hypertension. Results from the European CTEPH registry. *J Thromb Haemost*. 2020;18(1):151-161.

42. Lahm T, Douglas IS, Archer SL, et al. Assessment of Right Ventricular Function in the Research Setting: Knowledge Gaps and Pathways Forward. An Official American Thoracic Society Research Statement. *Am J Respir Crit Care Med*. 2018;198(4):e15-e43.

43. Trip P, Rain S, Handoko ML, et al. Clinical relevance of right ventricular diastolic stiffness in pulmonary hypertension. *Eur Respir J*. 2015;45(6):1603-1612.

44. Vanderpool RR, Hunter KS, Insel M, et al. The Right Ventricular-Pulmonary Arterial Coupling and Diastolic Function Response to Therapy in Pulmonary Arterial Hypertension. *Chest*. 2022;161(4):1048-1059.

45. Ait-Mou Y, Hsu K, Farman GP, et al. Titin strain contributes to the Frank–Starling law of the heart by structural rearrangements of both thin- and thick-filament proteins. *Proc Natl Acad Sci*. 2016;113(8):2306-2311.

46. Hardie BA, Huberts J, Valdez-Jasso D. Right Ventricular Myocardium Remodeling in Pulmonary Arterial Hypertension is Sex-Specific and Ovarian Hormone-Dependent. In: ; 2023.

47. Vélez-Rendón D, Pursell ER, Shieh J, Valdez-Jasso D. Relative Contributions of Matrix and Myocytes to Biaxial Mechanics of the Right Ventricle in Pulmonary Arterial Hypertension. *J Biomech Eng*. 2019;141(9):091011.

48. Cheng TC, Tabima DM, Caggiano LR, et al. Sex differences in right ventricular adaptation to pressure overload in a rat model. *J Appl Physiol*. 2022;132(3):888-901.

49. Kossaify A. Echocardiographic assessment of the right ventricle, from the conventional approach to speckle tracking and three-dimensional imaging, and insights into the “Right Way” to explore the forgotten chamber. *Clin Med Insights Cardiol*. Published online 2015.

50. Wang L, Chen X, Wan K, et al. Diagnostic and prognostic value of right ventricular eccentricity index in pulmonary artery hypertension. *Pulm Circ*. Published online 2020.

51. Mauger C, Gilbert K, Lee AM, et al. Right ventricular shape and function: Cardiovascular magnetic resonance reference morphology and biventricular risk factor morphometrics in UK Biobank. *J Cardiovasc Magn Reson*. Published online 2019.

52. Leary PJ, Kurtz CE, Hough CL, Waiss MP, Ralph DD, Sheehan FH. Three-dimensional analysis of right ventricular shape and function in pulmonary hypertension. *Pulm Circ*. Published online 2012.

53. Ryan T, Petrovic O, Dillon JC, Feigenbaum H, Conley MJ, Armstrong WF. An echocardiographic index for separation of right ventricular volume and pressure overload. *J Am Coll Cardiol*. Published online 1985.

54. Burkett DA, Patel SS, Mertens L, Friedberg MK, Ivy DD. Relationship between Left Ventricular Geometry and Invasive Hemodynamics in Pediatric Pulmonary Hypertension. *Circ Cardiovasc Imaging*. Published online 2020.

55. Loncaric F, Nunno L, Mimbrero M, et al. Basal Ventricular Septal Hypertrophy in Systemic Hypertension. *Am J Cardiol*. Published online 2020.

56. Abraham S, Weismann CG. Left Ventricular End-Systolic Eccentricity Index for Assessment of Pulmonary Hypertension in Infants. *Echocardiography*. Published online 2016.

57. Rosenkranz S, Howard LS, Gomberg-Maitland M, Hoeper MM. Systemic Consequences of Pulmonary Hypertension and Right-Sided Heart Failure. *Circulation*. Published online 2020.

58. Vachiéry JL, Tedford RJ, Rosenkranz S, et al. Pulmonary hypertension due to left heart disease. In: *European Respiratory Journal*. ; 2019.

Chapter 4 COMPUTATIONAL MODELS OF RV BIOMECHANICS

4.1 Introduction

Numerous mechanical, biological and electrophysiological systems operate in harmony to perform cardiac functions. By decoupling cardiac function into smaller systems, we can breakdown complex changes to provide better insights into pathophysiology. The study of cardiac biomechanics through clinical and experimental descriptions has been conducted for the past century, but computational tools have more recently been used to describe complex biomechanical changes. Computational representations of cardiac biomechanics allow for the investigation of specific isolated molecular or cellular mechanisms, as well as can directly or indirectly link organ-level clinical or experimental measurements of RV function to specific cellular or molecular mechanisms.

Computational models of the heart are typically built from clinical or experimental data. By applying clinical or experimental data to a mathematical framework, parameters of the model can be tuned and fitted to generate new insights into health and disease mechanisms. The model can be subsequently perturbed in a manner that may be unfeasible or impossible in patients, such as to generate predictions about response to new or existing therapies, for example. Commonly, computational cardiac models can be designed to model the cardiac anatomy, passive and active myocardial mechanics, cardiac coupling with the circulatory system, and electrophysiology.

In this chapter, our approach to building computational models of the RV represent the RV's anatomy and applies passive and active myocardial mechanical behavior to these anatomical representations. In our first approach the RV anatomy is first represented using a simplified spherical geometry, with constitutive mechanics related using Laplace's Law. We follow this approach up by describing a finite-element approach to representing the RV anatomy, with constitutive mechanics ascribed using standard biomechanical descriptions of myocardium passive and active properties. Material property parameters of the model are fitted to experimental RV hemodynamic and morphologic data.

4.2 Approach

4.2.1 Implementing a Laplace Model of Right-Ventricular Biomechanics

Right-ventricular pressure, myocardial wall mechanics and morphology were analyzed with a biomechanics model described previously[1] to estimate the contributions of altered RV geometry *vs.* changes in intrinsic myocardial material properties to measured changes in RV P-V relations during the progression of hypertensive remodeling.

Kinematics

The total ventricular space was modeled with a spherical geometry comprised of right and left ventricular portions. The spherical geometry was first adapted from Guccione's cylindrical model of the left ventricle[2] by Velez-Rendon *et al.*[1] and the geometric parameters were adjusted to fit our data based on measurements of excised myocardial mass and hemodynamic volumes. In our geometric model, the RV was comprised of the RV chamber volume, the RV myocardial free wall, and the septum myocardium wall. Therefore, the total RV volume was determined as the sum of the volumes of the three components,

$$Kr\ \frac{4}{3}\pi R^3 = V_{rv} + V_w + V_{sw} \qquad \text{Eq. 4.1}$$

In Equation 4.1, the total volume of the right ventricle is defined as a fraction K_r of a total sphere of the biventricular myocardium with a radius *R* and a myocardial wall thickness *H*. From measurements of excised myocardial mass and hemodynamic volumes in control and hypertensive rats, 0.55 was determined to be a suitable value for this fraction. Measurements in hundreds of animals reveal the geometric parameter K_r to fall in the range 0.45-0.62. The fraction K_r does not affect the kinetics and/or the stress-strain analysis of the model and was chosen only to best reflect the relative proportions of each of the designated constituent components of the RV according to experimental measurements. The independence of K_r and model material parameters $k_{1\text{-}3}$ can be validated by analytical proof.

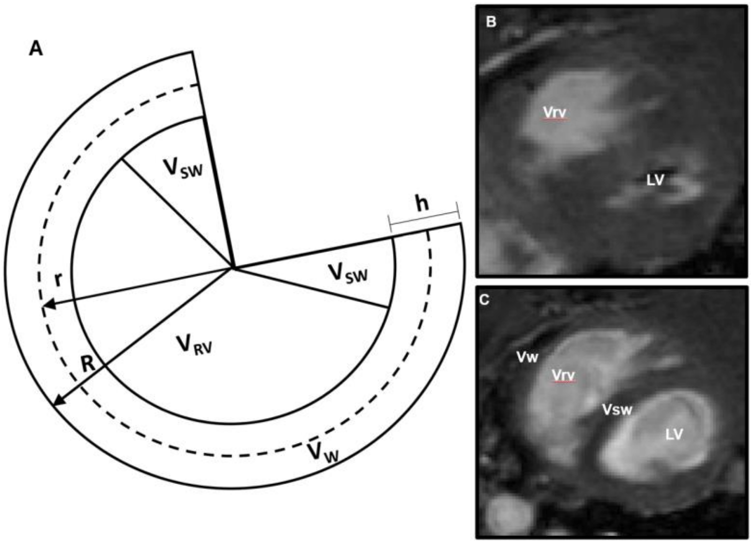

Figure 4.1. Model representation of the RV chamber geometry (**A**), comprised of a sphere of radius R, wall thickness of *h* and mid-wall radius *r*. The RV was composed of RV chamber (V_{RV}), RV free wall (V_W), and Septal wall (V_{SW}) volumes, as indicated from cardiac magnetic resonance images at end of systole (**B**) and end of diastole (**C**).

The RV chamber volume V_{RV} was determined from *in-vivo* measurements of the RV chamber volume at end systole and at end-diastole. The septum wall volume V_{SW} was determined based on *ex-vivo* measurements of the myocardial left ventricle and septal wall masses, converted to myocardial wall volumes using a myocardial density of 1.053g/mL[1,3]. The proportion ξ of the combined LV and septal cylindrical myocardial chamber that was determined to be the septum was set to 45% based on *ex-vivo* measurements of myocardial masses. This assumption was validated by isolating the septum and LV wall in control and PAH rats and measuring the relative masses. This assumption was also validated via a small number of noninvasive CMR-based measurements of septum and left ventricle wall volume.

Table 4.1. RV to RV+LV volume ratios obtained from cardiac MRI. This ratio increased with SuHx treatment, primarily due to RV wall hypertrophy.

ANIMAL ID	RV/(RV+LV) VOLUME FROM MRI
CONTROL	.4158 ± .009
W4	.5822 ± .021
W8	.5378 ± .018

The full range of CMR measured RV:RV+LV ratios were in the range (0.386-.695), with a mean in the controls of .4158 ± .009 increasing with PAH treatment to means of .5822±.021 and .5378±.018. Therefore, we conclude that our geometric model's constraint of K_r = 0.55 is reasonable. As previously noted, the model's material parameters k_1-k_3 are not sensitive to changes in K_r, so this decision did not affect the predictions of mechanical stress and strain.

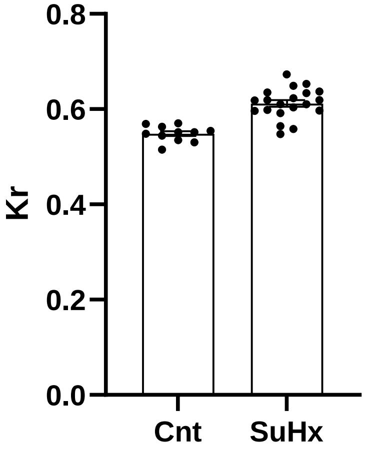

Figure 4.2. RV to RV + LV volume ratios obtained from invasive morphological measurements from excised hearts. The ratio had a mean of 0.54 in controls and 0.61 in SuHx, justifying the model assumption of 0.55.

The stress reference state was determined based on the theoretical unloaded RV chamber volume V_o. V_o was derived from PV measurements during vena caval occlusion. From these data, the pressure-volume measurement corresponding to the smallest values of end-diastolic pressure and end-diastolic volume during complete caval occlusion were obtained. The minimum RV EDP was noted. Based on the assumption that the right ventricle wall is stress-free in the unloaded (zero pressure) configuration, and the physiological constrain of V_o being positive, the pressure volume point (P_{min}, V_{min}) was set to (P_o, V_o) = (P_{min}, V_{min}) – P_{min} + θ = (~0, V_o) by subtracting a value of the RV minimum pressure from pressure measurements such that the minimum RV pressure used in the modeling was ~0. The secondary reason for this decision was to normalize pressure data to account for potential drifts in the pressure-volume catheter over the duration of surgical procedures. A θ value of 0.02 mmHg was chosen to approximate the minimum RV ED pressure. We note that the simplifying assumption of θ = 0.02 mmHg did not affect the results of any model analysis indicated by a sensitivity analysis.

To simulate diastolic filling and systolic contraction, the RV geometrical model is subjected to deformation to simulate a corresponding symmetrical inflation and deflation. In the physiologically loaded states, the RV geometry is defined with a myocardial mid-wall radius of r and an outer radius of R, where

$$R = \sqrt[3]{\frac{V_{rv}+V_w+V_{sw}}{\frac{4}{3}\pi k_r}} \qquad \text{Eq. 4.2}$$

To avoid over constraining the model, measured myocardial wall thicknesses were not used as model inputs but rather analytically defined. Based on our model geometry, the 3D myocardial wall volume can be divided by the myocardial 2D surface area to obtain a 1D average myocardial wall thickness h, where

$$h = \frac{V_w}{4\pi R^2 k_r}$$

In the unloaded state, we set $V_{rv} = V_0$ with the myocardial outer radius $R = R_0$, such that

$$R_0 = \sqrt[3]{\frac{V_0 + V_w + V_{sw}}{\frac{4}{3}\pi k_r}} \qquad \text{Eq. 4.3}$$

Hereby, we have a geometric model with which to describe RV shape and kinematics throughout the cardiac cycle, matched to experimental measurements of the volumes of the RV constituents. Myocardial strain is calculated from the changes in RV volume as follows. 3D "volumetric strain" is determined by using the end-systolic and end-diastolic RV volume measurements as inputs into the RV geometric model, compared against the theoretical unloaded RV volume Vo. Volumetric strain in three dimensions is converted to 1D deformation of the model's radius according to the defined RV geometry. 1D strain of the RV mid-wall radius *r* is converted to 1D sarcomere wall strain corresponding to 1D strain.

$$\lambda = \frac{L_s}{L_r} = \frac{r}{r_0} \qquad \text{Eq. 4.4}$$

where λ is the sarcomere stretch determined from the ratio of loaded to unloaded RV radius, assumed to be proportional to the ratio of deformed sarcomere length *Ls* to reference sarcomere length *Lo*. In this formulation sarcomere deformation is derived directly from volumetric measurements via the RV geometric model.

Constitutive Models of Myocardial Mechanics

The constitutive biomechanics of our computational model were defined at the sarcomere level. The passive myocardium was generally assumed to be a homogeneous incompressible hyperelastic material, with the sarcomere assumed to undergo spatially independent one-dimensional deformation. The passive sarcomere length-tension relationship was modeled based on the general Fung-type strain energy density equation. The Fung strain energy density equation describes the energy stored per unit volume as a function of strain, commonly written for cardiac tissue (myocardium) as

$$W = \frac{1}{2}c(e^{Q} - 1) \qquad \text{Eq. 4.5}$$

Where Q is a quadratic represent the Green-Lagrange strain tensor components and c is a material constant dependent on the material properties of the tissue. In uniaxial contraction and relaxation, the Green-Lagrange strain tensor Q can be written as

$$Q = E = \frac{1}{2}(\lambda^2 - 1) \qquad \text{Eq. 4.6}$$

Where λ is the one-dimensional stretch ratio. Therefore, the total strain energy within the myocardial tissue can be found by integrating the strain energy density function W over the volume V, where

$$U = V\,W = V\frac{1}{2}c\left(e^{\left(\frac{1}{2}(\lambda^2-1)\right)} - 1\right) \qquad \text{Eq. 4.7}$$

The passive tension of the myocardium T is then found by differentiating the total strain energy with respect to the stretch ratio lambda

$$T = \frac{dU}{d\lambda} \qquad \text{Eq. 4.8}$$

The final length-tension relationship we are left with is $T = k\lambda e^{\frac{1}{2}(\lambda^2-1)}$

Where $k = \frac{1}{2}cV$ can be represented by a material constant identified from experimental data, that encapsulates the material properties and volume of the myocardium. If we assume the strains are relatively small, the stretch ratio λ is approximately 1. Therefore, if we assume zero-tension is developed when the stretch ratio is 1, we arrive at a passive length-tension equation

$$T_p = k_1(e^{k_2(\lambda-1)} - 1) \qquad \text{Eq. 4.9}$$

In this equation, k_1 and k_2 are passive material parameters representing material stiffness and λ is the stretch ratio from Eq. 4.4 derived from the deformation of the RV radius.

Active myocardial stress was adapted from an elastance model described by Guccione *et al*[4] which was itself adapted from an earlier model by Hill *et al*[5]. The Hill model, originally used to describe chemical equilibrium, was fitted to experimental measurements to model the sigmoidal active tension – intracellular calcium relation in cardiac muscle[5]. This model excluded the additional effects of isometric twitch force-velocity according to an elastance model framework, shown to accurately reproduce sarcomere length and fiber stress data[4]. Based on the observation that calcium sensitivity is length-dependent, the Hill equation was modified to describe active tension development, dependent on intracellular calcium sensitivity, calcium concentration and sarcomere length.

$$T_a = T_{max} \frac{k_3^2}{k_3^2 + \frac{C^2}{e^{B(l-l_0)-1}}} \qquad \text{Eq. 4.10}$$

Here, the material parameter *k3* represents the peak (~end-systolic) intracellular calcium concentration. In this equation, the calcium sensitivity is described in the denominator term, where it is defined as a function of the sarcomere length. l_o is the constant sarcomere length at which zero active isometric tension is developed (*C* is set to 4.35 μM[2], T_{max} is the constant maximal isometric tension achieved at normal activation (set to 20000 mmHg[2]), and the exponent *B* (set to 11)[2] modulates the shape of peak isometric tension-length relation.

This equation scales the relative calcium concentration according to the sarcomere length, which scales the maximum isometric tension to developed tension according to the Hill equation. C represents the maximum peak isometric calcium concentration. The relationship between the sarcomere length *L* and reference sarcomere length *Lo* (set to 1.6 μm[2,6]) are defined in Eq. 4.4, determined from hemodynamic measurements of RV volume. The model parameter *B* determined the shape of the isometric length-tension relation. A range of parameter fits for *B* were investigated, shown across a range of fits in Fig. 4.3. The value used by Guccione's LV model was 4.75[4], and which produced good fits for control RV pressures, however, we observed increased values of *B* resulted in an improvement in the ES PVR fit for the more elevated SuHx RV pressures. Across all animals and range of control and SuHx pressures, we found a model parameter value of $B = 11$ to best fit our pressure-volume data.

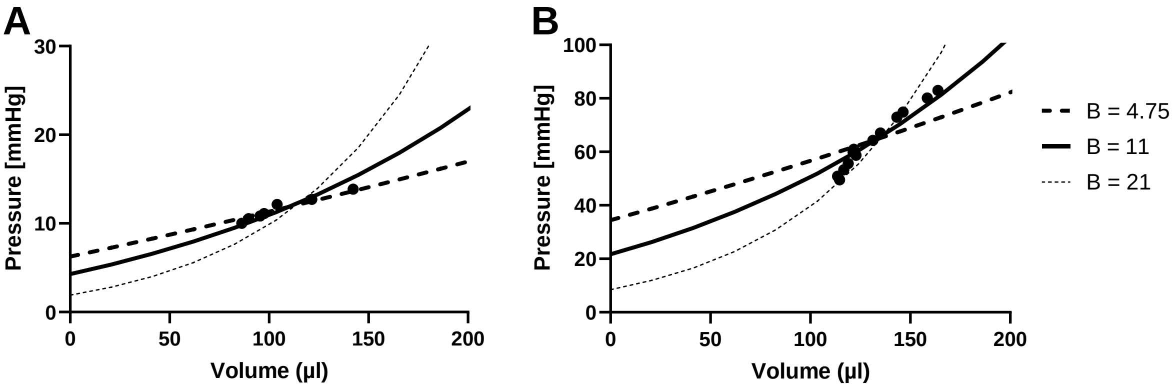

Figure 4.3. Model predictions of the end-systolic pressure volume relationship in a representative control (**A**) and SuHx Week 8 (**B**) male rat, based on changing the isometric length-tension shape parameter *B*. The best parameter fit that captured the ES PV relationship across control and SuHx ranges of RV pressure was determined to be $B = 11$, as shown across three examples here.

Mid-ventricular circumferential wall stress was related to RV pressure-volume measurements using the Laplace relation for a thin-walled sphere

$$T = \frac{Pr}{2h} \qquad \text{Eq. 4.11}$$

Where *T* is the Cauchy stress in the plane of the RV mid-wall, *P* is the blood pressure developed inside the ventricle chamber, *r* is the deformed radius of the ventricle, and *h* is the thickness of the myocardial wall. The Cauchy stress tensor was decomposed into active and passive components according to Eq. 4.12. At end-diastole, the ventricular wall stress *T* was assumed to be entirely composed of passive contributions, with active stress set to zero. At end-systole, the ventricular wall stress T was determined as the sum of passive and active tension.

$$T = T_p + T_a \qquad \text{Eq. 4.12}$$

The model assumption of a thin-walled sphere was validated over a range of normotensive and hypertensive data. Importantly, myocardial hypertrophy is a key feature of remodeling due to PAH. However, as previously noted, the ratio of RV radius to wall thickness often remains greater 5:1[1] even in models of RV hypertrophy, justifying a thin-walled assumption[7,8]. We validated this ratio in our own data in both control and PAH data over a range of time points. While the radius-to-wall thickness ratio did decrease due to PAH, we note that the ratio remained greater than 5:1 (Table 4.2).

Table 4.2. Model-derived radius and radius-to-wall-thickness ratios for a range of control and PAH treated animals demonstrate the radius to wall-thickness ratio remaining above 5:1 in all groups, justifying the Laplace thin-walled assumption.

	Control	**Week 3**	**Week 4**	**Week 5**	**Week 6**	**Week 8**	**Week 10**
Radius [mm]	7.33±.06	7.84±.14	7.88±.10	8.55±.13	8.24±.13	8.74±.18	8.48±.17
Radius-to-Wall Thickness Ratio	11.1±.4	7.7±.6	7.6±.2	7.2±.5	6.7±.2	6.4±.3	6.5±.2

To predict pressure-volume data, animal-specific models were fitted to pressure-volume data obtained during preload variation via complete occlusion of the inferior vena cava. The computational models were implemented in the forms

$$V = (P, G, k) \qquad \text{Eq. 4.13}$$

$$P = (V, G, k) \qquad \text{Eq. 4.14}$$

In Eq. 4.12 and 4.13, P represents RV chamber pressure and V represents RV chamber volume obtained from catheter measurements. These two equations demonstrate that pressure and volume were related with the computational model using the set of geometric/morphologic measurements G and the set of model material parameters k. The passive model parameters k_1 and k_2 were optimized to predict RV end-diastolic volumes using RV end-diastolic pressures and morphological measurements as inputs according to Eq. 4.12. Subsequently, the optimized material parameters k_1 and k_2 were input into Eq. 4.13, where the active model parameter k_3 was optimized to predict RV end-systolic pressures using RV end-systolic volumes.

Parameter optimization was carried out using a quasi-Newton gradient descent algorithm (the Broyden-Fletcher-Goldfarb-Shanno method). Selection of this algorithm was based on computational efficiency, convergence reliability and accuracy. Computational efficiency was not a major consideration for improvement, as average run-time was extremely quick, averaging less than 50 ms per animal. Optimizations were primarily run on a 6 core AMD Ryzen 5 5625U CPU with Radeon GPU. Model convergence was generally more of a consideration for the nonlinear ED PV relation than the quasilinear ES PV relation. We believe the choice to fit two model material parameters for end-diastole facilitated convergence of the model for a range of ED PVR values, slopes, and shapes, however we also note that one-parameter optimization produces highly accurate fits for most measured data. The root mean-squared error between predicted and observed volumes was minimized in Eq. 4.13 and between predicted and observed pressures was minimized in Eq. 4.14.

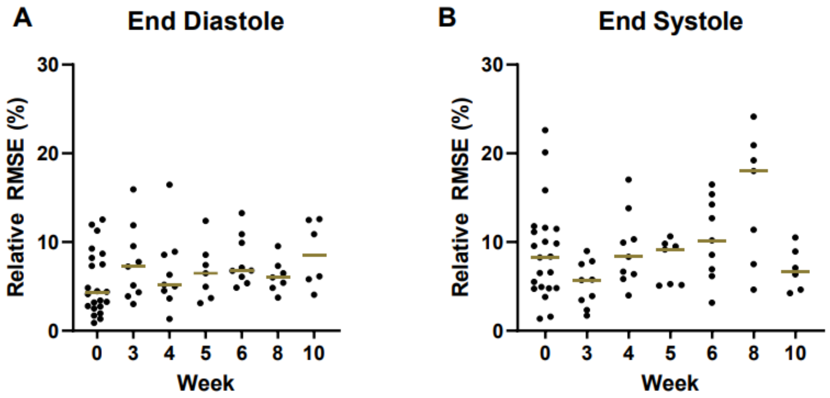

Figure 4.4. Root mean squared errors for the male rat models over a range of timepoints fitted to end-diastolic (**A**) and end-systolic (**B**) pressure-volume data shown as a percent of the measured end-diastolic volume and end-systolic pressure. For each animal group, the median RMSE is shown.

The resting material parameters k_1 and k_2 were optimized to give the best fit of model-predicted ED volumes to measured ED volumes, as a function of ED pressure. The calcium dependent myofilament activation material parameter k_3 was chosen to fit model-predicted ES pressures to measured ES pressures as a function of ES volume in each animal. This model fitting was first produced for control rats to establish a set of control material parameters. Importantly, while the models are rat-specific, our experimental design does not allow for paired control-PAH measurements, so a method to perform group comparisons had to be chosen (Fig. 4.5).

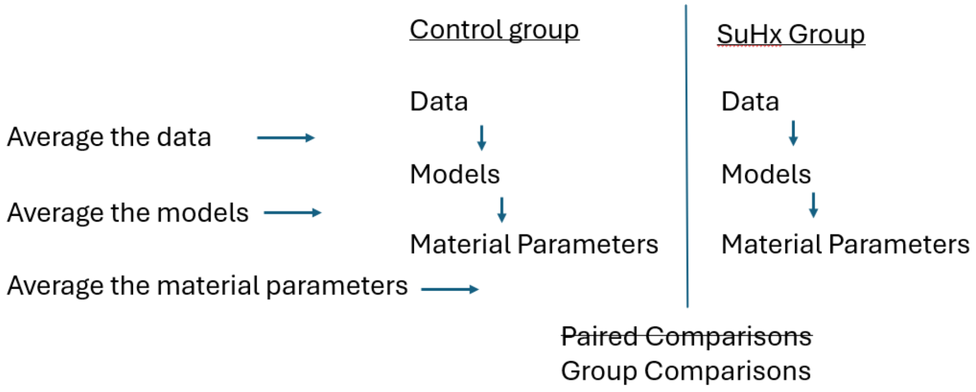

Figure 4.5. Illustration of the rat-specific modeling pipeline which inputs hemodynamic and morphologic data, fits biomechanics models, and identifies the material parameters of those rat-specific models. Because control and SuHx data is not paired, groups could be compared by averaging the PV data, averaging the models, or averaging the material parameters before continuing down the pipeline.

We next compared the performance of the model built on the average PV data of the group vs the performance of the average of rat-specific models of the group based on the ability to match the original P-V data. This comparison is shown in Fig. 4.6 below for a subset of PAH W8 data.

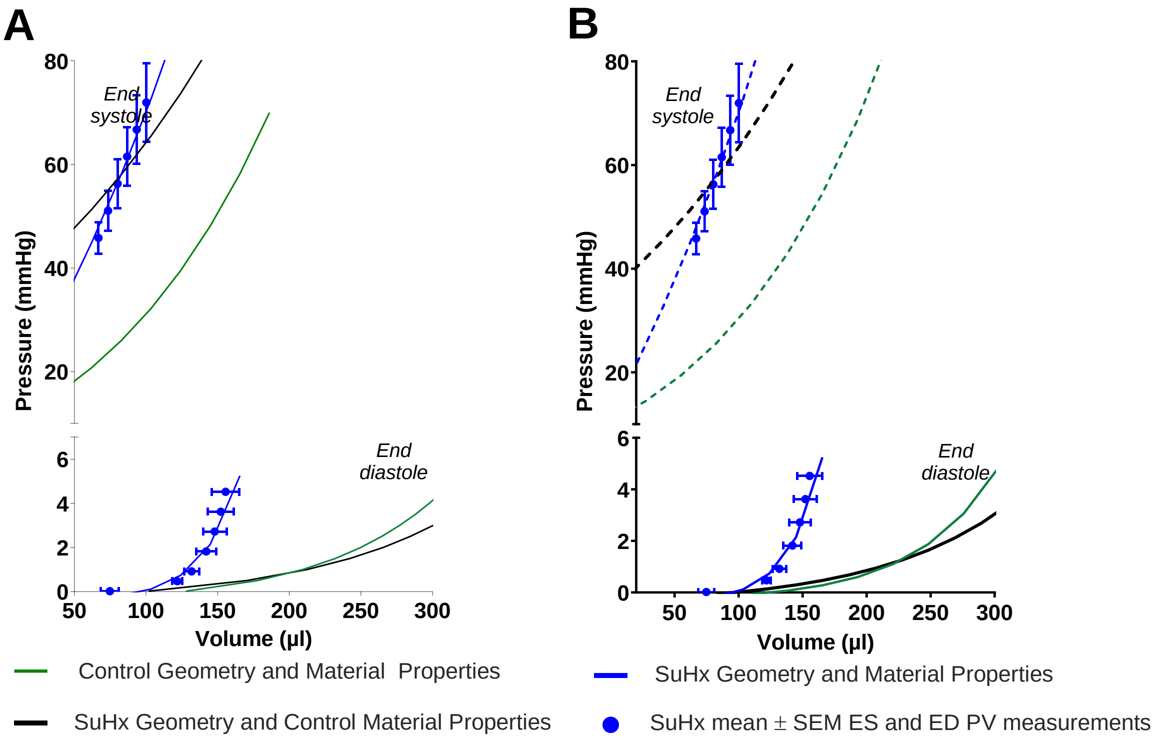

Figure 4.6. Comparison of the accuracy of the models of the male group average PV data (**A**) compared to models fitted to rat-specific average data (**B**). This analysis indicates that both models reproduce the measured PV data.

Based on the results of the above analysis, control material parameters were identified based on the model fitted to average control group PV and average morphologic data.

Table 4.3. Model material parameters of stiffness (k_1, k_2) and calcium dependent contractility (k_3) for male, female, and ovariectomized female control groups.

	k_1	k_2	k_3
Male control	3.9 ± 1.1	26.8 ± 7.0	.113 ± .007
Female control	2.6 ± 0.8	20.5 ± 2.3	.110 ± .009
OVX control	2.9 ± 1.1	34.5 ± 8.3	.110 ± .010

Male controls had the highest k_1 material stiffness parameter while intact females had the lowest k_1 and k_2 stiffness parameters. All control groups had similar calcium-dependent contractility parameters k_3. We note that these nonlinear material parameters cannot be directly averaged and compared without the additional context of the RV hemodynamics and morphologic measurements, however the general trends of material stiffness do align with the models' predictions of passive stiffness. The model's material stiffness parameters were the smallest for the female control group. Consistent with the observation that end-diastolic pressures were consistently lower in female rats than in male or OVX rats, we observed that the R^2 values of the model fits were generally worse than the R^2 values of the male SuHx model fits.

To validate whether our choice of a single constitutive model for the ED PVR was sufficient, we investigated a subset of the female control group which demonstrated representative pressure-volume hemodynamics. To investigate whether the general nonlinear exponential form of the ED PVR was indeed the best fit in such cases, we formulated a general linear equation of the form $P = \alpha(V) + C$ with one material parameter (α) and fitted it to the group (the female controls) in which we observed the smallest R^2 values. As the average end-diastolic pressure change (increase) with SuHx treatment, we then repeated this analysis in a subset of female SuHx rats. Those results are shown below.

Table 4.4. In a subset of female control animals, ED PV relations were fitted based on general linear and exponential formulations. The linear EDPVR showed a small improvement (n.s.) in the R^2 value. Data shown as mean ± standard error.

Animal ID	*Treatment*	*Linear EDPVR R^2*	*Exponential EDPVR R^2*
4	Female Control Wk 1	.7937	.7680
8	Female Control Wk 5	.4783	.4339
9	Female Control Wk 5	.9565	.9753
10	Female Control Wk 5	.5735	.1542
11	Female Control Wk 5	.8491	.9171
12	Female Control Wk 5	.7632	.8033
16	Female Control Wk 21	.3511	.3524
Average Control		**.6808±.0824**	**.6292±.1188**

Table 4.5. In a subset of female SuHx animals, ED PV relations were fitted based on general linear and exponential formulations. While the non-linear EDPVR showed a larger mean R^2 compared to the linear EDPVR (n.s.), the differences were negligible. Both models showed improved fits compared to the model fits in female control animals. Data shown as mean ± standard error.

Animal ID	*Treatment*	*Linear EDPVR R^2*	*Exponential EDPVR R^2*
W49	Female SuHx Wk 8	0.7981	0.7303
W52	Female SuHx Wk 8	0.8158	0.9767
W58	Female SuHx Wk 8	0.8793	0.9731
W59	Female SuHx Wk 8	0.5785	0.4219
W61	Female SuHx Wk 8	0.7496	
W85	Female SuHx Wk 8	0.8967	
W86	Female SuHx Wk 8	0.8740	
Average Control		**.7679±.0655**	**.7755±.1312**

Table 4.4 and 4.5 indicate no significant improvement from fitting a general linear EDPVR compared to the general exponential EDPVR commonly used in the field. The group standard errors suggest a larger variation in the quality of model fits from the exponential EDPVR compared to the linear EDPVR. This is consistent with the observation that some fits were extremely good ($R^2 > 0.9$) while others were poor. The data indicates that while the ED PV relation for the female control group may be more linear, this relation is sex dependent. Therefore, we conclude that using the linear EDPVR for all female rats would result in minimal improvements in the quality of the model fits - improvements that would be limited to the female control group. By contrast, the exponential EDPVR is consistent with published literature and may more accurately reflect variation in the data that is otherwise diminished by fitting a linear curve.

We aimed to use our model to answer two specific questions: 1) to decouple the effects of changes in its input parameters (Eq. 4.13 & Eq. 4.14) from each other and identify the relative contributions to organ-level changes in systolic and diastolic RV function 2) to predict the biomechanical properties of the RV myocardium (the material stress-strain relationships). First, with an established set of control material parameters (Table 4.3), we analyzed the incremental effects of changes in volume, geometry, and material properties.

Table 4.6. The model was used to decouple the relative effects of volume, geometry, and material properties on systolic and diastolic function.

	PAH volume	**PAH geometry**	**PAH material properties**
Case 1: Control model			
Case 2: Effects of Volume	X		
Case 3: Effects of geometry	X	X	
Case 4: PAH model	X	X	X

The fitted model material parameters were used to calculate rat-specific passive and active sarcomere length-tension relations according to Eq. 4.9 and Eq. 4.10. Mean passive sarcomere stress-sarcomere length relations were computed by averaging the rat-specific length-tension relations interpolated over a range of physiological lengths and stresses.

4.3 Results

4.3.1 10-week SuHx male longitudinal study

As discussed in Chapter 2, we observed evolving hemodynamic and RV properties over 10 weeks in a study of SuHx-treated male rats. We found that both RV ES and ED pressure increased from controls as measured in the first time point (week 3, $p < 0.05$). Both ES and ED pressure doubled by week 5 and the increases continued and were sustained through week 10. Importantly, however, we observed differences between the patterns of ED chamber elastance and ED chamber elastance, whereby ES chamber elastance plateaued by week 6 and was maintained through week 10 (Fig. 2.6C). By contrast, ED chamber elastance only increased after 5 weeks of SuHx, peaking at 8 weeks of SuHx and returning to levels like week 5 at week 10 (Fig 2.6D). Therefore, the model was applied to distinguish the relative contributions of volume, geometry, and material properties to these distinct patterns of changes in organ-level systolic and diastolic function.

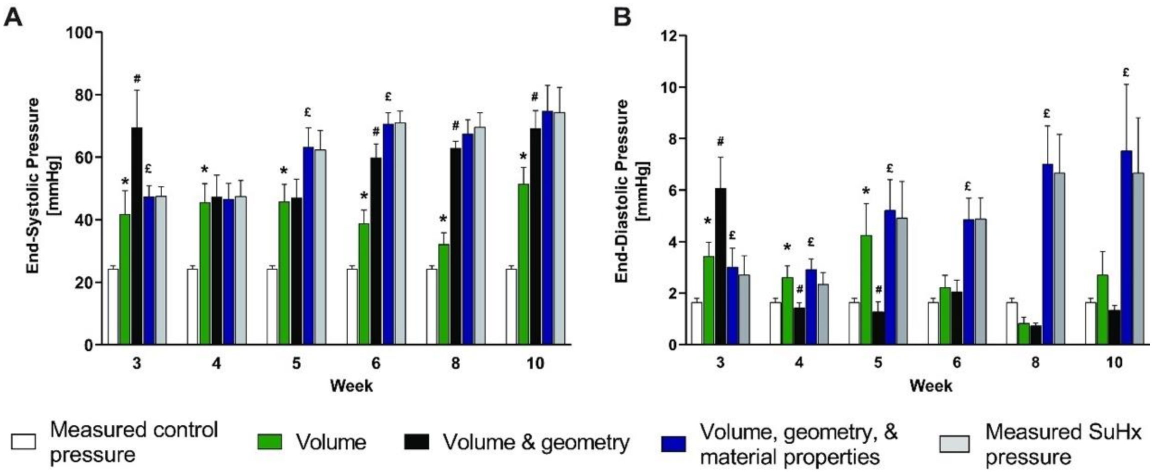

Figure 4.7. Measurements of control (white bars) and SuHx (gray bars) RV pressure for end systole (**A**) and end diastole (**B**) compared with model predictions of pressure using SuHx volume with control geometry and material properties (green); SuHx volume and geometries with control material properties (black); and SuHx volume, geometries, and material properties (blue). Green bars with * indicate a significant contribution of RV volume to increased ES or ED pressure compared with control (white bars). Black bars with # indicate a significant contribution of RV hypertrophy to increased ES (**A**) or ED (**B**) pressure compared with the contributions of volume alone (green bars). Blue bars with £ indicate a significant contribution of altered myofilament activation (**A**) or myocardial resting stiffness (**B**) to increased ES or ED pressure compared with volume and geometry (black bars). Data are shown as means ± SE, $p < 0.05$. ED, end-diastolic; ES, end-systolic; RV, right ventricle; SuHx, sugen-hypoxia. Figure 4.7. is a reproduction in part of data published in the American Journal of Physiology. doi: 10.1152/ajpheart.00046.2021. Epub 2021 Aug 27. PMID: 34448637; PMCID: PMC8794227.

Models (Fig. 4.7A) with measured geometries and control ES material properties were sufficient to explain most or all the significant increases in ES elastance that were measured in SuHx rats after week 4, except at week 5, where there was also a significant contribution of increased myofilament activation. In contrast, the significant increase in ED elastances were not explained by RV geometric remodeling. Hence, the increased ED chamber elastance in SuHx rats after week 5 were explained almost entirely by increased passive myocardial material stiffness. Although increased RV ES volume alone was sufficient to generate all the increased RV ES pressure at weeks 3 and 4, at weeks 5 and 6, there was also a significant, transient contribution of increased myofilament activation to RV ES pressure (blue bars). After week 5, significant contributions of geometry (RV hypertrophy, black bars) explained all or nearly all the measured increases in end-systolic pressure generation.

The same analysis for end-diastole (Fig. 4.7B) indicated that the significant increases in RV ED pressure were initially explained by increased RV ED volumes (at week 5), but subsequently (from week 6 to week 10) were due almost entirely to increased passive myocardial stiffness (blue bars) with no significant contributions of altered RV volume (green bars) or geometry (black bars). Passive myocardial stiffness peaked after 8 weeks and was maintained through 10 weeks, matched by increases to ED pressure, but not by ED chamber elastance, which decreased from week 8 to week 10. The model identified a greater contribution from volume and geometry (and a correspondingly smaller contribution from passive material properties) at week 10 compared to week 8, consistent with the finding that passive myocardial stiffness peaked at week 8.

The optimized model fits and material parameters matched to PV data were then used to predict passive and active sarcomere length-tension relations. Here (Fig. 4.8), passive sarcomere length between 1.85-2.2um and passive stresses between 0-10kPa were considered. Active sarcomere length between 1.8-1.86um and active stresses between 0-60kPa were considered.

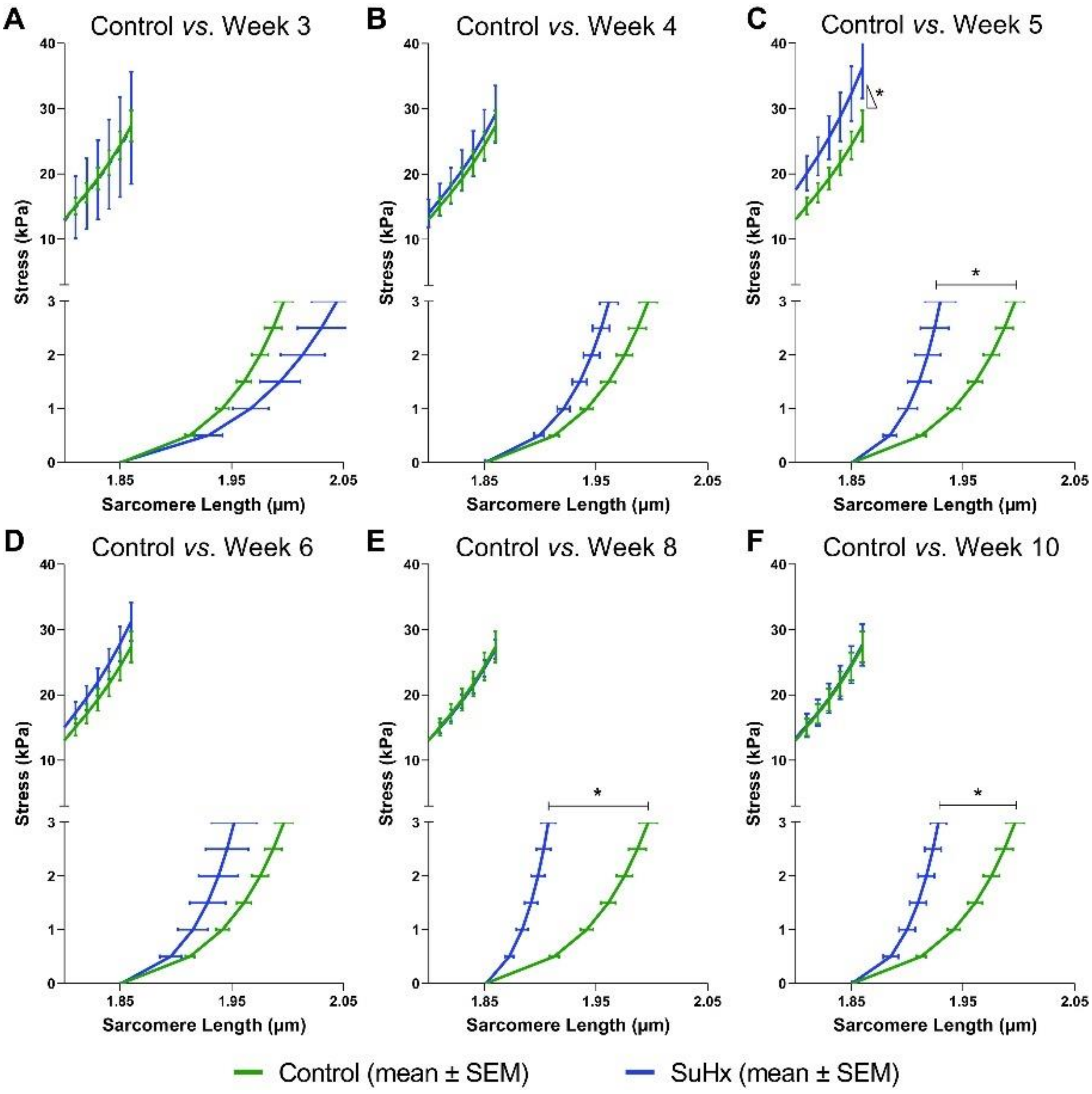

Figure 4.8. Model-predicted mean active end-systolic (*top*) and passive end-diastolic (*bottom*) fiber stress-sarcomere length relations for control (green) and SuHx (blue) male rats at weeks 3 (**A**), 4 (**B**), 5 (**C**), 6 (**D**), 8 (**E**), and 10 (**F**). The slope of the active stress-sarcomere length relation was only significantly higher than control in week 5 ($p < 0.05$). Predicted mean passive stress-sarcomere length relations were significantly stiffer in SuHx than in control rats at weeks 5, 8, and 10 (*$P < 0.05$). SuHx, sugen-hypoxia. Figure 4.8 is a reproduction in part of data published in the American Journal of Physiology. doi: 10.1152/ajpheart.00046.2021. Epub 2021 Aug 27. PMID: 34448637; PMCID: PMC8794227.

Mean passive fiber stress-sarcomere length relations of each group from each computed from the fitted rat-specific values of k_1 and k_2 were stiffer than control relations by week 5 and the stiffest at week 8. Two-factor ANOVA revealed sarcomere lengths at matched fiber stresses were significantly lower ($p < 0.05$) than control values at weeks 5, 8, and 10. There were no significant differences between groups in the computed active stress-sarcomere length relations, except in the SuHx *week 5* group. A two-factor ANOVA of model-computed systolic fiber stress showed a significant interaction effect between experimental group and sarcomere length ($p < 0.01$). A post hoc comparison showed that the slope of the active stress-sarcomere length relation was significantly greater than control only at week 5 ($p < 0.01$).

An analysis of the evolution of the computational model parameters over ten weeks of SuHx treatment is shown in Fig. 4.9. While the non-linear passive (k_1 and k_2) and active (k_3) material parameters should not be numerically averaged for comparison, we note the general evolution of material parameter values over ten weeks. For the passive parameters, we observed an increase in the material stiffness k_2 in occurring after five weeks that was maintained through ten weeks of treatment. The product of the material parameters showed the largest median value in the W8 group, matching the large increases in diastolic chamber elastance and consistent with the interpretation that passive myocardial stiffening was the greatest after eight weeks of SuHx. Conversely, the active material parameter k_3 did not show significant changes over ten weeks of SuHx. This suggests that the increases to end-systolic elastance were not matched by changes to myocardial material properties and instead explained by hypertrophic increases to the RV wall.

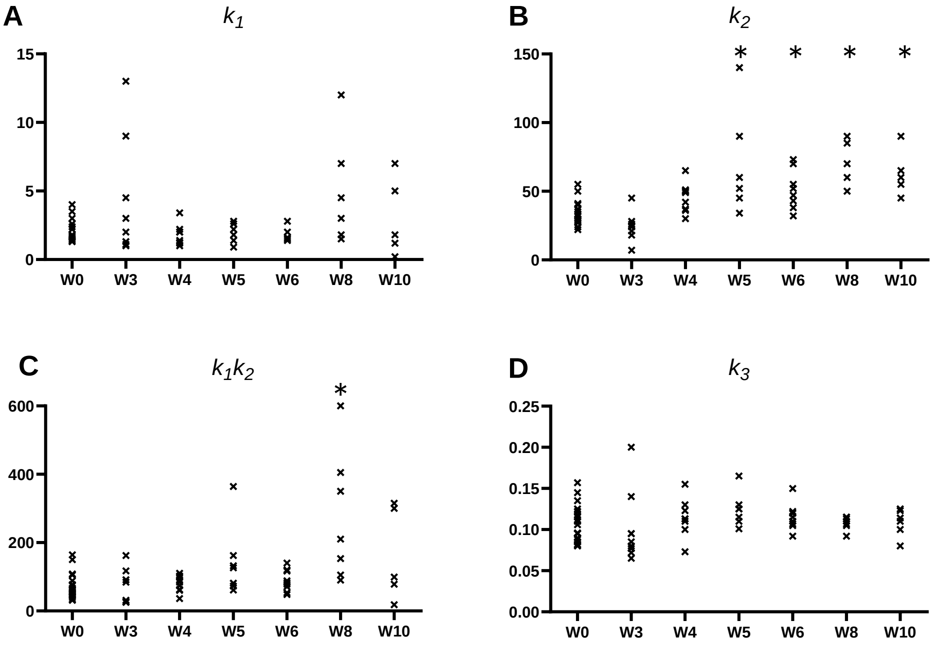

Figure 4.9. Model material parameters used to fit the measured pressure-volume relation for each male rat included in the study. Passive material parameters k_1 (**A**), k_2 (**B**), their product k_1k_2 (**C**), and myofilament activation material parameter k_3 (**D**). $^*p < 0.05$ compared with control group.

Right ventricular systolic active fiber stress increased from a mean of 14.6 kPa at control to 25.8 kPa at week 3 and did not change significantly thereafter (Table 4.7). Had the RV not remodeled in SuHx rats, the model indicated the increase in ES pressure would have caused fiber stresses to double by week 3 (from 14.6 to 31.4 kPa) and more than triple by week 10 (from 14.6 to 48.8 kPa). Decoupling the RV changes revealed RV geometric remodeling caused active fiber stress in weeks 5–10 SuHx rats to be about half as high as it would have been without hypertrophy (26.7–29.8 kPa vs. 41.8–48.8 kPa). End-diastolic RV free wall fiber stress did not increase from the control mean (1.05 kPa) until week 5 (2.10 kPa) and continued to increase further to 2.6 kPa by weeks 8 and 10. Had the RV not remodeled, the increase in ED pressure would have more than tripled passive wall stresses by week 5 (from 1.05 to 3.61 kPa) and increased fivefold by weeks

8 and 10. Hence, although RV anatomic and material property remodeling were not sufficient to completely normalize ED and ES fiber stresses, they did offset the majority of the increases that would otherwise have occurred. These results are consistent with the interpretation that the reduction of both passive and active myocardial wall stress occurs through time-dependent RV changes that are differentially activated over 10 weeks of SuHx. These results also suggest these time-dependent changes to passive and active wall stress and biomechanics underlie changes to systolic and diastolic RV function.

Table 4.7. Average myocardial fiber stress in the four model conditions is shown across 10 weeks of SuHx in males. Active stress and strain were calculated based on end-systolic pressure and volume while passive stress and strain were based on end-diastolic pressure and volume. Table 4.7. is a reproduction in part of data published in the American Journal of Physiology. doi: 10.1152/ajpheart.00046.2021. Epub 2021 Aug 27. PMID: 34448637; PMCID: PMC8794227.

	Week						
	Control	***3***	***4***	***5***	***6***	***8***	***10***
Control geometry and control mechanics							
ED fiber strain	1.05	1.07	1.06	1.08	1.08	1.09	1.09
ED fiber stress, kPa	1.12	1.91	1.50	3.61	3.58	5.00	5.00
ES active fiber strain	0.98	1.01	1.01	1.03	1.03	1.03	1.04
ES active fiber stress, kPa	14.6	31.4	29.7	41.8	46.9	46.1	48.8
SuHx geometry and control mechanics							
ED fiber strain		1.06	1.05	1.07	1.07	1.08	1.08
ED fiber stress, kPa		1.21	1.03	2.31	2.20	2.93	2.93
ES active fiber strain		0.99	0.99	1.00	1.01	1.01	1.01
ES active fiber stress, kPa		19.4	19.9	26.7	29.7	27.6	29.8
SuHx geometry and SuHx mechanics							
ED fiber strain		1.06	1.04	1.03	1.04	1.02	1.04
ED fiber stress, kPa		1.21	0.99	2.10	2.04	2.56	2.64
ES active fiber strain		1.00	1.00	0.99	1.00	1.00	1.00
ES active fiber stress, kPa		25.8	21.5	26.3	27.7	25.6	27.1

4.3.3 Sex differences

We next applied our computational model analysis to study sex- and ovarian-hormone differences. We compared sex-dependent changes to RV remodeling as described in Chapter 2.

While SuHx treatment increased ED and ES pressures, the increases to ED pressures were the most severe in male SuHx and the least in female SuHx. Similarly, ED chamber elastance showed a 6-fold increase that was more severe than the increases seen in the OVX SuHx and the female SuHx group. We aimed to use the model analysis to decouple the relative effects of changes to RV volume, geometry, and material properties on systolic and diastolic function.

Pressure-Volume Relative Contributions

The model was initially used to assess the relative contributions of geometry and material properties to changes in systolic and diastolic P-V measurements. Increases in end-systolic pressures (Fig. 4.10A) were primarily attributed to RV wall hypertrophy (geometry) in both male and ovary-intact female groups, with statistically insignificant contributions ($p = 0.34$) from changes in myocardial wall material properties. In the OVX group, significant increases in end-systolic pressure were attributed to both geometry and systolic material properties ($p = 0.029$). The rise in end-diastolic pressure (Fig. 4.10B) in male SuHx rats aligns with previously documented alterations in myocardial wall properties.[9] Conversely, in ovary-intact female SuHx rats, the elevated diastolic pressure was primarily attributed to geometric changes. Notably, in the OVX SuHx group, both geometric and material property changes significantly contributed to the increase in diastolic pressure, collectively explaining the observed rise. The greatest increases in ED pressure were observed in male SuHx rats, while the smallest were in female SuHx rats, reflecting the largest and smallest contributions from material property changes, respectively.

Thus, while changes in ES pressures among the hypertensive animals were primarily due to RV hypertrophy with significant contributions from systolic material changes in the OVX group, increases in ED pressures were associated with material stiffening in male and OVX SuHx rats which were most pronounced in males and to hypertrophy in female SuHx.

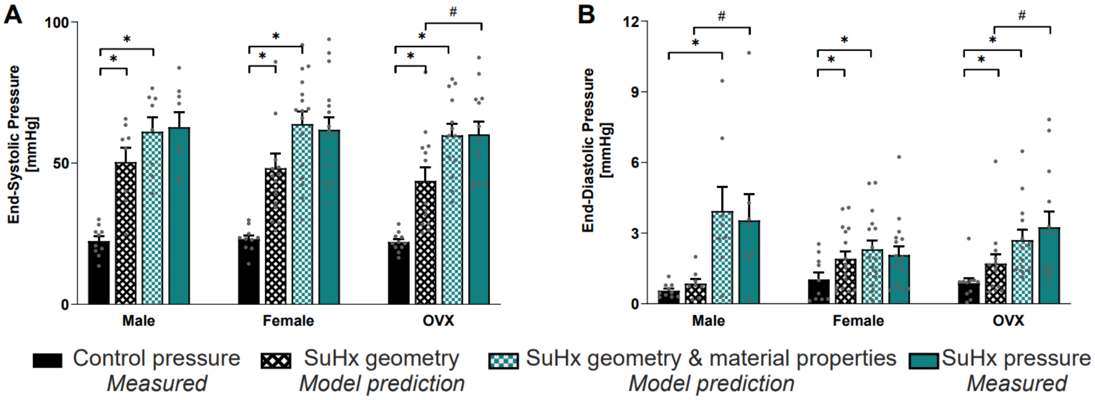

Figure 4.10. The relative contributions of changes in RV geometry (black, patterned) and myocardial material properties (teal, patterned) to changes in ES pressure (**A**) and ED pressure (**B**) were distinguished using the model. Increases in ES pressure were largely explained by RV wall hypertrophy in both male and female rats with contributions from contractility recruitment that were significant in OVX female rats. Increases in ED pressure were primarily due to myocardial material stiffening in male rats. Conversely, geometric remodeling was a contributor in both ovary-intact and OVX female groups in addition to material properties, but stiffening was much less pronounced in ovary-intact females. Figure 4.10. is a reproduction in part of data published in the American Journal of Physiology. doi: 10.1152/ajpheart.00098.2024. Epub 2024 Jul 15. PMID: 38847755.

Sarcomere length-tension relations

The rat-specific model fits were subsequently used to predict the myocardium mechanical properties via sarcomere length-tension relations. The model predicted significant increases in the passive stress-sarcomere length relation due to SuHx in all three groups ($p < 0.001$, Fig 4.11) with the stiffening being the most pronounced in the male SuHx group (Fig. 4.11A). The increase in passive stress corresponds to passive myocardial stiffening. While the slope of the active stress-sarcomere length increased due to SuHx in all groups ($p < 0.001$), the difference between active stresses was only significant in the OVX SuHx group ($p < 0.05$). This was partially explained by the OVX rats demonstrating lower active stresses at baseline relative to the male or female group. The increase in active stress-sarcomere length-relations in the OVX group alone indicates increased myocardial contractility (Fig. 4.11C).

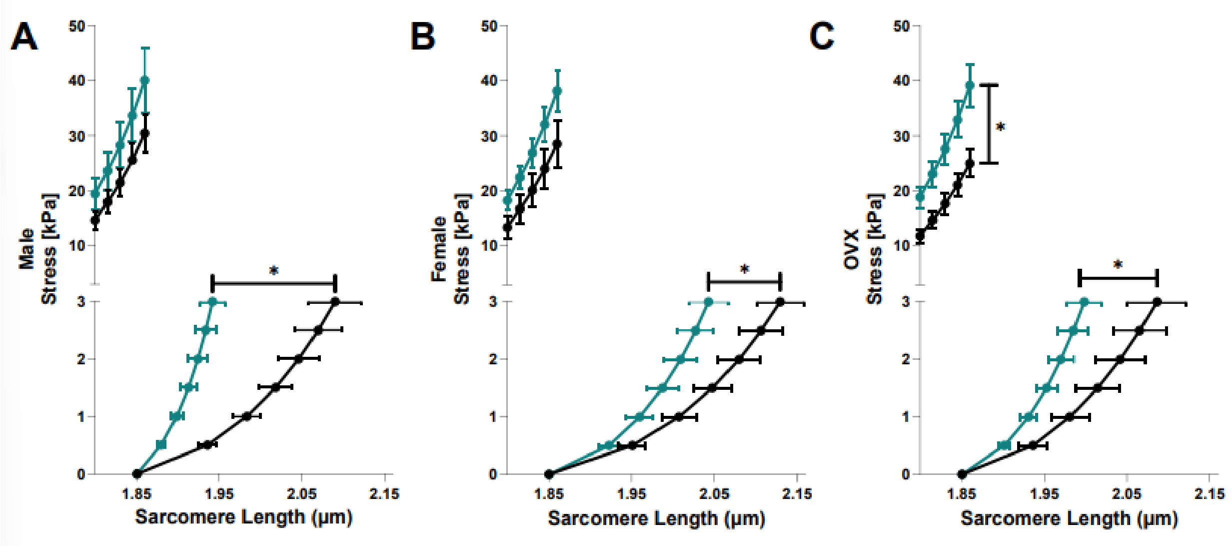

Figure 4.11. Model predicted sarcomere length-tension relations in control (black) and SuHx (teal) animals. The model predicted significant passive myocardial stiffening in SuHx-treated male (**A**), female (**B**), and ovariectomized female rats (**C**) with the most severe stiffening in male SuHx. While the slopes of the active length-tension relation increased in all SuHx groups, only the OVX group showed significant differences in active tension. $*p < 0.05$ compared with control group. Model predictions were based on data from control (10 male, 10 female, and 8 OVX) and SuHx (8 male, 13 female, and 10 OVX) rats. Figure 4.11. is a reproduction in part of data published in the American Journal of Physiology. doi: 10.1152/ajpheart.00098.2024. Epub 2024 Jul 15. PMID: 38847755.

Increases to myocardial wall stiffness were most severe in male PAH but were not enough to fully eliminate increases to ED fiber stress, which still showed a 6-fold increase in males (Fig. 4.12). By contrast, the ED fiber stress in both female and OVX female groups was completely tempered by the combination of geometric and material changes, showing only a 0.25kPa increase in female SuHx and a 0.014kPa increase in OVX SuHx compared to a 2.3kPa increase in male SuHx (Table 4.8).

Table 4.8. Wall stresses calculated for control and SuHx rats show that ED fiber stress significantly increased in the male SuHx group but not the female and OVX female groups. Conversely, ES fiber stress showed similar increases in all three SuHx groups.

	Male	***Female***	***OVX Female***
Control geometry and control mechanics			
ED fiber strain	1.041	1.056	1.060
ED fiber stress, kPa	0.436	0.879	1.040
ES active fiber strain	0.998	1.004	1.008
ES active fiber stress, kPa	13.654	13.847	14.956
SuHx geometry and SuHx mechanics			
ED fiber strain	1.0345	1.049	1.042
ED fiber stress, kPa	2.7189	1.126	1.054
ES active fiber strain	1.0158	1.011	1.010
ES active fiber stress, kPa	26.011	24.988	23.164

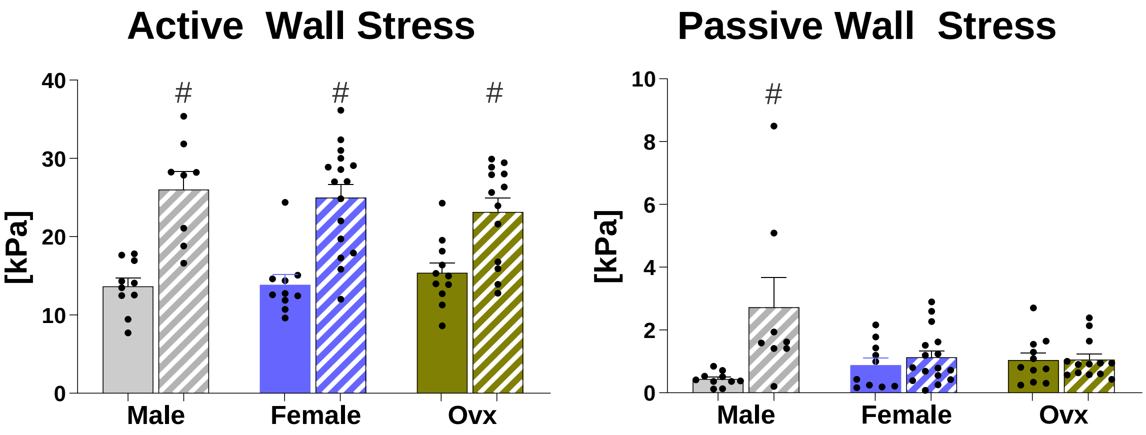

Figure 4.12. Active and passive wall stresses were computed at the average end-systolic and end-diastolic point for each group. While active wall stresses significantly increased in all groups, increases to passive wall stress were significant only in male SuHx.

4.4 Discussion

In this chapter we presented a mathematical framework for describing right ventricular biomechanics, particularly in the setting of the PAH-remodeled RV. We adapted a Laplace-type model of RV biomechanics with three material parameters. We optimized our model parameters to match experimental RV data, first in a study across longitudinal PAH timepoints and second in a study of sex-differences in PAH. When comparing the effect of sex-differences, our model provided novel insights in differential remodeling underlying systolic and diastolic RV function. Despite similarities in RV end-systolic chamber pressure and mean pulmonary arterial pressures, the adaptation of the myocardial mechanical properties in response to pressure overload was distinct depending on sex and the presence or absence of ovaries.

4.4.1 Model Analysis Insights into Longitudinal Right-Ventricular Changes

In the longitudinal study of RV remodeling, our results indicated there was an initial decrease in ejection fraction by week 4 with no significant changes in the ES PV relation. Pressure-volume analysis explained this decrease by the increased end-systolic volume due to the observed increase in RV end-systolic pressure. Ejection fraction and end-systolic volumes stabilized after week 4 despite further substantial increases in RV ES pressures (from 48±5 mmHg at week 4 to 74±8 mmHg at week 10). Our model analysis showed that this preservation of systolic function was due to increasing E_{es} that was primarily attributable after week 5 to continued RV hypertrophy rather than recruitment of myofilament activation. From the model equations, this effect was due to the increase in RV wall thickness to radius ratio, corresponding to the observed increase in RV mass to volume ratio from 3.4 mg/ul at week 4 to 4.3 mg/ul by week 10. End-systolic active fiber stress almost doubled by week 3 and remained essentially unchanged thereafter. In contrast, if RV geometry had not remodeled, end-systolic fiber stress would have tripled by week 10 (Fig x). Therefore, the stabilized response of RV systolic function to pulmonary arterial pressure overload after week 4 was primarily due to RV hypertrophy with only transient changes in myofiber contractility in the ten-week time-course of this study.

This result may reflect a recruitment of myocyte contractility in compensated PAH but did not eliminate the possibility that RV hypertrophy or dysfunction in the control group may have depressed myocyte force generation. In human skinned cardiomyocytes isolated from PAH patients, Rain *et al.*[10] measured greater maximal active tension development, but no change in myofilament calcium sensitivity or length-dependent activation compared with cells from patients suspected of PAH but confirmed with normal pulmonary pressures after right-heart catheterization. Hsu *et al.*[11] compared myocyte contractility in patients with severe systemic sclerosis–associated PAH and patients with less severe idiopathic PAH. Skinned myocytes from idiopathic PAH patients had significantly greater maximal steady-state tension development than control myocytes, but those from systemic sclerosis-associated PAH patients generated significantly lower maximal force. These findings are consistent with our observation of a transient increase in myofilament activation at week 5 and with the interpretation that RV myocytes can recruit myofilament force generation in response to RV pressure overload but may not be able to maintain this contractile upregulation indefinitely. Wang *et al.*[12] reported a similar time-course of changes in RV systolic function over 8 weeks in a sugen-hypoxia *mouse* model of PAH. They reported no changes in crossbridge kinetics or sarcomere length-dependent myofilament activation in skinned trabeculae from these animals. While our model predictions of sarcomere length-dependent tension development did not fall significantly below control during the ten-week study, it is possible that a downregulation of myocyte force development may occur later as seen in more severe PAH patients[11]. Although other studies have also reported decreased RV systolic function in small animal models of pulmonary hypertension, there have not been enough long-term studies in SuHx rats to conclude whether or when they decompensate and fail.

Although RV hypertrophy did not contribute significantly to increased end-diastolic chamber stiffness, it was important for reducing end-diastolic stress in the free wall. In fact, without the observed RV geometric remodeling, the model showed that RV ED fiber stress would have been substantially greater. Hence, while changes in passive material properties were primarily responsible for preventing increased RV ED volumes during PAH, geometric remodeling acted primarily to limit increased fiber stress.

In a follow-up study with collaborators Odeigah *et al.* at Simula - University of Oslo, our experimental data was integrated into a finite element biventricular model to similarly investigate the evolution of RV biomechanics[13], described in detail in the supplemental section of Chapter 4.7. In the experimental design of Odeigah *et al.*, experimental data collected from the study described in Chapter 2 was compared at the SuHx Week 4, 8, and 12 timepoints. The analysis of Odeigah *et al.* revealed that RV wall thickening dominated the ED and ES fiber stress and strain responses, with an additional contribution from material myocardial properties to ED fiber strain. These results are consistent with our own, highlighting the role of rapid and significant RV hypertrophy in reducing wall stress, strain, and stabilizing the ejection fraction. Notably, these contributions were maintained through all longitudinal timepoints (10 weeks in our study and 12 weeks in the study of Odeigah *et al*.). The biventricular model also revealed a large transmural fiber stress gradient at ED and at ES that progressed with the weeks of SuHx treatment[13]. These results are consistent with the findings of Avazmohammadi *et al,* who reported an increase in the transmural wall stress[14]. In their study, a PAH-induced realignment of RV free wall myofibers was a key contributor to these changes in transmural wall stress distributions. Correlations between the partial adaptive restoration of RV wall stress in PAH and the re-orientation of RV myofibers has been previously found[15,16]. These results suggest that the relation between the hypertensive pressure overload in the RV chamber and the distributions of wall stress in the significantly thickened RV wall may be an important link to region-specific RV remodeling and long-term dysfunction. In addition, the results of Odeigah *et al.* demonstrate a progressive flattening of the RV septum, revealed by the 3D biventricular model. These longitudinal findings reveal that the RV shape does still change in male SuHx rats, further underscoring the magnitude of the sex-dependent RV shape changes described in Chapter 3, whereby females and OVX female rats demonstrated far greater RV shape change than male rats treated with SuHx. These findings are not inconsistent and taken altogether, suggest that RV geometric remodeling in response to pressure overload can be a mediator of RV wall stress or contribute to alterations in systolic and diastolic function in the long-term.

The longitudinal male study revealed that the passive stiffening secondary to thickening prevented RV dilation but also prevented potential adaptive gain of function, similar to left-sided diastolic dysfunction in heart failure with preserved ejection failure[17]. Moreover, our computational model analysis revealed the contributions of underlying biomechanical and structural changes to the RV to systolic and diastolic organ function. These contributions were dynamic over the range of timepoints studied and revealed previously unknown patterns of hypertrophic and mechanical alterations. These findings also suggest diastolic stiffness as an independent predictive biomarker for determining which patients respond to therapeutic unloading of the RV[18].

4.4.2 Sex Differences in Patients with PAH

Several studies have indicated that women with PAH often exhibit a less pronounced reduction in ejection fraction compared to men with PAH, even with similar RV afterload.[19,20] In our study, no significant differences in ejection fraction were found between groups, although male and OVX SuHx groups showed a decline in ejection fraction that was 1.5 times greater (over 2 times in the male group) greater than the decline observed in the female group. However, none of the SuHx groups had an ejection fraction below 50%. Changes to ejection fraction observed in this study are consistent with previous reports in similar male rat SuHx models.[21,22] Although female patients with PAH may tolerate RV pressure overload for a longer duration, they may experience more severe RV impairment at the end-stage of the disease,[23] as observed in a Dutch PAH cohort by van Wezenbeek *et al*.. Interestingly, post-menopausal women in this cohort demonstrated preserved RV function prior to adverse events, indicating that this prolonged period of tolerated RV pressure-overload may occur independently of menopausal status, although this finding may be confounded by other age-related comorbidities. Tello *et al.* recently investigated sex differences in ventricular-vascular coupling in patients with PAH and found that women with PAH had improved ventricular-vascular coupling than men with PAH, despite similar RV afterload parameters, pulmonary arterial pressure and resistance, and RV chamber volumes.[24] Similarly, sex differences in survival were linked to improved systolic function and RV-PA coupling in women with CTEPH.[25] In our study, no differences in ventricular-vascular coupling were observed between groups or due to SuHx, and the E_{es}/E_a ratio remained within the healthy coupling ratio of 1.1-1.5.[26] Nevertheless, our findings are consistent with clinical reports, highlighting sex-dependent RV adaptations that occur independently of RV afterload.

RV diastolic stiffening (E_{ed} increase) is known to be a strong prognostic indicator for patients with PAH.[10,27] However, the relationship between diastolic stiffening and systolic output is complex and influenced by various factors such as RV loading conditions, RV wall thickness, myocardial fibrosis, and myocyte properties. Studies by Trip *et al.* and Vanderpool *et al.* have emphasized the importance of E_{ed} as an early predictor of therapeutic response in advanced PAH and as a potential mediator of age-related differences in PAH prognosis.[27,28] E_{ed} alterations are suggested to improve stroke volume by restoring the Frank-Starling volume reserve independently of contractility recruitment.[28,29] Additionally, diastolic stiffening may serve as an adaptive mechanism that helps prevent or delay RV dilation and dysfunction.[9]

However, the relationship between sex and diastolic stiffening in the RVs of patients with PAH remains unclear. Previous studies investigating diastolic stiffening in patients with PAH either did not examine sex differences or found no significant differences.[10,23,27,28] In our study, we observed increased end-diastolic chamber elastance in male and female (both ovary-intact and OVX) SuHx rats, with the most severe myocardial stiffening in male SuHx rats. Thus, we provide novel evidence of sex differences in RV diastolic stiffening and myocardial passive diastolic stiffening in the remodeled RV. When the RV myocardium is tested *ex vivo* via planar biaxial loading, significant stiffening was found in SuHx-treated animals, with the most pronounced stiffening in males and the least in females.[30,31] Conversely, Cheng *et al*. reported diastolic stiffening without sex differences in a pressure overload murine model.[32] These discrepancies may be attributed to the specific animal model or stage of the disease. It is very likely that diastolic stiffening in PAH is a dynamic process that evolves over time, even during the early-stage of compensated RV remodeling.[9] Therefore, additional studies on diastolic function in PAH, particularly with respect to age and sex, are warranted.

4.5 Conclusion

In this chapter, we described a mathematical and computational framework to characterize the remodeling of the biomechanics of the right ventricle in both systole and diastole. We subsequently applied this modeling framework to experimental data in two different studies. First, in a longitudinal study of male SuHx rats, our model analysis revealed that systolic ventricular function was stabilized by hypertrophic wall thickening, with only transient changes in myofiber contractility, whereas end-diastolic chamber stiffness was explained by myocardium passive stiffening. This previously unrecognized sequence by which rapid hypertrophy stabilized systolic function and was followed by myocardial stiffening reveals the robust RV changes underlying a largely compensated stage of RV function. We then applied this model analysis to study sex-differences in end-systolic and end-diastolic chamber mechanics. Model analysis revealed that passive myocardial stiffening was present in all SuHx groups, most severe in the male. In the OVX group, stiffness was not sufficient to prevent diastolic volume increases and myofiber contractility recruitment was upregulated in ovariectomized female SuHx alone. The ovary-intact female rats responded to pressure overload mainly through hypertrophy, with fewer alterations to myocardial mechanics and the least passive stiffening. These differences may explain differences in long-term RV function.

4.6 Acknowledgements

Chapter 4, in part, is a reprint of the material as it appears in Distinct Time Courses of Right Ventricular Hypertrophy and Diastolic Stiffening in a Male Rat Model of Pulmonary Arterial Hypertension. Kwan, Ethan D.; Velez-Rendon, Daniela; Zhang, Xiaoyan; Mu, Hao; Patel, Megh; Pursell, Erica; Stowe, Jennifer; Valdez-Jasso, Daniela. American Journal of Physiology Heart and

Circulatory Physiology. 2021. The dissertation author was the primary investigator and author of this paper.

Chapter 4, in part, is a reprint of the material as it appears in Sex-dependent Remodeling of Right-Ventricular Function in a Rat Model of Pulmonary Arterial Hypertension. Kwan, Ethan D.; Hardie, Becky A.; Garcia, Kristen M.; Mu, Hao; Wang, Tsui-Min; Valdez-Jasso, Daniela. American Journal of Physiology Heart and Circulatory Physiology. 2024. The dissertation author was the primary investigator and author of this paper.

Chapter 4, in part, is a reprint of the material as it appears in A Computational Study of Right Ventricular Mechanics in a Rat Model of Pulmonary Arterial Hypertension. Odeigah, Oscar O.; Kwan, Ethan D.; Garcia, Kristen M.; Valdez-Jasso, Daniela; Sundnes, Joakim. Frontiers in Physiology. 2024. The dissertation author was the second author of this paper.

4.7 References

1. Vélez-Rendón D, Zhang X, Gerringer J, Valdez-Jasso D. Compensated right ventricular function of the onset of pulmonary hypertension in a rat model depends on chamber remodeling and contractile augmentation. *Pulm Circ*. 2018;8(4):1-13.

2. Guccione JM, McCulloch AD. Mechanics of actiwe contraction in cardiac muscle: Part I—constitutive relations for fiber stress that describe deactivation. *J Biomech Eng*. 1993;115(1):72-81.

3. Yipintsoi T, Scanlon PD, Bassingthwaighte JB. Density and Water Content of Dog Ventricular Myocardium. *Proc Soc Exp Biol Med*. 1972;141(3):1032-1035.

4. Guccione JM, Waldman LK, McCulloch AD. Mechanics of actiwe contraction in cardiac muscle: Part II—cylindrical models of the systolic left ventricle. *J Biomech Eng*. Published online 1993.

5. Hill AV. The heat of shortening and the dynamic constants of muscle. *Proc R Soc Lond Ser B - Biol Sci*. 1997;126(843):136-195.

6. Zhang X, Haynes P, Campbell KS, Wenk JF. Numerical Evaluation of Myofiber Orientation and Transmural Contractile Strength on Left Ventricular Function. *J Biomech Eng*. 2015;137(4):044502.

7. Vonk-Noordegraaf A, Westerhof N. Describing right ventricular function. *Eur Respir J*. 2013;41(6):1419-1423.

8. Lee LC huan, Zhihong Z, Hinson A, Guccione JM. Reduction in left ventricular wall stress and improvement in function in failing hearts using Algisyl-LVR. *J Vis Exp JoVE*. 2013;74:50096.

9. Kwan ED, Velez-Rendon D, Zhang X, et al. Distinct time courses and mechanics of right ventricular hypertrophy and diastolic stiffening in a male rat model of pulmonary arterial hypertension. *Am J Physiol - Heart Circ Physiol*. Published online 2021.

10. Rain S, Handoko ML, Trip P, et al. Right ventricular diastolic impairment in patients with pulmonary arterial hypertension. *Circulation*. 2013;128(18):2016-2025.

11. Hsu S, Kokkonen-Simon KM, Kirk JA, et al. Right ventricular myofilament functional differences in humans with systemic sclerosis-associated versus idiopathic pulmonary arterial hypertension. *Circulation*. 2018;137(22):2360-2370.

12. Wang Z, Patel JR, Schreier DA, Hacker TA, Moss RL, Chesler NC. Organ-level right ventricular dysfunction with preserved Frank-Starling mechanism in a mouse model of pulmonary arterial hypertension. *J Appl Physiol*. 2018;124(5):1244-1253.

13. Odeigah OO, Kwan ED, Garcia KM, Finsberg H, Valdez-Jasso D, Sundnes J. A computational study of right ventricular mechanics in a rat model of pulmonary arterial hypertension. *Front Physiol*. 2024;15.

14. Avazmohammadi R, Mendiola EA, Li DS, Vanderslice P, Dixon RAF, Sacks MS. Interactions Between Structural Remodeling and Hypertrophy in the Right Ventricle in Response to Pulmonary Arterial Hypertension. *J Biomech Eng*. 2019;141(9):910161-910613.

15. Avazmohammadi R, Hill M, Simon M, Sacks M. Transmural remodeling of right ventricular myocardium in response to pulmonary arterial hypertension. *APL Bioeng*. 2017;1(1):016105.

16. Mendiola E, Da D, Gonçalves S, et al. Right Ventricular Architectural Remodeling and Functional Adaptation in Pulmonary Hypertension. *Circ Heart Fail*. Published online February 7, 2023.

17. Golla MSG, Shams P. Heart Failure With Preserved Ejection Fraction (HFpEF). In: *StatPearls*. StatPearls Publishing; 2024.

18. Walker M, Moore H, Ataya A, et al. A perfectly imperfect engine: Utilizing the digital twin paradigm in pulmonary hypertension. *Pulm Circ*. 2024;14(2):e12392.

19. Jacobs W, Van De Veerdonk MC, Trip P, et al. The Right Ventricle Explains Sex Differences in Survival in Idiopathic Pulmonary Arterial Hypertension. *Chest*. Published online 2014.

20. Swift AJ, Capener D, Hammerton C, et al. Right Ventricular Sex Differences in Patients with Idiopathic Pulmonary Arterial Hypertension Characterised by Magnetic Resonance Imaging: Pair-Matched Case Controlled Study. *PLOS ONE*. 2015;10(5):e0127415.

21. Jayasekera G, Wilson KS, Buist H, et al. Understanding longitudinal biventricular structural and functional changes in a pulmonary hypertension Sugen–hypoxia rat model by cardiac magnetic resonance imaging. *Pulm Circ*. 2020;10(1):1-11.

22. Vanderpool RR, Gorelova A, Ma Y, et al. Reversal of Right Ventricular Hypertrophy and Dysfunction by Prostacyclin in a Rat Model of Severe Pulmonary Arterial Hypertension. *Int J Mol Sci*. 2022;23(10):5426.

23. van Wezenbeek J, Groeneveldt JA, Llucià-Valldeperas A, et al. Interplay of sex hormones and long-term right ventricular adaptation in a Dutch PAH-cohort. *J Heart Lung Transplant*. 2022;41(4):445-457.

24. Tello K, Richter MJ, Yogeswaran A, et al. Sex Differences in Right Ventricular–Pulmonary Arterial Coupling in Pulmonary Arterial Hypertension. *Am J Respir Crit Care Med*. 2020;202(7):1042-1046.

25. Barco S, Klok FA, Konstantinides SV, et al. Sex-specific differences in chronic thromboembolic pulmonary hypertension. Results from the European CTEPH registry. *J Thromb Haemost*. 2020;18(1):151-161.

26. Lahm T, Douglas IS, Archer SL, et al. Assessment of Right Ventricular Function in the Research Setting: Knowledge Gaps and Pathways Forward. An Official American Thoracic Society Research Statement. *Am J Respir Crit Care Med*. 2018;198(4):e15-e43.

27. Trip P, Rain S, Handoko ML, et al. Clinical relevance of right ventricular diastolic stiffness in pulmonary hypertension. *Eur Respir J*. 2015;45(6):1603-1612.

28. Vanderpool RR, Hunter KS, Insel M, et al. The Right Ventricular-Pulmonary Arterial Coupling and Diastolic Function Response to Therapy in Pulmonary Arterial Hypertension. *Chest*. 2022;161(4):1048-1059.

29. Ait-Mou Y, Hsu K, Farman GP, et al. Titin strain contributes to the Frank–Starling law of the heart by structural rearrangements of both thin- and thick-filament proteins. *Proc Natl Acad Sci*. 2016;113(8):2306-2311.

30. Hardie BA, Huberts J, Valdez-Jasso D. Right Ventricular Myocardium Remodeling in Pulmonary Arterial Hypertension is Sex-Specific and Ovarian Hormone-Dependent. In: ; 2023.

31. Vélez-Rendón D, Pursell ER, Shieh J, Valdez-Jasso D. Relative Contributions of Matrix and Myocytes to Biaxial Mechanics of the Right Ventricle in Pulmonary Arterial Hypertension. *J Biomech Eng*. 2019;141(9):091011.

32. Cheng TC, Tabima DM, Caggiano LR, et al. Sex differences in right ventricular adaptation to pressure overload in a rat model. *J Appl Physiol*. 2022;132(3):888-901.

Chapter 5 REMODELING OF RIGHT VENTRICULAR MYOCYTE MECHANICS IN PULMONARY ARTERIAL HYPERTENSION

5.1 Introduction

Excitation-Contraction Coupling in Pulmonary Hypertension

Important differences in incidence and response based on sex have been described in patients with pulmonary arterial hypertension. These differences in patient outcomes may be attributed, at least in part, to sex-differences in the structure and function of the RV, the most critical determinant of survival in PAH[1]. Given these differences, alongside the sex-differences characterized in Chapters 3 & 4, the question arises whether the cardiac myocyte cell unit themselves demonstrate differences in the response to PAH. Acknowledging the important regulatory, protein synthesis, cell signaling, and passive mechanical and structural role that all cells provide, the primary function of the cardiomyocyte is its role in shortening and generating contractile force in support of systolic cardiac function and its lusitropic role in support of diastolic function. These differences may include variations in mechanical properties such as the intrinsic ability to generate force and contractile reservoir that may be recruited to adapt against pressure overload.

Experimental studies have investigated whether sex differences in the ability of isolated cardiomyocytes to contract contribute towards differences in organ-level cardiac function. These results have often been conflicting and highly dependent on the species, strain, preparation, isolation technique, and experimental parameters. Key species differences in cardiac action potential and membrane currents exist. Rabbit models of ion channel function, repolarization, and arrhythmia are well characterized and resemble human electrophysiology, but may not develop robust pulmonary hypertension compared with rats[2]. While mice and rats are widely used in RV studies, they have a low action potential plateau (-40mV membrane potential), in contrast to rabbits and guinea pigs that have more similar action potential plateaus to humans, but whose [3,4]. Farrell *et al.* reported that peak contractions are significantly smaller in female rat ventricular myocytes compared to cells from males[5]. This finding supported some previous studies in Fischer and Wistar rats[6,7], which generally showed a decrease in the contractile shortening of cardiac myocytes isolated from females compared to males. By contrast, Vizgirda *et al.* found no differences in the peak contraction between isolated male and female rat ventricular myocytes[8]. Schwertz *et al*. found contractile shortening was increased in isolated female rat myocytes compared to males, a difference that was negated by increasing extracellular calcium[9].

Previous work has been done investigating the mechanisms underlying differences in myocyte contractile function in health and in various cardiovascular diseases. Changes to calcium cycling over the cardiac cycle are of high interest due to the fundamental relationship between myocyte contraction and calcium[5,10]. Most changes to the intracellular calcium concentration can be attributed to the release of stored calcium in the intracellular sarcoplasmic reticulum (SR) into the intracellular space during systole and the subsequent re-sequestration of calcium back into the SR during diastole. Previous studies have reported that increased contraction in male hearts may be explained by increased peak calcium transients in male hearts compared to female hearts. This finding of smaller calcium transient amplitudes in female rat myocytes compared to males has been shown by many studies of field stimulated ventricular myocytes[6,11,12]. By contrast, other others have reported that calcium transient amplitudes are not dependent on sex[7,13].

These results demonstrate a lack of consensus regarding sex-differences in cardiomyocyte contractile properties at baseline, let alone in the pathologically remodeled RVs of pulmonary arterial hypertension. Additionally, key differences in cardiomyocyte properties may differentially contribute towards the holistic myocyte contractility in healthy cells compared to cells isolated from pathologically challenged RVs. Even in reports where contractile function appears unchanged by sex in healthy hearts, sex-differences in the contractile reserve or the capability to recruit additional contractile force may exist that become relevant in the PAH-challenged RV[5].

Changes to the right ventricular myocyte and myocyte-level mechanical properties have been described in PAH. Frequently, fiber and myocyte-level mechanical properties are characterized by direct measurements of isolated skinned RV trabeculae or papillary muscles in preparations that involve chemical permeabilization of cell attachments, thereby approximating myocyte mechanics in the absence of extracellular matrix mechanical contributions. In a study of mice treated with 2-4 weeks of sugen-hypoxia, Wang et al suggested that impairment of myocyte-level function occurs subsequent to organ-level dysfunction, by which organ-level contractility increased after two weeks of PAH, but myofilament contractile forces were similarly elevated at all stages of disease (with preserved Frank-Starling mechanisms) implying the RV dysfunction occurred prior to and was not explained by myocyte dysfunction[14]. In skinned isolated rat myocytes isolated from pressure overloaded RVs with hypertrophy, maximal myocyte force was increased, but maximal tension was reduced, with a decrease in calcium sensitivity in the hypertrophied group[15]. Changes in myocyte contractility may contribute to alterations in systolic organ function, or they may not be significant contributors to organ-level contractility compared to other alterations such as reorientation of RV myofibers, as Avazmohammadi *et al.* reported[16]. Myocyte Ca^{2+} activated peak tension has been shown to increase in clinical and pre-clinical studies of PAH[14,17]. While it is likely that the recruitment of myocyte contractility may serve as an adaptive mechanism, particularly in the early stages of PAH, the relationship between myocyte contractility and systolic function remains unclear. It has been reported that elevated myocyte contractile function may remain maintained even as RV organ-level function begins to decline[14], both suggesting that systolic function is not solely explained by myocyte contractility changes and that impairment of organ function may itself lead to further myocyte level contractility dysfunction[18]. Additionally, it has been widely reported that myocyte contractile dysfunction is a component of the progression of PAH, particularly in later stages of RV dysfunction[15,19,20]. While myocyte peak tension may be transiently upregulated in response to pressure overload, declines in myofiber peak tension development have been found about 250 days of pulmonary arterial banding, associated with reduced calcium sensitivity[15]. These changes are consistent with the finding of decreased calcium sensitivity due to alterations in the phosphorylation of contractile proteins such as troponin, a key regulator of calcium and activator of myosin ATPase[21], as well as myosin heavy chain[22], a key regulator of myosin-actin cross-bridge cycling that results in myocyte contraction[23]. Andersen et al reported differences in both the phosphorylation of myosin heavy chain and the primary myosin heavy chain isoform expressed in PAH rats that was associated with a reduction in myocyte contraction[22]. These changes match reports in MCT-treated rats that also demonstrated reduced contractile shortening associated with changes in myosin heavy chain isoform[24]. Changes to myocyte contractility may also differentially associated with cardiomyocyte hypertrophy depending on sex[25] and the stage of disease. While myocyte hypertrophy and cross-sectional area increases are consistently shown in experimental and clinical studies of PAH [14,17,26], the factors determining pathological recruitment of hypertrophy vs contractility remains unclear, nor is it clear how and when hypertrophic changes become insufficient to compensate cardiac demands.

5.2 Approach

To validate the finding of increased systolic elastance seen at the organ level between sex groups (presented in Chapter 4) and to validate the finding of an increase in myocardial material calcium dependent contractility, we designed a study of RV myocyte mechanics in male, female, and ovariectomized female SuHx-treated rats. Seven- and eight-week-old Sprague Dawley rats were induced with PAH using the sugen-hypoxia animal model described in Chapter 2-3. After 8 weeks of total SuHx treatment, experiments were conducted to study myocyte mechanics.

5.2.1 Right-Ventricular Cardiomyocyte Isolation

RV myocytes were isolated from ~15 week old male, female, and ovariectomized female Sprague-Dawley rats treated with 8 weeks of sugen-hypoxia to induce PAH. Hypertension status was confirmed prior to isolation by PV catheter measurements during open-chest terminal procedures. After RV pressure measurements were obtained, the hearts were immediately excised, cannulated through the aorta, and mounted on a Langendorff apparatus. The coronary vasculature was retrogradely perfused with a series of wash and digestion solutions to flush excess blood, remove fibroblast cells, and digest the ventricles. All perfusion solutions were mixed from soluble reagents at room temperature, pH balanced (pH 7.4), then heated to 37°C using thermal circulation from a heated water bath before perfusion. Digestion was achieved by serial washes of calcium-free Tyrode's solution (0.134 M NaCl, 0.00268 M KCl, 0.00556 M glucose, 0.0119 M $NaHCO_3$) totaling 3-5 minutes on average, followed by an enzymatic digestion solution (0.001 M collagenase type II, 0.0015 M protease) until the right ventricular free wall appeared digested, compliant and translucent (on average 8-12 minutes), leading to an increase in the perfusion rate.[27,28] After digestion, calcium was gradually reintroduced by perfusing Tyrode's solution with three serial dilutions of $CaCl_2$ up to 1.8 mM. The RV was isolated and separated from the septum, finely chopped, gently triturated, and manually agitated to dissociate individual cells.

The RV myocytes were then incubated in the dark at room temperature for 30 minutes in Tyrode's solution containing 2 μM of Fura 2-AM (Invitrogen, Thermo Fisher). The myocytes were subsequently seeded onto a microscopy platform and continuously superfused with Tyrode's solution containing 1.8 mM [Ca^{2+}]. Platinum electrodes were used to stimulate the isolated seeded cardiomyocytes. Biphasic squared electrical pulses (1Hz, 1ms peak width, 5-15V) were applied from an analogue output terminal. Electrodes were typically placed approximately 5-10mm from the cardiomyocytes, but myocyte seeding patterns were not controlled.

A laser scanning fluorescent photometer (Calcium and Contractility System, IonOptix, MA, USA) equipped with a 40x immersion objective was used to record fluorescence excitation wavelengths of 340 nm and 380 nm.[29] Intracellular calcium timeseries and myocyte shortening measurements were recorded using IonWizard software (IonOptix, version 6.6).

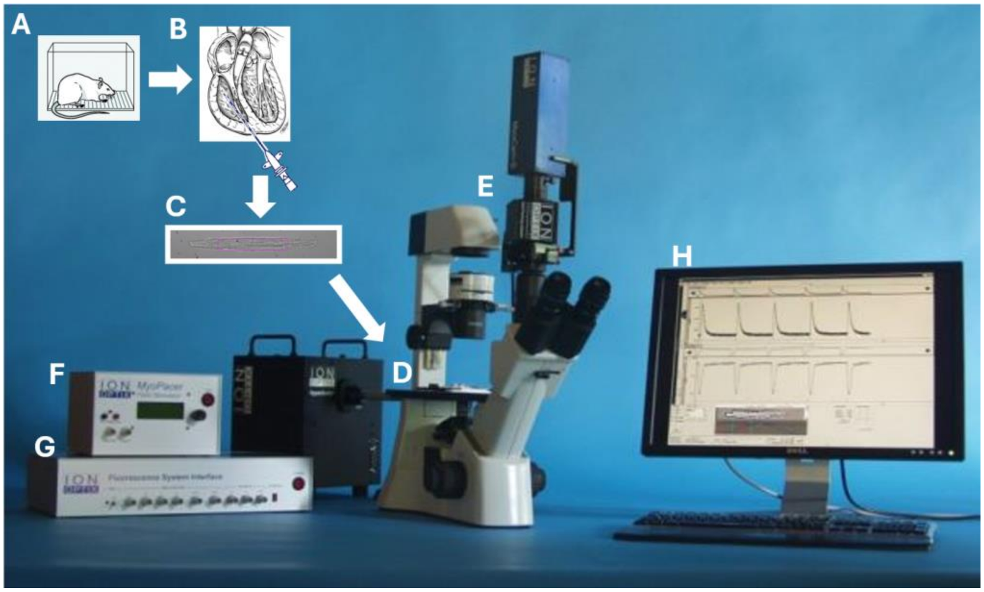

Figure 5.1. Diagram illustrating the myocyte experimental pipeline. Animals (**A**) were studied with invasive hemodynamic measurements (**B**), after which myocytes were isolated via Langendorff enzymatic digestion (**C**), then seeded onto a microscopy platform (**D**), viewed through a fluorescent 40x immersion objective lens (**E**). Myocytes were subjected to electrical field stimulation (**F**) and a laser scanning fluorescent photometer (**G**) used to record fluorescence. Sarcomere length and calcium transients were visualized using IonWizard software (**H**).

Only rod-shaped cells with clear striations, which remained quiescent without electrical stimulation and exhibited no sarcolemmal blebbing were included. Continuous timeseries of sarcomere length and fluorescence intensity lasting 10-15 seconds were recorded at 1000Hz during pacing. For each animal, 7-15 myocytes were analyzed. We decided on these values in order to obtain a thorough and representative sampling of myocyte data from each individual heart and to reduce inter-cell variability was minimized[30]. Cardiomyocyte contractile shortening was measured as the difference between diastolic sarcomere length at rest and peak sarcomere length during contraction. Fluorescence intensity signal was normalized by dividing the peak fluorescent intensity (F) by the average resting fluorescence (F_o) after background subtraction and presented as the ratio F/F_o to represent the cytosolic calcium concentration.

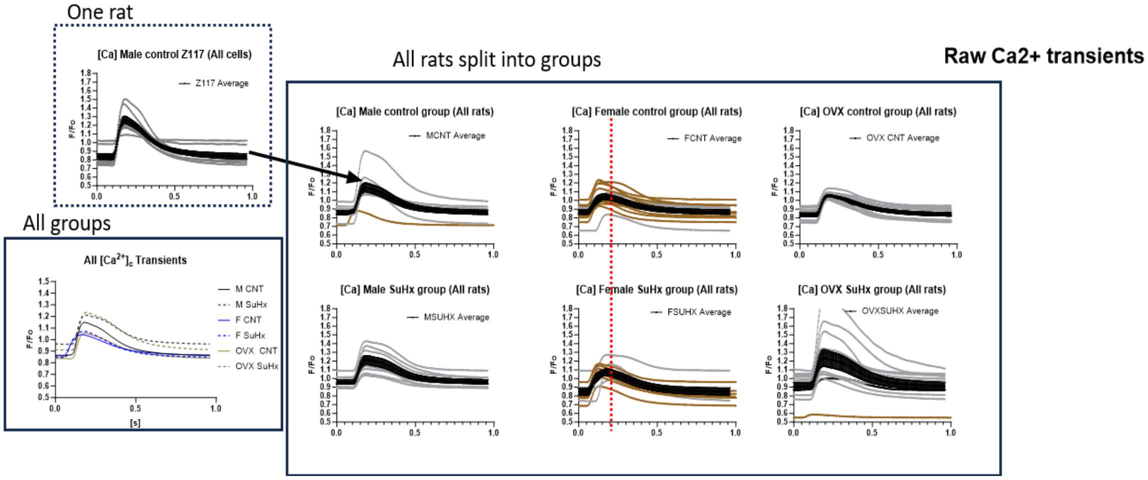

Figure 5.2. Repeated rat-specific and cell-specific measurements were represented as group measurements as indicated by the schematic. From each animal, multiple cells (typically 8-15) were measured (top left), with the mean calcium transient shown in bold. Mean calcium transients for each rat for each treatment group were peak aligned and averaged to produce a mean calcium transient representing the group (right). Group average behaviors were illustrated (bottom left).

5.2.2 Right-Ventricular Myocyte Drug Testing

The cells' electrophysiological responses to the ryanodine receptor agonist caffeine were studied. Caffeine-induced ryanodine channel opening results in a bolus release of calcium stores within the SR into the intracellular space, triggering a hyper-physiological myocyte contraction. This allowed measurement of the total calcium stored within the SR, as well the response of the myocyte to the hyper-physiological calcium release. Following measurements of steady state myocyte sarcomere shortening and calcium transients, recorded under 1Hz electric field stimulation, the electrodes were switched off. A solution containing the acute ryanodine receptor agonist caffeine was prepared by adding [60mM] caffeine to the Tyrode’s buffered solution and superfused (continuous external addition and aspiration of solution)[31]. Sarcomere length and intracellular calcium fluorescence was recorded continuously. The caffeine-induced response was quantified as the normalized calcium transient amplitude $(Ca^{2+}_{baseline}- Ca^{2+}_{peak})/ Ca^{2+}_{baseline}$, the caffeine-induced calcium transient response (ratio of normalized calcium transient amplitudes for steady state and caffeine-induced calcium transients), the caffeine-induced sarcomere shortening $(SL_{baseline} - SL_{peak})/ SL_{baseline}$ and the caffeine-induced sarcomere shortening response (ratio of sarcomere shortening for steady state and caffeine-induced sarcomere shortening).

5.2.3 Statistical Analysis

Group comparisons of myocyte mechanics were analyzed with descriptive statistics using the JMP Pro Statistical software package (version 16, SAS Institute Inc., NC, USA). For myocyte measurements, the Shapiro-Wilkes test was used to determine normality of data. Non-normally distributed data was analyzed using the Wilcoxon-Kruskal-Wallis statistic, followed by the Dunnett’s test for treatment comparisons and the Dunn test or animal group comparisons. For normally distributed data, two-way repeated measures ANOVA was used to analyze the effects of treatment (SuHx *vs* control) and group (male *vs* female *vs* ovariectomized female) on myocyte measurements. Post-hoc comparisons were performed using the Dunnett’s test for treatment comparisons and the Tukey test for animal group differences. Following two-factor ANOVA, simple main effects were analyzed with the F-statistic for group and treatment. For caffeine-treated data, normality was again assessed for each factor using the Shapiro-Wilkes goodness of fit test. Afterwards, non-normally distributed data was analyzed using the Wilcoxon-Kruskal Wallis ranked-sum statistic, followed by the Dunnet's method for control and SuHx comparisons. For all statistical tests, a p-value < 0.05 was considered statistically significant.

5.3 Results

Langendorff perfusion and enzyme digestion was successful and allowed for the isolation and testing of RV myocytes. We observed a decrease in the cell survival of all groups in animals treated with SuHx (Fig. 5.3), however for the purposes of mechanical characterization, all cells that passed the inclusion criteria were weighted equally and differences in cell survival were not considered.

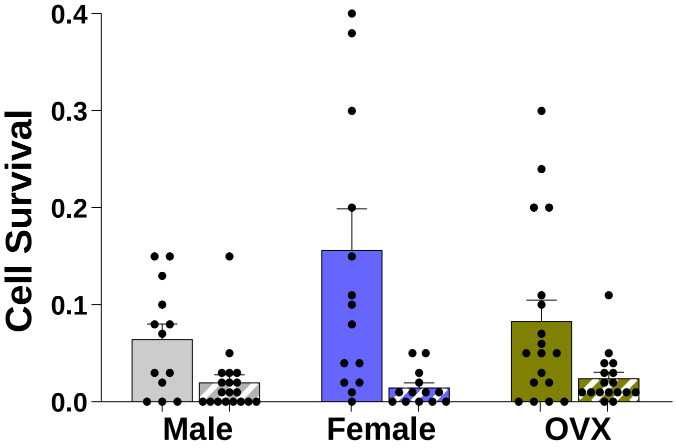

Figure 5.3. RV myocyte cell survival was determined following isolation. Across all groups, SuHx treatment resulted in decreased cell survival. Data shown as mean ± standard error.

5.3.1 Myocyte Shortening and Calcium

Isolated right ventricular myocytes from OVX female SuHx rats showed a significant increase in sarcomere shortening (Fig. 5.4D, 2.6%, $p = 0.003$). However, no significant changes were observed in the male (0.9%) or ovary-intact female SuHx groups (0.4% respectively). Two-factor ANOVA revealed significant differences between the animal groups ($p = 0.028$), but not due to treatment ($p = 0.072$), with no significant interaction effects ($F_{1,2} = 0.83$, $p = 0.44$). In male SuHx rats, changes in intracellular calcium concentration were more prominent at diastole ($p < 0.001$) rather than at peak ($p = 0.089$) calcium concentrations, resulting in a net decrease in the calcium transient amplitude (Fig. 5.4E**,** $p = 0.17$). Despite this decrease and the considerable increase to diastolic calcium in SuHx-treated male rats (Fig. 5.4A), sarcomere shortening remained elevated. In both the female ($p = 0.08$) and OVX ($p = 0.37$) SuHx groups, the calcium transient amplitude remained unchanged. However, the OVX group showed the most pronounced increase in peak intracellular calcium ($p = .0467$, Fig. 5.4C), which corresponded to the largest increase in shortening ($p = .0027$). In ovary-intact female rats, changes due to SuHx in both diastolic and peak intracellular calcium were small ($p = 0.44$), the calcium transient shape remained largely unchanged, and shortening was maintained ($p = 0.29$, Fig. 5.4B).

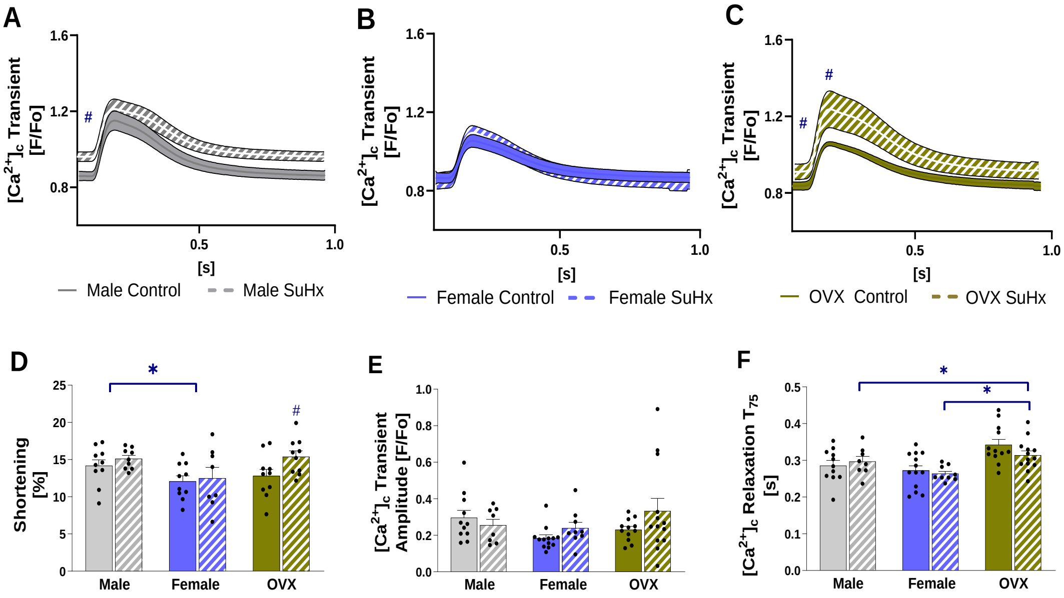

Figure 5.4. Calcium transients (**A-C**) in isolated RV myocytes derived from male (grey), ovary-intact female (blue), and ovariectomized female (green) normotensive (solid) compared with SuHx (patterned) rats. SuHx treatment increased diastolic calcium concentration in males and OVX females, and intracellular calcium in OVX females. Sarcomere shortening (**D**) increased in the OVX SuHx group, while no significant changes were observed in the male or female groups. While SuHx caused no significant changes to calcium transient amplitude (**E**), the most pronounced changes to amplitude and to peak calcium concentration (**C**) were in the OVX group. While the time to 75% reduction from peak Ca^{2+} (T_{75}) was prolonged in the OVX group compared to both male and female groups, no significant differences were observed due to SuHx treatment (**F**). *$p < 0.05$ between groups. #$p < 0.05$ compared with control group. Data shown as mean ± standard error. Measurements obtained from control (11 male, 13 female, and 12 OVX) and SuHx (11 male, 9 female, and 13 OVX) rats. Figure 5.4. is a reproduction in part of data published in the American Journal of Physiology. doi: 10.1152/ajpheart.00098.2024. Epub 2024 Jul 15. PMID: 38847755.

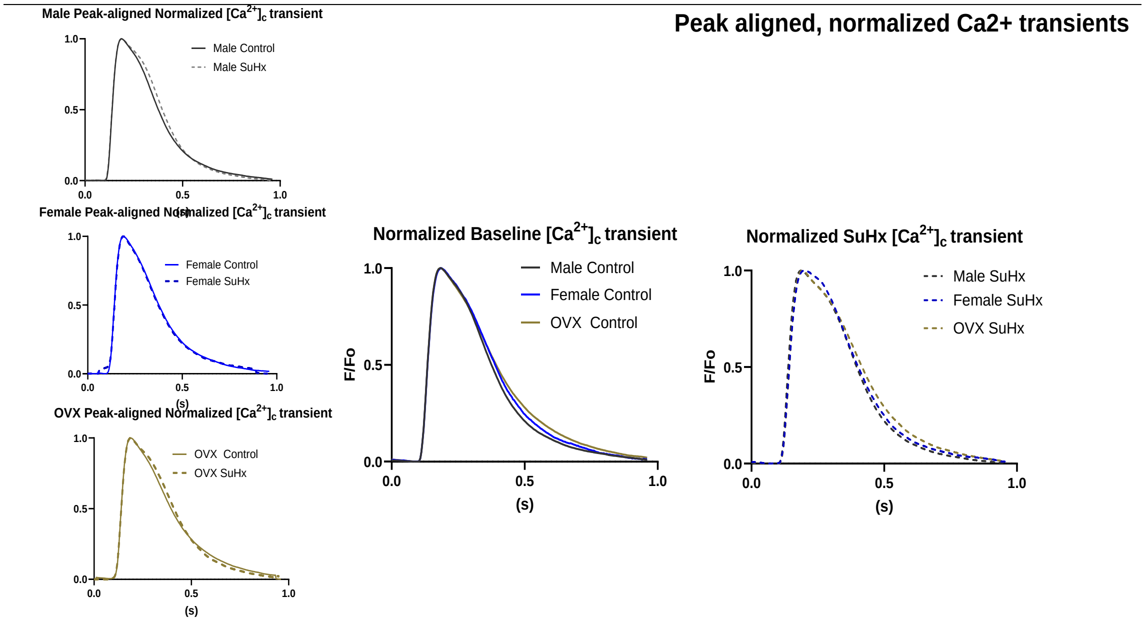

Figure 5.5. Peak-aligned and amplitude normalized calcium transients were compared for male, female, and OVX groups (left), and illustrated for baseline and SuHx groups (right). While there were no significant differences in the calcium transient shape across treatment or groups, the OVX group showed the most prolonged relaxation compared to male or ovary-intact female groups.

Amplitude-normalized calcium transients showed no significant differences in the shape across groups (Fig. 5.4). There were no significant effects of treatment on the $T_{75\%}$ calcium relaxation time ($p = 0.44$), although the OVX group showed prolonged relaxation compared to the male ($p = 0.02$) or ovary-intact female groups ($p < 0.001$, Fig. 5.5).

5.3.2 SR Calcium Load

Superfusion of caffeine resulted in the acute release of SR calcium stores into the intracellular space and triggered a large myocyte contraction. A representative response is shown in Fig. 5.6 below.

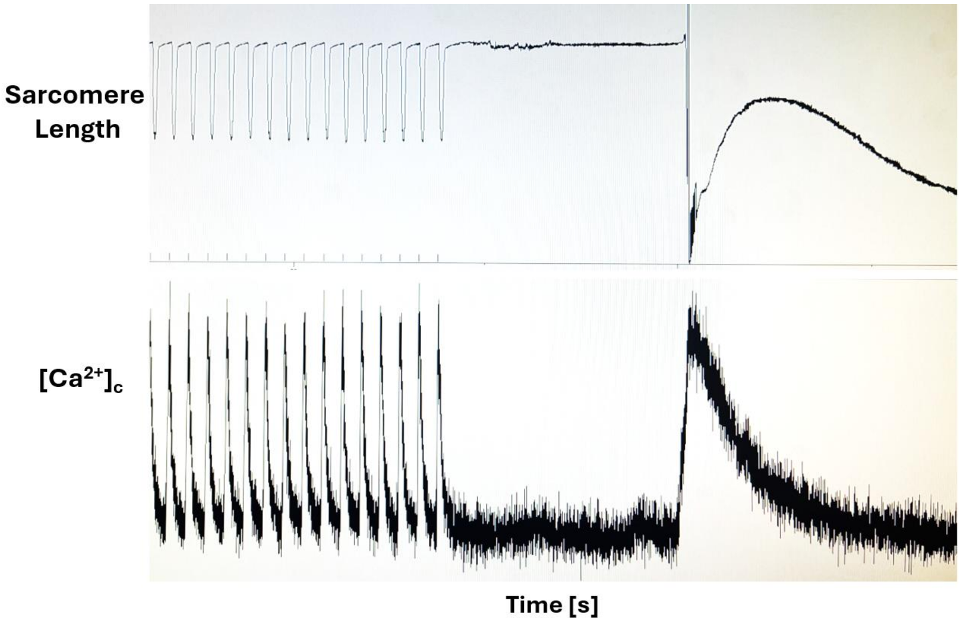

Figure 5.6. Acute administration of the drug caffeine resulted in acute complete release of the calcium reserves within the sarcoplasmic reticulum. The subsequent calcium transient profile was captured, along with the sarcomere length during contraction.

A significant increase in diastolic intracellular calcium concentration was seen in myocytes derived from SuHx-treated male and OVX rats ($p < 0.05$, Fig. 5.7). Despite the increases in diastolic calcium, the calcium transient amplitude was maintained in male SuHx and was significantly increased in OVX SuHx (Fig. 5.4E). Myocytes derived from female rats showed no changes in calcium transient amplitude nor in diastolic intracellular calcium.

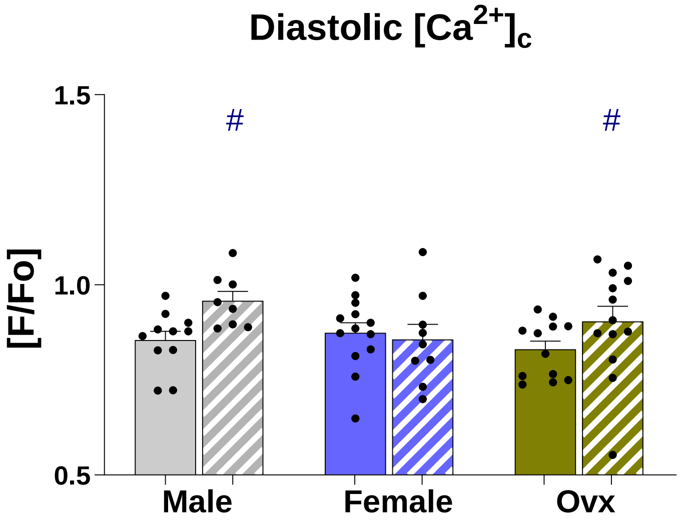

Figure 5.7. Diastolic intracellular calcium showed a significant increase in myocytes derived from SuHx treated male and ovariectomized female rats, but not in ovary-intact female rats. The increase was the greatest in male SuHx. #$p < 0.05$ compared with control group. Data shown as mean ± standard error.

Caffeine-induced sarcoplasmic reticulum calcium release revealed a significant ($p < 0.05$) decrease in the total sarcoplasmic reticulum calcium stores in myocytes from male SuHx treated rats compared to male controls (Fig. 5.8B), with a corresponding 26% decrease in the caffeine-induced normalized calcium transient amplitude for male SuHx, although this was not statistically significant ($p = 0.089$, Fig. 5.8A). Neither the female nor the OVX female group showed a change with SuHx. The decrease in total SR calcium load in male SuHx alone is consistent with the large increase in diastolic intracellular calcium seen in male SuHx. The contractile response to the caffeine-induced SR calcium release revealed a similar trend, in which SuHx treatment significantly reduced the caffeine-induced shortening only in the myocytes ($p < 0.05$) derived from the male group (Fig 5.8C-D).

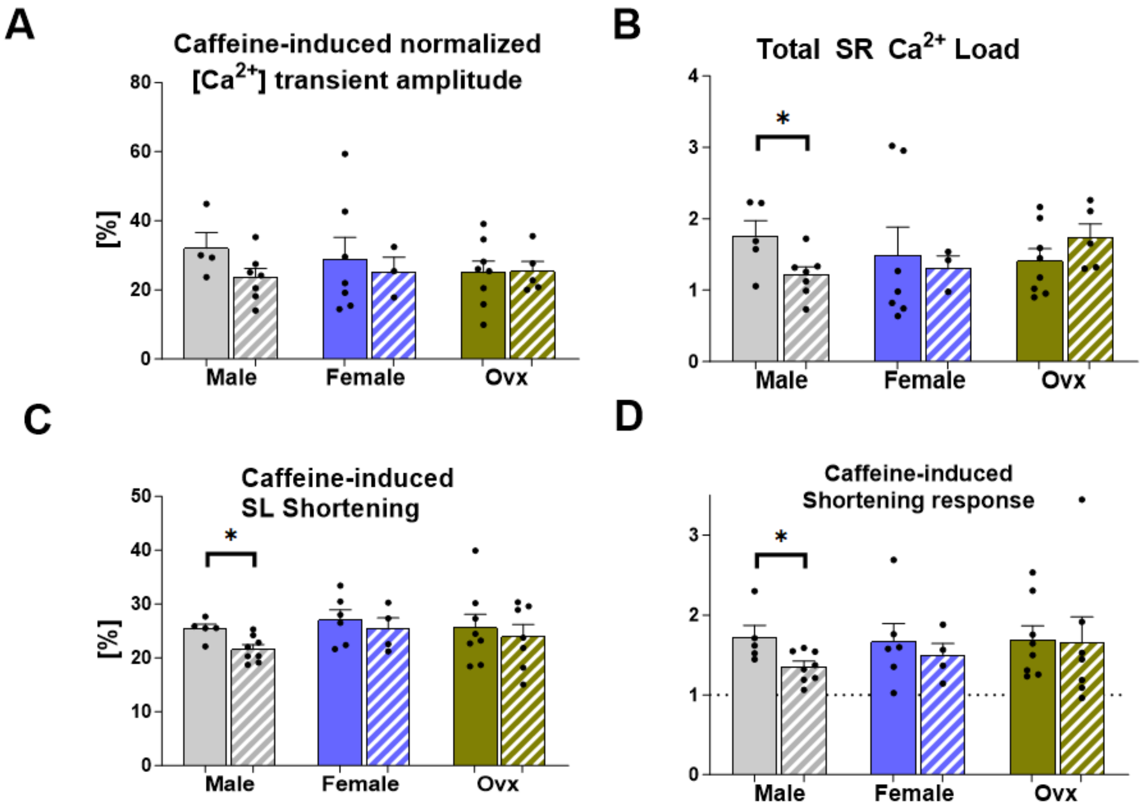

Figure 5.8. Administration of the drug caffeine resulted in acute release of SR calcium stores. The caffeine-induced calcium transient (**A**) was unchanged in all three groups, although the male SuHx group showed a 27% reduction ($p = 0.08$). The total SR calcium load (**B**) was reduced in male SuHx ($p = 0.0399$) compared to male controls alone. The contractile response to the caffeine-induced SR calcium release revealed a similar trend, in which SuHx treatment significantly reduced the caffeine-induced shortening (**C**), as well as the normalized shortening response (**D**) only in the myocytes derived from the male group. $^*p < 0.05$, data shown as mean ± standard error.

5.4 Discussion

While our study revealed greater myocyte shortening compared to some studies using similar isolated preparations,[28,32,33] our findings on myocyte contraction and calcium transients are in agreement with other previous studies and within physiological ranges.[5–7] Our results align with previous measurements of field-stimulated rat ventricular myocytes, which showed greater myocyte shortening in young adult males compared to age-matched females.[5–7] It is well-documented that myocyte Ca^{2+}-dependent active tension increases early in PAH and remains elevated before the onset of RV decompensation.[14,17,20] During decompensation, myocyte peak tension is often downregulated due to intrinsic contractile protein dysfunction or other changes.[14,15,34] However, the progression and relationship between myocyte contractility and organ-level RV compensation remains unclear. Our study did not find evidence of RV decompensation or reduced contractility but did reveal sex and ovarian-hormone dependent changes in myocyte contractility.

In male SuHx rats, diastolic intracellular calcium increased significantly in male SuHx with a corresponding decrease in calcium transient amplitude. This finding aligns with previous reports showing reduced RV myocyte calcium transients in experimental models of severe RV hypertrophy,[10,35] as well as previous reports that male rat cardiomyocytes have higher diastolic calcium concentrations than females.[5,7] Previous studies have attributed impaired intracellular calcium removal to decreased sarco/endo-plasmic reticulum Ca^{2+} ATPase (SERCA) expression[36,37] or ryanodine receptor calcium leakage.[38–42] However, these differences have not been found between male and female rats at baseline.[43–45] Our data suggest that impairment of SR Ca^{2+} load may be a characteristic of this stage of male SuHx, as seen in left heart failure.[46] The increase in diastolic intracellular calcium may contribute to the dysregulation of excitation-contraction coupling and progressive contractility downregulation observed in male PAH.[19] This finding aligns with evidence that β_1–adrenoceptor blockade delays the onset of right heart failure by mitigating excitation-contraction coupling defects.[33,47] Interestingly, male SuHx-derived myocytes maintained their shortening despite reduced calcium transient amplitude, suggesting potential upregulation of myofilament calcium sensitivity, as previously reported in PAH.[48,49] However, this phenomenon was not observed in the female groups. Calcium hypersensitivity has been shown in OVX female rats but was inhibited by exogenous estrogen repletion.[12,50,51] It is possible that calcium hypersensitivity is present in both the male and OVX groups but is masked by calcium transient increases in OVX SuHx, as noted in previous reports. Changes in myocardial diastolic stiffness and myocyte calcium transient remodeling in male SuHx animals may act as complementary adaptive mechanisms to stabilize ejection fraction or may lead to progressive diastolic dysfunction.

Our data suggests that there is a sex-dependence reduction to the total SR calcium load when male rats are challenged with PAH treatment, but not in female or OVX female rats. The reduction in total SR calcium load corresponded to a reduction in the sarcomere shortening response to the hyper-physiological caffeine-induced calcium release, suggesting myofiber contraction and calcium concentrations remained coupled. This finding is consistent with our data showing an increased intracellular diastolic calcium that was the most significant in the male SuHx group. While increases to intracellular diastolic calcium have been reported in studies of heart failure, there is no clear indication that this is a phenotype of right heart failure due to PAH. Previous studies have investigated whether differences in SR calcium load exist between sexes by acutely administering caffeine in isolated cardiomyocytes and largely concluded that SR calcium stores are similar in isolated male and female rat cardiomyocytes[6,7,13,45]. However, there is also evidence that SR calcium content is higher in isolated female myocytes compared to males, demonstrated in a study of guinea pigs by Mason *et al*[52]. Moreover, pulmonary hypertension-specific studies have reported changes in Ca2+ handling in RV myocytes. Medvedev *et al.* found that alterations to calcium cycling in monocrotaline-treated pulmonary hypertensive rat RVs were not related to reductions in SERCA and may instead be associated with abnormal RyR2 activity[53,54]. Ca^{2+}/calmodulin-dependent protein kinase II (CamKII) oxidation of ryanodine receptors have been previously implicated in ryanodine receptor function, whereby reactive oxygen species elevated in lung disease regulate RyR2 activity[55]. Increases in the frequency and magnitude of calcium sparks have been show in PH RV myocytes and can be attributed to altered RyR2 function[53,55]. Alterations to RyR2 activity in male SuHx would explain the decreased SR calcium load we observed in our study, although it is also possible reductions in the expression and phosphorylation of SERCA contribute as well.

While depletion of the SR calcium load and increases to cytosolic diastolic calcium concentrations have been shown in other forms of right and left heart failure, functional shortening remained unchanged in this study. Huang *et al.* demonstrated MCT-induced PAH rats exhibit significant SR diastolic calcium leakage, explained by RyR2 dysfunction. Importantly, SR calcium leakage was shown in their study in both compensated and decompensated stages and survival was improved by administration of the ryanodine receptor stabilizer Dantrolene[42]. Our results are consistent with these results, providing increasing evidence of the reduction in SR calcium load in a stage of PAH where myocyte contraction and organ-level systolic function (Chapter 2) remained adapted. This in and of itself is an interesting finding, showing that contractile function can be and is maintained despite the underlying mechanical alterations at this stage. This also suggests that chronic or progression depletion of the SR calcium reserve may contribute to the exhaustion of potentially adaptive mechanisms (contractile reservoir) that could otherwise be upregulated and eventually leading to contractile dysfunction. Additionally, our data reveals a sex-dependent alteration to SR calcium load, which was reduced in male SuHx alone. These PAH-induced changes are highly sex- and endogenous ovarian-hormone dependent potentially contributing to sex-differences in long-term outcomes. We observed a decrease in the cell survival of all groups in animals treated with SuHx, however, for the purposes of mechanical characterization, all cells that passed the inclusion criteria were weighted equally and differences in cell survival were not considered, although we note that these differences could be considered an important feature of remodeling, with SuHx treatment reducing cell viability. Further research into the differential progression of sex-specific alterations in myocyte function are warranted.

5.5 Conclusion

In this chapter, we designed an experimental study to compare the sex-dependent differential remodeling of the right ventricular cardio myocyte in response to pulmonary arterial hypertension. In cardiac myocytes excised from male, female, and ovariectomized female rats induced with eight weeks of sugen-hypoxia treatment, we measured the myocyte contractile response to electrical stimulation, the intracellular calcium transient, and measured the total calcium load of the sarcoplasmic reticulum by administering the drug caffeine. We identified sex-specific differences in myocyte shortening in the OVX SuHx group alone, which was matched by enhancement of the calcium transient. While sarcomere shortening was maintained in male SuHx, we observed a significant increase in the diastolic intracellular calcium concentration. This was matched by a corresponding decrease in the total SR calcium load as well as the caffeine-induced sarcomere shortening. These data provide novel evidence of sex-dependent differential myocyte remodeling in PAH. These results also suggest sex-dependent alterations to SR calcium reserve in PAH underlie adapted myocyte and systolic function, but which may contribute to progressive long-term RV dysfunction.

5.6 Acknowledgements

Chapter 5, in part, is a reprint of the material as it appears in Sex-dependent Remodeling of Right-Ventricular Function in a Rat Model of Pulmonary Arterial Hypertension. Kwan, Ethan

D.; Hardie, Becky A.; Garcia, Kristen M.; Mu, Hao; Wang, Tsui-Min; Valdez-Jasso, Daniela. American Journal of Physiology Heart and Circulatory Physiology. 2024. The dissertation author was the primary investigator and author of this paper.

Chapter 5 contains unpublished material coauthored with Kwan, Ethan D; Wang, Tsui-Min; and Valdez-Jasso, Daniela. The dissertation author was the primary author of this chapter.

5.7 References

1. Jacobs W, van de Veerdonk MC, Trip P, et al. The Right Ventricle Explains Sex Differences in Survival in Idiopathic Pulmonary Arterial Hypertension. *Chest*. 2014;145(6):1230-1236.

2. Guihaire J, Bogaard HJ, Flécher E, et al. Experimental models of right heart failure: a window for translational research in pulmonary hypertension. *Semin Respir Crit Care Med*. 2013;34(5):689-699.

3. Clauss S, Bleyer C, Schüttler D, et al. Animal models of arrhythmia: classic electrophysiology to genetically modified large animals. *Nat Rev Cardiol*. 2019;16(8):457-475.

4. Blackwell DJ, Schmeckpeper J, Knollmann BC. Animal Models to Study Cardiac Arrhythmias. *Circ Res*. 2022;130(12):1926-1964.

5. Farrell SR, Ross JL, Howlett SE. Sex differences in mechanisms of cardiac excitation-contraction coupling in rat ventricular myocytes. *Am J Physiol - Heart Circ Physiol*. Published online 2010.

6. Curl CL, Wendt IR, Kotsanas G. Effects of gender on intracellular [Ca2+] in rat cardiac myocytes. *Pflugers Arch*. Published online 2001.

7. Howlett SE. Age-associated changes in excitation-contraction coupling are more prominent in ventricular myocytes from male rats than in myocytes from female rats. *Am J Physiol - Heart Circ Physiol*. Published online 2010.

8. Vizgirda VM, Wahler GM, Sondgeroth KL, Ziolo MT, Schwertz DW. Mechanisms of sex differences in rat cardiac myocyte response to beta-adrenergic stimulation. *Am J Physiol Heart Circ Physiol*. 2002;282(1):H256-263.

9. Schwertz DW, Beck JM, Kowalski JM, Ross JD. Sex differences in the response of rat heart ventricle to calcium. *Biol Res Nurs*. 2004;5(4):286-298.

10. Kuramochi T, Honda M, Tanaka K, Enornoto K -i, Hashimoto M, Morioka S. CALCIUM TRANSIENTS IN SINGLE MYOCYTES AND MEMBRANOUS ULTRASTRUCTURES

DURING THE DEVELOPMENT OF CARDIAC HYPERTROPHY AND HEART FAILURE IN RATS. *Clin Exp Pharmacol Physiol*. Published online 1994.

11. Leblanc N, Chartier D, Gosselin H, Rouleau JL. Age and gender differences in excitation-contraction coupling of the rat ventricle. *J Physiol*. Published online 1998.

12. Wasserstrom JA, Kapur S, Jones S, et al. Characteristics of intracellular Ca2+ cycling in intact rat heart: A comparison of sex differences. *Am J Physiol - Heart Circ Physiol*. Published online 2008.

13. Yaras N, Tuncay E, Purali N, Sahinoglu B, Vassort G, Turan B. Sex-related effects on diabetes-induced alterations in calcium release in the rat heart. *Am J Physiol-Heart Circ Physiol*. 2007;293(6):H3584-H3592.

14. Wang Z, Patel JR, Schreier DA, Hacker TA, Moss RL, Chesler NC. Organ-level right ventricular dysfunction with preserved Frank-Starling mechanism in a mouse model of pulmonary arterial hypertension. *J Appl Physiol*. 2018;124(5):1244-1253.

15. Fan D, Wannenburg T, de Tombe PP. Decreased Myocyte Tension Development and Calcium Responsiveness in Rat Right Ventricular Pressure Overload. *Circulation*. 1997;95(9):2312-2317.

16. Avazmohammadi R, Mendiola EA, Li DS, Vanderslice P, Dixon RAF, Sacks MS. Interactions Between Structural Remodeling and Hypertrophy in the Right Ventricle in Response to Pulmonary Arterial Hypertension. *J Biomech Eng*. 2019;141(9):910161-910613.

17. Rain S, Handoko ML, Trip P, et al. Right ventricular diastolic impairment in patients with pulmonary arterial hypertension. *Circulation*. 2013;128(18):2016-2025.

18. Sharifi Kia D, Kim K, Simon MA. Current Understanding of the Right Ventricle Structure and Function in Pulmonary Arterial Hypertension. *Front Physiol*. 2021;12:641310.

19. Hsu S, Kokkonen-Simon KM, Kirk JA, et al. Right ventricular myofilament functional differences in humans with systemic sclerosis-associated versus idiopathic pulmonary arterial hypertension. *Circulation*. 2018;137(22):2360-2370.

20. Walker LA, Walker JS, Glazier A, Brown DR, Stenmark KR, Buttrick PM. Biochemical and myofilament responses of the right ventricle to severe pulmonary hypertension. *Am J Physiol-Heart Circ Physiol*. 2011;301(3):H832-H840.

21. Gomes AV, Potter JD, Szczesna-Cordary D. The role of troponins in muscle contraction. *IUBMB Life*. 2002;54(6):323-333.

22. Andersen S, Schultz JG, Andersen A, et al. Effects of bisoprolol and losartan treatment in the hypertrophic and failing right heart. *J Card Fail*. 2014;20(11):864-873.

23. Piao S, Yu F, Mihm MJ, et al. A simplified method for identification of human cardiac myosin heavy-chain isoforms. *Biotechnol Appl Biochem*. 2003;37(Pt 1):27-30.

24. Vescovo G, Harding SE, Jones SM, Dalla Libera L, Pessina AC, Poole-Wilson PA. Comparison between isomyosin pattern and contractility of right ventricular myocytes isolated from rats with right cardiac hypertrophy. *Basic Res Cardiol*. 1989;84(5):536-543.

25. Kwan ED, Hardie BA, Garcia KM, Mu H, Wang TM, Valdez-Jasso D. Sex-dependent Remodeling of Right-Ventricular Function in a Rat Model of Pulmonary Arterial Hypertension. *Am J Physiol-Heart Circ Physiol*. Published online June 7, 2024.

26. Kwan ED, Velez-Rendon D, Zhang X, et al. Distinct time courses and mechanics of right ventricular hypertrophy and diastolic stiffening in a male rat model of pulmonary arterial hypertension. *Am J Physiol - Heart Circ Physiol*. Published online 2021.

27. Li D, Wu J, Bai Y, Zhao X, Liu L. Isolation and culture of adult mouse cardiomyocytes for cell signaling and in vitro cardiac hypertrophy. *J Vis Exp*. 2014;87:e51357.

28. Sabourin J, Boet A, Rucker-Martin C, et al. Ca2+ handling remodeling and STIM1L/Orai1/TRPC1/TRPC4 upregulation in monocrotaline-induced right ventricular hypertrophy. *J Mol Cell Cardiol*. 2018;118:208-224.

29. Qian L, Altschuld RA, Stokes BT. Quantitation of intracellular free calcium in single adult cardiomyocytes by fura-2 fluorescence microscopy: Calibration of fura-2 ratios. *Biochem Biophys Res Commun*. Published online 1987.

30. Law ML, Metzger JM. Cardiac myocyte intrinsic contractility and calcium handling deficits underlie heart organ dysfunction in murine cancer cachexia. *Sci Rep*. 2021;11:23627.

31. Abi-Gerges N, Indersmitten T, Truong K, et al. Multiparametric Mechanistic Profiling of Inotropic Drugs in Adult Human Primary Cardiomyocytes. *Sci Rep*. 2020;10(1):7692.

32. Lai N, Lu W, Wang J. Ca2+ and ion channels in hypoxia-mediated pulmonary hypertension. *Int J Clin Exp Pathol*. 2015;8(2):1081-1092.

33. Fowler ED, Drinkhill MJ, Norman R, et al. Beta1-adrenoceptor antagonist, metoprolol attenuates cardiac myocyte Ca2+ handling dysfunction in rats with pulmonary artery hypertension. *J Mol Cell Cardiol*. 2018;120.

34. Avazmohammadi R, Mendiola EA, Soares JS, et al. A Computational Cardiac Model for the Adaptation to Pulmonary Arterial Hypertension in the Rat. *Ann Biomed Eng*. 2019;47(1):138-153.

35. Xie YP, Chen B, Sanders P, et al. Sildenafil prevents and reverses transverse-tubule remodeling and Ca 2+ handling dysfunction in right ventricle failure induced by pulmonary artery hypertension. *Hypertension*. Published online 2012.

36. Røe ÅT, Ruud M, Espe EK, et al. Regional diastolic dysfunction in post-infarction heart failure: Role of local mechanical load and SERCA expression. *Cardiovasc Res*. Published online 2019.

37. Zsebo K, Yaroshinsky A, Rudy JJ, et al. Long-Term Effects of AAV1/SERCA2a Gene Transfer in Patients With Severe Heart Failure. *Circ Res*. Published online 2014.

38. Fischer TH, Maier LS, Sossalla S. The ryanodine receptor leak: How a tattered receptor plunges the failing heart into crisis. *Heart Fail Rev*. Published online 2013.

39. Marx SO, Reiken S, Hisamatsu Y, et al. PKA phosphorylation dissociates FKBP12.6 from the calcium release channel (ryanodine receptor): Defective regulation in failing hearts. *Cell*. Published online 2000.

40. Kushnir A, Santulli G, Reiken SR, et al. Ryanodine receptor calcium leak in circulating B-lymphocytes as a biomarker in heart failure. *Circulation*. Published online 2018.

41. Lehnart SE, Terrenoire C, Reiken S, et al. Stabilization of cardiac ryanodine receptor prevents intracellular calcium leak and arrhythmias. *Proc Natl Acad Sci U S A*. Published online 2006.

42. Huang Y, Lei C, Xie W, et al. Oxidation of Ryanodine Receptors Promotes Ca2+ Leakage and Contributes to Right Ventricular Dysfunction in Pulmonary Hypertension. *Hypertension*. 2021;77(1):59-71.

43. Tappia PS, Dent MR, Aroutiounova N, Babick AP, Weiler H. Gender differences in the modulation of cardiac gene expression by dietary conjugated linoleic acid isomers. *Can J Physiol Pharmacol*. Published online 2007.

44. Chu SH, Sutherland K, Beck J, Kowalski J, Goldspink P, Schwertz D. Sex differences in expression of calcium-handling proteins and beta-adrenergic receptors in rat heart ventricle. *Life Sci*. Published online 2005.

45. Chen J, Petranka J, Yamamura K, London RE, Steenbergen C, Murphy E. Gender differences in sarcoplasmic reticulum calcium loading after isoproterenol. *Am J Physiol - Heart Circ Physiol*. Published online 2003.

46. Alvarado FJ, Valdivia HH. Mechanisms of ryanodine receptor 2 dysfunction in heart failure. *Nat Rev Cardiol*. 2020;17(11):748-748.

47. Bogaard HJ, Natarajan R, Mizuno S, et al. Adrenergic Receptor Blockade Reverses Right Heart Remodeling and Dysfunction in Pulmonary Hypertensive Rats. *Am J Respir Crit Care Med*. 2010;182(5):652-660.

48. Petre RE, Quaile MP, Rossman EI, et al. Sex-based differences in myocardial contractile reserve. *Am J Physiol - Regul Integr Comp Physiol*. Published online 2007.

49. Schwertz DW, Beck JM, Kowalski JM, Ross JD. Sex differences in the response of rat heart ventricle to calcium. *Biol Res Nurs*. Published online 2004.

50. Wattanapermpool J, Reiser PJ. Differential effects of ovariectomy on calcium activation of cardiac and soleus myofilaments. *Am J Physiol - Heart Circ Physiol*. Published online 1999.

51. Bupha-Intr T, Wattanapermpool J, Peña JR, Wolska BM, Solaro RJ. Myofilament response to Ca2+ and Na+/H+ exchanger activity in sex hormone-related protection of cardiac myocytes from deactivation in hypercapnic acidosis. *Am J Physiol - Regul Integr Comp Physiol*. Published online 2007.

52. Mason SA, MacLeod KT. Cardiac action potential duration and calcium regulation in males and females. *Biochem Biophys Res Commun*. 2009;388(3):565-570.

53. Medvedev R, Sanchez-Alonso JL, Alvarez-Laviada A, et al. Nanoscale Study of Calcium Handling Remodeling in Right Ventricular Cardiomyocytes Following Pulmonary Hypertension. *Hypertension*. 2021;77(2):605-616.

54. Pieske B, Kockskämper J. Alternans goes subcellular: a “disease” of the ryanodine receptor? *Circ Res*. 2002;91(7):553-555.

55. Wang L, Ginnan RG, Wang YX, Zheng YM. Interactive Roles of CaMKII/Ryanodine Receptor Signaling and Inflammation in Lung Diseases. In: Wang YX, ed. *Lung Inflammation in Health and Disease, Volume I.* Springer International Publishing; 2021:305-317.

Chapter 6 CORRELATIONAL AND CLUSTER ANALYSES OF HEMODYNAMIC DATA USING MACHINE LEARNING

6.1 Introduction

Machine learning analyses have become increasingly used to uncover new relationships in large datasets. This is of high interest for clinical applications, particularly when the relationship between disease progression, patient health, and the molecular mechanisms of disease are unknown[1]. Large cohort studies demonstrate that the health and function of the RV during the progression of PAH is highly heterogeneous and necessitates early and accurate predictors of patient outcome[2–4]. Machine learning analyses have become increasingly used to attempt to identify cardiac remodeling "phenotypes" within large cohorts of adult patients with PAH[5–7]. However, clinical studies are confounded by age, stage of disease, and other cardiac comorbidities.

Experimental data described in Chapters 2-3 consists of hemodynamic and morphologic measurements of PAH-induced male, female, and ovariectomized rats obtained to study the effects of sex on RV remodeling at various stages of disease. In this chapter, we asked the question whether machine learning tools could provide new and generalizable insights into our SuHx dataset. We conducted both supervised and unsupervised analyses below to answer a range of questions to both validate hypotheses, gain insights into our predictors, and to discover new relationships in our data. We aimed to identify unique groupings of RV remodeling in PAH rats and identify primary features that could enhance our understanding of PAH progression/categorization.

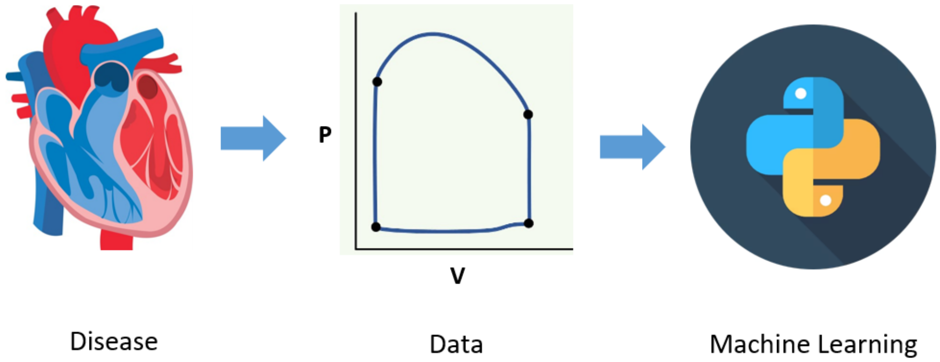

Figure 6.1. An illustration of the analysis approach. Pressure-volume hemodynamic measurements obtained at various stages of disease are the primary data to input into machine learning analyses.

From our SuHx dataset, multi-factor analyses of treatment, sex, and time-points commonly reported significant multi-factor interaction effects and hemodynamic responses could not be fully explained by simple main effects. While the distributions of hemodynamic values could be compared by their means with respect to sex and treatment, consistent overlaps remained in the distributions between samples of these main effects (i.e. a male w4 animal and a female w8 treated animal producing similar hemodynamics and RV remodeling). Therefore, we asked the question if machine learning methods could supplement our research and provide additional novel data-driven insights.

6.2 Approach

The following research questions were posed: 1) Can we identify distinct groupings of our PAH rats based on their hemodynamic and structural characteristics that correspond to different RV function 2) Which primary features capture the essential characteristics of the PAH dataset. We designed an unsupervised machine learning analysis to answer these questions using k-means clustering.

6.2.1 Data

Eight-week-old Sprague Dawley rats were induced with PAH using the established Sugen-Hypoxia model, as described in Chapters 2 & 3. This study included multiple groups of rats (male, female, and ovariectomized female) treated with distinct durations of SuHx (4, 8, and 12 weeks), to study the effects of sex and ovarian hormones, as described in chapter 3. Hemodynamic and morphological data were collected using a 1.9F admittance catheter to measure right-ventricular (RV) and left-ventricular (LV) blood pressures and volumes during an open chest procedure[8,9]. Hemodynamic metrics derived from invasive pressure-volume measures were calculated from these readings[10]. Morphological data, such as RV thickness, RV mass, Fulton index, and liver mass, were recorded post-procedure. To investigate whether distinct groupings of PAH could be identified based on hemodynamic and structural characteristics that corresponded to different RV function. The following hemodynamic and structural measurements were considered as predictors:

Table 6.1. In total, 27 experimental measurements were categorized as structural or hemodynamic predictors and input into the analysis.

Structural Measurements	**Hemodynamic Measurements**	
RV free wall Thickness	Heart Rate	Pulmonary Vascular Resistance
RV free wall Mass	RV Stroke Volume	RV minimum Pressure
Fulton Index	RV end-diastolic Volume	RV end-diastolic Pressure
Animal Body Mass	RV end-systolic Volume	RV end-systolic Pressure
Right Atrial Mass	RV Ejection Fraction	RV end-systolic elastance
Left Atrial Mass	RV Cardiac Output	RV end-diastolic elastance
Septum: LV free wall Mass	RV dP/dt_{max}	Pulmonary arterial elastance
Liver Mass	RV dP/dt_{min}	RV-PA coupling

Datasets were curated from the total database of experimental measurements, which comprised over 1000 samples. First, Dataset One was curated by selecting animals from which paired measurements across over 80% of all predictors were made. This inclusion criteria was designed to minimize imputation requirements. Data imputation was performed using mean imputation for samples of the same discrete and continuous labels. This curated Dataset consisted of n = 179 total samples with two discrete labels: sex group (male, female, ovariectomized), treatment group (control, SuHx), and one continuous label (weeks of SuHx treatment: 0, 4, 8, 12). Dataset Two was curated from Dataset One by including only SuHx-treated animals at Weeks 4, 8, and 12, to investigate differences specific to the weeks of SuHx treatment in hypertensive animals. Dataset Two consisted of n = 132 samples, with one discrete label (sex group), and one continuous label (weeks of SuHx treatment: 4, 8, 12).

6.2.2 Numerical Methods

Principal component analysis (PCA) was performed followed by a hierarchical agglomerative clustering using Ward's minimum variance method. Clustering is a statistical technique that utilizes unsupervised (unbiased) algorithms to categorize samples into "clusters" that maximize the similarity within each group and minimize it between groups. Similarity was determined using Ward's method - an agglomerative clustering algorithm for separating quantitative variables by minimizing the sum of squared errors, rather than the Euclidean distance, as is done in k-means clustering. For this reason, Ward's method is better suited for quantitative continuous predictors, which were common in our dataset[11]. We selected k = 3 for our analysis based on a silhouette analysis of our dataset.

6.3 Results

To visualize our datasets, pair plots were generated to illustrate correlations between our predictors (Fig. 6.2). Particular attention was paid to correlations between functional hemodynamic predictors and structural predictors, between pressure and volume measurements, and between RV and PA measurements. Dataset One, comprising both normotensive and hypertensive samples were included here.

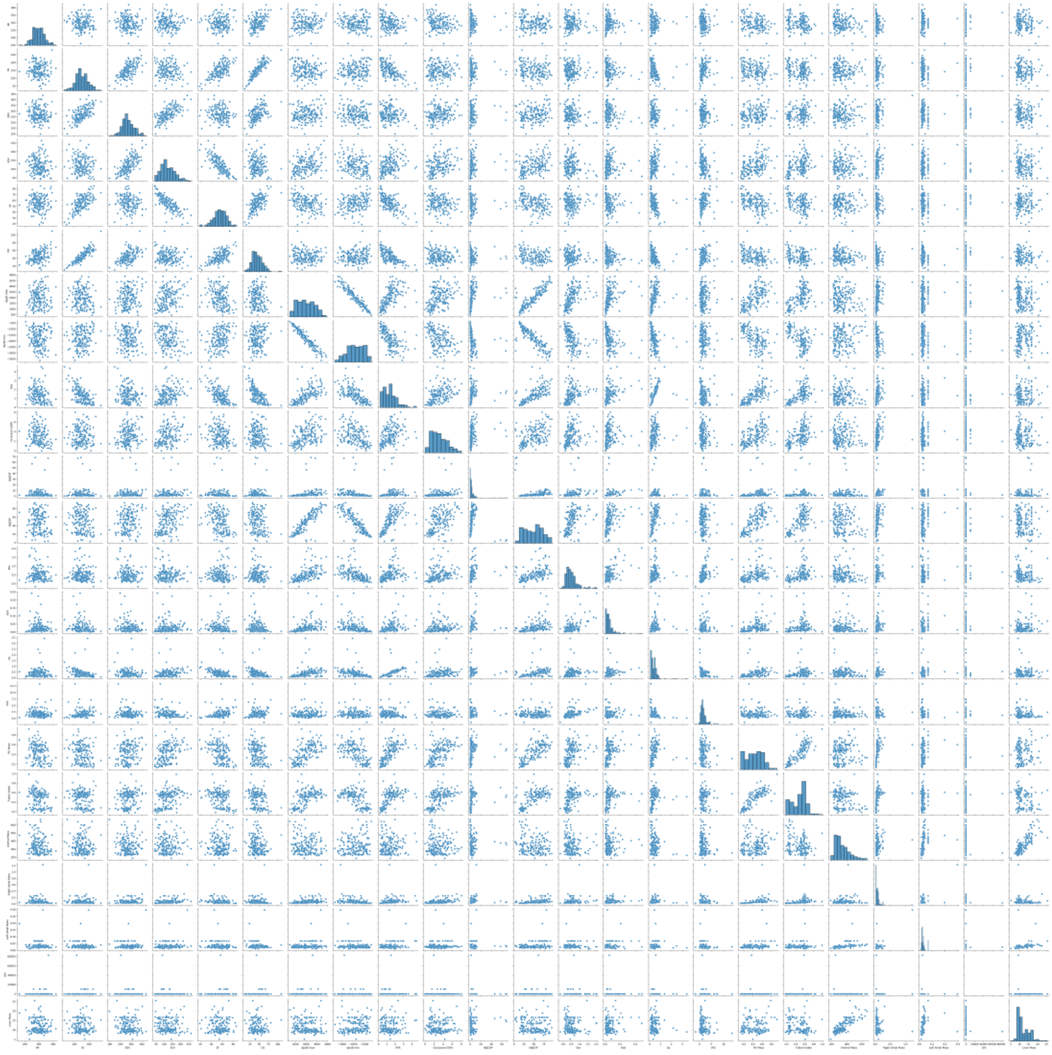

Figure 6.2. Pair plots illustrate correlations between predictors. Included predictors were heart rate, stroke volume, ED volume, ES volume, ejection fraction, cardiac output, dP/dt_{max}, dP/dt_{min}, pulmonary vascular resistance, minimum RV pressure, ED pressure, ES pressure, ES elastance, ED elastance, arterial elastance, ventricular-vascular coupling, RV mass, Fulton index, bodyweight, LA mass, RA mass, liver mass, and septum : LV mass ratio.

This visualization revealed strong linear correlations between hemodynamic parameters such as contractile function (dP/dt$_{max}$), systolic chamber mechanics (E$_{es}$), pulmonary vascular resistance, and the Fulton Index of RV hypertrophy.

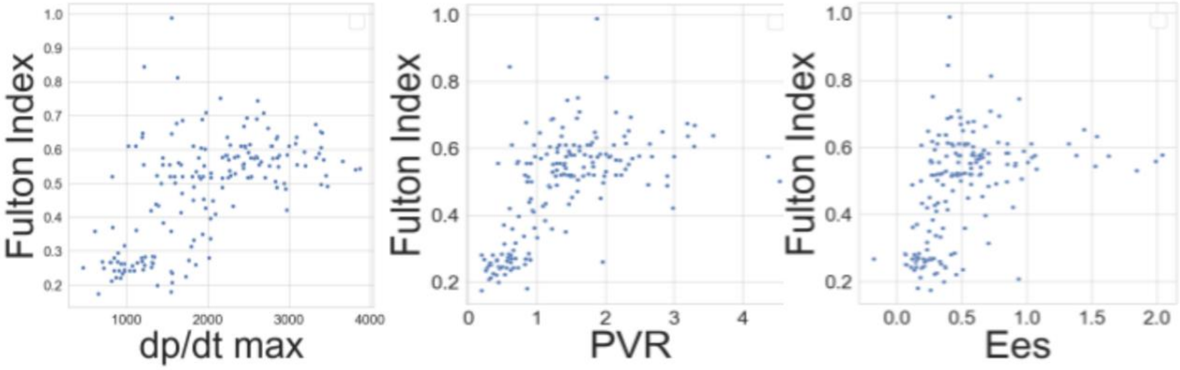

Figure 6.3. Pair plots were used to investigate correlations between parameters of interest, such as the relation between RV hypertrophy (y-axis), and RV systolic function (dP/dt$_{max}$, E$_{es}$), and pulmonary vascular resistance (PVR). In these three cases, hypertrophy correlated to increases in these hemodynamic parameters, but the hypertrophic response also plateaued in the samples with high dP/dt$_{max}$, PVR, and E$_{es}$.

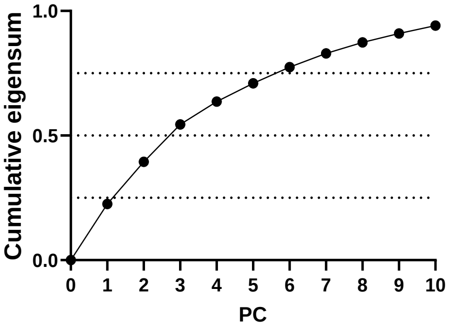

Figure 6.4. The cumulative eigensum, representing the proportion of variance in the dataset explained by each additional principal component was calculated for the first ten principal components. The majority of the variance in the dataset was explained by the first three principal components (PC1-3).

Principal component analysis revealed the top 4 principal components and the corresponding loadings of important predictors. The largest loadings of PC1 were RV ES pressure, pulmonary vascular resistance, dp/dtmin, and dp/dtmax. These predictors can be generally described as hemodynamic pressure-related metrics. In addition, these predictors all have clearly defined numerical thresholds separating hypertensive and normotensive animals. The contributions of PC1 explained a total of ~29% of variance in the total dataset.

PC2 explained 18% of the variance in the dataset. The largest loading contributors to PC2 were the clinical systolic function metrics RV cardiac output/stroke volume/ejection fraction (note that these three predictors are all linear related), followed by dP/dt_{max} and dP/dt_{min}.

PC3 explained 16% of the total variance, to which the largest loading contributions were ES volume, ED volume, and the ES elastance. By contrast to PC1 (pressure-related metrics), PC3 was dominated by contributions from ES and ED RV chamber volume measurements.

PC4 contributed 13% of the total variance and was dominated by the effects of heart rate. With a loading of 0.65, over 42% of the total variance in heart rate across the entire dataset was captured by PC4, which was one of the strongest predictor-PC relationships observed.

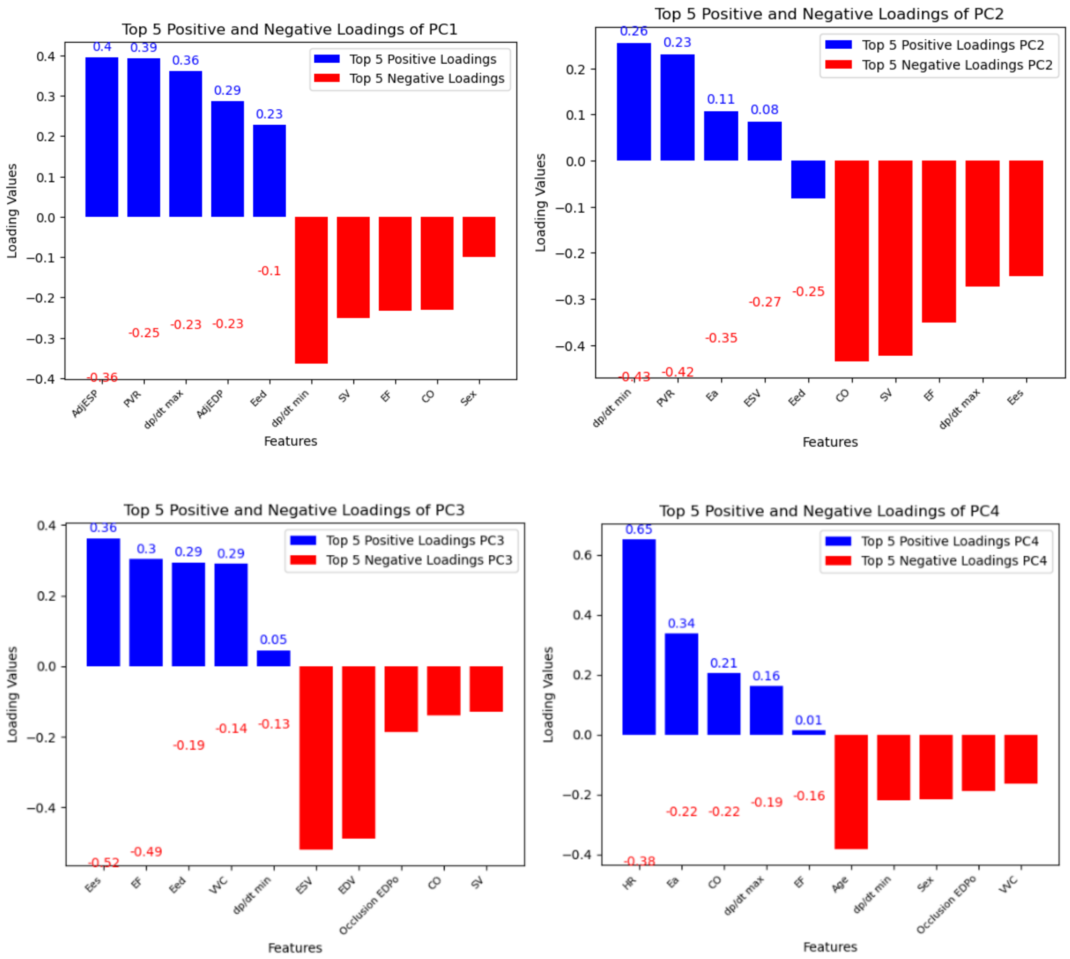

Figure 6.5. The loadings for Principal components 1-4 are shown (left to right, top to bottom) and reveal which predictors were most important for explaining each principal component. For PC 1, ES pressure was the most important predictor. For PC2-4, cardiac output, ES volume, and heart rate were the most important predictors respectively.

Clustering Results

Hierarchical clustering was used to sort Dataset Two, comprising of n = 132 samples across nine groups (male, female, and OVX females treated with 4, 8, or 12 weeks of SuHx). We chose k = 3 based on the combination of an elbow analysis of the dataset (Fig. 6.6) which revealed multiple inflection points and the experimental design that grouped both factors by three categories.

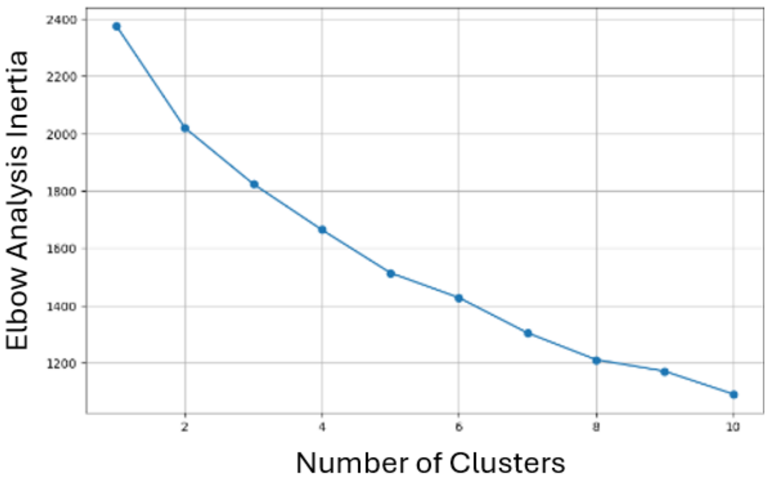

Figure 6.6. Elbow analysis was used to select the number of clusters *n* to include in the analysis. Elbow analysis revealed multiple inflection points, including at *n* = 2, 3, and 6.

Results of hierarchical clustering (Table 6.2) sorted the 132 sample dataset into three clusters. Of the three clusters, Cluster 1 was the smallest by number of samples, with a relatively even mix of sex groups and weeks. Cluster 2 was the largest cluster, comprising 66 of the 132 samples. Cluster 2 preferentially selected earlier week (W4 and W8) samples rather than later week (W12) samples, with 32 of the 66 Cluster 2 samples treated with four weeks of SuHx. Cluster 2 also preferentially selected female (n = 26) and OVX (n = 24) rather than male samples (n = 16). Cluster 3 comprised 43 out of the 132 samples and preferentially selected males (n = 23) rather than female (n = 11) or OVX females (n = 9). Cluster 2 primarily differentiated female samples and early week samples, while Cluster 3 primarily selected for male and later week samples.

Table 6.2. Hierarchical clustering results. Cluster 1 discriminated the role of sex and Cluster 2 discriminated the role of weeks, while Cluster 3 was primarily composed of later-week male animals. Group-treatment combinations that were primarily sorted (>66%) into a single cluster were bolded for emphasis.

		Cluster				
		Cluster 1	Cluster 2	Cluster 3	Group size (sex & week)	Group size (sex)
Male						Male
	Week 4	1	**11**	5	17	48
	Week 8	6	2	10	18	
	Week 12	2	3	8	13	
Female	male subtotal	9	16	23		Female
	Week 4	3	**10**	1	14	44
	Week 8	1	**12**	5	18	
	Week 12	3	4	5	12	
OVX	female subtotal	7	26	11		OVX
	Week 4	2	**11**	0	13	40
	Week 8	2	9	5	16	
	Week 12	3	4	4	11	
	OVX subtotal	7	24	9		
	Cluster total	23	66	43	132	132

The averages of predictor values for the three clusters revealed hemodynamics, rather than group or treatment week distinguished the clusters (Fig. 6.7). Cluster 2, which was revealed to preferentially select female and early week samples, corresponded to the lowest hemodynamic pressure load, with the smallest average ES pressure, PV resistance, and the most moderate diastolic function (dP/dt_{min}). By contrast, cluster 3 which was shown to preferentially select male and later week samples, was shown to have the higher hemodynamic pressure load, including the highest mean ES pressure and PV resistance. Cluster 3 also had the most reduced ejection fraction (Fig. 6.7), with a group mean below 50%. While Cluster 1 did not clearly distinguish sex or weeks of SuHx treatment, it revealed a distinct combination of hemodynamics and RV remodeling, where the pressure load was high (ES pressure, PV resistance, dP/dt$_{min}$), but the ejection fraction remained maintained, the most adapted function of any group.

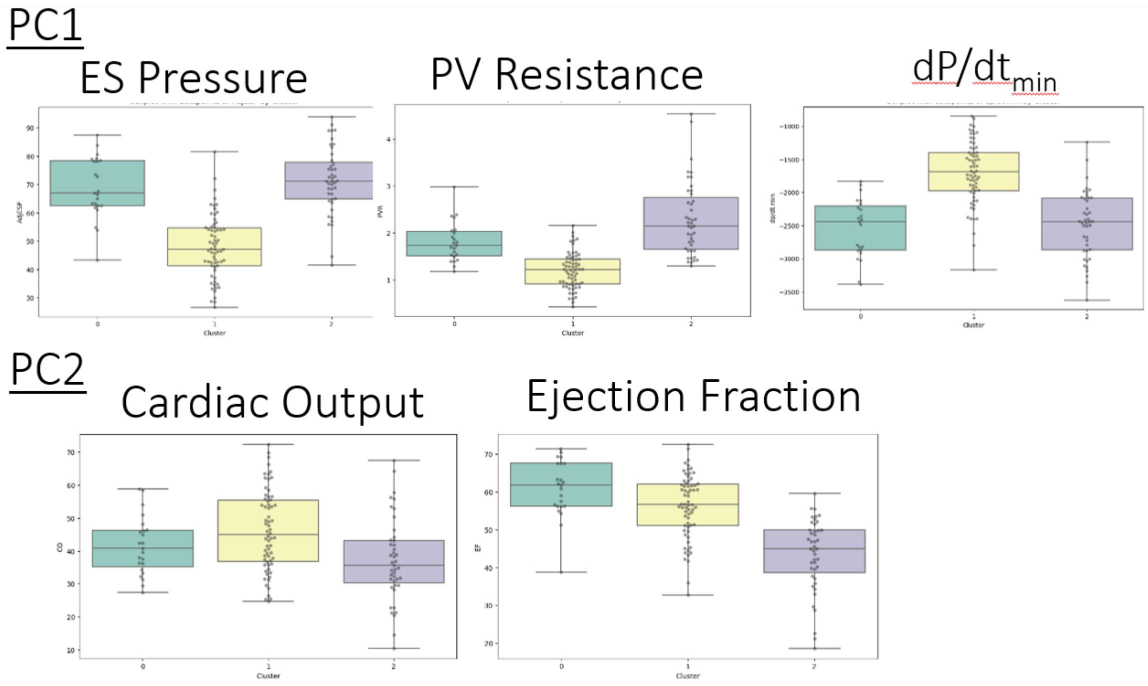

Figure 6.7. Average predictor values for each cluster are shown for the top contributors to the first two principal components, which comprised half (~47%) of the total variance in the dataset. In the first row, ES pressure, PV resistance, and dP/dt$_{min}$ revealed that cluster 2 had the lowest pressure load while cluster 1 and 3 had high pressure load. In the second row, ejection fraction averages revealed cluster 1 maintained high RV efficiency while cluster 3 had the lowest RV efficiency.

6.4 Discussion

Machine learning analyses have become increasingly used to uncover new relationships in large datasets. This is of high interest for clinical applications, particularly when the relationship between disease progression, patient health, and the molecular mechanisms of disease are unknown. Recently, unsupervised cluster analyses have been applied towards characterize clinical PAH data[5–7]. Parikh *et al.* demonstrated the value of such analyses in 2017, designing a cluster analysis of patients from the FREEDOM clinical trials of oral treprostinil. Their analysis identified 4 distinct clusters which showed patients who were newly diagnosed, older, and had severe baseline symptoms and exercise capacity had the greatest response to oral treprostinil treatment. This analysis also found that clusters differed by PAH etiology, but not by sex (or race), factors which have been previously shown to correspond to differential RV function and patient outcomes (Chapter 3). Importantly, this study precluded key descriptive quantitative variables such as RV hemodynamics. Badagliacca *et al.* conducted a cluster analysis of 252 patients with idiopathic PAH based on hemodynamic and cardiopulmonary clinical assessments[7]. The results of this study identified 4 PAH phenotypes: 1) patients with severe PH and RV dilation and high oxygenation, 2) patients with mild PH and mild RV dilation and high oxygenation 3) patients with severe PH and RV dilation and low oxygenation and 4) patients with mild PH, mild RV dilation and low oxygenation. In this way, the combination of mean pulmonary arterial pressure, RV size, and oxygen pulse measurements were the most important determinants for stratifying patients into unique phenotypes that associated with clinical worsening[7].

Hoeper *et al.* performed a retrospective cluster analysis of 841 patients with idiopathic PAH from the Comparative, Prospective Registry of Newly Initiated Therapies for Pulmonary Hypertension (COMPERA). This cluster analysis distinguished itself from previous studies by incorporating cardiopulmonary risk factors and comorbidities as predictors of the cluster analysis which sought to identify PAH clinical phenotypes, as well as analyzed patient outcomes and responses to medical therapy. From this analysis, Hoeper *et al.* identified 3 distinct groupings of patients: a “classic” idiopathic PAH phenotype characterized by young age, female sex, and an absence of other cardiopulmonary risk factors; elderly patients (primarily female) with left-sided disease (primarily heart failure with preserved ejection fraction), but primarily with no history of smoking or pulmonary disease and largely preserved lung function; elderly patients (primarily men) with a history of smoking and risk factors for left heart disease with impaired lung function.

Importantly, patients in these clusters demonstrated not only differences in their risk factors and demographics, but also key differences in responses to PAH therapy and survival[6].

Taken altogether, these studies confirm that the patient response to PAH is heterogeneous. Our data is consistent with these results and provides further evidence that part of this heterogeneity can be captured by experimental PAH models, from which more detailed descriptions of RV remodeling can be analyzed and distinguished. Our results, which demonstrate the presence of distinct sub-groups of SuHx-treated animals with significant hypertension and either maintained or impaired RV function, are consistent with these results and emphasize potential for disease heterogeneity to be targeted by specific therapies. It is interesting to note that Cluster 3 was identified as the most severe group and consisted of a primarily older male subgroup with elevated pressures and reduced RV function, characteristics which would make the group likely candidates for therapy. Given these results and the results of Chapter 4, in which diastolic myocardial stiffening was identified as a hypertrophy-independent biomarker, our cluster analysis here suggests that subjects in cluster 3 may correspondingly be likely candidates that would respond well to RV unloading. In this way, such conclusions, drawn from large cohort analyses may be supportive of clinical efforts. It remains unclear why and how heterogeneity in RV remodeling in response to PAH occurs. Further investigations can provide key insights into the identification of heterogeneous, patient-specific, and differential comorbidities to facilitate new and specific treatment strategies.

6.5 Conclusion

In this chapter, we designed retrospective studies of experimental data acquired in Chapters 2-3 using statistical and machine learning-based analyses. We identified distinct subsets of SuHx-treated animals that responded to treatment with high and low pressures, as well as *distinct subsets of SuHx-treated animals that responded to high pressures with high and low RV function. These responses were independent of the prescribed experimental groups of sex- and the duration of treatment, however male sex and prolonged SuHx treatment correlated to the cluster with the most elevated pressure and reduced function. Future similar analyses can provide insights into the complex relationship between hemodynamics and structural remodeling, sex and age, and disease progression to potentially discover new phenogroups of PAH.*

6.6 Acknowledgements

Chapter 6 contains unpublished material coauthored with Kwan, Ethan D; Hui, Jingwen; Moylan, Leah; and Valdez-Jasso, Daniela. The dissertation author was the primary investigator and author of this chapter.

6.7 References

1. Shu S, Ren J, Song J. Clinical Application of Machine Learning-Based Artificial Intelligence in the Diagnosis, Prediction, and Classification of Cardiovascular Diseases. *Circ J Off J Jpn Circ Soc*. 2021;85(9):1416-1425.

2. Naeije R, Manes A. The right ventricle in pulmonary arterial hypertension. *Eur Respir Rev*. 2014;23(145):476-487.

3. Cheron C, McBride SA, Antigny F, et al. Sex and gender in pulmonary arterial hypertension. *Eur Respir Rev*. 2021;30(162):200330.

4. Van De Veerdonk MC, Bogaard HJ, Voelkel NF. The right ventricle and pulmonary hypertension. *Heart Fail Rev*. 2016;21(3):259-271.

5. Parikh KS, Rao Y, Ahmad T, Shen K, Felker GM, Rajagopal S. Novel approach to classifying patients with pulmonary arterial hypertension using cluster analysis. *Pulm Circ*. 2017;7(2):486-493.

6. Hoeper MM, Pausch C, Grünig E, et al. Idiopathic pulmonary arterial hypertension phenotypes determined by cluster analysis from the COMPERA registry. *J Heart Lung Transplant*. 2020;39(12):1435-1444.

7. Badagliacca R, Rischard F, Papa S, et al. Clinical implications of idiopathic pulmonary arterial hypertension phenotypes defined by cluster analysis. *J Heart Lung Transplant*. 2020;39(4):310-320.

8. Kwan ED, Velez-Rendon D, Zhang X, et al. Distinct time courses and mechanics of right ventricular hypertrophy and diastolic stiffening in a male rat model of pulmonary arterial hypertension. *Am J Physiol - Heart Circ Physiol*. Published online 2021.

9. Kwan ED, Hardie BA, Garcia KM, Mu H, Wang TM, Valdez-Jasso D. Sex-dependent Remodeling of Right-Ventricular Function in a Rat Model of Pulmonary Arterial Hypertension. *Am J Physiol-Heart Circ Physiol*. Published online June 7, 2024.

10. Vonk-Noordegraaf A, Westerhof N. Describing right ventricular function. *Eur Respir J*. 2013;41(6):1419-1423.

11. Meunier B, Dumas E, Piec I, Béchet D, Hébraud M, Hocquette JF. Assessment of Hierarchical Clustering Methodologies for Proteomic Data Mining. *J Proteome Res*. 2007;6(1):358-366.

Chapter 7 CONCLUSIONS

In this dissertation, we investigated the remodeling of the RV during PAH, using a combination of *in-vivo* and *in-vitro* measurements and experiments. These data were combined with mathematical models of RV biomechanics and used to elucidate the relative contributions of myocardial material and shape changes to explain evolving systolic and diastolic RV function. In the first principal aim, we sought to investigate the relative contributions of material properties vs geometric remodeling towards changes in systolic and diastolic function. We hypothesized that male rats increase their diastolic stiffness while female rats increase their contractility in their adaptive responses. This work addresses this hypothesis by first demonstrating the ability to decouple the effects of material properties and geometric remodeling in PAH using our modeling approach and subsequently performing this analysis in three groups. Our results revealed and described distinct adaptations in each group. As we hypothesized, our model analysis revealed that diastolic stiffening was the primary mechanical change in male SuHx and further provided the insight that sequences of rapid stiffening preventing RV dilation after the initial hypertrophic response to pressure overload stabilized systolic function. We found that males initially responded to pressure overload with rapid hypertrophy that stabilized systolic function with only a transient recruitment of contractility. After the initial hypertrophic response, we uncovered a subsequent period of rapid diastolic pressure rise, matched by pronounced diastolic stiffening, which was revealed to be the primary mechanical adaptation in male SuHx. Our model analysis revealed that this contrasted with female SuHx, in which hypertrophy was the primary contributor to maintaining systolic and diastolic function, with significant but less severe diastolic stiffening. While we hypothesized that myocyte contractility would increase to adapt RV systolic function in female SuHx, our results indicated this was not the case. However, we then investigated ovariectomized female rats depleted of endogenous estrogens and it was in this group where we observed that SuHx resulted in significant recruitment of myocyte contractility corresponding to changes in the calcium transient as well as hypertrophy to stabilize systolic function. By contrast, ovary-intact female rats responded to SuHx with some diastolic stiffening, but the fewest mechanical alterations of any group and instead stabilized RV function primarily via hypertrophy. While the total hypertrophic response in male SuHx was as pronounced as the response in female SuHx, the resulting contributions of the hypertrophic response to systolic and diastolic function was greater in female than male SuHx.

Our second principal aim was to investigate mechanisms of the changes in systolic and diastolic material properties, and we hypothesized that myocyte calcium transient remodeling and force development is upregulated in females and not males while diastolic stiffening was derived from changes to the collagen fiber matrix in males. Our results revealed that diastolic stiffening was most severe in males and not explained by fibrotic collagen accumulation, nor in changes to collagen type or crosslinking in either males or female. When we compared male and female SuHx, we observed some evidence of fibrosis in RV myocardium (of the apex and infundibulum) that was consistent between male, female, and OVX females, which corresponded to increases in diastolic stiffening in all three groups. Our results provide some evidence of fibrosis in the RVs, but also suggest that fibrosis alone does not solely explain diastolic stiffening. It remains a possibility that changes to the collagen fiber architecture play a role, as well as myocyte stiffness. We observed large increases in in diastolic intracellular calcium in two of our SuHx groups with the most pronounced increases in males. This result was validated by a total decrease in the SR calcium load in male SuHx, the group with the greatest myocardial stiffening. These sex-dependent alterations to diastolic cytosolic calcium may cause impairment of myofiber relaxation in the long-term, contributing to diastolic myocardial stiffening. While we hypothesized calcium transient upregulation would explain systolic changes in females but not male, our results revealed that this was only true for the ovariectomized females. In this group, our model found that large increases to chamber elastance were matched by myocardial contractility upregulation, not hypertrophy. Myocyte experiments revealed that indeed sarcomere shortening was upregulated along with the intracellular calcium transient in the ovariectomized females, but not in the ovary-intact or male SuHx groups. This result suggests that neither sex nor ovarian-hormone status alone lead to the recruitment of contractility at the studied stage of SuHx, but instead a combination of the two factors warrant this remodeling response. Unexpectedly, we observed RV shape change to be a distinguishing feature between sexes. Whether this result corresponds to myocardial stiffening and pressure overload, or properties of the intraventricular septum remains unclear, but it is likely that these geometric changes affect RV function in the long-term. The results of this dissertation conclude that both the remodeling of myocardial geometric and material properties and the contributions of these changes towards affecting systolic and diastolic function are dependent on sex- and ovarian hormones, as well as the stage of disease.

Hemodynamic data obtained at multiple time points emphasized the PAH-induced development of RV remodeling is a complex and dynamic process, involving the regulation of many myocardial properties. These time courses differed based on sex, revealed by comparative studies of male, female, and ovariectomized female rats. We affirmed the importance of diastolic stiffness as an indicator of PAH and the remodeled RV. Our works specifically added to the knowledge of the role of stiffening by revealing distinct time courses of RV remodeling during the progression of PAH. We first observed that rapid RV hypertrophy initially stabilizes systolic function (in the first 4 weeks of male SuHx). Our work revealed a phase of subsequent remodeling, between 5-10 weeks of SuHx, where pronounced RV diastolic stiffening occurred and prevented RV dilation. These results affirm that RV stiffening is not strictly a deleterious phenomenon and may be beneficial in the adapted stage. However, maintained RV diastolic stiffening may contribute towards long-term dysfunction by inhibiting RV relaxation and filling. Our comparative study of males and females revealed that, even when pressure overload was of similar magnitude, the RV adaptation was sex- and ovarian-hormone dependent, with distinct mechanical alterations. The difference between the adaptation of males and females was in the size and shape of the RVs and the severity of the diastolic stiffening. The difference between females and ovariectomized females was in the severity of diastolic stiffening and the recruitment of myocyte contractility.

These findings validate the complexity of PAH and the corresponding RV adaptation. Our experimental and computational approach demonstrated the ability to decouple these complex patterns into isolated parameters to pinpoint what myocardial changes are important to RV function at what timepoint and how these features change with sex. These conclusions affirm the need for patient-specific strategies for managing PAH that are considerate of sex and that consider targeting diastolic stiffening. These conclusions contribute significant steps towards furthering our understanding of the remodeling of the right ventricle and its function in health and disease.

7.1 Clinical applications

We posit that the modeling approach described in this work reveals underlying mechanical changes that 1) provide insights into the relative contributions of myocardial changes in PAH and 2) identify myocardial alterations at distinct stages of PAH that could benefit the development of targeted therapies. Our *model can accurately predict myocardial material alterations* with pressure-volume and morphologic data, as a low computational cost. The morphologic and hemodynamic inputs into our model could be acquired clinically using noninvasive (CMRI) and invasive (catheterization) methods. These types of fitted computer model predictions could provide meaningful insights into the severity of mechanical alterations without requiring clinically unfeasible characterizations or biopsied tissue. Given that pressure data is often difficult to acquire and commonly require invasive catheterization measurements that could results in complications, the ability to utilize non-invasively derived cardiac chamber and myocardium volumes to make predictions of the end-systolic and end-diastolic pressure-volume relationships could also be of clinical value. We have generated such data in our large SuHx rat PAH cohorts, validating the potential of such an approach.

As discussed in Chapter 4, the ovary-intact female SuHx group (designed to represent young adult women with PAH) corresponded to the fewest mechanical alterations. Clinically, this patient group has been shown to demonstrate the most adapted RV function. Therefore, such mechanical alterations could reasonably be associated with PAH progression, as seen in our data.

One such mechanical alteration, a significant and novel contribution of our work, is the finding that diastolic stiffening precedes contractility changes in the SuHx animal model of PAH. This is clinically significant because increased RV stiffness is well correlated with multiple parameters depicting disease severity and can be used as a biomarker of poor prognosis. Studies by Rain et al. suggested diastolic stiffening is both a compensatory mechanism to increased afterload and also a contributor to disease progression[1,2]. We added to this, showing in male rats treated with 5-10 weeks of SuHx that rapid sequences of RV hypertrophic wall thickening preceded any stiffening, but which was followed by rapid diastolic stiffening that stabilized the RV diastolic volume, preventing RV dilation. This could be seen as a compensatory mechanism, acting to maintain the ejection fraction, but this diastolic stiffening also prevents the gain-of-function that could result from an increased stroke volume. Importantly, once diastolic stiffening occurred, it remained. This finding emphasizes that diastolic stiffening develops during a largely compensated phase and may have both beneficial short-term and detrimental long-term implications. This *affirms that diastolic stiffening can serve as an indicator of PAH progression* and as a *hypertrophy and fibrosis-independent indicator of which patients may respond* to RV unloading. These insights also pave the way for more precise risk stratification, that might improve early intervention and management of PAH. Given that RV diastolic stiffness could be a significant indicator, there is also a potential to stratify patients with RV stiffness based on the type and severity of the stiffness they have. There is similar precedent in the LV, where therapeutic sodium glucose co-transporter inhibition (dapagliflozin) enhances protein kinase G activity and lowers titin-derived myocyte stiffness, which could be viable for patients with diastolic stiffness caused by myocyte stiffness and endothelial dysfunction but would be much less effective in patients with myocardial stiffness due to extensive fibrosis. This finding also suggests that chronic diastolic stiffness likely has detrimental effects, inhibiting RV relaxation and filling, and contributing to diastolic dysfunction.

Furthermore, our work revealed, for the first time, sex- and ovarian hormone dependent differences in the severity of diastolic stiffness development. This revelation alone has implications for the personalized treatment of PAH, by allowing for the development of targeted therapies that account for these differences. The severity of diastolic stiffness corresponded to the generally reported severity of RV dysfunction and outcomes in patients with PAH, with SuHx males experiencing the most severe stiffness and ovary-intact SuHx females experiencing the least severe stiffening and the fewest myocardial mechanical alterations.

7.2 Limitations

7.2.1 Animal Model

The animals used in this study remained relatively young at the time of study, with SuHx treatment at 7-8 weeks of age. After 8 weeks of SuHx treatment, for example, experimental measurements were made at 15 weeks of age. Our study does not account for the effects of aging, shown to be a risk factor for PAH in patients[3–5]. The question of age and age-related comorbidities in PAH is often considered in parallel to the question of age-related menopause in women with PAH, who form the overwhelming PAH patient demographic, and key differences pre- and post-menopause exist[6]. However, studies have also suggested that age- related changes are not solely explainable by menopausal status.[7] In fact, Van Wezenbeek and colleagues showed that that RV pressure overload tolerance may occur independent of menopause, but instead be confounded by age-related comorbidities[7]. It is important to note that most pre-clinical studies of PAH are performed in relatively young animals, as our study was. We believe this approach was appropriate for our study, noting that the effects of SuHx treatment were much more pronounced than the negligible effects of age on RV hemodynamics in untreated normotensive animals.

A primary research question we asked was regarding the role of sex and, by extension, ovarian hormones on the health and function of the RV in PAH. However, we found circulating ovarian hormone levels to vary greatly depending on the stage of the estrous cycle, which we did not control or tracked in our data. These hormonal fluctuations could impact sex-dependent alterations in ventricular mechanics[8,9]. Ongoing and future work aims to characterize these estrous-cycle dependent effects on RV mechanics. In the context of the current study, we concluded that hormonal fluctuations due to the estrous cycle are likely smaller than the effects of SuHx treatment nor of the effects of sex.

7.2.2 Experimental Measurements

Hemodynamic measurements, as described in Chapter 2.2 and Chapter 3.2, were performed in an opened chest, pericardiectomized setting while animals were externally ventilated. This preparation precludes the effects of intra-thoracic pressures, transmural myocardial pressure gradients, and the pericardial boundary condition. We conducted noninvasive CMRI measurements to investigate these effects. Resultingly, we observed differences between cardiac chamber volumes during end-systole and end-diastole between the closed- and opened-chest measurements (Chapter 2.2 Table 2.8). Importantly, however, we noticed good agreement between the so-called functional measurements of RV output, including the RV ejection fraction, and the stroke volume. These findings are consistent with previous experimental studies, showing agreement between CMRI measures of ejection fraction and invasive catheter measurements[10]. Furthermore, we note that the differences in ejection fraction are of similar magnitude to the decreases in ejection fraction observed in patient studies of PAH[1,11,12]. Therefore, we concluded that effects due to the measurement technique were likely small compared to the differences we sought to recapitulate with the SuHx animal model.

It is well documented that isoflurane and other volatile inhaled anesthetics cause effects on cardiovascular function, such as altered vascular resistance, sympathetic output, or myocardial contractility[13]. However, in our studies with over 400 rats, the effect of isoflurane has been found to be very small when compared to the effects of sugen-hypoxia[14,15], monocrotaline-induced pulmonary hypertension[16–18] and pulmonary arterial banding[19]. While isoflurane and other anesthetics can alter cardiovascular function, we note that isoflurane was carefully regulated throughout terminal surgeries, below reported doses that drastically alter heart rate and hemodynamics[20,21]. Therefore, we concluded that the effects of isoflurane were likely small compared with the differences due to SuHx treatment, and that these effects would be relatively consistent between treatment and sex groups.

Importantly, the animal measurements made in our study were primarily performed during terminal procedures. We primarily described the evolution of RV organ-level systolic and diastolic function via catheter-based hemodynamic measurements. These comparisons were made by averaging groups of individual animals treated with specific durations of SuHx, rather than performed on paired-animal measurements. This decision was made to facilitate a thorough characterization of RV hemodynamics and relate it to underlying tissue and cell changes, however this decision also precluded the ability to easily pair measurements. Therefore, we cannot confirm specific changes to RV function and hemodynamics, but our conclusions are based on statistical analyses of changes to the means of large animal group sizes. Given the heterogeneity of RV remodeling in patients with PAH, an ideal clinical management for patients with PAH might warrant patient-specific phenotyping and treatment strategies. In the context of this study, we aimed to characterize the underlying changes to the RV to better understand the changes to systolic and diastolic function that could support the identification and development of these treatment changes in the future.

While we made functional measurements of isolated cardiac myocytes (sarcomere shortening) that were supported by measurements of the intracellular calcium transient, we note that the isolated preparation does not capture the native myocyte microenvironment, omitting extracellular matrix structural support and inter-cell signaling. Sarcomere shortening in our study was higher than results previously reported in studies using similar isolated preparations[22–24]. However our results do align with other previous studies and are well within physiological ranges of shortening[5,25]. Furthermore, our results are consistent with previous measurements of field-stimulated rat myocytes showing increased shortening in males compared to females[26].

7.2.3 Computational Modeling

The biomechanics model primarily used in our study utilized a simplified RV anatomy which consisted of a fraction of a sphere scaled to animal-specific measurements. The Laplace thin-walled simplifying approximation used to relate intra-ventricular pressure and myocardial wall stress was justified by measurements of the radius to wall thickness ratio, which remained above 6 in all treatment groups (Chapter 4.2 Table 4.2) but does not consider potential transmural wall stress and strain gradients.

One of the model parameters kept constant was the fraction of the spherical cardiac geometry occupied by the RV. The CMRI data presented in Chapter 3.3 suggests that changes to this spherical geometry's fractional components could be considered an important feature of the sex-dependent RV remodeling seen in PAH. As we noted in Chapter 4.2, our model currently describes an independent relationship between this fraction and the constitutive biomechanics model's material parameters, but this description may be a target for future improvements.

Changes to the RV shape could correspond to remodeling of intraventricular septum mechanical properties. Although our mathematical model does account for the effects of septum myocardial hypertrophy, it does not account for intra-ventricular (trans-septal) pressure gradients. In the context of the current study, these modeling assumptions were sufficient as tuning our model's material parameters allowed for accurate predictions of in-vivo measurements across all studied groups.

7.3 Future directions

While much has been done to further our understanding of RV remodeling in PAH, future work remains. As alluded to in Chapter 7.1, more robust computational models that incorporate rat-specific geometric changes may provide further insights into the role of RV shape change on RV biomechanics. Work by Odeigah *et al.* demonstrated the insights that complementary studies using Laplace-type and finite-element computational models could provide for understanding longitudinal RV biomechanics. One such application of these modeling frameworks would be the study of multiple longitudinal timepoints in female and ovariectomized female rats. Our results suggest these models could reveal evolving biomechanical properties of the septum wall because of the dramatic changes to the trans-septal pressure gradient in PAH. These descriptions, alongside detailed descriptions of the shape-changes to the RV free wall could benefit our understanding of the role of RV wall compliance and RV dilation as an adaptive or detrimental long-term mechanism in PAH.

One of the key findings of this work was the role of diastolic stiffening in the evolution of RV hemodynamics during PAH. However, the mechanisms responsible for and regulating the progression of diastolic stiffening remains unclear. Much work has done here and previously to describe the deposition and remodeling of myocardial collagens, however none of the investigated changes fully explained the progressive stiffening of the RV myocardium. One such ongoing project in our group aims to characterize the extracellular matrix collagen fibrillar structure. Ongoing and future research aims to decouple myocardial stiffening into contributions by 1) chemically decellularizing the myocardium and characterizing the remaining matrix scaffold at the tissue scale and by 2) enzymatically digesting the myocardium to isolate and characterize the cardiac myocytes at the cell scale. By obtaining passive force-length measurements of isolated myocytes, we would learn about the myocyte-derived contributions to passive stiffening, usually attributed to phosphorylation of the protein titin. These results would also validate the differential stiffening seen at the organ level across multiple time points in male SuHx and between male, female, and OVX female SuHx.

Future studies explaining the affected molecular and cellular mechanisms that regulate diastolic calcium are motivated. It remains unclear whether alterations in the regulation, phosphorylation, and function of ryanodine receptors resulting in the inability to maintain calcium reserves in the SR may contribute to contractile dysfunction in the long-term[27]. It is possible that alterations in the regulation, phosphorylation, and function of SERCA also impairs the sequestration of calcium following contraction. The SR membrane protein phospholamban is another key regulator of SERCA and of myocyte diastolic function, reported to be altered in PAH[28]. Future investigation of the expression, quantity, phosphorylation, and function of these proteins at multiple timepoints and considerate of sex are warranted. These molecular mechanisms may explain the changes to diastolic calcium observed in this work and may contribute to long-term remodeling of myocyte contractility.

7.4 References

1. Rain S, Handoko ML, Trip P, et al. Right ventricular diastolic impairment in patients with pulmonary arterial hypertension. *Circulation*. 2013;128(18):2016-2025.

2. Rain S, Andersen S, Najafi A, et al. Right Ventricular Myocardial Stiffness in Experimental Pulmonary Arterial Hypertension. *Circ Heart Fail*. 2016;9(7):e002636.

3. D’Andrea A, Vriz O, Carbone A, et al. The impact of age and gender on right ventricular diastolic function among healthy adults. *J Cardiol*. 2017;70(4):387-395.

4. Thenappan T, Ormiston ML, Ryan JJ, Archer SL. Pulmonary arterial hypertension: pathogenesis and clinical management. *The BMJ*. 2018;360:j5492.

5. Howlett SE. Age-associated changes in excitation-contraction coupling are more prominent in ventricular myocytes from male rats than in myocytes from female rats. *Am J Physiol Heart Circ Physiol*. 2010;298(2):H659-670.

6. Lahm T, Douglas IS, Archer SL, et al. Assessment of Right Ventricular Function in the Research Setting: Knowledge Gaps and Pathways Forward. An Official American Thoracic Society Research Statement. *Am J Respir Crit Care Med*. 2018;198(4):e15-e43.

7. van Wezenbeek J, Groeneveldt JA, Llucià-Valldeperas A, et al. Interplay of sex hormones and long-term right ventricular adaptation in a Dutch PAH-cohort. *J Heart Lung Transplant*. 2022;41(4):445-457.

8. Hester J, Ventetuolo C, Lahm T. Sex, Gender, and Sex Hormones in Pulmonary Hypertension and Right Ventricular Failure. *Compr Physiol*. 2019;10(1):125-170.

9. James AF, Arberry LA, Hancox JC. Gender-related differences in venticular myocyte repolarization in the guinea pig. *Basic Res Cardiol*. Published online 2004.

10. Andersen S, Schultz JG, Andersen A, et al. Effects of bisoprolol and losartan treatment in the hypertrophic and failing right heart. *J Card Fail*. 2014;20(11):864-873.

11. Li JH, Zhang HD, Wang ZZ, et al. Acute iloprost inhalation improves right ventricle function in pulmonary artery hypertension: A cardiac magnetic resonance study. *Front Pharmacol*. 2019;9:1550.

12. Swift AJ, Capener D, Johns C, et al. Magnetic resonance imaging in the prognostic evaluation of patients with pulmonary arterial hypertension. *Am J Respir Crit Care Med*. 2017;196(2):228-239.

13. Loushin MK. The Effects of Anesthetic Agents on Cardiac Function. In: Iaizzo PA, ed. *Handbook of Cardiac Anatomy, Physiology, and Devices*. Humana Press; 2005:171-180.

14. Kwan ED, Velez-Rendon D, Zhang X, et al. Distinct time courses and mechanics of right ventricular hypertrophy and diastolic stiffening in a male rat model of pulmonary arterial hypertension. *Am J Physiol - Heart Circ Physiol*. Published online 2021.

15. Kwan ED, Hardie BA, Garcia KM, Mu H, Wang TM, Valdez-Jasso D. Sex-dependent Remodeling of Right-Ventricular Function in a Rat Model of Pulmonary Arterial Hypertension. *Am J Physiol-Heart Circ Physiol*. Published online June 7, 2024.

16. Vélez-Rendón D, Zhang X, Gerringer J, Valdez-Jasso D. Compensated right ventricular function of the onset of pulmonary hypertension in a rat model depends on chamber remodeling and contractile augmentation. *Pulm Circ*. 2018;8(4):1-13.

17. Gerringer JW, Wagner JC, Vélez-Rendón D, Valdez-Jasso D. Lumped-parameter models of the pulmonary vasculature during the progression of pulmonary arterial hypertension. *Physiol Rep*. 2018;6(3):e13586.

18. Vélez-Rendón D, Pursell ER, Shieh J, Valdez-Jasso D. Relative Contributions of Matrix and Myocytes to Biaxial Mechanics of the Right Ventricle in Pulmonary Arterial Hypertension. *J Biomech Eng*. 2019;141(9):091011.

19. Hill MR, Simon MA, Valdez-Jasso D, Zhang W, Champion HC, Sacks MS. Structural and Mechanical Adaptations of Right Ventricle Free Wall Myocardium to Pressure Overload. *Ann Biomed Eng*. 2014;42(12):2451-2465.

20. Yang B, Liang G, Khojasteh S, et al. Comparison of Neurodegeneration and Cognitive Impairment in Neonatal Mice Exposed to Propofol or Isoflurane. *PLoS ONE*. 2014;9(6):e99171.

21. Eis S, Kramer J. Anesthesia Inhalation Agents and Their Cardiovascular Effects. In: *StatPearls*. StatPearls Publishing; 2024.

22. Lai N, Lu W, Wang J. Ca2+ and ion channels in hypoxia-mediated pulmonary hypertension. *Int J Clin Exp Pathol*. 2015;8(2):1081-1092.

23. Sabourin J, Boet A, Rucker-Martin C, et al. Ca2+ handling remodeling and STIM1L/Orai1/TRPC1/TRPC4 upregulation in monocrotaline-induced right ventricular hypertrophy. *J Mol Cell Cardiol*. 2018;118:208-224.

24. Fowler ED, Drinkhill MJ, Norman R, et al. Beta1-adrenoceptor antagonist, metoprolol attenuates cardiac myocyte Ca2+ handling dysfunction in rats with pulmonary artery hypertension. *J Mol Cell Cardiol*. 2018;120.

25. Farrell SR, Ross JL, Howlett SE. Sex differences in mechanisms of cardiac excitation-contraction coupling in rat ventricular myocytes. *Am J Physiol - Heart Circ Physiol*. Published online 2010.

26. Curl CL, Wendt IR, Kotsanas G. Effects of gender on intracellular [Ca2+] in rat cardiac myocytes. *Pflugers Arch*. Published online 2001.

27. Huang Y, Lei C, Xie W, et al. Oxidation of Ryanodine Receptors Promotes Ca2+ Leakage and Contributes to Right Ventricular Dysfunction in Pulmonary Hypertension. *Hypertension*. 2021;77(1):59-71.

28. Zhang J, Cao Y, Gao X, et al. Lipopolysaccharide acutely suppresses right-ventricular strain in rats with pulmonary artery hypertension. *Pulm Circ*. 2017;8(1):2045893217744504.